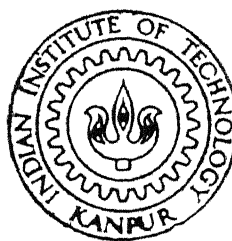


DYNAMICS OF A BEARINGLESS HELICOPTER ROTOR BLADE WITH A NON-LINEAR ELASTOMERIC CONSTRAINT

by

Goutam Pohit



TH
ME/1999/P
P754d

DEPARTMENT OF MECHANICAL ENGINEERING
INDIAN INSTITUTE OF TECHNOLOGY KANPUR

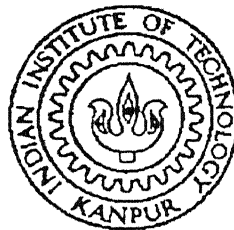
February, 1999

DYNAMICS OF A BEARINGLESS HELICOPTER ROTOR BLADE WITH A NON-LINEAR ELASTOMERIC CONSTRAINT

A Thesis Submitted
In Partial Fulfilment of the Requirements
for the Degree of
Doctor of Philosophy

by

Goutam Pohit



to the
DEPARTMENT OF MECHANICAL ENGINEERING
INDIAN INSTITUTE OF TECHNOLOGY KANPUR
INDIA

February, 1999

74 JUN 2000 ME
CENTRAL LIBRARY
I. I. T., KANPUR

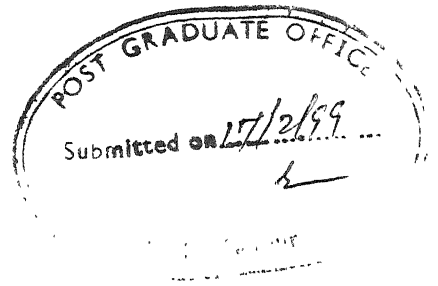
A 131087

TH
ME/1977 P

P78110



A131087



Certificate

It is to certify that the work contained in the thesis entitled **Dynamics of a Bearingless Helicopter Rotor Blade with a Non-linear Elastomeric Constraint** by Goutam Pohit, has been carried out under our supervision and that this work has not been submitted elsewhere for a degree.


A. K. Mallik

Department of Mechanical Engineering
IIT Kanpur


C. Venkatesan

Department of Aerospace Engineering
IIT Kanpur

February, 1999

Acknowledgment

It is a rare opportunity to have Prof. A. K. Mallik and Prof. C. Venkatesan as my thesis supervisors. I am highly indebted to them for their inspiring guidance and useful discussions I had with them throughout the course of this work.

I would like to thank to all my friends in Vibration Laboratory, especially Goutam Chakroborty, Ahmed Ali Khan, Animesh Chatterjee and Chandrashekhar for their help and suggestions. It was a pleasure to work with them during my stay at I.I.T. My special thanks to Arun Saha for his kind assistance on different occasions.

Finally, I wish to thank my wife, Jhilly, and daughter Jhimkini, without whose patience, encouragement, and support, this work might never have been completed.

Goutam Pohit

Synopsis

The dynamic characteristics of the rotor blades play a significant role in the overall performance and stability of a helicopter. There has been a continued effort to develop a mechanically simple yet efficient rotor blade and hub configuration. Early rotor blades were provided with flap (out-of-plane) and lag (in-plane) hinges at the root of the blade. These rotor systems having complicated construction are usually referred to as articulated rotors. With the advancement in fibre-reinforced composite material technology, increasing emphasis has been placed on the development of hingeless and bearingless rotor systems. Both articulated and hingeless rotors are provided with external hydraulic dampers to increase damping in the lag mode and thereby to avoid aeroelastic and/or aeromechanical instabilities. In a bearingless rotor, external damper is eliminated by incorporating a specialised elastomer with high loss factor.

For the last two decades, considerable effort has been put in by industry and R & D establishments to develop a bearingless main rotor. Though a bearingless rotor is mechanically simple, its dynamic analysis becomes very complicated because of multiple load paths, presence of non-linear elastomeric damper and existence of kinematic constraint at the pitch link. With the consolidation of rotor blade structural dynamic and aeroelastic formulation applicable for articulated and hingeless rotor blades, academic research has now focussed on the fundamental understanding of the effects of non-linearities of elastomer on the dynamics of bearingless rotor blades.

In general, the elastomer used in a bearingless rotor exhibits highly non-linear characteristics both in stiffness and damping with respect to the amplitude of deformation. It is expected that due to the presence of the elastomer, the lag and flap frequencies should dependent on the amplitude of motion which is a typical feature of a non-linear system. But so far no attempt has been made to study the effect of amplitude on the frequencies of a bearingless blade. Although several researchers have proposed different non-linear models for the elastomer, while performing the stability analysis, only linearised equations of the blade and elastomer are solved. In addition, all the aeroelastic response studies of the rotor blade have focussed on the steady state response. No information is available on the transient response characteristics of a bearingless rotor with the inclusion of kinematic constraint and multiple load paths.

The major objectives of the present study are as follows.

- (i) Formulate a simple non-linear model to capture the non-linear stiffness and damping characteristics of an elastomer.
- (ii) Study the influence of non-linear stiffness of the elastomer on the free vibration characteristics of uncoupled flap and lag dynamics of the blade.
- (iii) Examine the amplitude dependent stability of an idealised bearingless rotor system under ground resonance.

and

- (iv) Analyse the transient response of an isolated bearingless rotor blade undergoing coupled flap-lag-torsional deformations in hovering condition. The transient response results are compared with those of a hingeless blade with identical blade properties.

A brief outline of the chapterwise contents of the thesis is summarised below. ✓

The experimental data on the non-linear stiffness and damping properties of an elastomer show very weak dependence on frequency in the range of interest for rotor blade analysis. In the light of this observation, the non-linear characteristics of the

elastomer is modelled in Chapter 2 by a parallel combination of a non-linear spring, a Coulomb damper and a hysteretic damper. The model is kept in a simple form so that it can be easily integrated with the blade model. The parameters of the analytical model are obtained by correlating with the experimental data available in the open literature.

In Chapter 3, both linear and non-linear free vibrations of an idealised bearingless rotating blade undergoing uncoupled flap and lag bending have been studied. First a linear problem has been solved using two different solution techniques, one based on power series expansion and the other based on the Rayleigh-Ritz method. The natural frequencies are obtained for different values of spring stiffnesses and elastomer locations. In the non-linear analysis, a numerical-perturbation technique based on multiple-time-scale is formulated to determine the frequency-amplitude relationship for the rotating blade.

In Chapter 4, an amplitude dependent stability analysis has been carried out for a coupled rotor/fuselage system under ground resonance condition. The stability analysis is carried out for different locations and amplitudes of motion of the elastomer.

In Chapter 5, a suitable numerical technique has been formulated to study the transient response of an isolated bearingless rotor blade to a step control pitch input. The blade is assumed to undergo coupled flap-lag-torsional deformation in hovering condition. A time varying inflow model (based on the dynamic inflow model) has been used for the analysis. The expressions for aerodynamic loads are treated by an implicit formulation. The study is carried out for different locations of the elastomer and pitch link. The transient response characteristics of the bearingless rotor blade is compared with that of the hingeless blade. The comparison is made to highlight the difference in their response behaviours. A quantitative measure of the aeroelastic couplings (pitch-flap, pitch-lag), based on the steady state response has been proposed and an attempt

is made to relate the couplings and the response characteristics of the blade.

An analysis has been carried out, in Chapter 6, to investigate the phenomenon of limit cycle oscillation and elastomer model. Finally, in Chapter 7, the overall conclusions are included. The major conclusions of the present thesis are summarised below.

- (i) Using an idealised model for a bearingless rotor, both linear and non-linear free vibrations of the rotating blade have been studied. Two different solution techniques are used for the linear analysis. The natural frequencies obtained by both techniques are in excellent agreement. The results of the non-linear free vibration analysis of the rotor blade indicate that upto a fairly high-value of amplitude, a seventh order approximation of the non-linear spring is sufficient to correctly predict the frequency-amplitude relationship.
- (ii) It is revealed from the ground resonance stability analysis that the elastomer amplitude does not significantly alter the stability of the system in the region of maximum instabilities. However, it exhibits appreciable influence in other regions. The elastomer locations seem to have considerable influence on the stability of the system. The results indicate that for a given location of the elastomer, there is an optimum location for the torque tube attachment.
- (iii) The transient response analysis to a step control pitch input is performed for both hingeless and bearingless rotor blade configurations having identical blade properties. It is observed that there is a qualitative difference in the nature of the response as well as in the dynamic overshoot of the rotor thrust for the two types of blades.
- (iv) It is noticed that the transient response characteristics of a bearingless blade depends on the pitch link locations. In particular, it is observed that the blade response with trailing edge pitch link configuration is significantly different from that of a leading edge configuration. For certain trailing edge configurations, the blade exhibits a

divergence transient response indicating instability. The reason for these significant differences in the response behaviour can be attributed to the changes in the aeroelastic couplings and the constraint loads due to the pitch link. The aeroelastic coupling measures are observed to be dependent on the magnitude of the control input, exhibiting a non-linear relationship.

(v) The results of the transient response characteristics with two different elastomer models (for the same experimental data) indicate that the phenomenon of limit cycle oscillation is highly dependent on the elastomer model. Therefore, sufficient care must be exercised in modelling the elastomer.

Contents

Certificate	i
Acknowledgment	ii
Synopsis	iii
Table of Contents	viii
List of Figures	xi
List of Tables	xvi
List of Symbols	xvii
1 INTRODUCTION	1
1.1 Introduction	1
1.2 Literature Review	4
1.2.1 Elastomeric Damper	4
1.2.2 Structural Modelling of Rotor Blades	8
1.2.3 Stability and Response Analyses	10
1.2.4 Non-linear Analysis	18
1.3 Objectives of the Present Study	20
2 ELASTOMERIC DAMPER MODEL	25
2.1 Introduction	25

2.2	Formulation of the Model	28
2.2.1	System Identification	29
2.3	Results and Discussion	30
2.4	Summary	31
3	NON-LINEAR DYNAMICS OF UNCOUPLED FLAP AND LAG MOTION	40
3.1	Introduction	40
3.2	Bearingless Rotor Model	41
3.3	Linear Analysis	42
3.3.1	Power Series	42
3.3.2	Rayleigh-Ritz Method	47
3.4	Non-Linear Analysis	50
3.4.1	Non-Linear Equation of Motion	50
3.5	Results and Discussion	57
3.5.1	Isolated Flap Motion	57
3.5.2	Isolated Lag Motion	62
3.6	Summary	64
4	AMPLITUDE DEPENDENT STABILITY OF AN IDEALISED BEARINGLESS ROTOR UNDER GROUND RESONANCE	78
4.1	Introduction	78
4.2	Formulation of Equations of Motion	79
4.2.1	Blade Equations	80
4.3	Solution Procedure	83
4.4	Results and Discussion	84
4.4.1	Baseline Configuration	84
4.4.2	Influence of Elastomer Location (ξ_1, ξ_2)	85
4.5	Summary	88

5	TRANSIENT RESPONSE IN HOVER TO A STEP CONTROL PITCH INPUT	99
5.1	Introduction	99
5.2	Formulation of Equation of Motion	100
5.2.1	Assumptions	101
5.2.2	Ordering Scheme	101
5.2.3	Coordinate Systems	102
5.2.4	Blade Model	104
5.2.5	Elastomeric Damper Model	110
5.2.6	Aerodynamic Model	112
5.2.7	Kinematic Constraint due to Pitch Link Motion	118
5.2.8	Treatment of the Axial Degree of Freedom	119
5.2.9	Equations of Motion	120
5.3	Solution Procedure	121
5.4	Results and Discussion	123
5.4.1	Hingeless Rotor Blade	123
5.4.2	Bearingless Rotor Blade	126
5.5	Summary	136
6	ELASTOMERIC DAMPER MODEL AND LIMIT CYCLE OSCILLATION	171
6.1	Introduction	171
6.2	Formulation of Elastomer Model	173
6.3	Results and Discussion	173
6.4	Summary	174
7	CONCLUSIONS	179
A	Derivation of Strain Expressions	183
A.1	Coordinate Transformation	183
A.2	Kinematics of Deformation	186
	REFERENCES	

List of Figures

1.1	Articulated rotor hub and blade configuration.	22
1.2	Hingeless rotor hub and blade configuration.	23
1.3	Bearingless rotor hub and blade configuration.	24
2.1	Non-linear dynamic characteristics of a visco-elastic material.	32
2.2	Hysteresis cycles of a non-linear material about zero equilibrium point.	32
2.3	Experimental data taken from Ref. 24.	33
2.4	Experimental data taken from Ref. 23.	34
2.5	Experimental data taken from Ref. 26.	35
2.6	Elastomer model.	36
2.7	Variation of G' (in-phase stiffness) with amplitude.	37
2.8	Variation of G'' (quadrature stiffness) with amplitude.	37
2.9	Hysteresis loops of the elastomer model for different amplitude of motion.	38
3.1	Idealised bearingless rotor blade.	65
3.2	Free-body diagram of the bearingless rotor blade and torque tube. . . .	66
3.3	Elastic deformation of the rotating blade.	67
3.4	First mode shape of the rotating beam in flap mode for various values of ξ_2	68
3.5	Second mode shape of the rotating beam in flap mode for various values of ξ_2	68
3.6	Third mode shape of the rotating beam in flap mode for various values of ξ_2	69

3.7	Influence of different geometric configurations (ξ_1 and ξ_2) on the first natural frequency in flap mode. $K^* = 2000$	69
3.8	Influence of different geometric configurations (ξ_1 and ξ_2) on the second natural frequency in flap mode. $K^* = 2000$	70
3.9	Influence of different geometric configurations (ξ_1 and ξ_2) on the third natural frequency in flap mode. $K^* = 2000$	70
3.10	Variation of the first non-linear frequency with amplitude of oscillation in flap mode.	71
3.11	Variation of the second non-linear frequency with amplitude of oscillation in flap mode.	71
3.12	Variation of the third non-linear frequency with amplitude of oscillation in flap mode.	72
3.13	Influence of different orders of approximation on the first non-linear natural frequency in flap mode.	72
3.14	First mode shape of the rotating beam in lag mode.	73
3.15	Second mode shape of the rotating beam in lag mode.	73
3.16	Influence of different geometric configurations (ξ_1 and ξ_2) on the first natural frequency in lag mode. $K^* = 2000$	74
3.17	Influence of different geometric configurations (ξ_1 and ξ_2) on the second natural frequency in lag mode. $K^* = 2000$	74
3.18	Variation of the first non-linear frequency with amplitude of oscillation in lag mode.	75
3.19	Variation of the second non-linear frequency with amplitude of oscillation in lag mode.	75
4.1	Idealised model of the coupled rotor/fuselage system.	89
4.2	Variation of modal frequencies as a function of rotational speed.	90
4.3	Variation of modal damping as a function of rotational speed.	90
4.4	Effect of amplitude of motion of the elastomer on modal damping.	91
4.5	Modal damping for different locations (ξ_1) of the elastomer.	92
4.6	Modal damping for different locations (ξ_2) of the torque tube attachment.	93

4.7	Modal damping for different locations (ξ_2) of the torque tube attachment.	94
4.8	Variation of maximum instability in roll mode for different combinations of ξ_1 and ξ_2 .	95
4.9	Optimum combination of ξ_1 and ξ_2 .	95
4.10	Effect of support damping on stability.	96
4.11	Effect of support damping on stability.	97
5.1	Hub fixed rotating coordinate system.	138
5.2	Undeformed cross-section fixed rotating coordinate system.	138
5.3	Undeformed curvilinear cross-sectional coordinate system.	139
5.4	Deformed cross-sectional coordinate system and components of blade velocity.	139
5.5	Components of sectional aerodynamic forces.	140
5.6	Bearingless rotor blade with pitch link at the leading edge side.	141
5.7	Hingeless blade response to a step pitch input.	142
5.8	Variation of inflow for hingeless blade to a step pitch input.	143
5.9	Variation of thrust coefficient for hingeless blade to a step pitch input.	143
5.10	Variation of $C_{T_{max}}/C_{T_s}$ for hingeless blade for various rates of pitch input.	144
5.11	Comparison of experimental and calculated ratios of $C_{T_{max}}/C_{T_s}$ for hingeless blade for various rates of pitch input.	145
5.12	Bearingless blade response to a step control pitch input.	146
5.13	Variation of inflow for bearingless blade to a step control pitch input.	147
5.14	Variation of constraint force F_P for bearingless blade to a step control pitch input.	147
5.15	Variation of out of plane root shear and thrust coefficient for bearingless blade to a step control pitch input.	148
5.16	Variation of out of plane root moment for bearingless blade to a step control pitch input.	148
5.17	Variation of in-plane root shear for bearingless blade to a step control pitch input.	149

5.18	Variation of in-plane root moment for bearingless blade to a step control pitch input.	149
5.19	Variation of torsional root moment for bearingless blade to a step control pitch input.	150
5.20	Bearingless blade response with different values for step control pitch input.	151
5.21	Bearingless blade response with different locations of the elastomer (ξ_1).	152
5.22	Bearingless blade response with different locations of the elastomer (ξ_1).	153
5.23	Bearingless blade response with different locations of the elastomer (ξ_1).	154
5.24	Bearingless blade response with different values for step control pitch inputs.	155
5.25	Bearingless blade response in flap mode with different pitch link locations.	156
5.26	Bearingless blade response in lag mode with different pitch link locations.	156
5.27	Bearingless blade response in torsional mode with different pitch link locations.	157
5.28	Variation of inflow for bearingless blade with different pitch link locations.	157
5.29	Variation of constraint force F_P for bearingless blade with different pitch link locations.	158
5.30	Variation of out of plane root shear for bearingless blade with different pitch link locations.	159
5.31	Variation of out of plane root moment for bearingless blade with different pitch link locations.	160
5.32	Variation of in-plane root shear for bearingless blade with different pitch link locations.	161
5.33	Variation of in-plane root moment for bearingless blade with different pitch link locations.	162
5.34	Variation of torsional root moment for bearingless blade with different pitch link locations.	163
5.35	Bearingless blade response for different pitch link locations.	164

5.36	Influence of pitch link location (b) and step control pitch input (w_p^s) on pitch-flap coupling of a bearingless blade. $a = 0.03$	165
5.37	Influence of pitch link location (b) and step control pitch input (w_p^s) on pitch-lag coupling of a bearingless blade. $a = 0.03$	165
5.38	Influence of pitch link location (b) and step control pitch input (w_p^s) on pitch-flap coupling of a bearingless blade. $a = 0.05$	166
5.39	Influence of pitch link location (b) and step control pitch input (w_p^s) on pitch-lag coupling of a bearingless blade. $a = 0.05$	166
6.1	Elastomer Model 2 with Rayleigh type damping.	175
6.2	Comparison of the experimental data with Model 1 and Model 2. . . .	175
6.3	Transient response in lag mode with Model 2 (with aerodynamic loading).176	
6.4	Transient response in lag mode with Model 1 (with aerodynamic loading).176	
6.5	Transient response in lag mode with Model 2 (without aerodynamic loading).	177
6.6	Transient response in lag mode with Model 1 (without aerodynamic loading).	177
A.1	Deformation sequence and Euler angles.	192

List of Tables

2.1	System parameters for the elastomeric damper model.	39
3.1	Blade data.	76
3.2	Natural frequencies of the rotating blade in flap mode without elastomer.	76
3.3	Natural frequencies of the rotating blade in flap mode with a linear elastomer.	76
3.4	Natural frequencies of the rotating blade in lag mode without elastomer.	77
3.5	Natural frequencies of the rotating blade in lag mode with a linear elastomer.	77
4.1	Input data for ground resonance analysis.	98
5.1	Input data for transient response analysis.	167
5.2	Variation of aeroelastic coupling with b and control input w_p^s . $a = 0.03$	168
5.3	Variation of aeroelastic coupling with b and control input w_p^s . $a = 0.05$	169
5.4	Variation of aeroelastic coupling with a and control input w_p^s . $b = 0.15$	170
6.1	System parameters of the elastomeric damper Model 1 and Model 2.	178

List of Symbols

a, b	geometric parameters defining the locations of pitch link
a_1	lift curve slope
\bar{a}	non-dimensional parameter, $\frac{EI}{m\Omega^2 L^4}$
A	cross-sectional area of the blade
A_i, \hat{A}_i	tip amplitude of motion of the blade in i th mode
b_1	blade semi chord
C_{eq}, K_{eq}	equivalent damping and stiffness coefficients of the elastomer
C^*	non-dimensional damping coefficient of the elastomer, $\frac{C_{eq}}{m\Omega L}$
\bar{C}	non-dimensional damping, $C^*\hat{\psi}_1^2$
C_k, D_k, E_K	coefficients of power series
C_x, C_y	non-dimensional linear damping coefficients of the support structure in roll and pitch mode, respectively.
C_{do}	blade profile drag coefficient
D	profile drag of the blade per unit span
D_o	amplitude of excitation force on elastomer
$\hat{e}_x, \hat{e}_y, \hat{e}_z$	unit vectors associated with hub fixed rotating coordinate system
$\hat{e}_{x1}, \hat{e}_{y1}, \hat{e}_{z1}$	unit vectors associated with undeformed cross-section fixed rotating coordinate system
$\hat{e}_x, \hat{e}_\eta, \hat{e}_\zeta$	unit vectors associated with the undeformed curvilinear cross-sectional coordinate system
$\hat{e}_{x'}, \hat{e}_{\eta'}, \hat{e}_{\zeta'}$	unit vectors associated with the deformed curvilinear cross-sectional coordinate system
$\mathbf{E}_x, \mathbf{E}_\eta, \mathbf{E}_\zeta$	base vectors associated with a point on the deformed elastic axis of the blade
EI	flexural rigidity of the blade
$EA, EA\eta_a, EI_{\eta\eta}, EI_{\zeta\zeta}$	sectional integrals of the blade
EAC_o, GJ, EAC_3	
EAC_1, EAD_3, EAD_2	

$f_{i,j}$	strain tensor in curvilinear coordinate system
F	coulomb damping coefficient
F_P	load at the pitch link
g	determinant of metric tensor $[g_k \cdot g_i]$
$\mathbf{g}_x, \mathbf{g}_\eta, \mathbf{g}_\zeta$	undeformed base vectors
$\mathbf{G}_x, \mathbf{G}_\eta, \mathbf{G}_\zeta$	deformed base vectors
G', G''	amplitude-dependent in-phase stiffness and quadrature stiffness of the elastomer
h	hysteretic damping coefficient of elastomer Model 1
h_1, h_3	damping coefficients of elastomer Model 2
\dot{h}_f	aerofoil plunging velocity
\bar{h}	height of the rotor above fuselage C.G.
H, Y	in-plane hub forces in non-rotating frame
I_x, I_y	non-dimensional mass moment of inertia of the support structure about the C.G. in roll and pitch mode, respectively
$Im_{\eta\eta}, Im_{\zeta\zeta}, Im_{\eta\zeta}$	moment of inertia of blade cross-section
Im	$Im = Im_{\eta\eta} + Im_{\zeta\zeta}$
K^*	non-dimensional spring stiffness, $\frac{K_1 L^3}{EI}$
K_1, K_3, K_5, K_7	stiffness parameters of the non-linear spring
K_x, K_y	non-dimensional stiffnesses of the support structure in roll and pitch mode, respectively
k_β, k_ζ	pitch-flap and pitch-lag couplings
L	blade length
L_1, L_2	length of the blade segments
L_A	aerodynamic lift per unit span
L_u, L_v, L_w	components of aerodynamic forces in the $(\hat{e}_x, \hat{e}_y, \hat{e}_z)$ system
m	mass per unit length of the blade
\bar{m}	apparent mass
M_A	aerodynamic moment per unit span
M_b^C	bending moment at point C due to pitch link load F_P
M_t^C	torsional moment at point C due to pitch link load F_P
\mathbf{M}, \mathbf{C} and \mathbf{K}	mass, damping and stiffness matrices for the isolated rotor blade problem
$\bar{\mathbf{M}}, \bar{\mathbf{C}}$ and $\bar{\mathbf{K}}$	mass, damping and stiffness matrices for the ground resonance problem
n	number of assumed modes
$n1, n2, n3$	number of rotating modes
N	number of blades
ND	number of experimental data points
p	non-dimensional parameter, $\xi_h \int_0^1 \bar{\phi}_1 d\xi$

p_i	generalised coordinates in torsional motion
p_{ji}	participating factor in i th mode
$p_{\eta'}, p_{\zeta'}$	components of aerodynamic forces per unit span in the $\hat{e}_{\eta'}$ and $\hat{e}_{\zeta'}$ directions, respectively
P	modal matrix
P_{NL}	vector representing non-linear terms
q_i	generalised coordinates in lag motion
q_x, q_y, q_z	components of aerodynamic moment per unit span in the $(\hat{e}_x, \hat{e}_y, \hat{e}_z)$ system
Q	generalised forces associated with aerodynamic loading
r_i	generalised coordinates in flap motion
R	position vector of a point on the deformed blade
R_o	position vector of a point on the deformed elastic axis
s_j	complex eigenvalues, $s_j = \sigma_j \pm i\omega_j$
S_v, S_r	in-plane and radial shear forces at the blade root
t	time
T	kinetic energy
\bar{T}	total thrust generated by the rotor
T_o	fast time scale associated with changes occurring with frequency close to ω_i
T_1, T_2, T_3	slow time scale
T	transformation matrix
\bar{u}	axial displacement
U_1	strain energy of the blade
U_2	strain energy of the spring
U_l, U_f	strain energy of the spring in lag and flap mode, respectively
U	velocity vector of a point on the elastic axis of the blade relative to air
U_R	resultant airfoil velocity relative to air
$U_{x'}, U_{\eta'}, U_{\zeta'}$	components of U in the $(\hat{e}_{x'}, \hat{e}_{\eta'}, \hat{e}_{\zeta'})$ system
v, v_i	non-dimensional in-plane displacement
v_{tip}	tip response in the lag mode
$(v_{tip})_{mean}$	mean value of tip response in the lag mode
\bar{v}, \bar{v}_i	in-plane displacement of the blade
V_f	free-stream velocity of aerofoil
V	velocity vector of a point on the blade with respect to inertial reference frame
V_A	velocity vector due to inflow
V_o	velocity vector of a point on the blade elastic axis
V_x^A, V_y^A, V_z^A	components of V_A in the $(\hat{e}_x, \hat{e}_y, \hat{e}_z)$ system

V_x^o, V_y^o, V_z^o	components of V_o in the $(\hat{e}_x, \hat{e}_y, \hat{e}_z)$ system
\bar{w}, \bar{w}_i	out-of-plane displacement of the blade
w_C	flap bending deflection at point C
w_{tip}	tip response in the flap mode
$(w_{tip})_s$	steady state value of tip response in flap mode
w'_C	flap bending slope at point C
w_P	vertical displacement of pitch link at point P
w_P^s	step control pitch input
\bar{W}_i	non-dimensional in-plane and out-of-plane displacement defined in Chapter 3
\bar{W}_i	in-plane and out-of-plane displacement defined in Chapter 3
\bar{x}, \bar{y}	perturbational motion of the hub centre
x_A	aerodynamic centre offset from elastic axis
y_1, y_2, y_3	local cartesian coordinate system
y_i	i th generalised coordinate in lag motion
z_i	i th generalised coordinate in flap motion
$z_u, z_v, z_w, z_{v'}, z_{w'}, z_\phi, \bar{z}_u, \bar{z}_v, \bar{z}_w, \bar{z}_{v'}, \bar{z}_{w'}, \bar{z}_\phi$	notation used for writing the blade kinetic energy in concise form
z_{im}	i th generalised coordinate in lag mode of the m th blade
z_{ic}, z_{is}	cyclic lag coordinates in the i th mode
z_p, z_r	progressive and regressive lag mode, respectively

Greek Symbols

α	amplitude of warping
$\alpha_1, \alpha_3, \alpha_5, \alpha_7$	non-dimensional spring stiffnesses
α_A	effective local angle of attack of the blade
γ	Lock number
$\bar{\gamma}_i$	i th rotating mode shape in torsional motion
$\gamma_{\eta\zeta}, \gamma_{x\zeta}, \gamma_{x\eta}$	engineering shear strain components
$(\delta W_e)_f$	virtual work due to distributed forces
$(\delta W_e)_m$	virtual work due to distributed moments
δW_{link}	virtual work due to pitch link load
Δ_l, Δ_f	spring deformations in lag and flap mode, respectively
ϵ	non-dimensional parameter representing the order of magnitude of elastic blade bending slope
ϵ_{ij}	strain tensor in the local cartesian coordinate system
ϵ_{xx}	axial strain at the elastic axis

θ	blade pitch angle with respect to free stream
θ_{tw}	blade pretwist angle
θ_{in}	blade pitch angle due to pitch step input
θ_x, θ_y	body modes in roll and pitch, respectively
$\theta_x, \theta_\eta, \theta_\zeta$	Euler angles used to describe the transformation from the undeformed coordinate system to the deformed coordinate system
$\kappa_\eta, \kappa_\zeta$	deformed curvature of the blade
λ	non-dimensional inflow velocity or eigenvalue
ν	inflow velocity
ξ	non-dimensional length, $\frac{x}{L}$
ξ_1, ξ_2	non-dimensional blade segments, $\frac{L_1}{L}, \frac{L_2}{L}$
ξ_h	non-dimensional rotor height, $\frac{h}{L}$
ρ	mass density of the blade
ρ_A	density of air
σ_j	modal damping (real part of s_j)
$\sigma_{xx}, \sigma_{x\eta}, \sigma_{x\zeta}$	components of stress tensor
τ	non-dimensional time, Ωt
τ_o	initial twist of the blade
ϕ	torsional elastic deformation of the blade
ϕ_o	second order elastic deformation of the blade
ϕ_{tip}	tip response in torsional mode
$\phi_{0.75}$	torsional response of the blade at $0.75L$ from the root
ϕ_C	torsional deformation at point C
Φ_1, Φ_2	error
$\hat{\phi}_i$	comparison functions
$\hat{\phi}'_i, \hat{\phi}''_i$	first and second derivatives of $\hat{\phi}_i$ with respect to ξ
$\hat{\phi}_i$	i th rotating mode shape in lag motion
ψ_m	azimuth angle of the m th blade
Ψ	out-of-plane warping function for the cross-section due to torsion
$\bar{\psi}_i^l, \bar{\psi}_i^f$	normalised deformation of the spring in lag and flap mode, respectively
$\hat{\psi}_i^l, \hat{\psi}_i^f$	deformation of the spring in lag and flap mode, respectively
$\bar{\varphi}_i$	i th rotating mode shape in flap motion
$\zeta_{\theta_x}, \zeta_{\theta_y}$	damping ratio of the support in roll and pitch mode, respectively
ω	frequency
ω_i	i th non-dimensional natural frequency of the rotating blade
ω_j	modal frequency (imaginary part of s_j)

ω_x, ω_y	support structure frequencies in roll and pitch mode, respectively
ω_{N_i}	i th non-linear natural frequency of the rotating blade
Ω	angular velocity of the rotor

Special Symbols

$(\)_{,x}, (\)_{,\eta}, (\)_{,\zeta}$	derivative of $(\)$ with respect to x, η, ζ , respectively
$\delta(\)$	variation of $(\)$
$(\dot{\ }), (\ddot{\ })$	derivative with respect to non-dimensional time τ
$[\]^T$	transpose of $[\]$

Chapter 1

INTRODUCTION

1.1 Introduction

The main rotor system of a helicopter is the most important component of the vehicle. The rotor system has to fulfil multiple roles of generating lift, propulsive and control forces. Therefore, the dynamic characteristics of rotor blades play a significant role in the overall performance and stability of the vehicle. There has been a continued effort to develop a rotor blade and hub configuration which is mechanically simple yet efficient. During operation, the blades experience large bending and centrifugal loads. In order to relieve the root bending moments experienced by the blades, early rotor blades were provided with flap (out of plane bending) and lag (in-plane bending) hinges at the root of the blade. In addition, a pitch control bearing was provided to control the pitch angle of the blade. Such rotor systems are usually referred to as articulated rotors. A schematic diagram of an articulated rotor system is shown in Fig. 1.1a. While the provision of hinges represents an efficient engineering solution to the problem of alleviating high bending loads at the root, there are several disadvantages of this type of arrangement. The large number of moving parts leads to a mechanically complex

rotor hub system, accompanied by the associated wear out problem requiring frequent maintenance and replacement of parts. The presence of hinges prevents generation of large control moments and thereby restricts the flight envelope and the range for C.G. travel in the helicopter. The mechanical complexity of an articulated rotor hub can be seen in Fig. 1.1b (taken from Ref. [1]).

With the advancement in fibre-reinforced composite material technology, increasing emphasis has been placed on the development of hingeless rotor systems. Figures 1.2a and 1.2b show respectively a schematic and an actual rotor hub configuration of a hingeless rotor. The construction of these rotors is relatively simple because of the absence of flap and lag hinges; but a pitch bearing is still provided for blade pitch control. Due to the absence of hinges, large control moments can be generated which in turn provide favourable control characteristics of the vehicle. Both articulated and hingeless rotors are provided with external hydraulic dampers to increase damping in the lag mode and thereby to avoid aeroelastic and/or aeromechanical instabilities.

The development of a bearingless rotor system aims to eliminate both the pitch bearing as well as the external damper by incorporating a specialised elastomer with high loss factor. In this rotor system (Fig. 1.3a), the blade is attached to the hub through a flexible structural element called flexbeam. The flexbeam is designed to provide the required stiffnesses in the flap and lag bending deformations of the blade, but it is highly flexible in torsion. Surrounding the flexbeam, there is a stiff cuff denoted as torque tube which is attached to the blade-flexbeam junction at the outboard end and to a pitch link at the inboard end as shown in Fig. 1.3a. The pitch control of the blade is achieved by rotating the torque tube through up/down movement of the point P which in turn twists the flexbeam. An elastomer is placed between the torque tube and the flexbeam to provide adequate lag damping. It also serves the purpose of a spacer between the torque tube and the flexbeam. Though a bearingless rotor is

mechanically simple (Fig. 1.3b), its dynamic analysis [2] becomes very complicated due to the presence of multiple load paths, non-linear elastomeric damper and existence of a kinematic constraint at the pitch link.

Over the years, considerable effort has been put in by the helicopter industries in developing soft-in-plane bearingless main rotors with acceptable performance and stability characteristics. Huber [3] presented a comprehensive review of the bearingless main rotor programme pursued at different helicopter industries in the world. A brief history on the development of bearingless rotors is provided in Refs. [4, 5]. Lockheed developed the first prototype of a bearingless rotor in mid 1960's having "matched stiffness" (equal stiffness in both in-plane and out of plane bending). During test flight, the prototype encountered an air-resonance instability which was eliminated by increasing the fuselage inertia. During late 1970's and early 1980's, intense activity continued in developing the prototype of a Bearingless Main Rotor (BMR). The Boeing Helicopter Company developed a BMR with a high fundamental flap frequency and tested it on an MBB BO-105 Helicopter. It was observed that the landing gear of BO-105 had to be stiffened in order to improve the ground resonance stability. Another design was proposed by Bell Helicopter with a four bladed M680 rotor. An elastomeric damper was provided to augment edgewise damping. In 1990, the Boeing-Sikorsky Company developed a five-bladed BMR (for the new helicopter known as RAH-66 Comanchi) with elastomeric dampers. This vehicle is currently undergoing tests. In Europe, Eurocopter recently built and flight tested EC135 helicopter with a BMR [6]. For the analysis and design of bearingless rotor blades, most of the rotorcraft manufacturers have developed their own in-house methodologies and computer codes. Hence, very little information is available about them in the open literature.

The structural dynamic and aeroelastic/aeromechanical analyses of bearingless rotors require the formulation of suitable analytical models and solution techniques.

These mathematical models must include the following important features:

- i) non-linear stiffness and damping characteristics of the elastomer,
 - ii) kinematic constraint at the pitch link
- and iii) multiple load paths.

Several research studies have been reported in the open literature on modelling and analysis of bearingless rotor blades. A survey of the available literature is provided in the following section.

1.2 Literature Review

The literature review is divided into four subsections with each one addressing a particular topic relevant to the study of bearingless rotor blades.

1.2.1 Elastomeric Damper

Elastomeric materials are becoming increasingly popular for vibration attenuation applications due to the tremendous advantages they offer over mechanical dampers. In the case of bearingless rotors, conventional hydraulic dampers are being replaced by specialised elastomeric material with high loss factor. It is well known that under dynamic conditions, elastomeric materials exhibit visco-elastic behaviour dissipating energy through hysteresis. Besides exhibiting frequency and temperature dependence, the characteristics of an elastomeric material are also non-linear with respect to the amplitude of motion. Consequently, it has been a challenging task to develop an analytical model that can accurately represent the behaviour of the elastomeric dampers.

For visco-elastic materials, the stress-strain relations depend on the time history. Classical linear constitutive relations for visco-elastic materials are formulated either in the time domain or in the frequency domain [7]. In the frequency domain approach,

the coefficients of complex moduli are obtained by fitting a curve to the steady-state experimental data obtained over a limited frequency range of interest.

In the time domain approach, the constitutive relationship can be formulated in two different ways [7]; (i) differential equation form involving derivative operators, and (ii) convolution integral approach. In the differential equation form, higher order time derivatives of stress and strain are required to represent the dynamic properties of material over a broad range of frequency. On the other hand, the integral formulation avoids the presence of higher order derivatives and is very useful for creep/relaxation studies of visco-elastic materials. However, in structural dynamic problems represented by a set of differential equations, the incorporation of integral representation of visco-elastic material behaviour leads to integro-differential equations which are cumbersome to solve.

The method of irreversible thermodynamics has been used by Lesieutre and Mingori [8] to develop coupled material constitutive relations. These equations are used to model frequency dependent material damping in finite element domain. Later, a time domain model for linear visco-elastic materials has been proposed by Lesieutre and Bianchini [9] using Anelastic Displacement Field (ADF). The Golla-Hughes-McTavish mini-oscillator model [10] is a similar type of visco-elastic formulation where the higher order derivatives are replaced by internal dissipation coordinates.

Instead of integer derivative operators in the constitutive equation, introduction of fractional derivative operators can reduce the number of terms and parameters required to model visco-elastic materials. This fractional derivative approach [11, 12], being a time domain approach, is suitable for transient analysis. Bagley and Calico [13] and Fenander [14] developed a finite element formulation using fractional derivative approach. In a later study [15], this formulation was applied to analyse the transient response of a damped beam. Recently, Enelund and Josefson [16] used the fractional

derivative approach to capture the weak frequency dependence of the loss factor of an elastomer.

Apart from the above described linear models, many theories [17]- [19] have been proposed to model the non-linear behaviour of visco-elastic materials using hereditary integral representation. Glockner and Szyszkowski [20, 21] proposed a semi-empirical constitutive model to predict creep, strain softening and relaxation behaviour. These non-linear models, being in the integral form, cannot be conveniently incorporated into the structural dynamics analysis.

Due to the presence of elastomeric damper in bearingless rotors, it is essential to characterise the non-linear behaviour of the elastomer and to develop a suitable model which can be easily integrated in the structural dynamic and aeroelastic analyses of the rotor blade. A review on the performance of elastomeric devices can be found in Ref. [22]. McGuire [23] conducted experiments at Lord Corporation to identify the non-linear behaviour of an elastomer. However, for subsequent analysis of the ground resonance problem, a linear mathematical model for the elastomer was used. Experiments carried out by Housmann [24, 25] indicated that most of the elastomeric materials show significant non-linear behaviour so far as the frequency and amplitude of motion are concerned. He modelled the elastomer in terms of strain-amplitude dependent complex moduli. In Ref. [24] he also proposed a thermo-mechanical model to include the temperature effects. Felker *et al.* [26] carried out experiments to determine the properties of an elastomeric lag damper used in the Bell Model 412 Helicopter. A non-linear model was proposed in which both the stiffness and damping characteristics were expressed as functions of displacement. Smith *et al.* [27, 28] extended the method of ADF [9] to include non-linearities and temperature effects. Recently, a model comprising of a series combination of a quartic spring and a linear Kelvin chain has been proposed by Gandhi *et al.* [29]. In this model, the values of the parame-

ters were determined by fitting the analytical curves with the experimental data. The non-linear hysteresis cycles at different equilibrium positions were examined. Later on, Gandhi and Chopra [30] proposed a modified elastomeric damper model to simulate a reduction in damping at very low dynamic amplitudes. With this improved elastomeric damper model, they showed a limit cycle oscillation for an autonomous system representing isolated lag dynamics of a blade.

Panda and Mychalowycz [4] conducted experiments on a Comanche bearingless rotor with fluidlastic (linear characteristics) and elastomeric (non-linear characteristics) dampers. However, in the aeroelastic analysis, the elastomeric damper was modelled by linear spring and damping elements placed between the flexbeam and the torque tube. Ormiston *et al.* [31] proposed a combination of a non-linear spring and a Kelvin chain with non-linear damping and spring elements. The damping element was represented by a linear combination of terms having fraction, linear, quadratic and cubic powers of velocity. In a recent publication, Kunz [32] discussed the merits and demerits of different modelling approaches for the elastomers, such as, ADF, complex modulus and VKS (Voigt-Kelvin-Solid). Based on the comparison of various models under harmonic excitation, he concluded that the non-linear VKS model would result in accurate estimates of energy dissipation and was suitable for the prediction of forced response. However, this elastomer model was found to be amplitude-dependent. Using linear and non-linear VKS models for the elastomer, simulation studies of rotor start-up condition were compared with experimental results of AH-64A Apache main rotor. It was observed that neither the linear nor the non-linear model was capable of accurately predicting the response of the blade under a large impulsive loading. Of course, the non-linear model performed better than the linear one. The general conclusion of this study is that all elastomer models have certain limitations for applications to the analyses of the transient response, steady-state response and stability of rotor blades.

1.2.2 Structural Modelling of Rotor Blades

Since helicopter rotor blades are long, slender beams undergoing moderate deformations, a non-linear strain-displacement model is used to describe the coupling effects between axial, bending and torsional modes. Generally, the strains are assumed to be very small in comparison to unity. Such an assumption is consistent with the design requirement based on the fatigue life consideration which requires that the rotor blades must have an operating strain level well below the elastic limit of the blade material.

The first structural model for a rotor blade undergoing flap-lag-torsional deformations was developed by Houbolt and Brooks [33]. This model did not include the non-linear coupling effects between bending and torsion, which were shown to be important by later researchers for the dynamic and aeroelastic analyses of helicopter rotor blades. The importance of these non-linear coupling effects has been discussed in a review article by Friedmann [34].

Depending on the method of formulation of non-linear beam theories, the structural model can be classified into two groups: (i) moderate deformation theories and (ii) large deformation theories. In the moderate deformation theories [35] - [40], higher order terms are eliminated using an ordering scheme. In the large deformation theories, no such ordering scheme is employed. While the large deformation theories [41]-[44] are mathematically elegant, these are not easily amenable to aeroelastic studies. Therefore, moderate deflection theories are usually employed in the aeroelastic analysis of the helicopter rotor blades.

Following the research and development efforts from late 70's to early 90's, the formulation of structural model of a rotor blade undergoing bending-torsion-axial modes has reached a level of maturity and is now more or less standardised. The procedure for the formulation of the structural model of a beam undergoing large (or moderate)

deformation consists of the following sequence of steps [45, 46].

- i) The position vector of any point P in the undeformed configuration of the beam is defined with respect to a coordinate system rotating with the angular velocity of the rotor.
- ii) The undeformed base vectors at point P are evaluated.
- iii) The position vector of the point P is defined in the deformed configuration of the blade.
- iv) The deformed base vectors are then evaluated.
- v) Using the strain tensor in the curvilinear coordinate system, Green's strain measures are obtained.
- vi) The strains defined in the curvilinear system are then transformed into a local cartesian system.
- vii) In moderate deflection theories, the expressions pertaining to the axial strain at the elastic axis, the curvature of the deformed elastic axis and the twist of the beam are substituted with approximate non-linear expressions defined in terms of the physical displacements and slopes of the reference (elastic) axis.

The moderate deformation beam theories developed by Hodges and Dowell [35] and Rosen and Friedmann [36] were validated by comparing the theoretical results with the experimental data obtained for the static deformation of a beam [40, 47]. These beam models were later used to formulate the inertial and aerodynamic operators for aeroelastic analysis of helicopter rotor blades [48] - [52]. In general, these models did not include the effects of cross-sectional warping and transverse shear, and were restricted to the treatment of isotropic blades. With the development of composite rotor blades, several researchers proposed structural models applicable for the analysis of composite rotor blades [53] - [59]. These composite blade models include cross-sectional warping and shear effects. A detailed review of structural models suitable for

composite rotor blades can be found in the literature [60] - [62].

While deriving the dynamic and aeroelastic equations of motion of a rotor blade, the inertia and aerodynamic operators generate a large number of higher order non-linear terms. A consistent ordering scheme is used to neglect all the higher order non-linear terms. The ordering scheme is based on assigning orders of magnitude to all nondimensional parameters of the problem, in terms of blade bending slope (which is assumed to be of the order of $\epsilon \approx 0.10$ to 0.15). A second order approximation assumes that terms of order ϵ^2 are neglected in comparison to the terms of order 1. *i.e.*,

$$1 + O(\epsilon^2) \approx 1$$

A few studies [38, 39] used a third order approximation where terms of order ϵ^3 were neglected in comparison to terms of order 1. It must be borne in mind that the ordering scheme is based on experience and one should use certain degree of flexibility during its implementation.

1.2.3 Stability and Response Analyses

The problems in the area of stability and response analyses of a helicopter can be broadly divided into two categories, namely, (i) the problems related to the aeroelastic stability and response analysis of an isolated blade involving coupling between axial, bending and torsional modes; and (ii) the coupled rotor-fuselage problems addressing the aeromechanical stability or flight mechanical stability or vibrations, depending on the range of frequency. In this thesis, the focus will be on the response analysis of an isolated bearingless rotor blade and aeromechanical stability (ground resonance) of a coupled rotor-fuselage system. In the following, a review of the pertinent literature is provided in two subsections each addressing a particular topic.

1.2.3.1 Aeroelastic Stability and Response Analyses of an Isolated Rotor Blade

An excellent review on aeroelastic stability and response of rotor blades can be found in [34]. Using moderate deflection beam theory, the aeroelastic stability analysis of an isotropic hingeless rotor blade was carried out by Hodges and Ormiston [48] and Shamie and Friedmann [49]. It was reported that a rotor blade configuration without precone is generally stable for all blade pitch angles; but a blade with precone can exhibit lead-lag instability for a variety of combinations of precone and pitch angles. The aeroelastic analysis of a hingeless rotor blade having a composite box beam in hover was presented by Hong and Chopra [63]. They observed that the coupling due to ply orientation has a strong influence on the stability of the blades. Later Panda and Chopra [64] extended this work to forward flight and demonstrated that aeroelastic stability could be improved by proper tailoring of the couplings generated by the composite lay-up. Recently Tracy and Chopra [65] compared experimental and theoretical results in hover of a composite hingeless rotor blade model.

The effect of tip sweep on the blade stability was first investigated by Celi and Friedmann [51]. They pointed out that tip sweep has a strong influence on the blade dynamics. Subsequently more studies have been carried out by different researchers [66, 67] to analyse the effects of swept tip on the rotor blade stability and response in both hover and forward flight. Yuan and Friedmann [46] made an analytical study on the aeroelasticity and structural optimization of composite hingeless blades with swept tip. It was observed that tip sweep has negligible influence on the fundamental flap and lag frequencies; but it can cause aeroelastic instability when there is a frequency coalescence between the first torsion and second flap modes.

In a paper published in 1977, Bielawa [68] identified the complexities involved in

modelling a bearingless rotor blade. Three types of torque tube configurations were considered in this study. Two of the configurations exhibited performance and blade response characteristics which are similar to that of the conventional hingeless rotor blades. He concluded that from a practical design point of view “a snubbed torque tube configuration would probably be a minimum risk blade design”. A snubbed torque tube design is essentially the one shown in Fig. 1.3a, having an elastomeric snubber between the torque tube and the flexbeam. Sivaneri and Chopra [69] applied finite element method for the analysis of bearingless rotor blades. They have presented flutter stability of flap bending, lead-lag bending, and torsion in hover for a stiff-in-plane blade. They observed that the flap and torsion modes are stable while the lead-lag mode becomes unstable at high levels of thrust. This work was further extended by Hong and Chopra [70] for composite bearingless rotor blades. Dull and Chopra [71] investigated the effect of pitch-flap coupling for three pitch link configurations in a bearingless rotor blade. The hover stability predictions showed good correlation with the experimental data. They observed that the pitch link at leading edge provides higher lag damping compared to a pitch link at trailing edge. All these earlier studies [68] - [71] on bearingless rotor blades did not consider the non-linear elastomeric damper in their model.

Recently, Gandhi and Chopra [30] developed a non-linear model for the elastomeric damper and integrated it with a blade model to examine the aeroelastic behaviour of a bearingless rotor blade. It was observed that due to the inclusion of the elastomeric damper, the fundamental lag frequency moved closer to the first rotor harmonic (1/rev.) resulting in an increase in the amplitude of periodic lag response. In a bearingless rotor, the pitch angle to the blade is provided by twisting the flexbeam by a control rod attached to the inboard end of the torque tube (Fig. 1.3a). Hence special attention must be paid to include the kinematic constraint at the inboard end of the torque

tube. The aeroelastic behaviour of the blade could also significantly depend on the initially deformed and twisted configuration of the flexbeam. Gandhi and Chopra [72] considered the effect of elastic twist of the flexbeam due to pitch link control to evaluate the aeroelastic stability characteristics of a bearingless rotor. It was observed that during the forward flight, for the same pitch setting of the blade, the leading edge pitch link configuration results in large positive torsional response of the blade (and hence an increase in the thrust) as compared to the trailing edge pitch link configuration which leads to a large negative torsional response (and hence a decrease in the thrust). It may be noted that in this study, the non-linear elastomer was not included.

1.2.3.2 Aeromechanical Stability of a Helicopter

The aeromechanical stability of a helicopter is a complex phenomenon, involving coupling between the rotor and body degrees of freedom. The rotor lead-lag regressing mode usually couples with the body pitch and roll modes to cause instability. This phenomenon is denoted as ground resonance when the helicopter is on ground and air-resonance when the helicopter is in flight. The aeromechanical instability is severe in nature. In the case of articulated and hingeless rotor systems, the air/ground resonance is usually avoided by providing external mechanical dampers in the lead-lag mode of the rotor system, whereas in case of bearingless rotors, a specialised elastomer with high loss factor is used as a damper. Apart from providing an external lag damper, there are also other means of increasing the inherent damping available in the lag mode by judiciously providing certain aeroelastic couplings in the rotor blade. Another approach is through the use of active controls based on fuselage and rotor feedback [73] - [77]. However, the safety and reliability of an active control scheme plays an important role which should be properly verified before its application to an actual helicopter.

The analysis of aeromechanical stability characteristics of a coupled rotor/fuselage

system requires the development of a mathematical model representing the dynamics of the coupled system incorporating various aeroelastic couplings. Over the years, considerable progress has been made in modelling the system dynamics. Using a simple mathematical model, Ormiston [78] examined the effects of pitch-lag and flap-lag couplings of a soft-in-plane hingeless rotor/fuselage system for both ground resonance and air resonance in hover. It was observed that aeroelastic couplings are generally not beneficial for ground resonance at zero-blade collective pitch. At higher collective pitch values, pitch-lag coupling is found to be more effective to stabilise the vehicle. In a later study, Ormiston [79] observed that the character of air-resonance was found to alter significantly at high rotor speeds for high lock number blade configurations. Following the theoretical approach of Ref. [78], an experimental study was performed by Bousman [80] to investigate the influence of aeroelastic couplings and collective pitch setting on the aeromechanical stability of a hingeless rotor helicopter model. It was observed that the configuration with matched stiffness blade is basically less unstable than the configuration with non-matched stiffness. For the matched stiffness configuration, addition of negative pitch-lag coupling (lag back-pitch up) was stabilising; however, for the non-matched stiffness case only slight improvement in the unstable region was observed. In general, the conclusions of Refs [78] and [80] indicate that the aeroelastic couplings offer a significant potential for augmenting the inherent damping in the lag mode.

Considering only the pitch-lag aeroelastic coupling, Zotto and Loewy [81] concluded that pitch-lag coupling could be effectively used to increase the damping in the lag mode under ground/air resonance conditions. Air resonance characteristics in forward flight with different dynamic inflow models have been studied by Nagabhushanam and Goankar [82]. The study included the effects of trimming conditions, lag structural damping and aeroelastic couplings. Johnson [83], and Friedmann and

Venkatesan [84, 85] developed analytical models for the aeromechanical stability of a coupled rotor/fuselage system and compared their theoretical results with the experimental data presented in Ref. [80]. In Ref. [83], various cases considered for comparison between theory and experiment, were restricted to zero collective pitch setting of the rotor and in Refs. [84] and [85] the comparisons were limited to the cases without aeroelastic couplings.

Venkatesan [86] analysed the effects of pitch-lag, pitch-flap and structural flap-lag couplings individually and in combination, on the stability of lag mode under ground resonance condition. He showed that the positive pitch-flap coupling increases the damping in resonance conditions, whereas the combination of the pitch-lag and flap-lag couplings do not have beneficial influence at resonance conditions. It was also observed that by a proper combination of flap-lag, negative pitch-lag and positive pitch-flap couplings, the lag regressing mode could be stabilised over the whole range of rotational speeds. However, this was done only at a single value of collective pitch. Recently, Gandhi and Hathway [87] extended the work of Venkatesan [86] by considering a combination of aeroelastic couplings that can stabilise ground resonance of a soft-in-plane hingeless rotor, over the entire range of rotational speeds, at various thrust levels and for various values of body frequencies. They considered the aeroelastic couplings as continuous variables and used optimization technique to reach a combination of couplings that completely stabilises the system under ground resonance.

Gandhi and Chopra [88] analysed the ground/air resonance stability of a helicopter in hover with non-linear elastomeric lag damper. In their study, the blade was assumed to be rigid with a root hinge simulating both the articulated and hingeless rotor system. A non-linear elastomer was placed at the lag hinge and consequently it has the same displacement as that of the blade in lag mode. They observed that the non-linear elastomeric damper has a stabilising influence on both ground and air resonances. In

all the above studies [78] - [88], the blade model corresponds to a hingeless rotor blade.

The dynamic analysis of a bearingless rotor blade is more complex than that of hingeless or articulated rotors owing to the presence of non-linear elastomeric damper and multiple load paths. One of the earliest analytical models for bearingless rotor was developed by Hodges [89, 90]. In the analysis, the main blade was assumed to be rigid. The flexbeam was treated as Euler-Bernoulli beam having elastic deformation in bending, torsion and axial directions. Based on finite element formulation of Ref. [69], Chopra and his associates examined the aeromechanical stability characteristics of a bearingless rotor in hover and forward flight conditions [91] - [93]. A study of the shaft-free aeromechanical stability characteristics of a bearingless rotor in hover [91] and in forward flight conditions [92] was carried out by Jang and Chopra. Tracy and Chopra [93] examined the aeromechanical stability of a bearingless rotor with composite flexbeam. This study indicated that a negative pitch-lag (lag back-pitch up) coupling has stabilizing effect on the regressive lag mode in hover and forward flight. In all these studies [89] - [93], the non-linear elastomeric damper was not included.

Using the elastomer model proposed in Ref. [29], along with a rigid blade model having an elastomers at the root hinge, Gandhi and Chopra [88] examined its influence on the aeromechanical behaviour in forward flight. It was observed that influence of damper dynamics on coupled regressive lag/fuselage motion could result in a diminished damping effect for some advance ratios. In another study, Gandhi and Chopra [72] also considered the effect of pitch link configuration on the shaft-free aeromechanical stability of a bearingless rotor without the elastomer. For the leading edge pitch link configuration, the regressive lag damping rapidly increases with advance ratios whereas for the trailing edge pitch link configuration, the regressive lag damping-decreases with

advance ratio.

A bearingless rotor model was developed and tested by Weller [5] to examine the aeromechanical stability margins in hover. Rotor design parameters included fundamental flap mode natural frequency, built-in cone and sweep angles of the blade, pitch link location at leading and trailing edge positions. It was observed that the stability characteristics at the higher collective pitch angles can be improved by attaching the pitch link to the leading edge. Recently, Panda and Mychalowycz [4] presented a correlation of wind tunnel tests and analytical studies for a scaled model of a RAH-66 Comanche bearingless main rotor. However, in the analytical model the elastomer was treated as a linear element. Hover air-resonance test results were presented for both fluidlastic (linear characteristics) and elastomeric (non-linear characteristics) dampers. The experimental results indicated that the non-linearities in stiffness and damping seem to have a significant influence on the limit cycle oscillations. The authors attributed the reason for limit cycle to the presence of rotor-body frequency coalescence between the lag regressive, flap regressive and body roll modes. Near coalescence, the damping is low and hence a limit cycle oscillation occurs at the lag regressive frequency. On the other hand, the fluidlastic damper due to its linear nature did not exhibit any limit cycle oscillation.

In Ref. [31], Ormiston *et al.* presented the capabilities of a Second Generation Helicopter Analysis System (2GCHAS). It is a finite element based comprehensive, multidisciplinary computer programme. Using 2GCHAS, they studied the air-resonance stability characteristics of a 3-bladed hingeless rotor with rigid blades and a 5-bladed bearingless rotor with flexible blades. In the case of hingeless blade, a non-linear elastomer was placed at the root; in the bearingless blade, the elastomer was placed between the torque tube and the flexbeam. The elastomer was modelled as a non-linear Kelvin chain. The damping force was assumed to be proportional to a linear combination of

different powers of velocity (e.g., powers of $1/2$, 1, 2 and 3). The phenomenon of limit cycle oscillation was demonstrated for both the configurations. It was concluded that “the effects of non-linear elastomeric dampers are significant and complex. Until the ideal bearingless rotor without auxiliary lead-lag damper is developed, the modelling and behaviour of elastomeric dampers warrant additional attention”.

1.2.4 Non-linear Analysis

Independent of the above studies related to helicopter blades, several researchers have made significant contributions to the study of non-linear dynamics of beams. The amount of literature available on the general non-linear problem is too vast to be considered in detail. In this section, the objective is to provide a review of the literature relevant to the present thesis.

For small oscillations the response of an elastic body can be adequately described by linear equations and linear boundary conditions. However, as the amplitude of oscillation increases, assumption of linearity does not hold good. In order to represent the dynamic motion, the non-linear effects have to be taken into account. The source of non-linearities may be geometric or material in nature. The geometric non-linearities may arise due to large deformation causing non-linear relationship between the strain and displacement. The material non-linearity occurs when the stress-strain relationship becomes non-linear in nature.

From the experimental observation, it is well known that the dynamic stiffness and damping characteristics of a typical elastomer are highly non-linear with respect to the amplitude of deformation. In bearingless rotors, the presence of elastomer gives rise to material non-linearities. Additionally, moderate deformation theory produces geometric non-linear terms in the equations of motion. In most of the non-linear dynamics problems, an exact solution is not available. Researchers generally follow either one

of the following schemes, namely, a) numerical techniques, b) approximate analytical techniques or, c) a combination of numerical-analytical methods.

Numerical techniques deal with dynamic deformation using finite element or finite difference schemes in space and time. However, the application of the purely numerical techniques to vibration problems are costly in terms of computation time. On the other hand, analytical techniques are suitable for simple structures with simple boundary conditions. For complicated structures, majority of the researchers follow the numerical-analytic approaches. Using linear undamped natural modes, the governing partial differential equations are converted into a system of coupled second order non-linear differential equations. These equations are solved by using perturbational technique such as method of averaging or method of multiple scales. This numerical-perturbational technique has been used for the determination of non-linear response of a continuous system with varying properties [94, 95].

Anderson [96] formulated the non-linear equations of motion of a rotating beam and obtained the natural frequencies. He concluded that the extensional and flapwise natural frequencies increase monotonically with rotational speed. However, his formulation contained certain errors which are pointed out in references [97, 98]. Non-linear flapping vibration of rotating blades had been studied by Venkatesan and Nagaraj [99] using the averaging technique. It was observed that the large amplitudes have a softening effect on the flapwise frequency. Experimental and theoretical analyses of a composite blade under large deformation were carried out by Minguet and Dugundji [43, 44]. The analytical results were obtained by using iterative finite difference solution scheme. The natural frequencies and mode shapes obtained from the analytical model compared well with the experiment results. It was shown that equilibrium static deflection has a significant influence on the torsion and lead-lag modes and frequencies.

Dowell [100] used the component mode analysis to examine the effect of material

non-linearity in the form of a non-linear spring-mass system attached to a simply supported beam. Pakdemirli and Nayfeh [101] extended the work of Dowell [100] by including the mid-plane stretching and damping. It was shown that both the mid-plane stretching and spring-mass system have a great effect on the frequency and force-response curves. Their relative effects depended on the system parameters and location of the spring-mass system. Birman [102] studied the free vibration of hinged beams on a non-linear elastic foundation. Szemplinska-Stupnicka [103] used generalised Ritz method to investigate the influence of non-linear boundary conditions on the frequency of beam vibration. Nayfeh and Nayfeh [104] obtained the non-linear normal modes and amplitude-frequency relation for a simply supported Euler-Bernoulli beam resting on an elastic foundation having quadratic and cubic non-linearities. Recently, non-linear normal mode shapes of a cantilever beam have been determined using the method of multiple time scale [105].

1.3 Objectives of the Present Study

The review of the literature clearly indicates that the elastomer used in a bearingless rotor shows highly non-linear characteristics both in stiffness and damping with respect to the amplitude of deformation. Therefore, it is expected that due to the presence of the elastomer, the lag and flap frequencies should be dependent on the amplitude of motion which is a typical feature that distinguishes a non-linear system from a linear one. But so far no attempt has been made to study the effect of amplitude on frequencies of a bearingless blade.

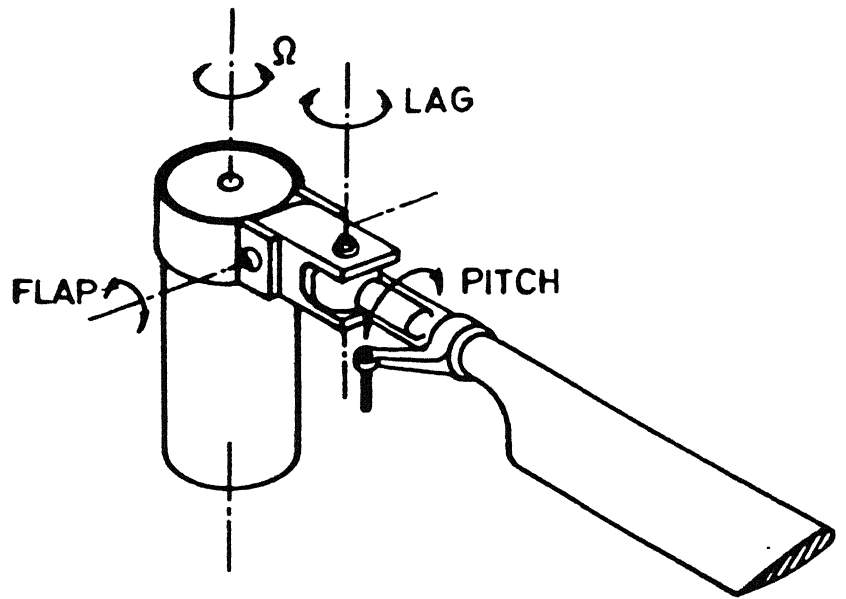
Several researchers have proposed different non-linear models with varying degree of complexity in order to capture the non-linear characteristics of the elastomer. However, while performing the stability analysis, only the linearised equations of the blade

and elastomer about an equilibrium point are solved. In this solution procedure, the dependence of stiffness and damping characteristics of the elastomer on the amplitude of motion is completely ignored.

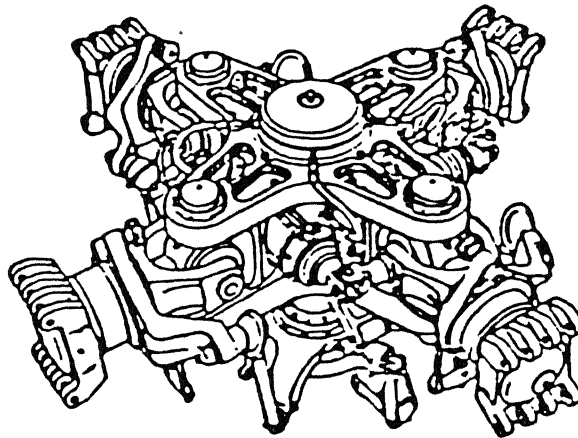
All the studies on aeroelastic response of the rotor blade consider only the steady state response [32]. It was experimentally observed [106] that for a step input in pitch angle, the transient response of a hingeless rotor blade exhibits dynamic overshoot leading to overstressing of the blade. No information is available on the transient response characteristics of a bearingless rotor blade. Also no result is available in the open literature whether there is any qualitatively significant difference in the transient response of a bearingless rotor blade as compared to a hingeless blade.

The objectives of the present study are to:

- i) formulate a simple non-linear model to represent the non-linear stiffness and damping characteristics of an elastomer;
 - ii) study its influence on the isolated lag and flap dynamics of a rotor blade;
 - iii) formulate a methodology for carrying out amplitude-dependent aeromechanical stability analysis under ground resonance condition considering only the elastomer non-linearity;
 - iv) examine the transient response, to a step pitch input, of an isolated bearingless rotor blade undergoing coupled flap-lag-torsional deformation in hovering condition and compare the results with that of a hingeless blade;
 - v) define a measure for the aeroelastic couplings in bearingless rotor blades, in terms of the steady state response (to a step pitch input) and study its dependence on the relevant geometric parameters.
- and
- vi) investigate the phenomenon of limit cycle oscillation of an isolated bearingless rotor blade, with and without aerodynamic loading.

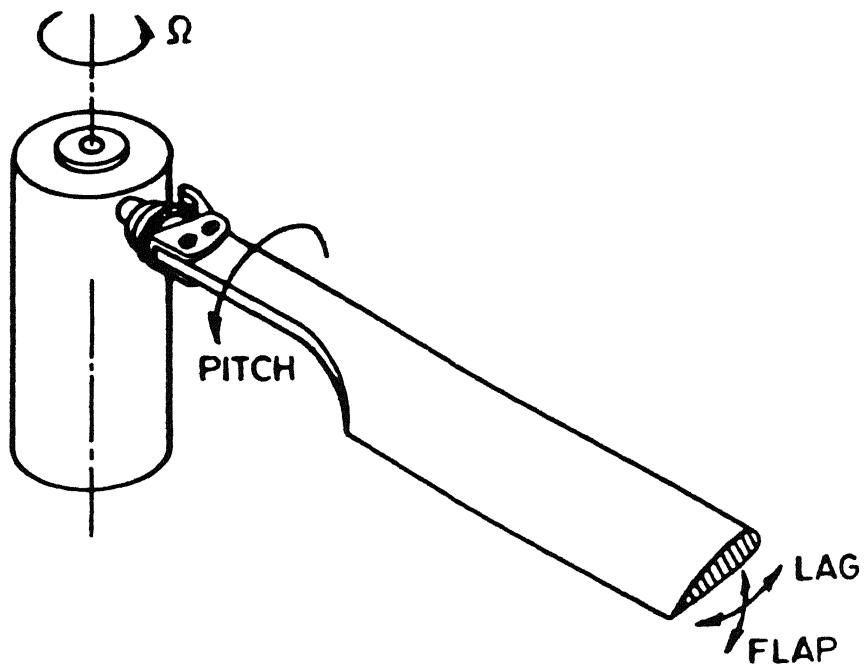


(a) Schematic diagram.

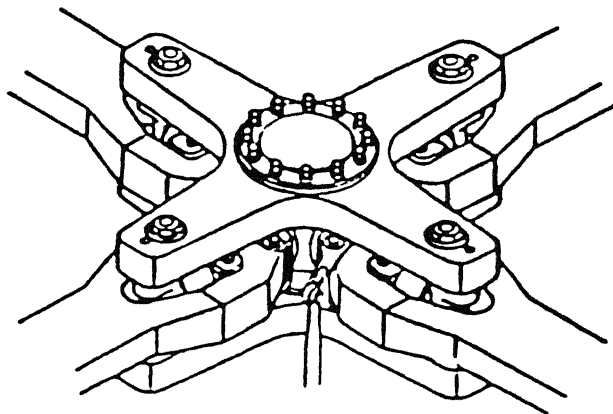


(b) Actual rotor hub (taken from Ref. [1]).

Figure 1.1: Articulated rotor hub and blade configuration.

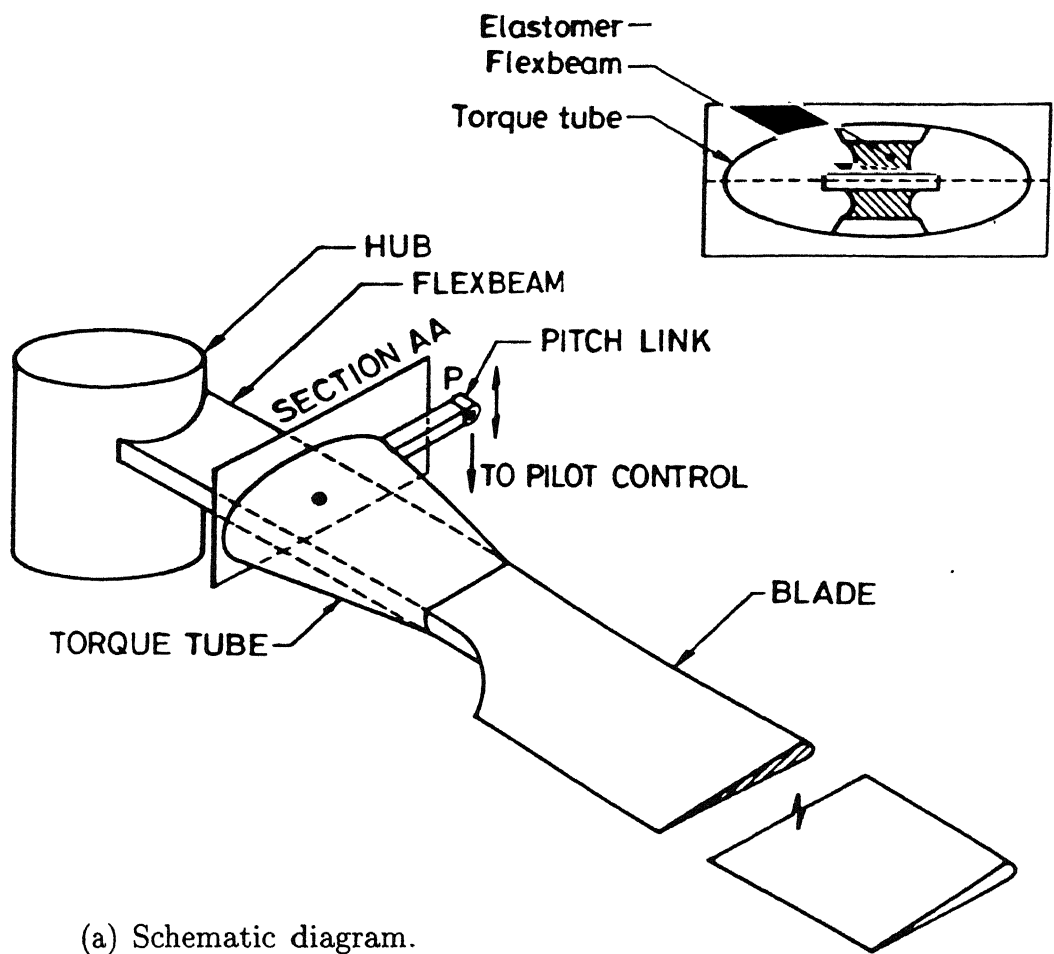


(a) Schematic diagram.

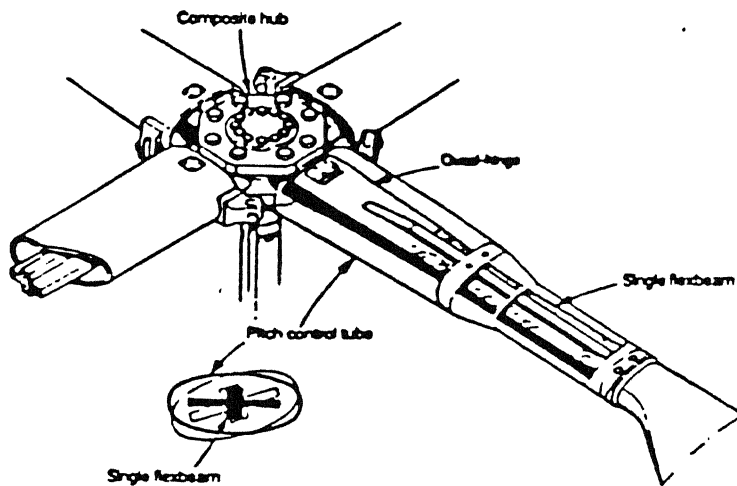


(b) Actual rotor hub (taken from Ref. [1]).

Figure 1.2: Hingeless rotor hub and blade configuration.



(a) Schematic diagram.



(b) Actual rotor hub (taken from Ref. [1]).

Figure 1.3: Bearingless rotor hub and blade configuration.

Chapter 2

ELASTOMERIC DAMPER MODEL

2.1 Introduction

In contrast to the conventional hydraulic dampers, elastomeric dampers contribute both damping and stiffness to the rotor blade. Due to the visco-elastic nature of the material, damping and stiffness properties of the elastomer are complex functions of the displacement amplitude, frequency and even temperature. A typical static load deflection curve for a non-linear visco-elastic material is shown in Fig. 2.1 by the curve $OABC$. Generally the static non-linear characteristics of the elastomer are described by the secant stiffnesses evaluated at different values of the deflection. For example, the secant stiffnesses at points A and B are defined by the slopes of the line OA and OB (Fig. 2.1), respectively.

The load-deflection curve of the elastomer under dynamic loading about these two equilibrium points A and B can be represented by the corresponding visco-elastic hysteresis loops superimposed on the equilibrium curve $OABC$ at the points A and

B , respectively. The dynamic stiffness values at A and B are defined by the slopes of the line pq and $p'q'$ where the points p , q , p' and q' are the points correspond to the maximum deflection of the elastomer as shown in Fig. 2.1. On the other hand, linearised stiffness is defined using static load-deflection curve. The slopes of the lines uv and $u'v'$ represent the linearised stiffness values in the vicinity of the equilibrium points A and B , respectively.

In most cases, the dynamic tests on an elastomer is carried out without any static preloading *i.e.* about an equilibrium position with zero deformation. The material is subjected to a harmonic displacement excitation and the required force is measured. The stiffness modulus is defined as the in-phase force component that is required to produce unit amplitude of deformation. Similarly, the damping modulus is defined as the required force component (for unit amplitude of deformation) that is in quadrature with the deformation. The dynamic stiffness and damping values can also be identified from hysteresis cycles for different amplitudes of motion. The area of the hysteresis loop provides the information about the amount of energy dissipated per cycles at a particular amplitude of deformation. Typical hysteresis cycles of a non-linear elastomeric material about zero equilibrium position are shown in Fig. 2.2. It can be observed from Fig. 2.2, that when the amplitude of motion is X_1 , the corresponding dynamic stiffness is given by the slope of the line a_1b_1 . When amplitude of motion is increased to X_2 , the slope of the line a_2b_2 represents the dynamic stiffness. It is evident that these two stiffness values can be different depending on the distortion of the hysteresis loop with the amplitude of motion. However, the linearised stiffness about the zero equilibrium point is given by the slope of the static load deflection curve $a_2a_1Ob_1b_2$ at O *i.e.* slope of the line lm . It is important to recognise that the linearised stiffness can be different from the dynamic stiffness for a given amplitude. Also, the dynamic stiffness is a function of the amplitude of motion. Therefore in any linearised stability

analysis, the effect of change in the stiffness due to a change in the amplitude of motion is not at all taken into account.

The energy dissipated by the viscoelastic material for a particular amplitude of motion is given by the area of the corresponding hysteresis loop. Figure 2.2 also indicates that the energy dissipation per cycle depends on the amplitude of motion. In case of a linearised analysis, a damping value has to be chosen based on an arbitrary value of amplitude of motion.

The above discussion clearly indicates that the elastomer model should capture the non-linear behaviour of the material so far as the stiffness and damping are concerned. In addition, it should be possible to integrate the model easily with a structural dynamic model of a rotor blade for subsequent aeroelastic and aeromechanical analysis without neglecting the effect of the amplitude of motion on the elastomer characteristics.

The experimental results of a single frequency bench test [23, 24, 26] of different elastomeric lag dampers are shown in Figs. 2.3-2.5. All the figures indicate that both the in-phase stiffness (denoted as K' or G') and the quadrature stiffness (denoted as K'' or G'') decrease as the amplitude of motion increases. The variation of loss tangent ($\tan \delta$) or loss factor (η) with amplitude is also shown in these figures. Loss tangent is generally defined as the ratio of G' and G'' . It can be noticed that there is no decrease in the quadrature stiffness at very low amplitude of motion for all the experimental data shown in Figs. 2.3-2.5. But in Ref. [30], Gandhi and Chopra assumed that there is a degradation of damping coefficient (G'') at very low amplitude. This is not consistent with the experimental evidence shown in Figs. 2.3-2.5. However, as shown in Fig. 2.3b, the loss factor (η) decreases at low amplitudes. The reason for the decrease in loss factor at low amplitude of motion is mostly due to the sharp rise in the value of in-phase stiffness (G') at low amplitude. The computed loss factors for the other experimental data also exhibit similar behaviour as shown in Figs. 2.4b and 2.5b.

In this chapter, an attempt is made to develop a model for the elastomer which would capture the amplitude dependent characteristics of stiffness and damping parameters. A simple model is considered so that it can be easily integrated with a structural dynamic model of the rotor blade for subsequent dynamic and aeroelastic analysis.

2.2 Formulation of the Model

The non-linear characteristics of an elastomeric material can be idealised by a combination of linear and non-linear restoring and dissipative elements. Since the static stress-strain curve of an elastomeric material is non-linear, it is logical to assume the restoring element to be non-linear. The experimental results of a single frequency bench test [26] of an elastomeric lag damper show that both in-phase (G') and quadrature (G'') stiffness decrease as the amplitude of motion increases; but neither of them display *any significant dependence on frequency* within the range of interest (3.3 Hz to 6.4 Hz). The experimental results taken from Ref. [26] are shown in Fig. 2.5, which are used in the present study. Figure 2.6 represents an idealised model consisting of a non-linear spring, a Coulomb damper and a hysteretic damper. The reason for choosing a Coulomb damper is that the damping force is very high at low amplitude. In addition, Coulomb and hysteretic dampers provide damping forces which are *independent of frequency*. This type of idealisation differs from the model proposed by Gandhi *et. al.* [30], in the sense that their model has a viscous damping element.

The non-linear force-deformation relation of the spring is assumed to be of the form:

$$F_S = K_1x - K_3x^3 + K_5x^5 - K_7x^7. \quad (2.1)$$

where F_S is the force exerted by the restoring element under a deformation x with K_1 , K_3 , K_5 and K_7 as constants. The constitutive differential equation of the elastomer

model under harmonic loading (Fig. 2.6) can then be written as

$$K_1x - K_3x^3 + K_5x^5 - K_7x^7 + F \operatorname{sgn} |\dot{x}| + \frac{h}{\omega} \dot{x} = D_o \sin \omega t. \quad (2.2)$$

2.2.1 System Identification

The parameters K_1 , K_3 , K_5 , K_7 , F and h of the elastomer model are identified from experimental data points, using error minimisation technique. The steady-state solution of Eq. 2.2 is assumed to be of the form

$$x = X \sin(\omega t - \beta). \quad (2.3)$$

Substituting Eq. 2.3 in Eq. 2.2 and rewriting $D_o \sin \omega t$ as $D_o[\sin(\omega t - \beta) \cos \beta + \cos(\omega t - \beta) \sin \beta]$, the following two equations are obtained by balancing the first harmonic.

$$K_1X - \frac{3}{4}K_3X^3 + \frac{5}{8}K_5X^5 - \frac{1}{2}K_7X^7 = D_o \cos \beta \quad (2.4)$$

$$\text{and} \quad \frac{4F}{\pi} + hX = D_o \sin \beta. \quad (2.5)$$

It may be noted that the first harmonic approximation of the function $F \operatorname{sgn} |\dot{x}|$ is given by [107]

$$F \operatorname{sgn} |\dot{x}| \cong F \left(\frac{4}{\pi} \right) \cos(\omega t - \beta).$$

Now, Eq. 2.3 can be rewritten as

$$x = X_C \cos \omega t + X_S \sin \omega t \quad (2.6)$$

$$\text{where } X_C = -X \sin \beta \text{ and } X_S = X \cos \beta. \quad (2.7)$$

Substituting for $\sin \beta$ and $\cos \beta$ in terms of X_C and X_S in Eqs. 2.4 and 2.5, the in-phase stiffness (G') and the quadrature stiffness (G'') are obtained, respectively, as

$$\begin{aligned}
G' &= \frac{D_o |X_S|}{X_C^2 + X_S^2} \\
&= K_1 - \frac{3}{4}K_3X^2 + \frac{5}{8}K_5X^4 - \frac{1}{2}K_7X^6
\end{aligned} \tag{2.8}$$

$$\begin{aligned}
\text{and } G'' &= \frac{D_o |X_C|}{X_C^2 + X_S^2} \\
&= \frac{4F}{\pi X} + h.
\end{aligned} \tag{2.9}$$

The experimentally obtained values for G' and G'' for different amplitudes of motion are given in Fig. 2.5. Let these be denoted by $G'(X)$ and $G''(X)$, respectively, where X is the amplitude of motion. The stiffness parameters K_1 , K_3 , K_5 and K_7 are obtained by minimising the error function:

$$\Phi_1 = \sum_{i=1}^{ND} [F_i(X)]^2 \tag{2.10}$$

$$\text{where } F_i(X) = K_1 - \frac{3}{4}K_3X^2 + \frac{5}{8}K_5X^4 - \frac{1}{2}K_7X^6 - G'(X),$$

and ND denotes the number of experimental data points used. Similarly, the values of the damping parameters F and h , are obtained by minimising the error

$$\Phi_2 = \sum_{j=1}^{ND} [F_j(X)]^2 \tag{2.11}$$

$$\text{with } F_j(X) = \frac{4F}{\pi X} + h - G''(X).$$

2.3 Results and Discussion

The experimental data is taken from Ref. [26]. These are given in FPS units which are converted to SI units for the present analysis. Number of data points ND is taken to be 5. The frequency used for parameter identification is $\omega = 3.3$ Hz. Gauss-Newton algorithm is used for the error minimisation problem. The system parameters so obtained

are given in Table 2.1. Figures 2.7 and 2.8 show the comparison of the experimental data with the theoretical results obtained using the idealised elastomer model. A fifth order approximation of the non-linear spring is also considered. From Fig. 2.7, it is evident that the seventh order approximation provides a better fit compared to the fifth order approximation.

Since the hysteresis loop of a viscoelastic material provides information regarding the energy dissipation, an attempt is made to draw the hysteresis loop of the elastomer model about the zero equilibrium point. Figure 2.9 shows the hysteresis loops for different amplitudes of motion ($X = 0.0005, 0.0010, 0.0015$ and 0.0020 m). At the tip of the amplitude, the hysteresis cycles become almost vertical. This behaviour is due to the presence of the Coulomb damper in the model.

2.4 Summary

The most important aspects of the non-linear characteristics of an elastomers are summarised for convenience. The key difference between the linearised stiffness and dynamic stiffness about an equilibrium point of the elastomer has been highlighted. Linearised stiffness is independent of amplitude of motion whereas dynamic stiffness is a function of the amplitude of motion. In addition, the damping of the elastomer is a function of the amplitude.

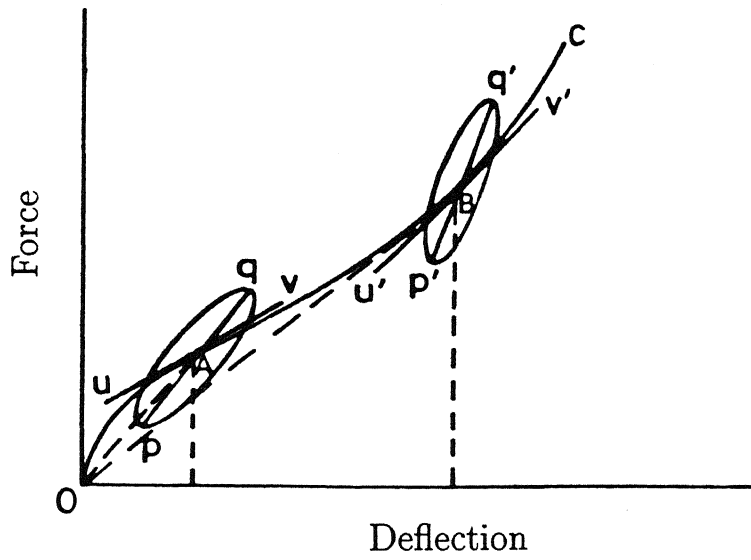


Fig. 2.1 Non-linear dynamic characteristics of a visco-elastic material.

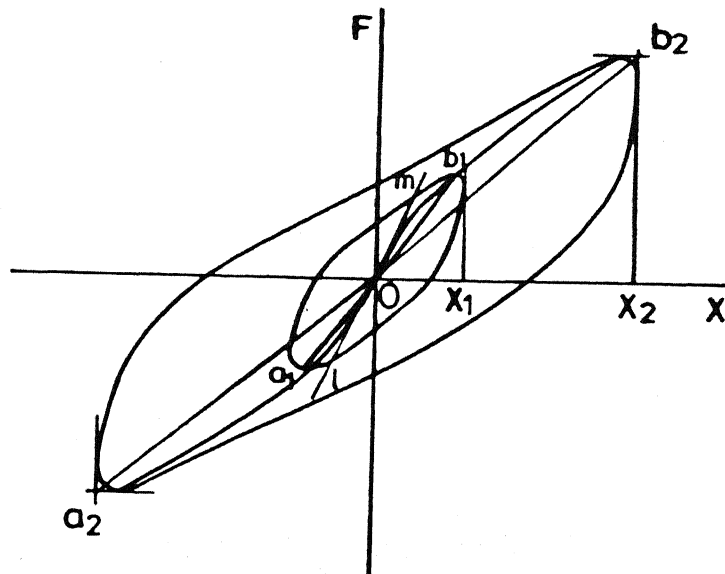
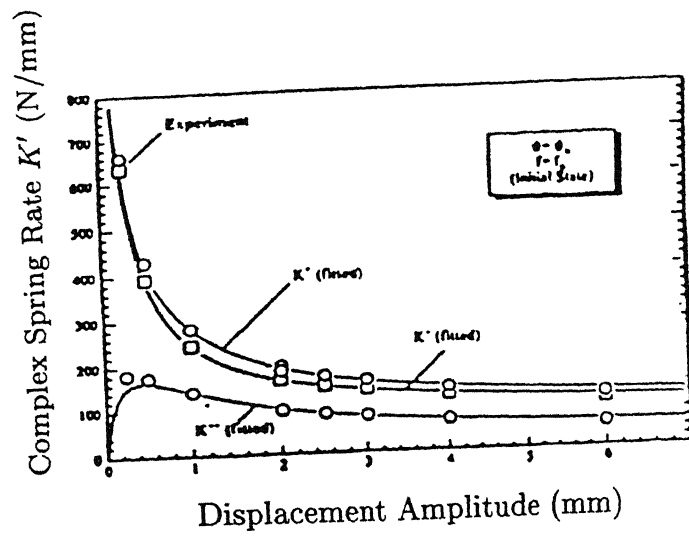
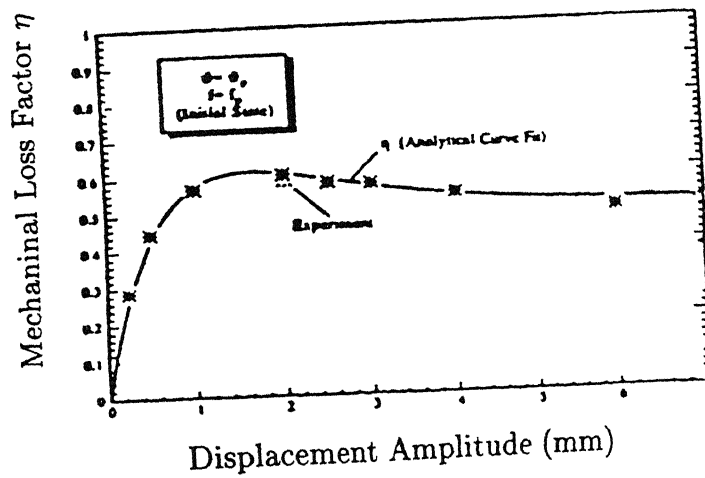


Fig. 2.2 Hysteresis cycles of a non-linear material about zero equilibrium point.

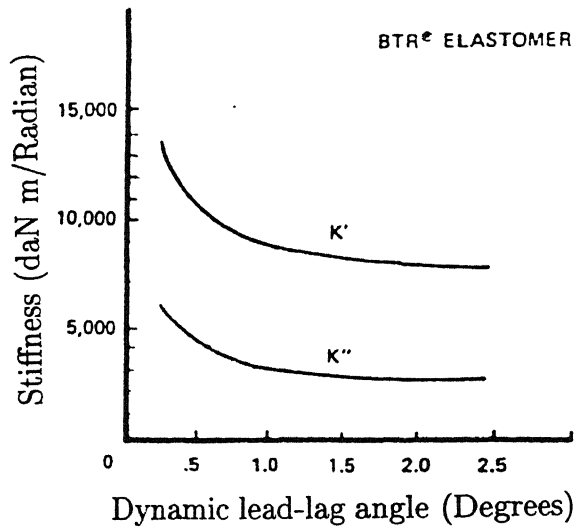


(a) Complex stiffness as a function of amplitude

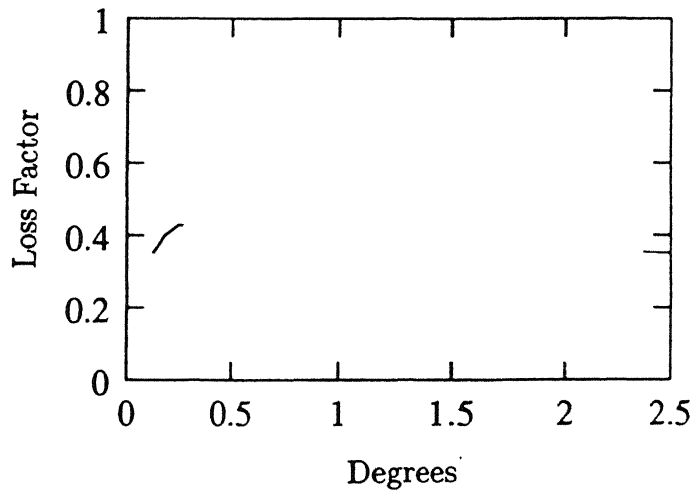


(b) Loss factor

Fig. 2.3 Experimental data taken from Ref. [24]

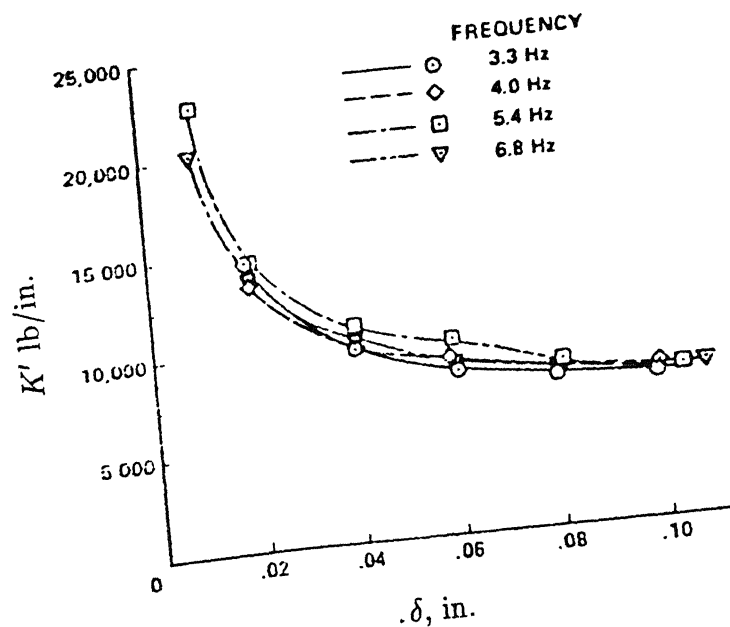


(a) Elastic and damping stiffness

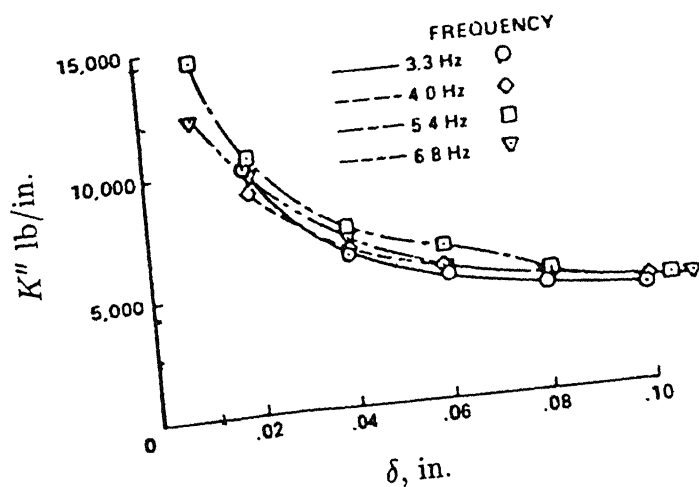


(b) Loss factor (computed)

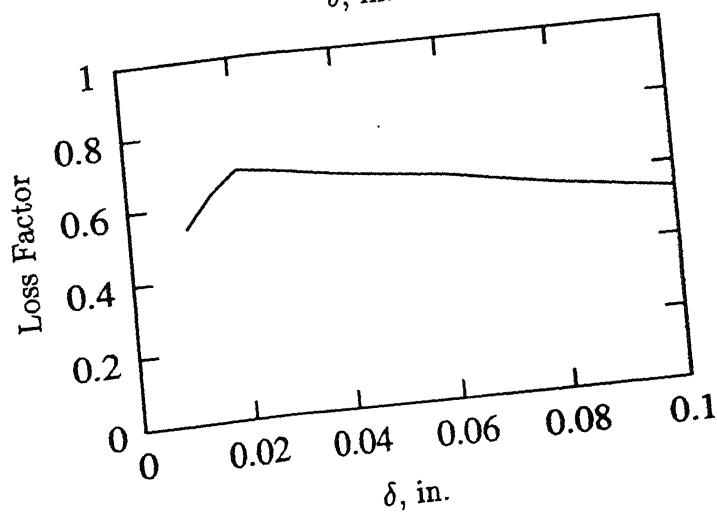
Fig. 2.4 Experimental data taken from Ref. [23]



(a) In-phase stiffness



(b) Quadrature stiffness



(c) Loss factor (computed)

Fig. 2.5 Experimental data taken from Ref. [26]

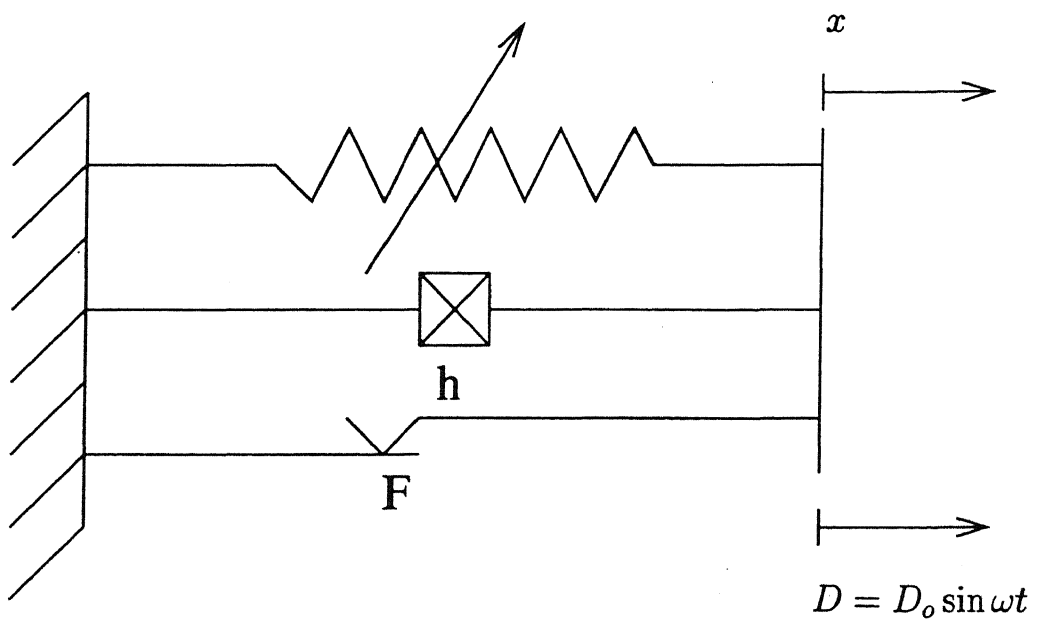


Figure 2.6: Elastomer model.

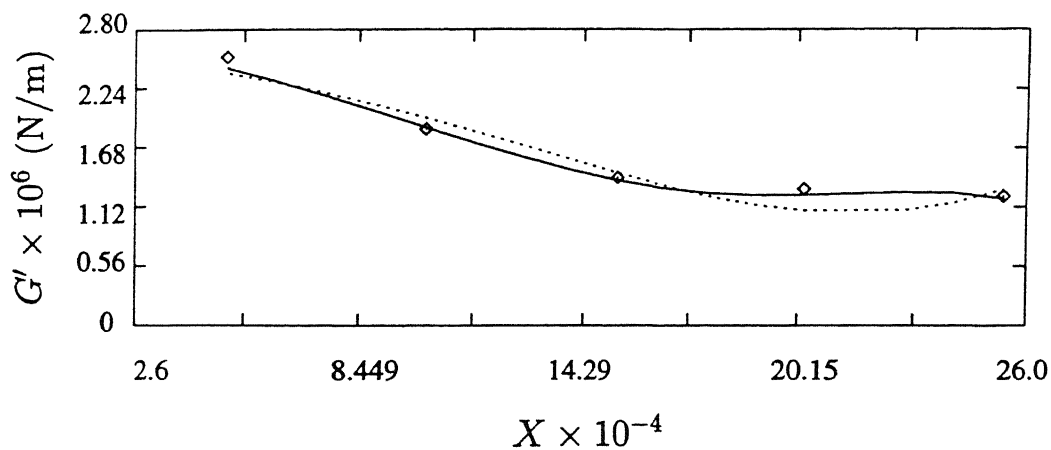


Fig. 2.7 Variation of G' (in-phase stiffness) with amplitude. \diamond experimental data; — seventh order spring model; fifth order spring model.

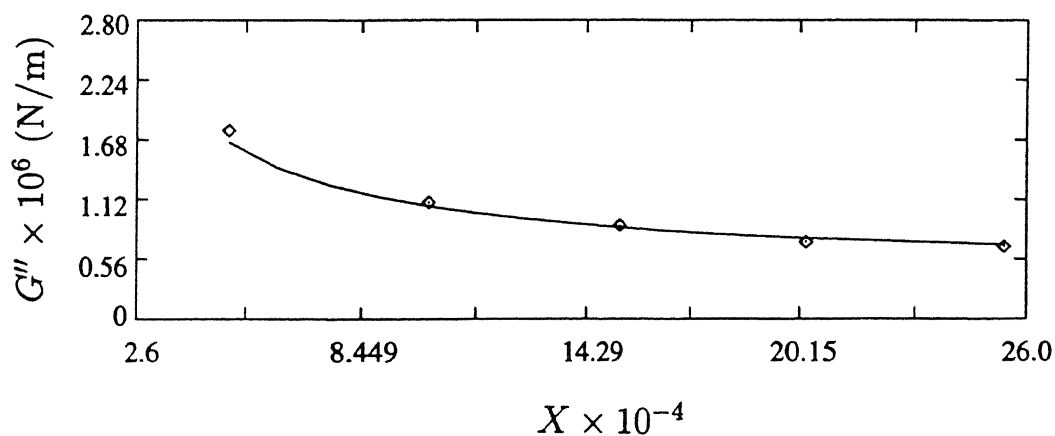


Fig. 2.8 Variation of G'' (quadrature stiffness) with amplitude. \diamond experimental data; — proposed model.

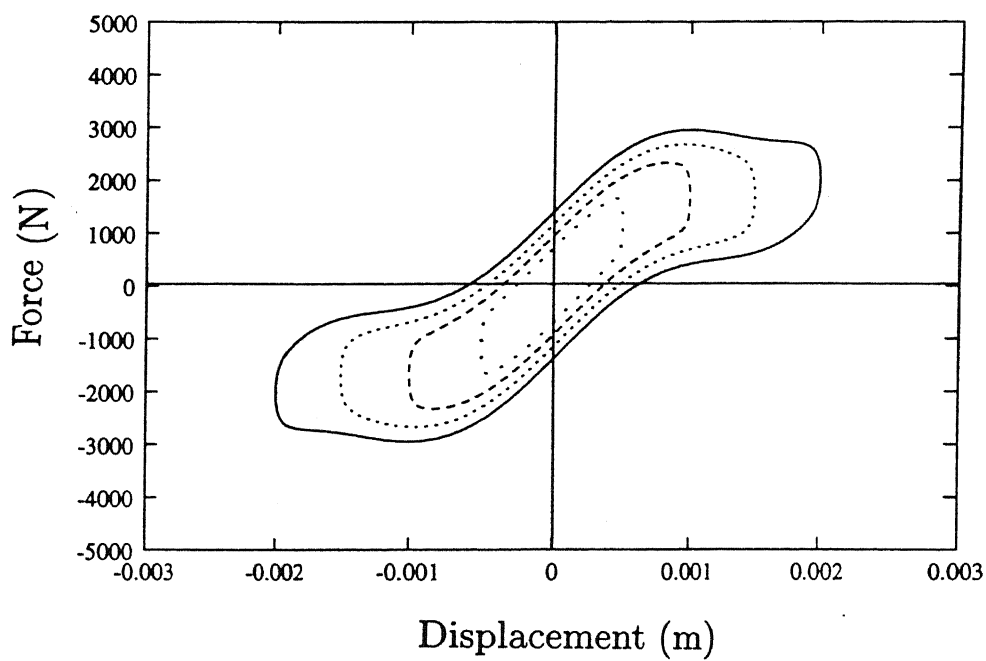


Fig. 2.9 Hysteresis loops of the elastomer model for different amplitudes of motion.

— $X = 0.002\text{m}$; $X = 0.0015\text{m}$; - - - $X = 0.0010\text{m}$;

..... $X = 0.0005\text{m}$.

Table 2.1 System parameters of the elastomeric damper model.

System Parameter	Fifth Order Approximation	Seventh Order Approximation
K_1 (N/m)	2.543437×10^6	2.673989×10^6
K_3 (N/m ³)	8.430654×10^{11}	1.315287×10^{12}
K_5 (N/m ⁵)	1.084698×10^{17}	3.519586×10^{17}
K_7 (N/m ⁷)	—	3.176266×10^{22}
F (N)	4.797347×10^2	4.797347×10^2
h (N/m)	4.569120×10^5	4.569120×10^5

Chapter 3

NON-LINEAR DYNAMICS OF UNCOUPLED FLAP AND LAG MOTION

3.1 Introduction

Dynamic analysis of rotating beams plays an important role in the design of various engineering systems such as turbo-machinery, robotic manipulators and helicopter blades. The natural frequencies and mode shapes of such structures have been a topic of constant interest and hence received considerable attention. In bearingless helicopter rotor, with the advancement in technology, the external hydraulic damper is replaced by an elastomeric damper. Experiments show that the stiffness and damping characteristics of an elastomer are highly non-linear in nature. Also the coupled equations of flap-lag-torsion and axial motions of a rotor blade are non-linear due to geometrical couplings. It may be noted that it is not known as to how much the non-linearities of the elastomer alter the dynamic characteristics of the rotor blade when the elastomer

is included as a sub-system.

Due to the presence of the non-linear elastomer, the lag and flap frequencies should be dependent on the amplitude of motion which is a typical feature of a non-linear system. In this chapter, the influence of elastomer non-linearity on the undamped natural frequencies of a rotating blade has been studied. First a linear analysis is carried out for the uncoupled flap and lag modes and the results are validated using two different solution techniques. For the non-linear problem, the frequency-amplitude relationships in flap and lag modes are derived in a closed form, using numerical-perturbation technique.

3.2 Bearingless Rotor Model

A schematic diagram of the bearingless rotor is shown in Fig. 1.3a. Figures 3.1 a and 3.1 b represent simplified models of the bearingless rotor under isolated flap and lag motions respectively. Since only the uncoupled flap and lag modes are considered, the rotor blade is idealised as a line element along the elastic (or reference) axis of the blade. The elastomeric damper is placed between the torque tube and the flexbeam to have adequate deformation and consequent lag damping. The torque tube is represented by a massless rigid link EC as shown in Fig. 3.1. The blade and flexbeam are assumed to be an Euler-Bernoulli beam with uniform cross-section and flexural rigidity. Since the damping does not play any significant role so far as the natural frequencies are concerned, elastomer is represented by a spring element. The effect of pitch link is not considered. Thus, for each mode, the bearingless rotor can be idealised as a rotating beam having a non-linear spring connected between the points B and C on the beam through the torque tube. A discussion on the free vibration analysis of the rotor blade system by assuming the spring to be first linear and then non-linear is presented in the

following..

3.3 Linear Analysis

The dynamics of a rotating beam differs from that of a non-rotating one due to the addition of centrifugal stiffness. The differential equations of motion for a rotating uniform beam contain variable coefficients while those for a non-rotating uniform beam have constant coefficients. For the case of isolated flap dynamic problem, it is assumed that the elastomer is acting in the transverse direction only. Thus, there is a transverse constraint at the point B (Fig. 3.1 a) in the form of a linear spring whose deformation depends not only on the deflection at B , but also on the deflection and slope at the point C . On the other hand, in the case of lag dynamics, the constraint is in the in-plane direction only (Fig. 3.1 b).

In this section, the equations of motion and the associated boundary conditions for the uncoupled flap and lag motion of the rotating beam are presented separately. For comparative purposes, two different solution techniques, one based on power series expansion and the other based on the Rayleigh-Ritz principle are used to determine the natural frequencies and the mode shapes.

3.3.1 Power Series

Referring to Figs. 3.1 a and 3.1 b, the partial differential equations for small amplitude of vibration of the rotating uniform Euler-Bernoulli beam can be given by

$$EI \frac{\partial^4 \bar{W}_1}{\partial x^4} - \frac{1}{2} m \Omega^2 \frac{\partial}{\partial x} \left[(L^2 - x^2) \frac{\partial \bar{W}_1}{\partial x} \right] = \begin{cases} -m \frac{\partial^2 \bar{W}_1}{\partial t^2} \\ -m \frac{\partial^2 \bar{W}_1}{\partial t^2} + m \Omega^2 \bar{W}_1 \end{cases} \quad \text{for } 0 \leq x \leq L_1,$$

$$\begin{aligned}
EI \frac{\partial^4 \bar{W}_2}{\partial x^4} - \frac{1}{2} m \Omega^2 \frac{\partial}{\partial x} \left[(L^2 - x^2) \frac{\partial \bar{W}_2}{\partial x} \right] &= \begin{cases} -m \frac{\partial^2 \bar{W}_2}{\partial t^2} & \text{for } L_1 \leq x \leq L_2 \\ -m \frac{\partial^2 \bar{W}_2}{\partial t^2} + m \Omega^2 \bar{W}_2 & \end{cases} \\
EI \frac{\partial^4 \bar{W}_3}{\partial x^4} - \frac{1}{2} m \Omega^2 \frac{\partial}{\partial x} \left[(L^2 - x^2) \frac{\partial \bar{W}_3}{\partial x} \right] &= \begin{cases} -m \frac{\partial^2 \bar{W}_3}{\partial t^2} & \text{for } L_2 \leq x \leq L \\ -m \frac{\partial^2 \bar{W}_3}{\partial t^2} + m \Omega^2 \bar{W}_3 & \end{cases}
\end{aligned} \tag{3.1}$$

where t denotes time, m denotes the mass per unit length, EI the flexural rigidity, Ω the angular velocity and \bar{W}_i ($i = 1, 2, 3$) the deflection at different segments of the beam. In Eq. 3.1, the top terms in the right hand side apply to the out of plane motion whereas the bottom terms apply to the in-plane motion. (Note: For convenience, in this section, the same notations (W , \bar{W}) have been used for both out of plane and in-plane motion.)

Introducing the following dimensionless quantities

$$W_i = \frac{\bar{W}_i}{L}, \quad \xi = \frac{x}{L}, \quad \tau = \Omega t, \quad \xi_j = \frac{L_j}{L} (j = 1, 2), \quad \bar{a} = \frac{EI}{m \Omega^2 L^4} \tag{3.2}$$

and assuming a harmonic solution of the form

$$W_i(\xi, \tau) = W_i(\xi) \exp(i\omega\tau),$$

Equations 3.1 reduce to

$$\begin{aligned}
\bar{a} \frac{d^4 W_1}{d\xi^4} - \frac{1}{2} \frac{d}{d\xi} \left[(1 - \xi^2) \frac{dW_1}{d\xi} \right] - \lambda W_1 &= 0 \text{ for } 0 \leq \xi \leq \xi_1, \\
\bar{a} \frac{d^4 W_2}{d\xi^4} - \frac{1}{2} \frac{d}{d\xi} \left[(1 - \xi^2) \frac{dW_2}{d\xi} \right] - \lambda W_2 &= 0 \text{ for } \xi_1 \leq \xi \leq \xi_2 \\
\text{and } \bar{a} \frac{d^4 W_3}{d\xi^4} - \frac{1}{2} \frac{d}{d\xi} \left[(1 - \xi^2) \frac{dW_3}{d\xi} \right] - \lambda W_3 &= 0 \text{ for } \xi_2 \leq \xi \leq 1,
\end{aligned} \tag{3.3}$$

$$\text{where } \lambda = \begin{cases} \omega^2 & \text{for out of plane vibration.} \\ 1 + \omega^2 & \text{for in-plane vibration.} \end{cases}$$

For the beam which is clamped at $\xi = 0$ and free at $\xi = 1$, the boundary conditions are

$$W_1(0) = 0, \quad \frac{dW_1(0)}{d\xi} = 0 \quad \text{and} \quad \frac{d^2W_3(1)}{d\xi^2} = 0, \quad \frac{d^3W_3(1)}{d\xi^3} = 0. \quad (3.4)$$

Consider the free body diagrams of the beam AD and the link EC , shown in Fig. 3.2, where V and M are respectively the force and the moment acting on EC and AD . Assuming the transverse/in-plane deflection to be positive along the Z/Y direction, the expression for V and M are given by

$$V = K_1 \Delta \quad \text{and} \quad M = V(\xi_2 - \xi_1) \quad (3.5)$$

where $\Delta = [W_C - (\xi_2 - \xi_1) W'_C - W_B]$ is the extension of the spring,

with W_C = deflection of the beam at C,

W_B = deflection of the beam at B,

W'_C = slope of the beam at C,

and K_1 = linear stiffness of the spring.

In addition to the boundary conditions given by Eqs. 3.5, the following continuity conditions at the locations B and C have to be satisfied:

$$W_1(\xi_1) = W_2(\xi_1), \quad \frac{dW_1(\xi_1)}{d\xi} = \frac{dW_2(\xi_1)}{d\xi}, \quad \frac{d^2W_1(\xi_1)}{d\xi^2} = \frac{d^2W_2(\xi_1)}{d\xi^2}$$

and $\frac{d^3W_1(\xi_1)}{d\xi^3} + K^* \left[W_2(\xi_2) - (\xi_2 - \xi_1) \frac{dW_2(\xi_2)}{d\xi} - W_1(\xi_1) \right] = \frac{d^3W_2(\xi_1)}{d\xi^3}; \quad (3.6)$

$$W_2(\xi_2) = W_3(\xi_2), \quad \frac{dW_2(\xi_2)}{d\xi} = \frac{dW_3(\xi_2)}{d\xi},$$

$$\frac{d^2W_2(\xi_2)}{d\xi^2} + K^* (\xi_2 - \xi_1) \left[W_2(\xi_2) - (\xi_2 - \xi_1) \frac{dW_2(\xi_2)}{d\xi} - W_1(\xi_1) \right] = \frac{d^2W_3(\xi_2)}{d\xi^2}$$

and $\frac{d^3W_2(\xi_2)}{d\xi^3} - K^* \left[W_2(\xi_2) - (\xi_2 - \xi_1) \frac{dW_2(\xi_2)}{d\xi} - W_1(\xi_1) \right] = \frac{d^3W_3(\xi_2)}{d\xi^3} \quad (3.7)$

where $K^* = \frac{K_1 L^3}{EI}$.

Equations (3.3) are linear ordinary differential equations with variable coefficients.

Their solutions can be expressed as a power series in the independent variable ξ as

$$\begin{aligned} W_1(\xi) &= \sum_{k=1}^{\infty} C_k \xi^{k-1} \quad \text{for } 0 \leq \xi \leq \xi_1, \\ W_2(\xi) &= \sum_{k=1}^{\infty} D_k \xi^{k-1} \quad \text{for } \xi_1 \leq \xi \leq \xi_2 \\ \text{and } W_3(\xi) &= \sum_{k=1}^{\infty} E_k \xi^{k-1} \quad \text{for } \xi_2 \leq \xi \leq 1. \end{aligned} \quad (3.8)$$

Inserting Eqs. 3.8 into Eqs. 3.3 and equating the coefficients of the like powers of ξ , the following recurrence relations are obtained after some algebraic manipulations :

$$\begin{aligned} 2a(k+3)(k+2)(k+1)kC_{k+4} - (k+1)kC_k + [k(k-1) - 2\omega^2]C_k &= 0 \\ 2a(k+3)(k+2)(k+1)kD_{k+4} - (k+1)kD_k + [k(k-1) - 2\omega^2]D_k &= 0 \\ 2a(k+3)(k+2)(k+1)kE_{k+4} - (k+1)kE_k + [k(k-1) - 2\omega^2]E_k &= 0 \end{aligned} \quad (3.9)$$

for $k = 1, 2, 3, \dots$

Similarly, inserting the expressions (3.8) into the boundary conditions (3.4), (3.6) and (3.7), one obtains

$$C_1 = 0, \quad C_2 = 0, \quad \sum_{k=1}^{\infty} E_k (k-1)(k-2) = 0, \quad \sum_{k=1}^{\infty} E_k (k-1)(k-2)(k-3) = 0; \quad (3.10)$$

$$\begin{aligned} \sum_{k=1}^{\infty} C_k \xi_1^{k-1} - \sum_{k=1}^{\infty} D_k \xi_1^{k-1} &= 0 \\ \sum_{k=1}^{\infty} C_k (k-1) \xi_1^{k-2} - \sum_{k=1}^{\infty} D_k (k-1) \xi_1^{k-2} &= 0 \\ \sum_{k=1}^{\infty} C_k (k-1)(k-2) \xi_1^{k-3} - \sum_{k=1}^{\infty} D_k (k-1)(k-2) \xi_1^{k-3} &= 0 \end{aligned} \quad (3.11)$$

$$\sum_{k=1}^{\infty} C_k (k-1)(k-2)(k-3) \xi_1^{k-4} + K^* \left[\sum_{k=1}^{\infty} D_k \xi_2^{k-1} - (\xi_2 - \xi_1) \sum_{k=1}^{\infty} D_k (k-1) \xi_2^{k-2} - \sum_{k=1}^{\infty} C_k \xi_1^{k-1} \right] - \sum_{k=1}^{\infty} D_k (k-1)(k-2)(k-3) \xi_1^{k-4} = 0$$

and

$$\begin{aligned} \sum_{k=1}^{\infty} D_k \xi_2^{k-1} - \sum_{k=1}^{\infty} E_k \xi_2^{k-1} &= 0 \\ \sum_{k=1}^{\infty} D_k (k-1) \xi_2^{k-2} - \sum_{k=1}^{\infty} E_k (k-1) \xi_2^{k-2} &= 0 \\ \sum_{k=1}^{\infty} D_k (k-1)(k-2) \xi_2^{k-3} + K^* (\xi_2 - \xi_1) \left[\sum_{k=1}^{\infty} D_k \xi_2^{k-1} - (\xi_2 - \xi_1) \sum_{k=1}^{\infty} D_k (k-1) \xi_2^{k-2} - \sum_{k=1}^{\infty} C_k \xi_1^{k-1} \right] - \sum_{k=1}^{\infty} E_k (k-1)(k-2) \xi_2^{k-3} &= 0 \quad (3.12) \\ \sum_{k=1}^{\infty} D_k (k-1)(k-2)(k-3) \xi_2^{k-4} - K^* \left[\sum_{k=1}^{\infty} D_k \xi_2^{k-1} - (\xi_2 - \xi_1) \sum_{k=1}^{\infty} D_k (k-1) \xi_2^{k-2} - \sum_{k=1}^{\infty} C_k \xi_1^{k-1} \right] - \sum_{k=1}^{\infty} E_k (k-1)(k-2)(k-3) \xi_2^{k-4} &= 0. \end{aligned}$$

If the power series is truncated at the P -th term, then there are altogether $3P$ unknown coefficients. From the recurrence relations (3.9) and the boundary conditions (3.10), (3.11) and (3.12), there are $3P$ simultaneous linear homogeneous equations. For non-trivial solution, the determinant of the coefficient matrix must vanish. Thus, setting this determinant equal to zero one gets the frequency equation which is solved numerically for unknown ω .

In order to obtain the mode shape, an additional normalising condition

$$W(1) = 1 \quad (3.13)$$

is imposed.

3.3.2 Rayleigh-Ritz Method

In this section, the equations of motion of the rotating blade under uncoupled flap and lag motion are separately derived using the Rayleigh-Ritz method.

3.3.2.1 Equation of Motion in Flap Mode

Figure 3.3 a shows the axial and out of plane deformations of a point A on the elastic axis due only to the flap bending motion of the rotating beam. The kinetic energy of the beam under is given by

$$T(t) = \frac{1}{2} \int_0^L m \left[\left\{ \frac{\partial \bar{u}}{\partial t} \right\}^2 + \left\{ \frac{\partial \bar{w}}{\partial t} \right\}^2 + \{\Omega x + \Omega \bar{u}\}^2 \right] dx. \quad (3.14)$$

Assuming that the blade is very stiff in the axial direction, the following inextensionality condition is imposed:

$$\bar{u} = -\frac{1}{2} \int_0^x \left(\frac{\partial \bar{w}}{\partial x} \right)^2 dx. \quad (3.15)$$

The strain energy must include the effects of the bending moment, and spring deformation. The expression for strain energy due to bending is

$$U_1 = \frac{1}{2} \int_0^L EI \left[\frac{\partial^2 \bar{w}(x, t)}{\partial x^2} \right]^2 dx \quad (3.16)$$

The strain energy of the spring due to deformation Δ_f is

$$U_2 = \frac{1}{2} K_1 \Delta_f^2 \quad (3.17)$$

$$\text{where } \Delta_f = \left[\bar{w}(L_2, t) - (L_2 - L_1) \frac{\partial \bar{w}(L_2, t)}{\partial x} - \bar{w}(L_1, t) \right]. \quad (3.18)$$

Hence the total strain energy of the system is

$$U = U_1 + U_2. \quad (3.19)$$

The equation of motion is derived after introducing the dimensionless quantities defined by Eq. 3.2. Assuming a solution in the form

$$w(\xi, \tau) = \sum_{i=1}^n \hat{\phi}_i(\xi) r_i(\tau) \quad (3.20)$$

motion. The above eigenvalue problem is solved numerically to determine the natural frequencies.

3.3.2.2 Equation of Motion in Lag Mode

Referring to Fig. 3.4, the kinetic energy of the beam under isolated lag motion is given by

$$T(t) = \frac{1}{2} \int_0^L m \left[\left\{ \frac{\partial \bar{u}}{\partial t} - \Omega \bar{v} \right\}^2 + \left\{ \frac{\partial \bar{v}}{\partial t} + \Omega x + \Omega \bar{u} \right\}^2 \right] dx. \quad (3.25)$$

The expression for strain energy due to in-plane bending is

$$U_1 = \frac{1}{2} \int_0^L EI \left[\frac{\partial^2 \bar{v}(x, t)}{\partial x^2} \right]^2 dx \quad (3.26)$$

The strain energy of the spring due to deformation Δ_l in the lag direction is given by

$$U_2 = \frac{1}{2} K_1 \Delta_l^2 \quad (3.27)$$

$$\text{where } \Delta_l = \left[\bar{v}(L_2, t) - (L_2 - L_1) \frac{\partial \bar{v}(L_2, t)}{\partial x} - \bar{v}(L_1, t) \right]. \quad (3.28)$$

Assuming a solution in the form

$$v(\xi, \tau) = \sum_{i=1}^n \hat{\phi}_i(\xi) q_i(\tau) \quad (3.29)$$

and following the same procedure as mentioned for the flap mode, the eigenvalue problem for the blade in lag mode can be written as

$$[\mathbf{K}] \{q\} = \lambda [\mathbf{M}] \{q\} \quad (3.30)$$

$$\text{where } [\mathbf{K}] = \int_0^1 \bar{a} \hat{\phi}_i'' \hat{\phi}_j'' d\xi + \int_0^1 \frac{1}{2} (1 - \xi^2) \hat{\phi}_i' \hat{\phi}_j' d\xi + \alpha_1 \hat{\psi}_i^l \hat{\psi}_j^l,$$

$$[\mathbf{M}] = \int_0^1 \hat{\phi}_i \hat{\phi}_j d\xi,$$

$$\bar{a} = \frac{EI}{m\Omega^2 L^4},$$

$$\alpha_1 = \frac{K_1}{m\Omega^2 L}$$

$$\text{and } \lambda = 1 + \omega^2.$$

3.4 Non-Linear Analysis

The elastomer is represented as a non-linear spring. Following Pakdemirli and Nayfeh [101], a numerical-perturbation technique is adopted for the non-linear analysis of the rotor blade. Accordingly, the continuous system has to be first discretized by any one of the methods of weighted residuals [108] (such as, Collocation, Galerkin, Rayleigh-Ritz etc.) to obtain a system of coupled non-linear ordinary differential equations. Then, one can apply any one of the perturbation techniques. Though Galerkin discretisation procedure is most common, Rayleigh-Ritz technique is used in this study, since it gives a symmetric stiffness matrix for this problem whereas, the Galerkin procedure leads to a non-symmetric matrix.

3.4.1 Non-Linear Equation of Motion

First, the derivation of the non-linear equation of motion and close form expression for the frequency-amplitude relationship in flap mode is given in detail. For the lag mode, the same procedure is followed.

3.4.1.1 Flap Motion

When the elastomer is represented as a non-linear spring, the expression for the strain energy of the spring is modified as

$$U_2 = \frac{1}{2}K_1\Delta_f^2 - \frac{1}{4}K_3\Delta_f^4 + \frac{1}{6}K_5\Delta_f^6 - \frac{1}{8}K_7\Delta_f^8 \quad (3.31)$$

Introducing the following dimensionless terms for the flap motion,

$$w = \frac{\bar{w}}{\gamma^4 L} , \quad \xi = \frac{x}{L} , \quad \tau = \Omega t \quad (3.32)$$

with, $\gamma = \frac{\bar{r}}{L}$ ($\ll 1$), where \bar{r} is the radius of gyration of the beam cross-section about the reference axis. Substituting for Δ_f in Eq. 3.31 from Eqs. 3.18 and using Eqs. 3.20

and 3.22, one can rewrite Eq. 3.31 as

$$U_2 = \frac{1}{2}K_1L^2\epsilon\left[\sum_{i=1}^n\hat{\psi}_i^f r_i(\tau)\right]^2 - \frac{1}{4}K_3L^4\epsilon^2\left[\sum_{i=1}^n\hat{\psi}_i^f r_i(\tau)\right]^4 + \frac{1}{6}K_5L^6\epsilon^3\left[\sum_{i=1}^n\hat{\psi}_i^f r_i(\tau)\right]^6 - \frac{1}{8}K_7L^8\epsilon^4\left[\sum_{i=1}^n\hat{\psi}_i^f r_i(\tau)\right]^8 \quad (3.33)$$

where $\epsilon = \gamma^8$ is the small parameter.

Replacing the strain energy expression of the linear spring (Eq. 3.21) by the strain energy expression of the non-linear spring given in Eq. 3.33 and following the procedure outlined in Sec. 3.3.2.1, the temporal equation of motion in flap mode can be obtained as

$$[M]\{\ddot{r}\} + [K]\{r\} + \{F_{NL}(r)\} = 0 \quad (3.34)$$

where $F_{NL}(r)$ contains the contribution of the non-linear terms in the spring force.

In order to decouple the linear part of the above equation, the following linear transformation is introduced.

$$r(\tau) = [P]z(\tau) \quad (3.35)$$

where $[P]$ is formed by the normalised (with respect to mass matrix) eigenvector of the linear eigenvalue problem obtained after neglecting the non-linear terms in Eq. 3.34.

Substituting Eq. 3.35 into Eq. 3.34 and premultiplying by $[P]^T$, the temporal equation is obtained in the form

$$\begin{aligned} \ddot{z}_i(\tau) + \omega_i^2 z_i(\tau) - \epsilon\alpha_3 \sum_{m=1}^n \sum_{s=1}^n \sum_{r=1}^n \Gamma_{imsr} z_m z_s z_r \\ + \epsilon^2\alpha_5 \sum_{m=1}^n \sum_{s=1}^n \sum_{r=1}^n \sum_{t=1}^n \sum_{u=1}^n \Gamma_{imsrtu} z_m z_s z_r z_t z_u \\ - \epsilon^3\alpha_7 \sum_{m=1}^n \sum_{s=1}^n \sum_{r=1}^n \sum_{t=1}^n \sum_{u=1}^n \sum_{v=1}^n \sum_{w=1}^n \Gamma_{imsrtuvw} z_m z_s z_r z_t z_u z_v z_w = 0 \end{aligned} \quad (3.36)$$

$i = 1, 2, 3, \dots, n$

where ω_i is i th linear natural frequency and

$$\begin{aligned}
\Gamma_{imsr} &= \bar{\psi}_i^f \bar{\psi}_m^f \bar{\psi}_s^f \bar{\psi}_r^f , \\
\Gamma_{imsrtu} &= \bar{\psi}_i^f \bar{\psi}_m^f \bar{\psi}_s^f \bar{\psi}_r^f \bar{\psi}_t^f \bar{\psi}_u^f , \\
\Gamma_{imsrtuvw} &= \bar{\psi}_i^f \bar{\psi}_m^f \bar{\psi}_s^f \bar{\psi}_r^f \bar{\psi}_t^f \bar{\psi}_u^f \bar{\psi}_v^f \bar{\psi}_w^f , \\
\alpha_3 &= \frac{K_3 L}{m \Omega^2} , \quad \alpha_5 = \frac{K_5 L^3}{m \Omega^2} , \quad \alpha_7 = \frac{K_7 L^5}{m \Omega^2} ,
\end{aligned} \tag{3.37}$$

and

$$\bar{\psi}_i^f = \hat{\psi}_1^f p_{1i} + \hat{\psi}_2^f p_{2i} + \dots + \hat{\psi}_n^f p_{ni} \tag{3.38}$$

$\bar{\psi}_i^f$ can be interpreted as the deformation of the spring in i th flap mode. In Eq. 3.38, p_{ij} represent the elements of the matrix $[\mathbf{P}]$. The linear part of Eq. 3.36 is no longer coupled. Now, using the method of multiple scales and seeking an expansion of the solution of Eq. 3.36 for small but finite amplitude in the form

$$z_i(\tau; \epsilon) = z_{i0}(T_0, T_1, T_2, T_3) + \epsilon z_{i1}(T_0, T_1, T_2, T_3) + \epsilon^2 z_{i2}(T_0, T_1, T_2, T_3) + \dots \tag{3.39}$$

where ϵ is the small non-dimensional parameter.

Different time scales are introduced as

$$T_n = \epsilon_n \tau , \quad n = 0, 1, 2, \dots \tag{3.40}$$

Here T_0 is a fast scale associated with the changes occurring with frequency close to ω_i , while T_n for $n \geq 1$ are slow scales associated with changes that can only be noticed after several cycles.

In terms of usual operator notations, we can write

$$\frac{d}{d\tau} = D_0 + \epsilon D_1 + \epsilon^2 D_2 + \epsilon^3 D_3 + \dots \tag{3.41}$$

$$\frac{d^2}{d\tau^2} = D_0^2 + 2\epsilon D_0 D_1 + \epsilon^2 (2D_0 D_2 + D_1^2) + \epsilon^3 (2D_0 D_3 + 2D_1 D_2) + \dots \tag{3.42}$$

where $D_i = \frac{d}{dT_i}$, $i = 0, 1, 2, \dots$

Substituting Eqs. 3.39 and 3.42 into Eq. 3.36 and equating the coefficients of like powers of ϵ , one obtains

$$\epsilon^0 : D_0^2 z_{i0} + \omega_i^2 z_{i0} = 0 \quad (3.43)$$

$$\epsilon^1 : D_0^2 z_{i1} + \omega_i^2 z_{i1} = -2D_0 D_1 z_{i0} + \alpha_3 \Gamma_{4i} z_{i0}^3 \quad (3.44)$$

$$\begin{aligned} \epsilon^2 : D_0^2 z_{i2} + \omega_i^2 z_{i2} = & -2D_0 D_1 z_{i1} - D_1^2 z_{i0} - 2D_0 D_2 z_{i0} + 3\alpha_3 \Gamma_{4i} z_{i0}^2 z_{i1} \\ & - \alpha_5 \Gamma_{6i} z_{i0}^5 \end{aligned} \quad (3.45)$$

$$\begin{aligned} \epsilon^3 : D_0^2 z_{i3} + \omega_i^2 z_{i3} = & -2D_0 D_1 z_{i2} - D_1^2 z_{i1} - 2D_0 D_2 z_{i1} - 2D_0 D_3 z_{i0} - 2D_1 D_2 z_{i0} \\ & + 3\alpha_3 \Gamma_{4i} z_{i0}^2 z_{i2} + 3\alpha_3 \Gamma_{4i} z_{i0} z_{i1}^2 - 5\alpha_5 \Gamma_{6i} z_{i0}^4 z_{i1} + \alpha_7 \Gamma_{8i} z_{i0}^7 \end{aligned} \quad (3.46)$$

where

$$\Gamma_{4i} = (\bar{\psi}_i^f)^4, \quad \Gamma_{6i} = (\bar{\psi}_i^f)^6, \quad \Gamma_{8i} = (\bar{\psi}_i^f)^8, \quad (3.47)$$

Assuming the solution of Eq. 3.43 as

$$z_{i0} = A_i(T_1, T_2, T_3) e^{i\omega_i T_0} + \bar{A}_i(T_1, T_2, T_3) e^{-i\omega_i T_0}. \quad (3.48)$$

Substitution of the first order solution given by Eq. 3.48 into Eq. 3.44, yields

$$D_0^2 z_{i1} + \omega_i^2 z_{i1} = -2i\omega_i D_1(A_i) e^{i\omega_i T_0} + \alpha_3 \Gamma_{4i} [A_i^3 e^{i3\omega_i T_0} + 3A_i^2 \bar{A}_i e^{i\omega_i T_0}] + c.c. \quad (3.49)$$

where *c.c.* indicates the complex conjugate.

In order that z_{i1}/z_{i0} be bounded for all T_0 , the secular terms must vanish. Hence

$$-2i\omega_i D_1(A_i) + 3\alpha_3 \Gamma_{4i} A_i^2 \bar{A}_i = 0 \quad (3.50)$$

and the solution for z_{i1} becomes

$$z_{i1} = -\frac{1}{8\omega_i^2} \alpha_3 \Gamma_{4i} A_i^3 e^{i3\omega_i T_0} + c.c. \quad (3.51)$$

In order to uniquely define the amplitude A_i of the fundamental frequency of oscillation, the homogeneous solution of Eq. 3.49 is not included.

To solve Eq. 3.50, one can assume

$$A_i = \frac{1}{2} a_i e^{i\beta_i} \quad (3.52)$$

where a_i and β_i are real functions of T_1, T_2, T_3 . Substituting equation (3.52) into equation (3.50) and separating the real and imaginary parts, one obtains

$$\begin{aligned} \frac{\partial a_i}{\partial T_1} &= 0, \quad \omega_i \frac{\partial \beta_i}{\partial T_1} + \frac{3}{8} \alpha_3 \Gamma_{4i} a_i^2 = 0 \\ \text{Hence } a_i &= a_i(T_2, T_3), \quad \beta_i = -\frac{3}{8\omega_i} \alpha_3 \Gamma_{4i} a_i^2 T_1 + \beta'_i(T_2, T_3). \end{aligned} \quad (3.53)$$

Substitution of Eqs. 3.48 and 3.51 into Eq. 3.45, one gets

$$\begin{aligned} D_0^2 z_{i2} + \omega_i^2 z_{i2} &= \frac{27}{32\omega_i^2} \alpha_3^2 \Gamma_{4i}^2 a_i^2 A_i^3 e^{i3\omega_i T_0} + \frac{9}{64\omega_i^2} \alpha_3^2 \Gamma_{4i}^2 a_i^4 A_i e^{i\omega_i T_0} - 2i\omega_i D_2(A_i) e^{i\omega_i T_0} \\ &\quad - \frac{3}{8\omega_i^2} \alpha_3^2 \Gamma_{4i}^2 A_i^5 e^{i5\omega_i T_0} - \frac{3}{8\omega_i^2} \alpha_3^2 \Gamma_{4i}^2 A_i^3 \bar{A}_i^2 e^{i\omega_i T_0} - \frac{3}{4\omega_i^2} \alpha_3^2 \Gamma_{4i}^2 A_i^4 \bar{A}_i e^{i3\omega_i T_0} \\ &\quad - \alpha_5 \Gamma_{6i} (A_i^5 e^{i5\omega_i T_0} + 5A_i^4 \bar{A}_i e^{i3\omega_i T_0} + 10A_i^3 \bar{A}_i^2 e^{i\omega_i T_0}) + c.c. \end{aligned} \quad (3.54)$$

Again the absence of any secular term in the solution of Eq. 3.54 requires

$$\frac{9}{128\omega_i^2} \alpha_3^2 \Gamma_{4i}^2 a_i^5 - 2i\omega_i D_2(A_i) - \frac{3}{8\omega_i^2} \alpha_3^2 \Gamma_{4i}^2 A_i^3 \bar{A}_i^2 - 10\alpha_5 \Gamma_{6i} A_i^3 \bar{A}_i^2 = 0. \quad (3.55)$$

Separating the real and imaginary parts, we have, after some algebraic manipulations,

$$\begin{aligned} \frac{\partial a_i}{\partial T_2} &= 0, \quad \frac{9}{128\omega_i^2} \alpha_3^2 \Gamma_{4i}^2 a_i^5 + \omega_i a_i \frac{\partial \beta'_i}{\partial T_2} - \frac{3}{256\omega_i^2} \alpha_3^2 \Gamma_{4i}^2 a_i^5 - \frac{5}{16} \alpha_5 \Gamma_{6i} a_i^5 = 0. \\ \text{Hence } a_i &= a_i(T_3), \quad \beta'_i = -\frac{15}{256\omega_i^3} \alpha_3^2 \Gamma_{4i}^2 a_i^4 T_2 + \frac{5}{16\omega_i} \alpha_5 \Gamma_{6i} a_i^4 T_2 + \beta''_i(T_3). \end{aligned} \quad (3.56)$$

The solution of Eq. 3.54 is given by

$$\begin{aligned} z_{i2} &= -\frac{27}{256\omega_i^4} \alpha_3^2 \Gamma_{4i}^2 a_i^2 A_i^3 e^{i3\omega_i T_0} + \frac{3}{32\omega_i^4} \alpha_3^2 \Gamma_{4i}^2 A_i^4 \bar{A}_i e^{i3\omega_i T_0} + \frac{3}{192\omega_i^4} \alpha_3^2 \Gamma_{4i}^2 A_i^5 e^{i5\omega_i T_0} \\ &\quad + \frac{1}{24\omega_i^2} \alpha_5 \Gamma_{6i} A_i^5 e^{i5\omega_i T_0} + \frac{5}{8\omega_i^2} \alpha_5 \Gamma_{6i} A_i^4 \bar{A}_i e^{i3\omega_i T_0} + c.c. \end{aligned} \quad (3.57)$$

Substitution of Eqs. 3.48, 3.51 and 3.57 into Eq. 3.46, yields

$$\begin{aligned}
D_0^2 z_{i3} + \omega_i^2 z_{i3} = & -2D_0 D_1 \left[-\frac{27}{256 \omega_i^4} \alpha_3^2 \Gamma_{4i}^2 a_i^2 A_i^3 e^{i3\omega_i T_0} + \frac{3}{32 \omega_i^4} \alpha_3^2 \Gamma_{4i}^2 A_i^4 \bar{A}_i e^{i3\omega_i T_0} \right. \\
& + \frac{3}{192 \omega_i^4} \alpha_3^2 \Gamma_{4i}^2 A_i^5 e^{i5\omega_i T_0} + \frac{1}{24 \omega_i^2} \alpha_5 \Gamma_{6i} A_i^5 e^{i5\omega_i T_0} \\
& \left. + \frac{5}{8 \omega_i^2} \alpha_5 \Gamma_{6i} A_i^4 \bar{A}_i e^{i3\omega_i T_0} + c.c. \right] \\
& -2D_0 D_2 \left(-\frac{1}{8 \omega_i^2} \alpha_3 \Gamma_{4i} A_i^3 e^{i3\omega_i T_0} + c.c. \right) - D_1^2 \left(-\frac{1}{8 \omega_i^2} \alpha_3 \Gamma_{4i} A_i^3 e^{i3\omega_i T_0} + c.c. \right) \\
& -2D_0 D_3 \left(A_i e^{i\omega_i T_0} + c.c. \right) - 2D_1 D_2 \left(A_i e^{i\omega_i T_0} + c.c. \right) \\
& + 3\alpha_3 \Gamma_{4i} \left(A_i e^{i\omega_i T_0} + c.c. \right) \left(-\frac{1}{8 \omega_i^2} \alpha_3 \Gamma_{4i} A_i^3 e^{i3\omega_i T_0} + c.c. \right)^2 \\
& -5\alpha_5 \Gamma_{6i} \left(A_i^4 e^{i4\omega_i T_0} + 4A_i^3 \bar{A}_i e^{i2\omega_i T_0} + 6A_i^2 \bar{A}_i^2 + c.c. \right) \\
& \left(-\frac{1}{8 \omega_i^2} \alpha_3 \Gamma_{4i} A_i^3 e^{i3\omega_i T_0} + c.c. \right) \\
& + 3\alpha_3 \Gamma_{4i} \left(A_i^2 e^{i2\omega_i T_0} + 2A_i \bar{A}_i + c.c. \right) z_{i2} + \alpha_7 \Gamma_{8i} \left(A_i e^{i\omega_i T_0} + c.c. \right)^7. \quad (3.58)
\end{aligned}$$

The condition for eliminating the secular term can be given, after some algebraic manipulations, as

$$-i\omega_i \frac{\partial a_i}{\partial T_3} + \omega_i a_i \frac{\partial \beta_i''}{\partial T_3} - \frac{5}{64 \omega_i^2} \alpha_3 \Gamma_{4i} \alpha_5 \Gamma_{6i} a_i^7 + \frac{111}{64 \times 128 \omega_i^4} \alpha_3^3 \Gamma_{4i}^3 a_i^7 + \frac{35}{128 \omega_i} \alpha_7 \Gamma_{8i} a_i^7 = 0. \quad (3.59)$$

Again, separating the real and imaginary parts of Eq. 3.59, one obtains

$$\begin{aligned}
\frac{\partial a_i}{\partial T_3} &= 0 \quad \text{or, } a_i = \text{constant} \\
\text{and } \frac{\partial \beta_i''}{\partial T_3} &= \frac{5}{64 \omega_i^3} \alpha_3 \Gamma_{4i} \alpha_5 \Gamma_{6i} a_i^6 - \frac{111}{64 \times 128 \omega_i^5} \alpha_3^3 \Gamma_{4i}^3 a_i^6 - \frac{35}{128 \omega_i} \alpha_7 \Gamma_{8i} a_i^6 \\
\text{or, } \beta_i'' &= \frac{5}{64 \omega_i^3} \alpha_3 \Gamma_{4i} \alpha_5 \Gamma_{6i} a_i^6 T_3 - \frac{111}{64 \times 128 \omega_i^5} \alpha_3^3 \Gamma_{4i}^3 a_i^6 T_3 \\
&\quad - \frac{35}{128 \omega_i} \alpha_7 \Gamma_{8i} a_i^6 T_3 + \beta_0 = 0 \quad (3.60)
\end{aligned}$$

From Eqs. 3.40, 3.53, 3.56 and 3.60 one can write the frequency-amplitude relation as

$$\omega_{Ni} = \omega_i - \epsilon \frac{3}{8 \omega_i} \alpha_3 \Gamma_{4i} a_i^2 - \epsilon^2 \frac{15}{256 \omega_i^3} \alpha_3^2 \Gamma_{4i}^2 a_i^4 + \epsilon^2 \frac{5}{16 \omega_i} \alpha_5 \Gamma_{6i} a_i^4.$$

$$+ \epsilon^3 \frac{5}{64 \omega_i^3} \alpha_3 \Gamma_{4i} \alpha_5 \Gamma_{6i} a_i^6 - \epsilon^3 \frac{111}{64 \times 128 \omega_i^5} \alpha_3^3 \Gamma_{4i}^3 a_i^6 - \epsilon^3 \frac{35}{128 \omega_i} \alpha_7 \Gamma_{8i} a_i^6 \quad (3.61)$$

where ω_{Ni} is the i -th non-linear natural frequency. Redefining the amplitude as

$$\hat{A}_i = \frac{a_i}{\sqrt{\epsilon}} \quad (3.62)$$

the final frequency-amplitude relation can be written as

$$\begin{aligned} \omega_{Ni} = \omega_i &- \frac{3}{8 \omega_i} \alpha_3 \Gamma_{4i} \hat{A}_i^2 - \frac{15}{256 \omega_i^3} \alpha_3^2 \Gamma_{4i}^2 \hat{A}_i^4 + \frac{5}{16 \omega_i} \alpha_5 \Gamma_{6i} \hat{A}_i^4 \\ &+ \frac{5}{64 \omega_i^3} \alpha_3 \Gamma_{4i} \alpha_5 \Gamma_{6i} \hat{A}_i^6 - \frac{111}{64 \times 128 \omega_i^5} \alpha_3^3 \Gamma_{4i}^3 \hat{A}_i^6 - \frac{35}{128 \omega_i} \alpha_7 \Gamma_{8i} \hat{A}_i^6. \end{aligned} \quad (3.63)$$

3.4.1.2 Lag Motion

The elastomer is represented by a non-linear spring. It is assumed to be effective in the in-plane direction only. The assumed mode solution in lag mode is given by

$$v(\xi, \tau) = \sum_{i=1}^n \bar{\phi}_i(\xi) y_i(\tau)$$

where $\bar{\phi}_i$ is the i -th rotating mode shape in lag motion. The expression for $\bar{\phi}_i$ can be written as

$$\bar{\phi}_i = \hat{\phi}_1 p_{1i} + \hat{\phi}_2 p_{2i} + \dots + \hat{\phi}_n p_{ni} \quad (3.64)$$

with p_{ij} as the elements of the matrix formed by the eigenvector of the linear eigenvalue problem.

The expression for the strain energy of the spring in nondimensional form can be written as

$$\begin{aligned} U_2 = & \frac{1}{2} K_1 L^2 \epsilon \left[\sum_{i=1}^n \bar{\psi}_i^l y_i(\tau) \right]^2 - \frac{1}{4} K_3 L^4 \epsilon^2 \left[\sum_{i=1}^n \bar{\psi}_i^l y_i(\tau) \right]^4 + \frac{1}{6} K_5 L^6 \epsilon^3 \left[\sum_{i=1}^n \bar{\psi}_i^l y_i(\tau) \right]^6 \\ & - \frac{1}{8} K_7 L^8 \epsilon^4 \left[\sum_{i=1}^n \bar{\psi}_i^l y_i(\tau) \right]^8 \end{aligned} \quad (3.65)$$

where $\bar{\psi}_i^l$ can be interpreted as the deformation of the spring in the lag mode.

Following the same procedure as outlined in the earlier section on flap vibration, the non-linear temporal equation for lag vibration can be obtained which will have the same form as given in Eq. 3.36. Using multiple-time-scales, the final expression for amplitude-frequency relation for the isolated lag mode of the rotating beam is obtained as

$$\begin{aligned} \omega_{Ni} = & \omega_i - \frac{3}{8\omega_i}\alpha_3\Gamma_{4i}\hat{A}_i^2 - \frac{15}{256\omega_i^3}\alpha_3^2\Gamma_{4i}^2\hat{A}_i^4 + \frac{5}{16\omega_i}\alpha_5\Gamma_{6i}\hat{A}_i^4 \\ & + \frac{5}{64\omega_i^3}\alpha_3\Gamma_{4i}\alpha_5\Gamma_{6i}\hat{A}_i^6 - \frac{111}{64 \times 128\omega_i^5}\alpha_3^3\Gamma_{4i}^3\hat{A}_i^6 - \frac{35}{128\omega_i}\alpha_7\Gamma_{8i}\hat{A}_i^6 \end{aligned} \quad (3.66)$$

where ω_i is i th linear natural frequency in the lag mode and

$$\begin{aligned} \Gamma_{imsr} &= \bar{\psi}_i^l \bar{\psi}_m^l \bar{\psi}_s^l \bar{\psi}_r^l, \\ \Gamma_{imsrtu} &= \bar{\psi}_i^l \bar{\psi}_m^l \bar{\psi}_s^l \bar{\psi}_r^l \bar{\psi}_t^l \bar{\psi}_u^l, \\ \Gamma_{imsrtuvw} &= \bar{\psi}_i^l \bar{\psi}_m^l \bar{\psi}_s^l \bar{\psi}_r^l \bar{\psi}_t^l \bar{\psi}_u^l \bar{\psi}_v^l \bar{\psi}_w^l, \\ \alpha_3 &= \frac{K_3 L}{m\Omega^2}, \quad \alpha_5 = \frac{K_5 L^3}{m\Omega^2}, \quad \alpha_7 = \frac{K_7 L^5}{m\Omega^2}. \end{aligned} \quad (3.67)$$

3.5 Results and Discussion

This section describes the numerical results obtained for the linear and non-linear dynamics of the blade in uncoupled flap and lag motions. First, the results pertaining to the rotating beam in the flap mode are presented.

3.5.1 Isolated Flap Motion

The results for the out of plane vibration of the rotating beam are given below in three parts.

3.5.1.1 Rotating Beam Without Elastomer

The beam is assumed to be uniform and the data used in the computations are given in Table 3.1. These values are taken from Refs. [109, 110] for correlation purpose. The natural frequencies and mode shapes of a rotating beam are obtained by using both the power series and the Rayleigh-Ritz method. The first three natural frequencies in the flap mode are calculated. The roots of the frequency equation obtained by the power series method are computed by an iterative search procedure. For the Rayleigh-Ritz analysis, the following comparison functions [111] satisfying all the boundary conditions are used :

$$\hat{\phi}_i(\xi) = \xi^i \left[\frac{(i+2)(i+3)}{6} \xi - \frac{i(i+3)}{3} \xi^2 + \frac{i(i+1)}{6} \xi^3 \right] \quad (3.68)$$

where i refers to the mode number.

The results so obtained are given in Table 3.2. It is observed that the results obtained by both the methods are in excellent agreement with those presented in Refs. [109, 110]. It may be noted that in Refs. [109, 110], the natural frequencies have been obtained by finite element analysis of the blade.

3.5.1.2 Rotating Beam with Linear Elastomer

The elastomer is idealised as a linear spring. The dynamic characteristics of a rotating beam are analysed for different values of elastomer $\xi_1 (= \frac{L_1}{L})$ and torque tube $\xi_2 (= \frac{L_2}{L})$ locations (see Fig. 3.1 a). Calculations are also performed for four values of the dimensionless spring constant $K^* = 1000, 2000, 3000$ and 4000 . To validate the results, the frequencies are evaluated by using both the power series method and Rayleigh-Ritz technique. The power series converges for $P = 50$, where P represents the number of terms in each series. Since the rotating beam is divided into three parts and each part is represented by a 50 term power series, there are in total 150 unknown coefficients.

While using the Rayleigh-Ritz technique, the natural frequencies converged when sixteen comparison functions ($i = 1$ to 16 in equation (3.68)) were used. Table 3.3 presents the first three natural frequencies of the rotating beam, evaluated by both techniques, for different values of the parameters (K^* , ξ_2). In most of the cases, the natural frequencies obtained by the two methods are in excellent agreement with each other. However, there is a difference of about 3% to 6% in the third natural frequency for $\xi_2 = 0.3$. For a given configuration, say $\xi_1 = 0.1$ and $\xi_2 = 0.25$, when the stiffness (K^*) is varied from 1000 to 4000, the percentage variation in natural frequency in the first mode is 0.6%; in the second mode the variation is 0.02% and in the third mode the variation is 2.17%. Similar behaviour is also observed for other values of ξ_2 .

The mode shapes corresponding to the first three natural frequencies are shown in Figs. 3.4-3.6, for $\xi_1 = 0.10$, $\xi_2 = 0.20, 0.25$ and 0.30 and $K^*=2000$. The mode shapes of the rotating beam without the spring are also included in these figures. It is observed that the presence of the linear spring affects the mode shape in the region between $\xi_1 = .10$ to $\xi_2 = .40$. The influence of the spring is more pronounced for the third mode (Fig. 3.6).

A detailed analysis is carried out to study the influence of different geometric configurations of the torque-tube on the natural frequencies. The value of ξ_1 was varied from 0.11 to 0.25 in steps of 0.02 and that of ξ_2 is varied from 0.25 to 1.0 in steps of 0.05. The results are generated for academic interest only since no practical blade will have $\xi_2 > 0.3$. The value of the spring stiffness was chosen as $K^* = 2000$. The natural frequencies are evaluated by the power series method. The variation of the first three natural frequencies are shown in Figs. 3.7-3.9. From Fig. 3.7, it can be seen that for all values of ξ_1 , the first natural frequency initially increases and then decreases with increasing ξ_2 . The maximum value of the frequency occurs around $\xi_2=0.40$. The second natural frequency also exhibits a similar trend (Fig. 3.8) with the exception that

the maximum value takes place around $\xi_2 = 0.70$. The third natural frequency shows more complicated nature of variation with increasing ξ_2 (Fig. 3.9). It may be noted that the point of attachment of the torque tube (i.e. ξ_2), rather than the location (ξ_1) and stiffness (K^*) of the spring, predominantly governs the natural frequencies.

3.5.1.3 Non-Linear Analysis

The force-deformation characteristics of the non-linear spring are represented by two models: one with a fifth order approximation and the other with a seventh order approximation as detailed in Chapter 2. The fifth and seventh order approximations are given as

$$F_S = K_1x - K_3x^3 + K_5x^5 \text{ and } F_S = K_1x - K_3x^3 + K_5x^5 - K_7x^7, \text{ respectively.}$$

The values of the constants are given in Table 2.1. For the fifth order approximation, corresponding to the value of K_1 , given in Table 2.1, is $K^*=3480.4$. Similarly for the seventh order approximation, $K^*=3658.8$. It should be noted that both these values are close to 4000 for which the numerical results with the linear analysis have already been presented. The non-linear dynamic analysis is carried out for a specific rotor blade configuration having $\xi_1 = 0.1$ and $\xi_2 = 0.25$. These are representative values corresponding to a realistic bearingless rotor.

The procedure of evaluating the frequency-amplitude (Eq. 3.63) relation is as follows. Using the linear stiffness term from the nonlinear force-deformation relation of the spring, a linear eigenvalue problem is solved for the natural frequencies, the transformation matrix $[P]$ (Eq. 3.35). $[P]$, the deformation of the spring in each mode ($\bar{\psi}_i^f$) is obtained from Eq. 3.38. Knowing α_i 's from Eq. 3.37 and using Eq. 3.47, the coefficients of the frequency-amplitude Eq. 3.63 are obtained. The final expressions of the frequency-amplitude relationships for the first three modes corresponding to the two spring models, are given below:

5th order spring model :

$$\omega_{N1} = 1.138 - 20.1568\hat{A}^2 - 1.487626454 \times 10^2\hat{A}^4 + 3.188617261 \times 10^4\hat{A}^4$$

$$\omega_{N2} = 3.408 - 3.947019815 \times 10^{-2}\hat{A}^2 - 1.904996008 \times 10^{-4}\hat{A}^4 + 4.780973363\hat{A}^4$$

$$\omega_{N3} = 7.924 - 8.797674851 \times 10^4\hat{A}^2 - 4.070122676 \times 10^8\hat{A}^4 + 2.426085485 \times 10^{10}\hat{A}^4$$

7th order spring model :

$$\begin{aligned}\omega_{N1} = & 1.138 - 2.793\hat{A}^2 - 2.8553 \times 10^2\hat{A}^4 + 8.657906 \times 10^4\hat{A}^4 + 1.41639283 \times 10^6\hat{A}^6 \\ & - 4.32084 \times 10^3\hat{A}^6 - 9.50547154 \times 10^7\hat{A}^6\end{aligned}$$

$$\begin{aligned}\omega_{N2} = & 3.408 - 6.7618 \times 10^{-2}\hat{A}^2 - 5.5908 \times 10^{-5}\hat{A}^4 + 17.8501\hat{A}^4 + 2.36143 \times 10^{-1}\hat{A}^6 \\ & - 6.8414 \times 10^{-7}\hat{A}^6 - 1.66869 \times 10^3\hat{A}^6\end{aligned}$$

$$\begin{aligned}\omega_{N3} = & 7.930 - 1.226218 \times 10^5\hat{A}^2 - 7.900145\hat{A}^4 + 6.650156\hat{A}^4 + 6.855182 \times 10^{14}\hat{A}^6 \\ & - 7.532292 \times 10^{13}\hat{A}^6 - 1.277168 \times 10^{16}\hat{A}^6\end{aligned}$$

The variations of the first three natural frequencies with the amplitude of oscillation at the free end are shown in Figs. 3.10-3.12. From Fig. 3.10, it can be seen that with the seventh order approximation, the first natural frequency decreases continuously with the amplitude. Where as, with the fifth order approximation, the frequency initially decerases upto an amplitude of 0.018 and then shows an increase with a further increase in the amplitude. The reason for this behaviour can be attributed to the stiffening nature of the fifth order approximation of the spring at high amplitudes, as shown in Figure 2.7. A similar behaviour is depicted by the third natural frequency as can be seen from Fig. 3.12. The second natural frequency is least affected by the amplitude upto a value of 0.1 as can be seen in Fig. 3.11.

Figure 3.13 shows the nature of variation of the non-linear first natural frequency with amplitude as one uses different orders of approximation for the spring. With the inclusion of higher order non-linear term (one at a time), the frequency-amplitude

relationship shows alternate softening and stiffening nature. Therefore, the range of validity of the frequency-amplitude relationship (for a particular order) is limited to the point beyond which there is appreciable variation.

3.5.2 Isolated Lag Motion

Numerical results corresponding to uncoupled lag motion are obtained using the method outlined in Secs. 3.3 and 3.4 and presented in three parts, each one concentrating on a particular problem. The data used are given in Table 3.1.

3.5.2.1 Rotating Beam without Elastomer

The natural frequencies and mode shapes of a rotating beam in the lag mode are obtained by using both the power series and the Rayleigh-Ritz method. Since the third natural frequency is usually very high for the lag mode, the analysis is restricted to the first two frequencies only. For the Rayleigh-Ritz analysis, the same comparison functions given in Eq. 3.68 satisfying all the boundary conditions are used. The results are given in Table 3.4. It is observed that the results obtained by both the methods are in excellent agreement with those presented in Refs. [109, 110].

3.5.2.2 Rotating Beam with Elastomer

The elastomer is idealised as a linear spring. Calculations are performed for three values of the dimensionless spring constant $K^* = 1000, 2000$ and 3000 . The dynamic characteristics of a rotating beam are analysed for different values of $\xi_1 (= \frac{L_1}{L})$ and $\xi_2 (= \frac{L_2}{L})$ (Fig. 3.2 b). For the in-plane vibration, the power series converges for $P = 30$, where P represents the number of terms in each series. Since the rotating beam is divided into three parts and each part is represented by a 30 term power series, there are in total 90 unknown coefficients. While using the Rayleigh-Ritz technique, the

natural frequencies converged when sixteen comparison functions ($i = 1$ to 16 in Eq. 3.68) were used. The first two natural frequencies of the rotating beam, evaluated by both techniques, for different values of the parameters (K^* , ξ_2) are included in Table 3.5. In most cases, the natural frequencies obtained by the two methods are in excellent agreement with each other. However, there is a difference of about 2.4% in the first natural frequency for $\xi_2 = 0.3$. The difference is less (about 0.17%) for the second natural frequency. The results indicate that the point of attachment of the torque tube (i.e. ξ_2) rather than the stiffness (K^*) of the spring, predominantly governs the natural frequencies.

The mode shapes corresponding to the first two natural frequencies are shown in Figs. 3.14 and 3.15, for the values $\xi_1 = 0.10$, $\xi_2 = 0.25$ and $K^* = 2000$. The mode shapes of the rotating beam without the spring are also included in these figures. It is observed that the influence of the spring stiffness (with $K^* = 2000$) is not much pronounced.

As in the case of the out of plane vibration, a detailed analysis is carried out to study the influence of different geometric configurations of the torque-tube on the natural frequencies. The value of the spring stiffness was chosen as $K^* = 2000$. The natural frequencies are evaluated by the power series method. The variation of the first and second natural frequencies are shown in Figs. 3.16 and 3.17. From Fig. 3.16, it can be seen that for all values of ξ_1 , the first natural frequency initially increases and then decreases with increasing ξ_2 . The maximum value of the frequency occurs around $\xi_2 = 0.40$. The second natural frequency also exhibits a similar trend (Fig. 3.17) with the exception that the maximum value takes place around $\xi_2 = 0.70$.

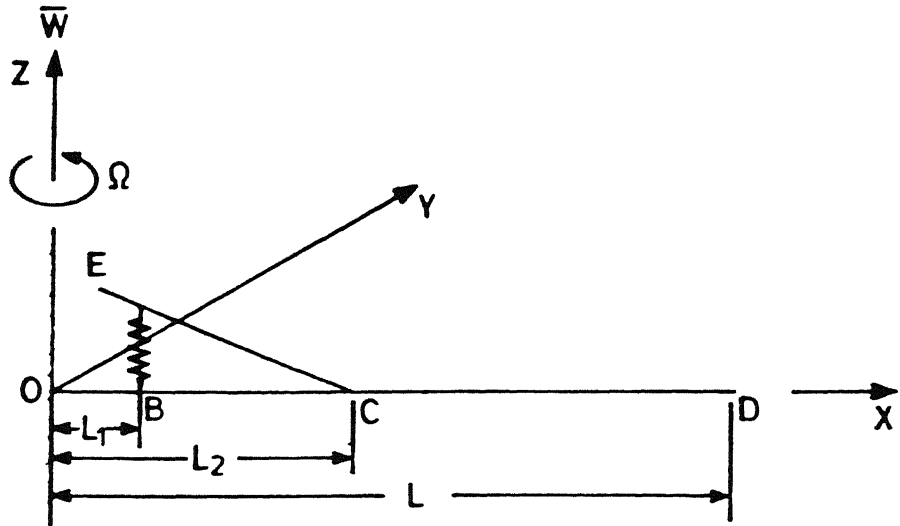
3.5.2.3 Non-Linear Analysis

The procedure of evaluating the frequency-amplitude relation of the flap vibration is mentioned in Sec. 3.5.1.3. Following the same procedure, the variation of the first two lag frequencies with amplitude of oscillation are obtained and are shown in Figs. 3.18 and 3.19. These results indicate that the frequency-amplitude behaviour in lag mode is similar to that obtained for flap mode.

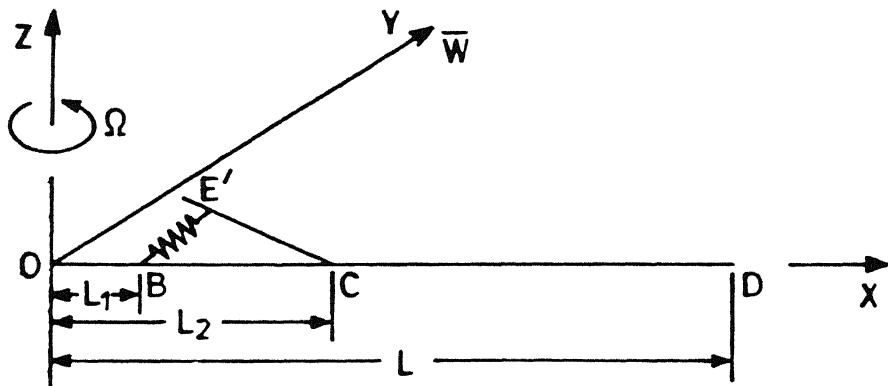
3.6 Summary

Both linear and non-linear free vibrations of a rotating blade under isolated flap and lag bending have been studied. For the linear problem, two different solution techniques, one based on the power series expansion and the other based on Rayleigh-Ritz principle, were used. Natural frequencies obtained from these two methods are found to be in excellent agreement for both types of beam motion.

In the non-linear analysis, a numerical-perturbation technique is applied to determine the frequency-amplitude relationship for isolated flap and lag motions of the rotating beam. It is concluded that up to a fairly high-value of amplitude, a seventh order expansion is sufficient to correctly predict the frequency- amplitude relationship for both cases. If the amplitude level is lower, one can use an expansion up to fifth order and still get accurate results while saving on the computational effort. The alternating signs in the polynomial expressing the restoring force prevents the non-linear characteristic to be monotonically softening or hardening.



(a) In flap mode



(b) In lag mode

Fig. 3.1 Idealised bearingless rotor blade.

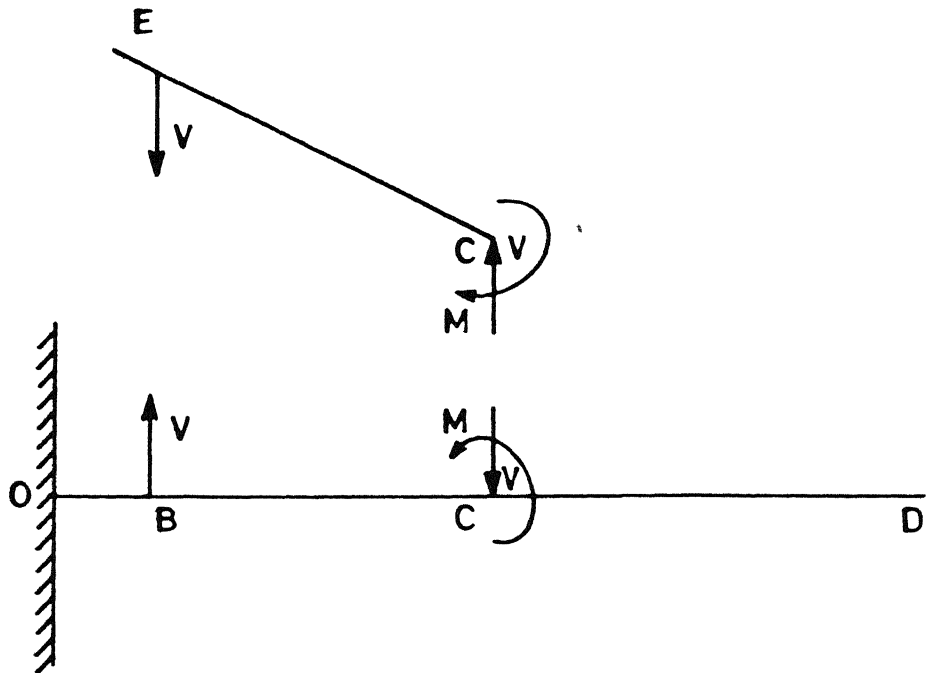
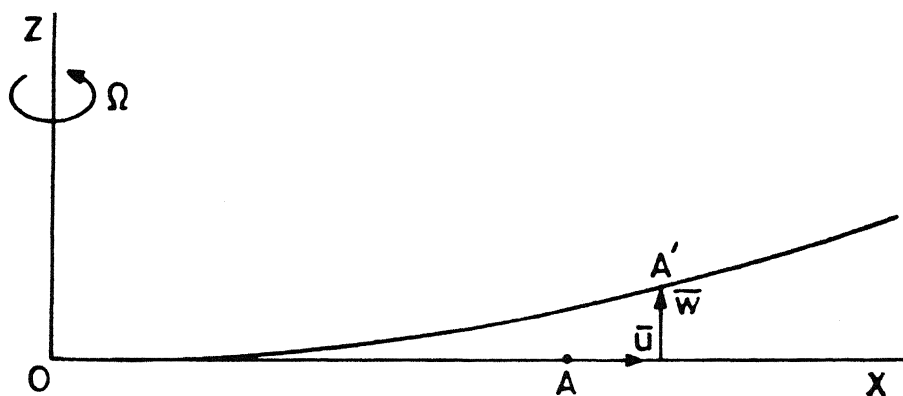
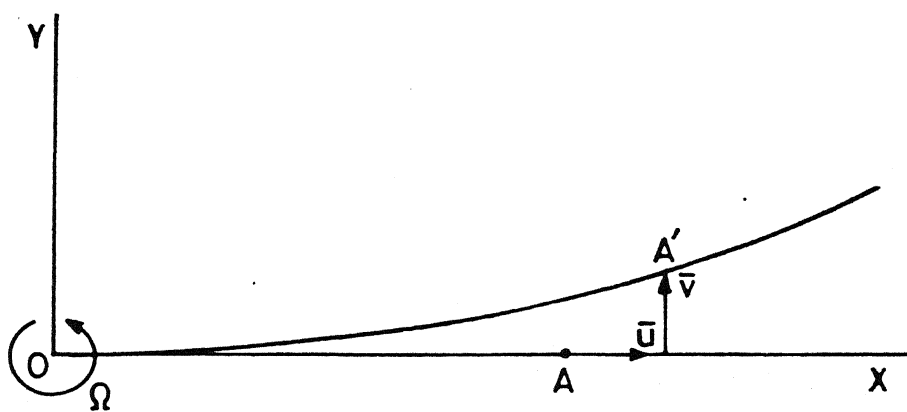


Fig. 3.2 Free-body diagrams of the bearingless rotor blade and torque tube.



(a) Flap



(b) Lag

Fig. 3.3 Elastic deformation of the blade.

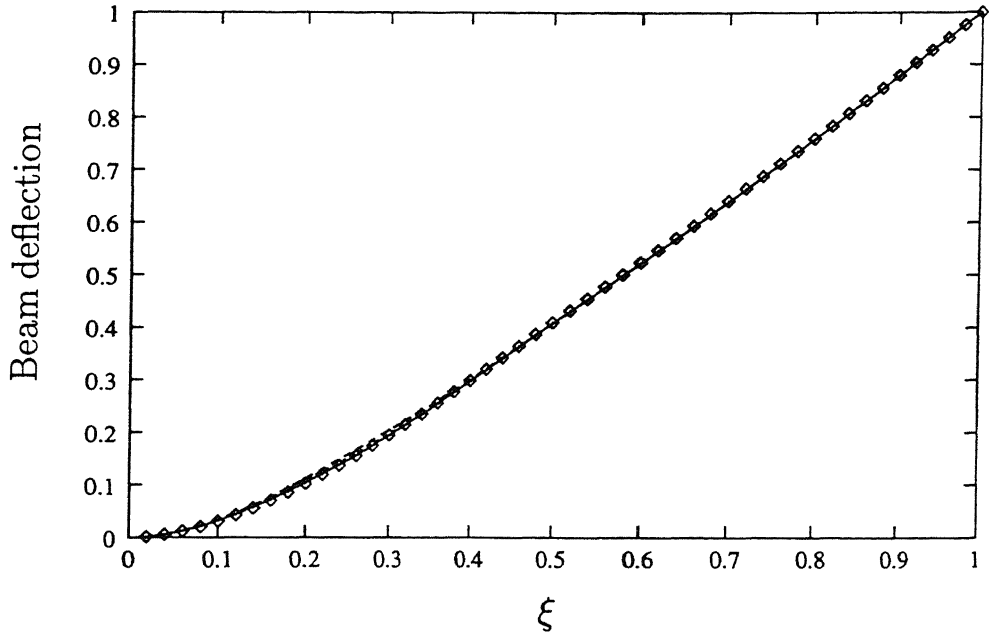


Fig. 3.4 First mode shape of the rotating beam in flap mode for various values of ξ_2 .

◇, no spring. — $\xi_2=0.20$; $\xi_2=0.25$; - - - $\xi_2=0.30$;

$\xi_1=0.10$, $K^*=2000$.

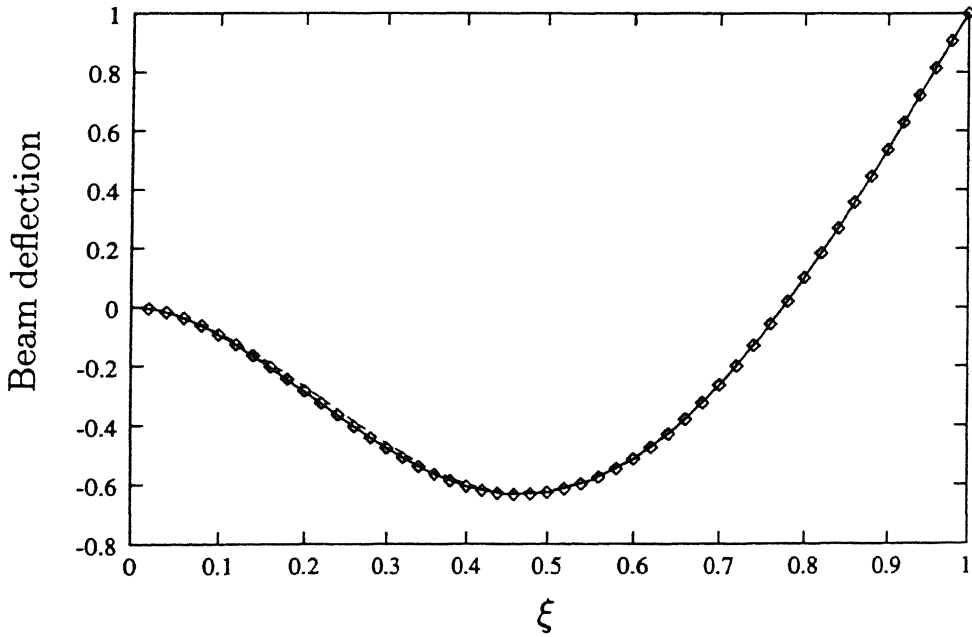


Fig. 3.5 Second mode shape of the rotating beam in flap mode for various values of ξ_2 .

◇, no spring. — $\xi_2=0.20$; $\xi_2=0.25$; - - - $\xi_2=0.30$;

$\xi_1=0.10$, $K^*=2000$.

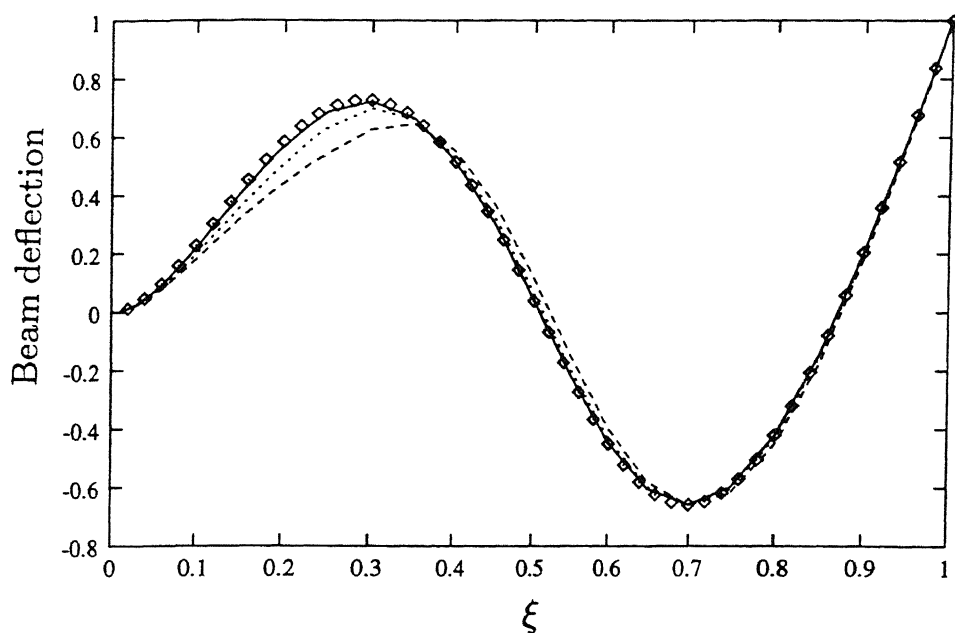


Fig. 3.6 Third mode shape of the rotating beam in flap mode for various values of ξ_2 .

\diamond , no spring. — $\xi_2=0.20$; $\xi_2=0.25$; ---- $\xi_2=0.30$;
 $\xi_1=0.10$, $K^*=2000$.

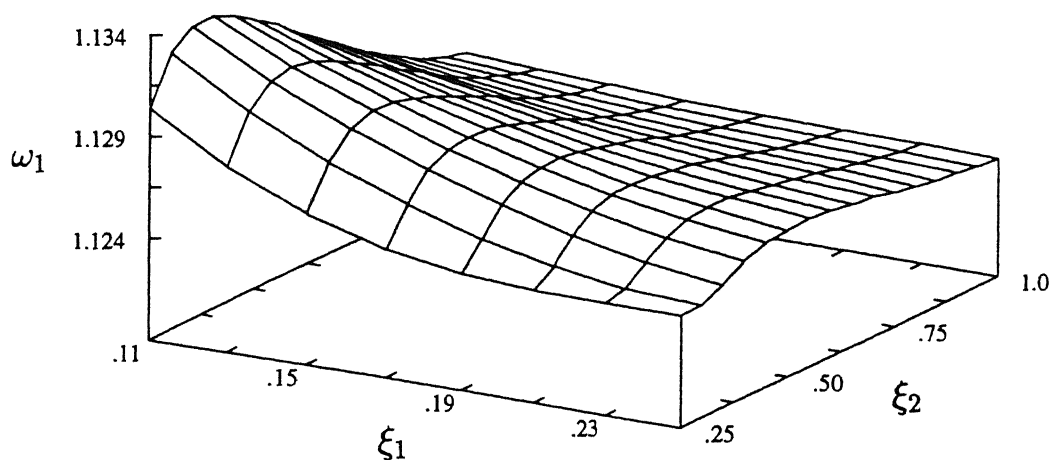


Fig. 3.7 Influence of different geometric configurations (ξ_1 and ξ_2) on the first natural frequency in flap mode. $K^*=2000$.

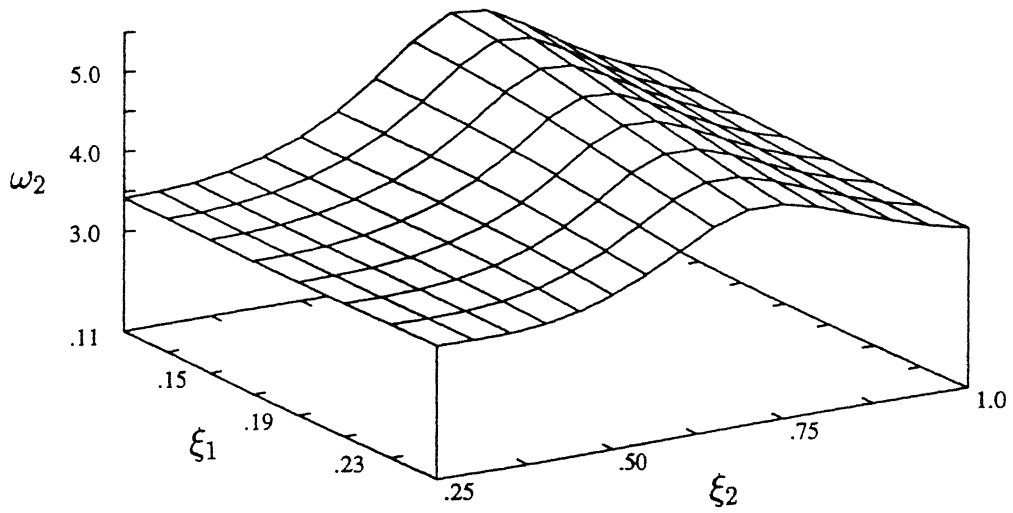


Fig. 3.8 Influence of different geometric configurations (ξ_1 and ξ_2) on the second natural frequency in flap mode. $K^*=2000$.

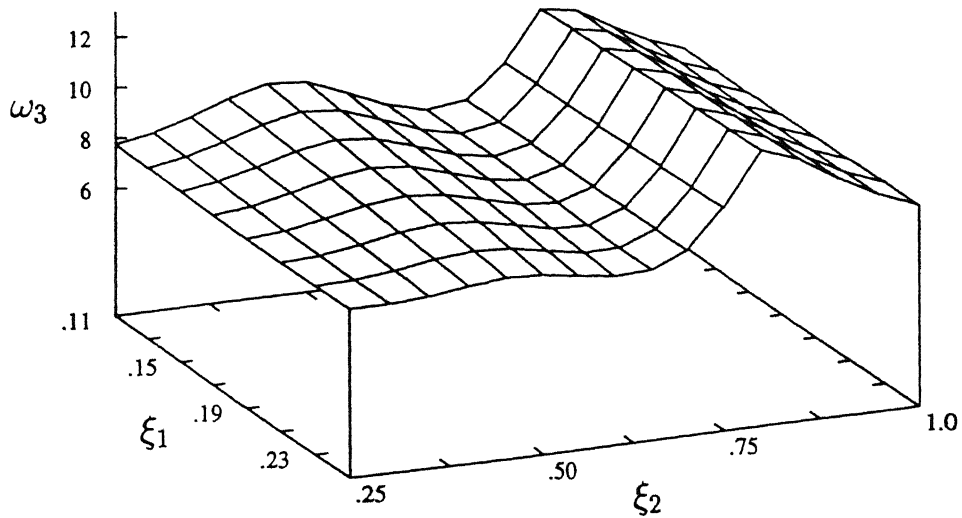


Fig. 3.9 Influence of different geometric configurations (ξ_1 and ξ_2) on the third natural frequency in flap mode. $K^*=2000$.

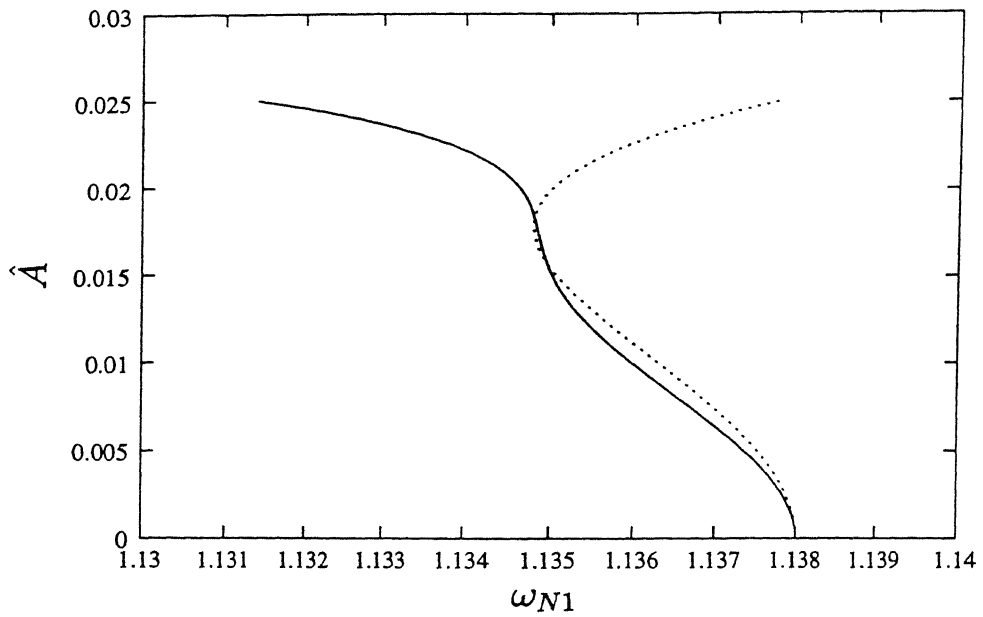


Fig. 3.10 Variation of the first non-linear frequency with amplitude of oscillation in flap mode.

..... fifth order approximation; — seventh order approximation.

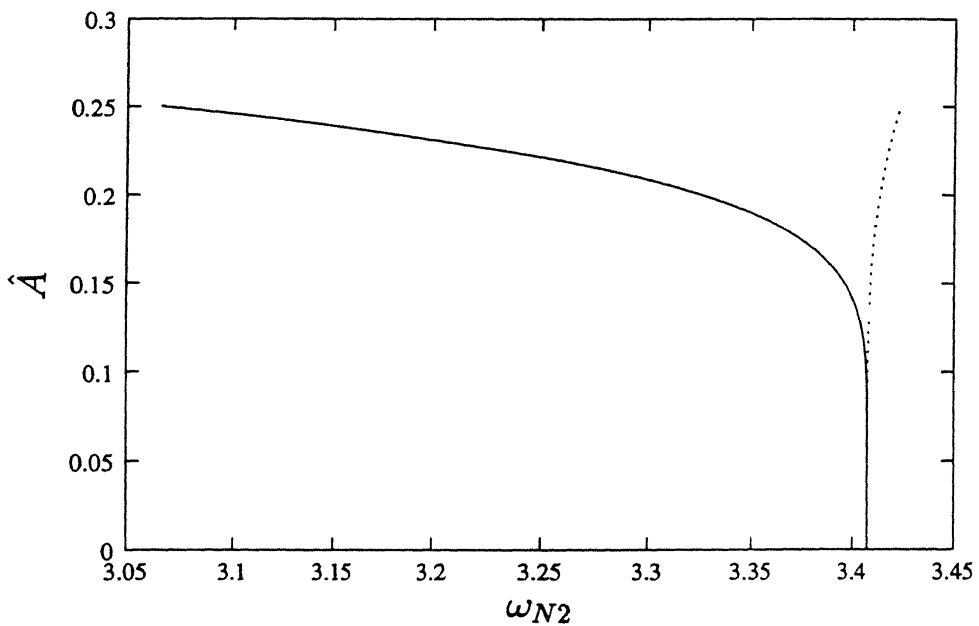


Fig. 3.11 Variation of the second non-linear frequency with amplitude of oscillation in flap mode.

..... fifth order approximation; — seventh order approximation.

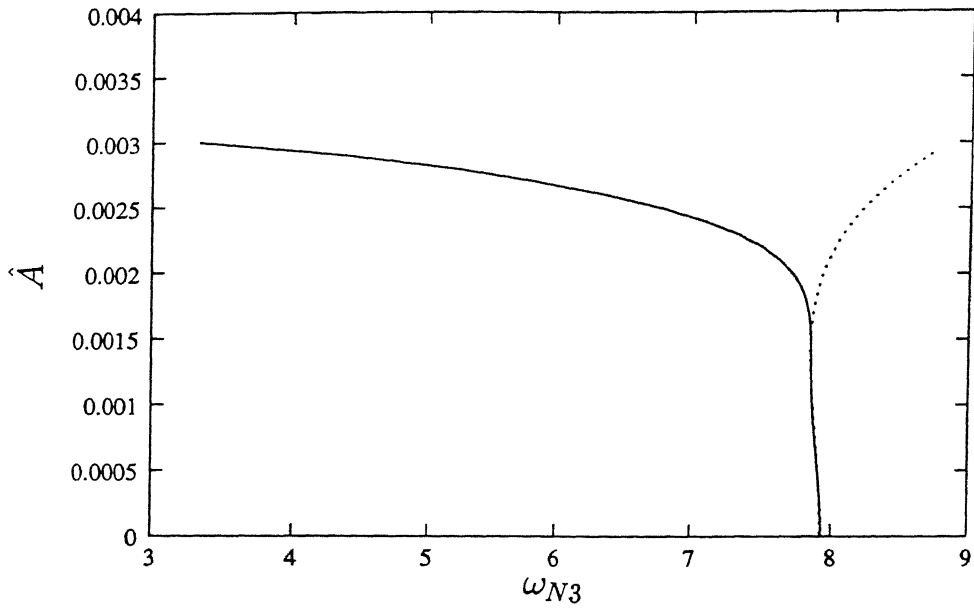


Fig. 3.12 Variation of the third non-linear frequency with amplitude of oscillation in flap mode.

..... fifth order approximation; — seventh order approximation.

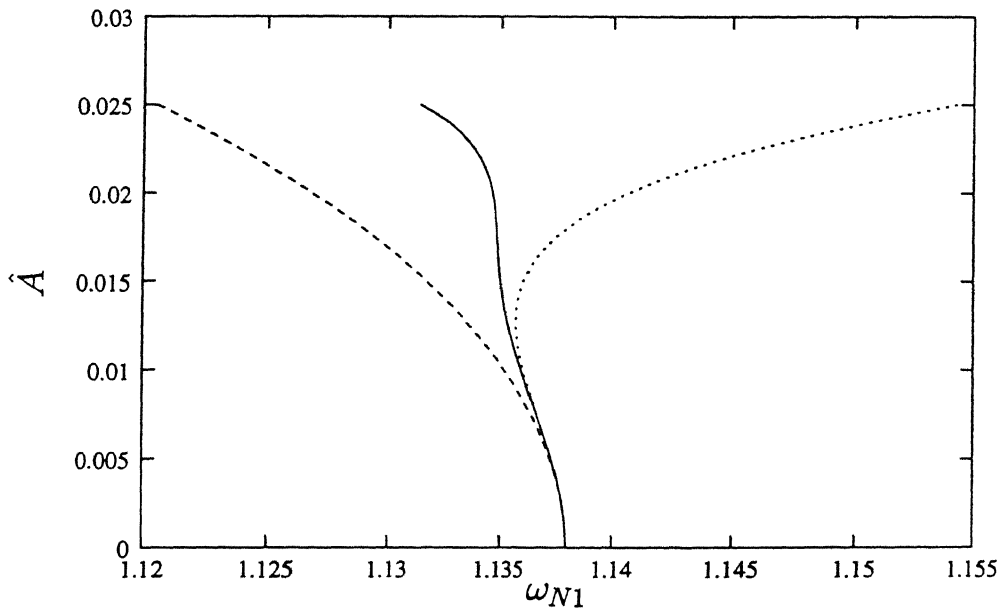


Fig. 3.13 Influence of different orders of approximation on the first non-linear natural frequency in flap mode.

---- third order approximation; fifth order approximation; — seventh order approximation.

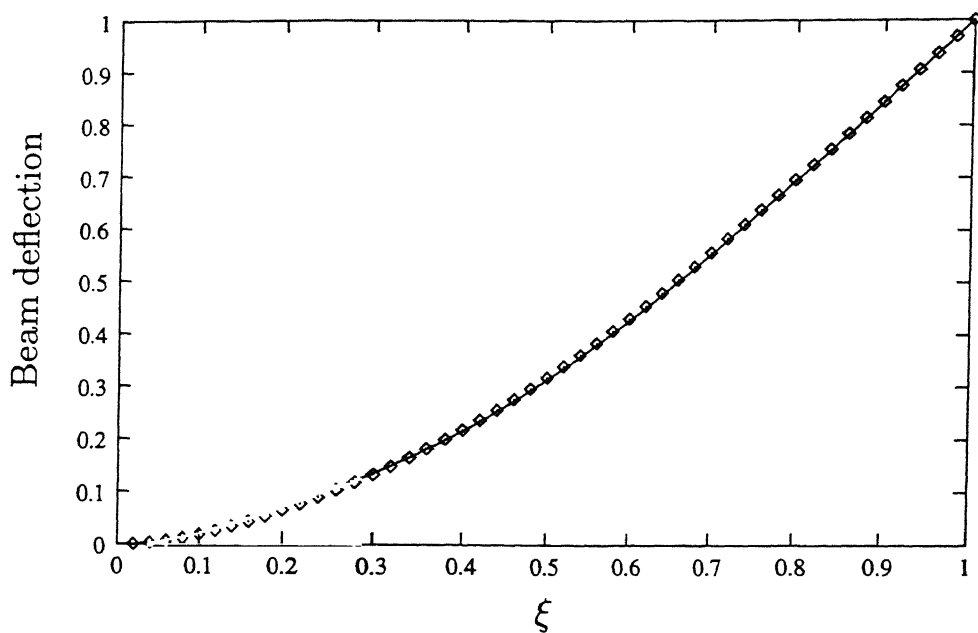


Fig. 3.14 First mode shape of the rotating beam in lag mode.

◇ without spring. — with spring.

$\xi_1 = 0.10$, $\xi_2 = 0.25$ and $K^* = 2000$.

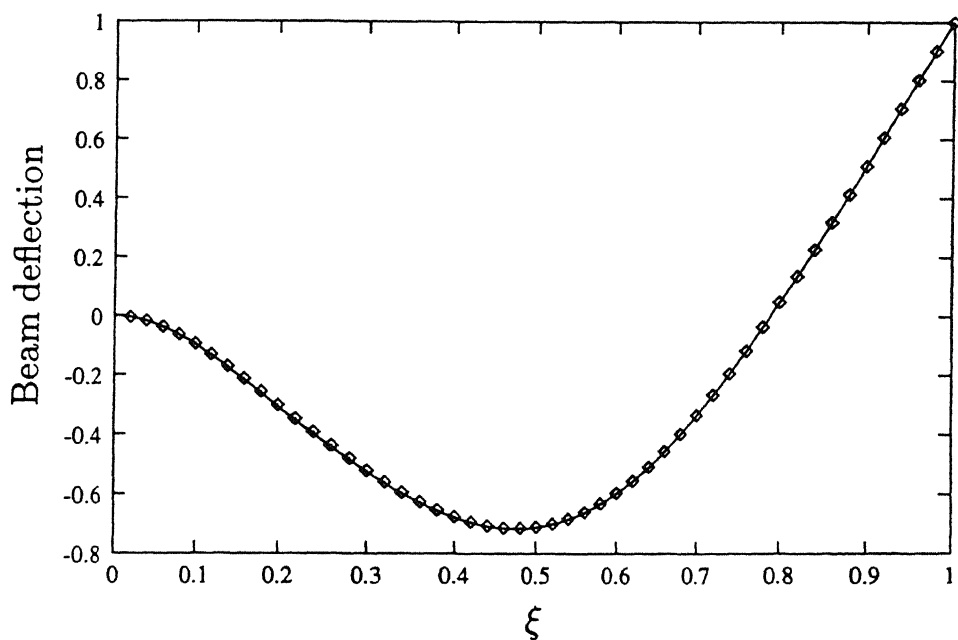


Fig. 3.15 Secone mode shape of the rotating beam in lag mode.

◇ without spring. — with spring.

$\xi_1 = 0.10$, $\xi_2 = 0.25$ and $K^* = 2000$.

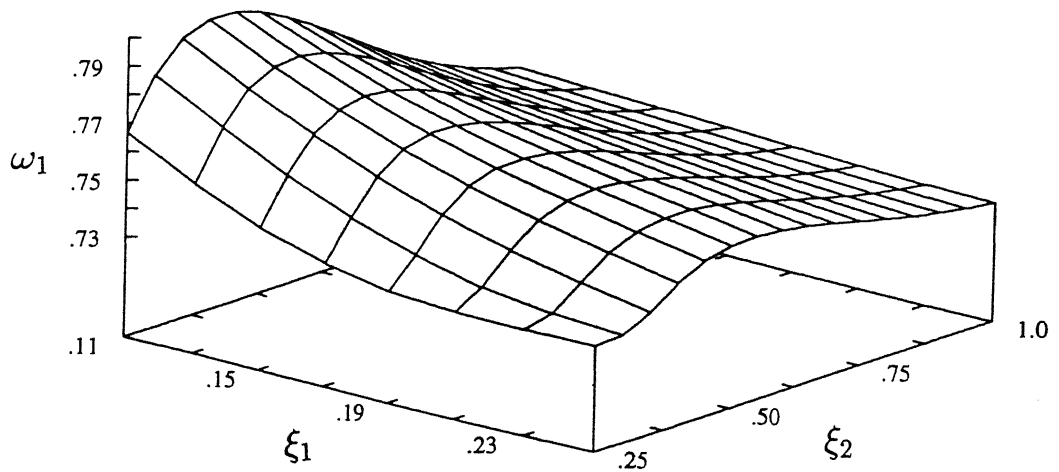


Fig. 3.16 Influence of different geometric configurations (ξ_1 and ξ_2) on the first natural frequency in lag mode. $K^*=2000$.

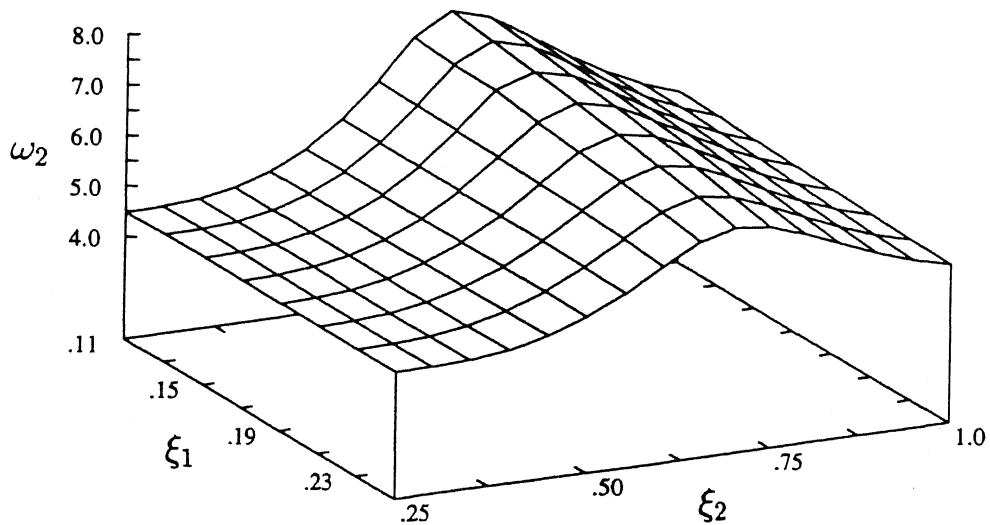


Fig. 3.17 Influence of different geometric configurations (ξ_1 and ξ_2) on the second natural frequency in lag mode. $K^*=2000$.

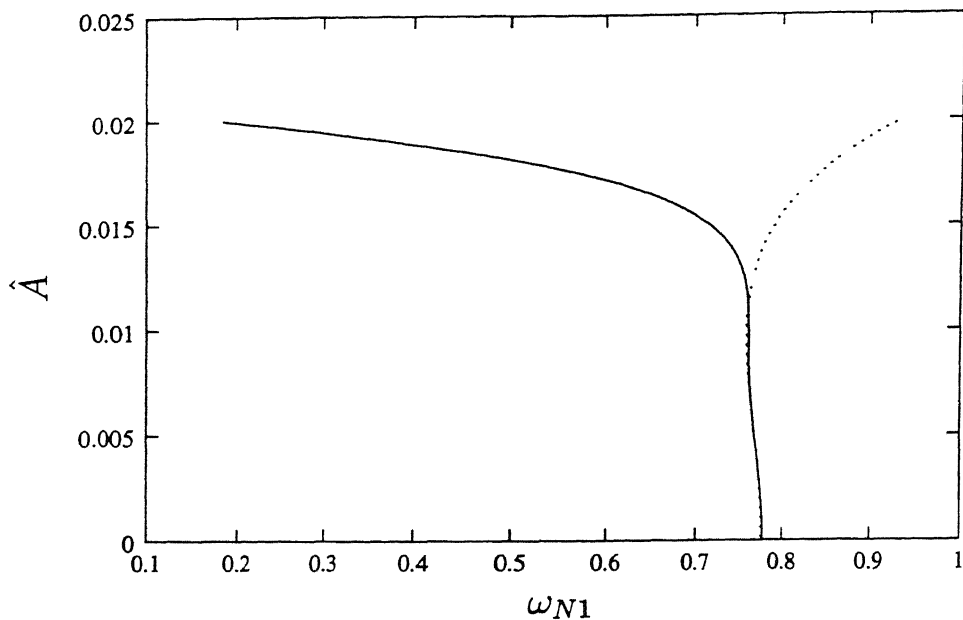


Fig. 3.18 Variation of the first non-linear frequency with amplitude of oscillation in lag mode. fifth order approximation; — seventh order approximation.

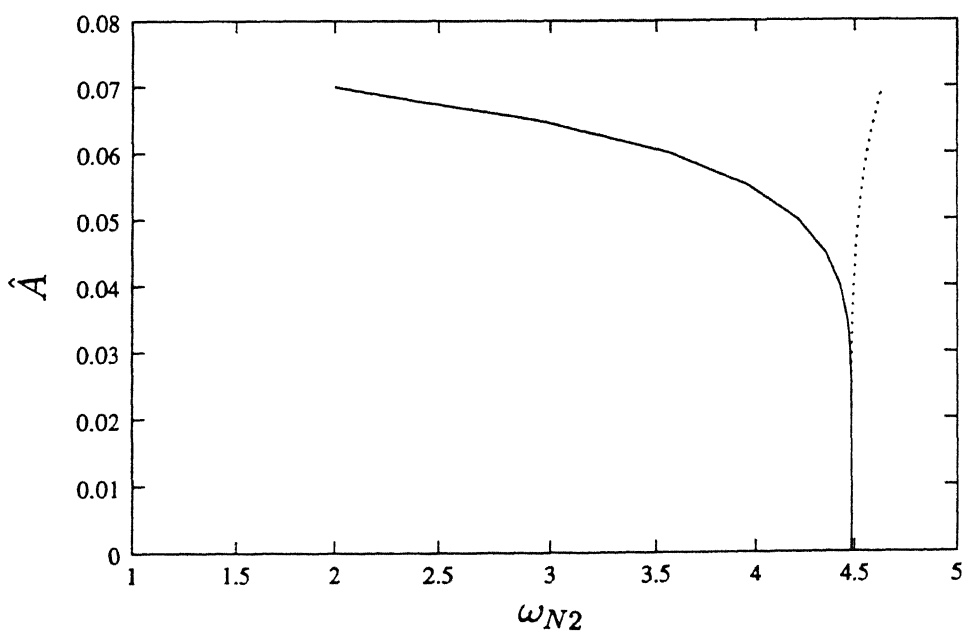


Fig. 3.19 Variation of the second non-linear frequency with amplitude of oscillation in lag mode. fifth order approximation; — seventh order approximation.

Table 3.1 Blade data.

m	L	$\frac{EI}{m\Omega^2 L^4}$ (Flap)	$\frac{EI}{m\Omega^2 L^4}$ (Lag)	r	Ω
9.7 Kg/m	6.6 m	0.0106	0.0301	$.5 \text{ m}$	32.8 rad/sec.

Table 3.2 Natural frequencies of the rotating blade in flap mode without elastomer.

Mode	Power Series	Rayleigh-Ritz	Ref. [109]	Ref. [110]
1st	1.1245	1.1244	1.125	1.1247
2nd	3.4073	3.4073	-	3.4089
3rd	7.6218	7.6216	-	7.6376

Table 3.3. Natural frequencies of the rotating blade in flap mode with a linear elastomer.

		$\xi_1 = 0.1, \xi_2 = 0.15$		$\xi_1 = 0.1, \xi_2 = 0.2$		$\xi_1 = 0.1, \xi_2 = 0.25$		$\xi_1 = 0.1, \xi_2 = 0.3$	
Mode	K^*	Power Series	Rayleigh-Ritz	Power Series	Rayleigh-Ritz	Power Series	Rayleigh-Ritz	Power Series	Rayleigh-Ritz
1st	1000	1.125	1.125	1.127	1.127	1.130	1.131	1.133	1.134
2nd		3.407	3.407	3.409	3.409	3.407	3.407	3.413	3.416
3rd		7.617	7.622	7.628	7.635	7.716	7.763	7.960	8.152
1st	2000	1.125	1.125	1.128	1.129	1.132	1.134	1.134	1.137
2nd		3.408	3.408	3.409	3.409	3.407	3.407	3.414	3.420
3rd		7.617	7.635	7.634	7.645	7.754	7.847	8.039	8.349
1st	3000	1.125	1.125	1.130	1.131	1.133	1.136	1.135	1.138
2nd		3.409	3.408	3.410	3.411	3.407	3.407	3.415	3.422
3rd		7.618	7.622	7.639	7.656	7.774	7.903	8.075	8.449
1st	4000	1.125	1.125	1.130	1.133	1.134	1.138	1.136	1.139
2nd		3.409	3.408	3.410	3.412	3.407	3.408	3.415	3.424
3rd		7.618	7.622	7.642	7.664	7.786	7.937	8.095	8.509

Table 3.4 Natural frequencies of the rotating blade in lag mode without elastomer.

Mode	Power Series	Rayleigh-Ritz	Ref. [109]	Ref. [110]
1st	0.7317	0.7317	0.732	0.7326
2nd	4.4825	4.4825	-	4.4563

Table 3.5. Natural frequencies of the rotating blade in lag mode with a linear elastomer.

		$\xi_1 = 0.1, \xi_2 = 0.15$		$\xi_1 = 0.1, \xi_2 = 0.2$		$\xi_1 = 0.1, \xi_2 = 0.25$		$\xi_1 = 0.1, \xi_2 = 0.3$	
Mode	K^*	Power Series	Rayleigh-Ritz	Power Series	Rayleigh-Ritz	Power Series	Rayleigh-Ritz	Power Series	Rayleigh-Ritz
1st	1000	0.733	0.733	0.744	0.745	0.763	0.768	0.781	0.792
2nd		4.484	4.484	4.487	4.488	4.484	4.484	4.489	4.493
1st	2000	0.734	0.734	0.751	0.755	0.774	0.786	0.791	0.808
2nd		4.485	4.485	4.490	4.492	4.484	4.485	4.490	4.497
1st	3000	0.735	0.735	0.756	0.764	0.779	0.796	0.796	0.815
2nd		4.486	4.486	4.492	4.496	4.484	4.485	4.491	4.499

Chapter 4

AMPLITUDE DEPENDENT STABILITY OF AN IDEALISED BEARINGLESS ROTOR UNDER GROUND RESONANCE

4.1 Introduction

The aeromechanical instability of a helicopter is a complex phenomenon, involving coupling between the rotor and the body degrees of freedom. The rotor lead-lag regressive mode usually couples with the body pitch and/or body roll to cause the instability. When the helicopter is on the ground, such instability is referred to as ground resonance. In the case of bearingless rotor, the ground resonance is usually avoided by providing elastomeric damper to the rotor blade and damping in the landing gear. Due to the inclusion of the elastomer, the dynamic characteristics of the bearingless rotor becomes very complicated.

Conventionally, the aeromechanical stability of a coupled rotor/fuselage system is analysed using a linearised perturbational technique. It is known that the elastomer stiffness and damping characteristics are dependent on amplitude of motion. It is also highlighted in Sec. 2.1 that any linearised technique fails to capture these amplitude-dependent characteristics of the elastomer. The formulation and solution presented in this chapter aim to understand the phenomenon of amplitude-dependent stability of the coupled rotor/fuselage dynamics under ground resonance condition. A methodology for analyzing the amplitude-dependent stability of the system under ground resonance condition is also presented.

4.2 Formulation of Equations of Motion

An idealised model of the coupled rotor/fuselage system is shown in Fig. 4.1. The blade is assumed to undergo only the lag motion. The elastomer is represented by non-linear spring and damping elements. The torque tube is assumed to be rigid and massless. The effect of pitch link in the lag mode is neglected. The hub is located at a height \bar{h} above the C.G. of the fuselage. The fuselage is allowed to undergo rigid body pitch and roll motions. The characteristics of the fuselage support (landing gear) is represented by a linear spring and a linear damper. Since emphasis is placed on the effect of non-linearity of the elastomer on the ground resonance problem, the aerodynamic effects are not considered. The dynamical equations of motion of the coupled rotor/fuselage model consist of two sets of equations: one corresponding to the blade motion and the other representing the motion of the fuselage.

4.2.1 Blade Equations

The equation of lag motion of an isolated blade is already presented in Sec. 3.2.2. Since the pitch and roll motions of the fuselage introduce additional inertia effects they must be included in the equation of lag motion of the blade. Accordingly, the kinetic energy of the k -th blade in a N -bladed rotor system can be written as

$$T(t) = \frac{1}{2} \int_0^L m \left[\left\{ \frac{\partial \bar{u}}{\partial t} - \Omega \bar{v} + \frac{d\bar{x}}{dt} \cos \psi_k + \frac{d\bar{y}}{dt} \sin \psi_k \right\}^2 + \left\{ \frac{\partial \bar{v}}{\partial t} + \Omega \bar{u} - \frac{d\bar{x}}{dt} \sin \psi_k + \frac{d\bar{y}}{dt} \cos \psi_k \right\}^2 \right] dx \quad (4.1)$$

where \bar{x} ($= \theta_y \bar{h}$) and \bar{y} ($= -\theta_x \bar{h}$) are the perturbational displacements of the hub centre due to fuselage motion in pitch and roll modes, respectively (Fig. 4.1), ψ_k is the azimuth angle of the k -th blade.

The expression for strain energy due to bending is

$$U_1 = \frac{1}{2} \int_0^L EI \left[\frac{\partial^2 \bar{v}(x, t)}{\partial x^2} \right]^2 dx \quad (4.2)$$

The strain energy of the non-linear spring due to the deformation Δ_l is

$$U_2 = \frac{1}{2} K_{eq} (\Delta_l) \Delta_l^2 \quad (4.3)$$

where K_{eq} is the equivalent stiffness which is dependent on the amplitude of motion of the blade. Hence the net strain energy of the system is

$$U = U_1 + U_2. \quad (4.4)$$

The work done by the dissipative element of the elastomer is given by

$$W_d = \frac{1}{2} C_{eq} (\Delta_l) \dot{\Delta}_l^2 \quad (4.5)$$

where C_{eq} is the equivalent (amplitude-dependent) damping coefficient. The equivalent stiffness K_{eq} and damping C_{eq} are taken as the dynamic stiffness (G') and damping

(G''') for a given amplitude of the elastomer. Accordingly, from Eqs. 2.8 and 2.9, one can write

$$\begin{aligned} G' &= K_{eq} = K_1 - \frac{3}{4}K_3X^2 + \frac{5}{8}K_5X^4 - \frac{1}{2}K_7X^6 \\ G''' &= C_{eq} = \frac{h}{\omega} + \frac{4F}{\pi\omega X} \end{aligned}$$

where X is the amplitude of motion of the elastomer.

The non-dimensional lag deformation of the blade is assumed to be of the form:

$$v(\xi, \tau) = \sum_{i=1}^{n1} \bar{\phi}_i(\xi) z_{ik}(\tau) \quad (4.6)$$

where $\bar{\phi}_i$ is the i th rotating mode shape of the k th blade. $n1$ is the number of rotating modes.

Since the equivalent stiffness of the elastomer is a function of the amplitude of motion, the rotating mode shape and frequencies will also be functions of amplitude of motion.

The expression for $\bar{\phi}_i$ can be written as a sum of n assumed modes

$$\bar{\phi}_i = \hat{\phi}_1 p_{1i} + \hat{\phi}_2 p_{2i} + \dots + \hat{\phi}_n p_{ni}$$

where $\hat{\phi}_i$ are the comparison function and p_{ji} is the i -th modal vector ($j = 1, 2, 3 \dots n$) of the eigenvalue problem

$$[K] \{q\} = \lambda [M] \{q\} \quad (4.7)$$

with the elements of $[K]$ and $[M]$ given by

$$\begin{aligned} K_{ir} &= \int_0^1 \frac{EI}{m\Omega^2 L^4} \hat{\phi}_i'' \hat{\phi}_r'' d\xi + \int_0^1 \frac{1}{2} (1 - \xi^2) \hat{\phi}_i' \hat{\phi}_r' d\xi + K_{eq} \hat{\psi}_i^l \hat{\psi}_r^l, \quad (4.8) \\ \text{and } M_{ir} &= \int_0^1 \hat{\phi}_i \hat{\phi}_r d\xi. \end{aligned}$$

The expression for $\hat{\psi}_i^l$ can be obtained following the procedure described in Sec. 3.3.2.2.

It is to be noted that since K_{eq} depends on the amplitude, the eigenvalues and the eigenvectors are also dependent on the amplitude of motion of the elastomer.

Substituting Eqs. 4.1, 4.4 and 4.5 in Hamilton's principle and neglecting higher order terms, the non-dimensional equation of motion of the i th lag mode of the k th blade can be written as

$$\ddot{z}_{ik}(\tau) + \omega_i^2 z_{ik}(\tau) + \sum_{i=1}^{n1} \sum_{r=1}^{n1} C^* \hat{\psi}_i^l \hat{\psi}_r^l \dot{z}_{ik} - \left[\int_0^1 \bar{\phi}_i d\xi \right] (\xi_h \ddot{\theta}_y \sin \psi_k + \xi_h \ddot{\theta}_x \cos \psi_k) = 0 \quad (4.9)$$

where $C^* = \frac{C_{eq}}{m\Omega L}$, $i = 1, 2, \dots, n1$ and $k = 1, 2, \dots, N$.

Considering only the first lag mode ($i = 1$), the equation of motion of the m -th blade reduces to

$$\ddot{z}_{1k}(\tau) + \omega_1^2 z_{1k}(\tau) + C^* (\hat{\psi}_1^l)^2 \dot{z}_{1k} - \left[\int_0^1 \bar{\phi}_1 d\xi \right] (\xi_h \ddot{\theta}_y \sin \psi_k + \xi_h \ddot{\theta}_x \cos \psi_k) = 0 \quad (4.10)$$

where $k = 1, 2, \dots, N$.

Applying the multi-blade-coordinate transformation, the above set of equations are converted into equations in rotor degrees of freedom. The collective and alternating modes are neglected as these do not participate in the ground resonance problem. The cyclic lag equations for the elastic lag mode can be written as

$$\ddot{z}_{1c} + \bar{C} \dot{z}_{1c} + 2\dot{z}_{1s} + (\omega_1^2 - 1) z_{1c} + \bar{C} z_{1s} - p \ddot{\theta}_x = 0 \quad (4.11)$$

$$\text{and } \ddot{z}_{1s} + \bar{C} \dot{z}_{1s} - 2\dot{z}_{1c} + (\omega_1^2 - 1) z_{1s} - \bar{C} z_{1c} - p \ddot{\theta}_y = 0 \quad (4.12)$$

$$\text{where } p = \xi_h \int_0^1 \bar{\phi}_1 d\xi \quad \text{and} \quad \bar{C} = C^* (\hat{\psi}_1^l)^2. \quad (4.13)$$

4.2.1.1 Fuselage Equations

The in-plane (S_v) and the radial (S_r) forces at the root of the k th blade are given by

$$S_v = \int_0^L (-m\ddot{v} + m\Omega^2 \bar{v}) dx - (\ddot{x} \sin \psi_k - \ddot{y} \cos \psi_k) \int_0^L m dx \quad (4.14)$$

$$\text{and } S_r = \int_0^L m\Omega^2 x dx - \int_0^L 2\Omega \dot{v} m dx - (\ddot{x} \cos \psi_k + \ddot{y} \sin \psi_k) \int_0^L m dx. \quad (4.15)$$

The forces acting on the hub can be obtained by resolving the blade-root shear forces in the non-rotating frame and summing over all the N -blades. Considering the support structure as a combination of mass-spring-damper system having pitch and roll motions, the equations of motion of the support in, non-dimensional form, are written as

$$I_y \ddot{\theta}_y + C_y \dot{\theta}_y + K_y \theta_y - \frac{N}{2} p \ddot{z}_{1s} = 0 \quad (4.16)$$

$$\text{and } I_x \ddot{\theta}_x + C_x \dot{\theta}_x + K_x \theta_x - \frac{N}{2} p \ddot{z}_{1c} = 0 \quad (4.17)$$

Equations 4.11, 4.12, 4.16 and 4.17 are arranged in the form

$$[\bar{M}] \{\ddot{X}\} + [\bar{C}] \{\dot{X}\} + [\bar{K}] \{X\} = 0 \quad (4.18)$$

where \bar{M} , \bar{C} and \bar{K} are the mass, the damping and the stiffness matrices, respectively. The vector $\{X\}$ represents the degrees of freedom, *i.e.*,

$$\{X\} = \{z_{1c} \ z_{1s} \ \theta_y \ \theta_x\}^T. \quad (4.19)$$

The ground resonance stability is determined by the eigenvalues of the 8×8 matrix $[G]$ where

$$[G] = \begin{bmatrix} 0 & I \\ -\bar{M}^{-1} \bar{K} & -\bar{M}^{-1} \bar{C} \end{bmatrix}. \quad (4.20)$$

4.3 Solution Procedure

The step-by-step technique for solving the amplitude-dependent stability of the coupled rotor-fuselage system is described below:

- (i) For a given amplitude of motion of the elastomer, equivalent stiffness (K_{eq}) and damping (C_{eq}) are evaluated.

(ii) Using K_{eq} , the natural frequency (ω_i) and the corresponding mode shape ($\bar{\phi}_i$) of the rotating blade in the lag mode are determined by solving the eigenvalue problem given by Eq. 4.7.

(iii) Since only the first lag mode is considered in the ground resonance problem, using the mode shape $\bar{\phi}_1$, the quantities \bar{C} and p given by Eqs. 4.13 are evaluated.

(iv) Knowing \bar{M} , \bar{C} and \bar{K} (Eq. 4.18), an eigen analysis of matrix \mathbf{G} is performed to determine the stability of the system under ground resonance condition. The eigenvalues appear as complex conjugate pairs $s_j = \sigma_j \pm i\omega_j$ where ω_j represents the frequency of the mode and σ_j represents the modal damping. The mode is stable if σ_j is negative and unstable when σ_j is positive.

Since the lag mode shape is dependent on the operating conditions and the blade and elastomer parameters, for any change in these parameters the above steps have to be repeated.

4.4 Results and Discussion

A thorough investigation is carried out to study the influence of the elastomer on the ground resonance stability of a bearingless rotor. The elastomer is idealised as a combination of a non-linear spring, a Coulomb damper and a hysteretic damper. The parameters of the non-linear elastomer are given in Table 2.1. The data used in the analysis are given in Table 4.1. The values of the stiffness parameters of the support are chosen to provide frequencies in pitch and roll modes as 2 Hz and 4 Hz, respectively.

4.4.1 Baseline Configuration

For the baseline configuration, the locations of the elastomer and torque tube are set at $\xi_1 = 0.1$, and $\xi_2 = 0.25$. The damping in pitch and roll modes of the fuselage is

assumed to be zero ($C_x = C_y = 0$). The amplitude of motion of the elastomer is taken as 0.001 m. Following the steps mentioned in Sec. 4.3, the eigenvalues of the matrix \mathbf{G} are calculated. Figures 4.2 and 4.3 show the variation of the modal frequencies (ω_j) and damping (σ_j), respectively, as a function of the rotational speed Ω . Figure 4.2 indicates that the coalescence of the regressive lag mode (z_r) with fuselage modes in pitch (θ_y) and roll (θ_x) occurs at three regions of rotational speed (namely 95-100 r.p.m, 350-400 r.p.m and 440-600 r.p.m). In the range 350-400 r.p.m, θ_y is unstable having maximum instability with $\sigma_j = 0.23 \text{ s}^{-1}$; while in the r.p.m range 440-600, θ_x is unstable with a maximum positive value of $\sigma_j = 1.67 \text{ s}^{-1}$. The coalescence of z_r with θ_y occurring at a very low r.p.m range 85-95 does not produce any instabilities in the system. The progressive lag mode (z_p) is always stable with a slight variation in damping the levels.

4.4.1.1 Effect of Amplitude

The ground resonance problem is solved for different three values of the amplitude of motion (0.0005 m, 0.001 m and 0.002 m) of the elastomer. The parameters are taken as $C_x = C_y = 0$, $\xi_1 = 0.1$ and $\xi_2 = 0.25$. The results, shown in Fig. 4.4, indicate that for this configuration, the damping in progressive lag mode decreases with the increase in amplitude. In other modes, the amplitude of motion of the elastomer has very little influence.

4.4.2 Influence of Elastomer Location (ξ_1, ξ_2)

A parametric study is undertaken to analyse the influence of ξ_1 and ξ_2 on the modal damping. The amplitude of motion of the elastomer is fixed at 0.001 m.

The analysis is carried out by varying the value of ξ_1 keeping ξ_2 fixed at 0.25. Figure 4.5 shows the results for four different values of ξ_1 (0.1, 0.07, 0.04 and 0.02). As ξ_1

maximum value of damping coefficient \bar{C} . These results indicate that by a judicious selection of the locations of the elastomer and torque tube, the stability of the system can be enhanced.

4.4.2.1 Effect Linear Support Damper

The analysis is carried out for the baseline configuration ($\xi_1 = 0.1$, $\xi_2 = 0.25$). The damping ratios in the pitch and roll modes are assumed to be $\zeta_{\theta_y} = .0529$ and $\zeta_{\theta_x} = .082$. The elastomer amplitude is taken as 0.001 m. Figure 4.10 shows that for the baseline configuration, the level of instability in the roll mode (θ_x) is $\sigma = 1.67 \text{ s}^{-1}$ in the speed range of 440-600 r.p.m. With the inclusion of support damper, the maximum level of instability in roll mode is brought down to 0.87 s^{-1} . But the region of instability spreads over a wider range of operating speeds (470-660 r.p.m). To highlight the importance of elastomer location on stability, the results corresponding to another configuration ($\xi_1 = 0.04$, $\xi_2 = 0.25$) are also shown in Fig. 4.10. With support damping, this configuration has a maximum level of instability of 0.53 s^{-1} in roll mode which is lower than that of the baseline configuration. The region of instability is also reduced to 515-580 r.p.m.

Keeping the other parameters same, when the support damping in the roll mode is further increased to $\zeta_{\theta_x} = 0.20$, the configuration ($\xi_1 = 0.04$, $\xi_2 = 0.25$) becomes stable for the entire range of rotational speeds, whereas the configuration ($\xi_1 = 0.1$, $\xi_2 = 0.25$) is not stable as shown in Fig. 4.11.

Inclusion of the support damper in addition to the elastomeric lag damper reduces the level of the instability considerably. In addition, for a given value of fuselage damping, a proper choice of elastomer location can improve the stability of the system over the entire r.p.m range.

4.5 Summary

An amplitude dependent stability analysis has been carried out for a coupled rotor/fuselage system under ground resonance condition. It is observed that the elastomer amplitude does not alter the stability of the system in the region of maximum instabilities. However, it exhibits appreciable influence on the progressive lag mode damping. The results also indicate that for a given location of the elastomer, there is an optimum location for the torque tube attachment from the point of view of ground resonance instability..

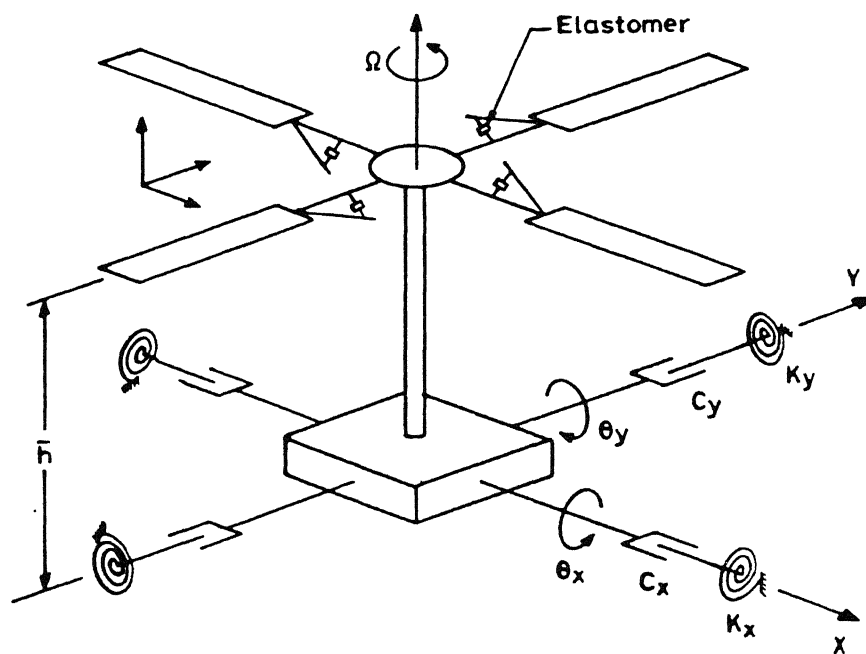


Fig. 4.1 Idealised model of the coupled rotor/fuselage system.

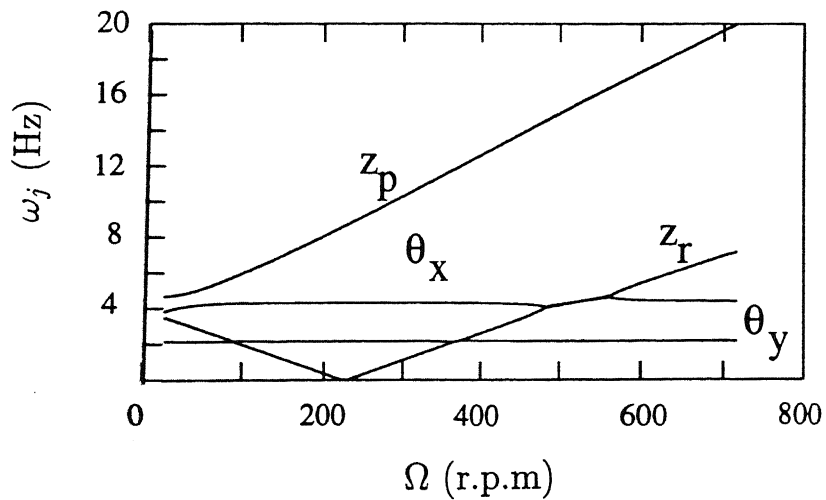


Fig. 4.2 Variation of modal frequencies as a function of rotational speed.

$$\xi_1 = 0.1, \xi_2 = 0.25.$$

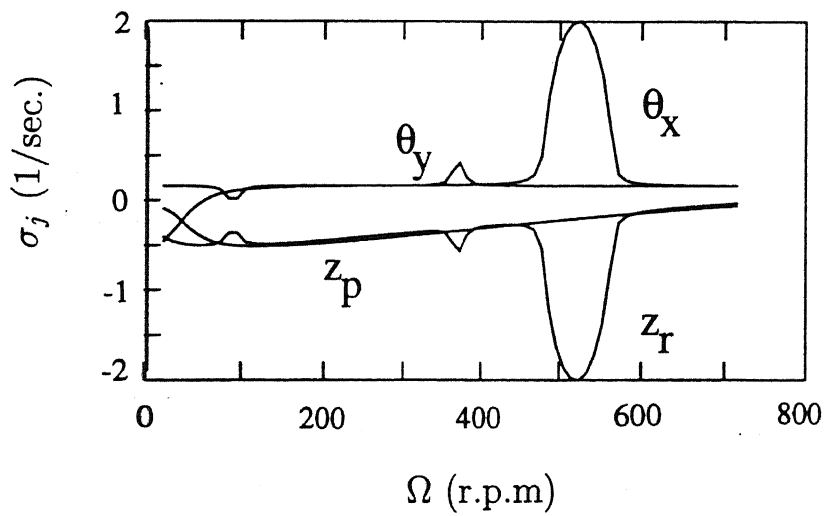


Fig. 4.3 Variation of modal damping as a function of rotational speed.

$$\xi_1 = 0.1, \xi_2 = 0.25.$$

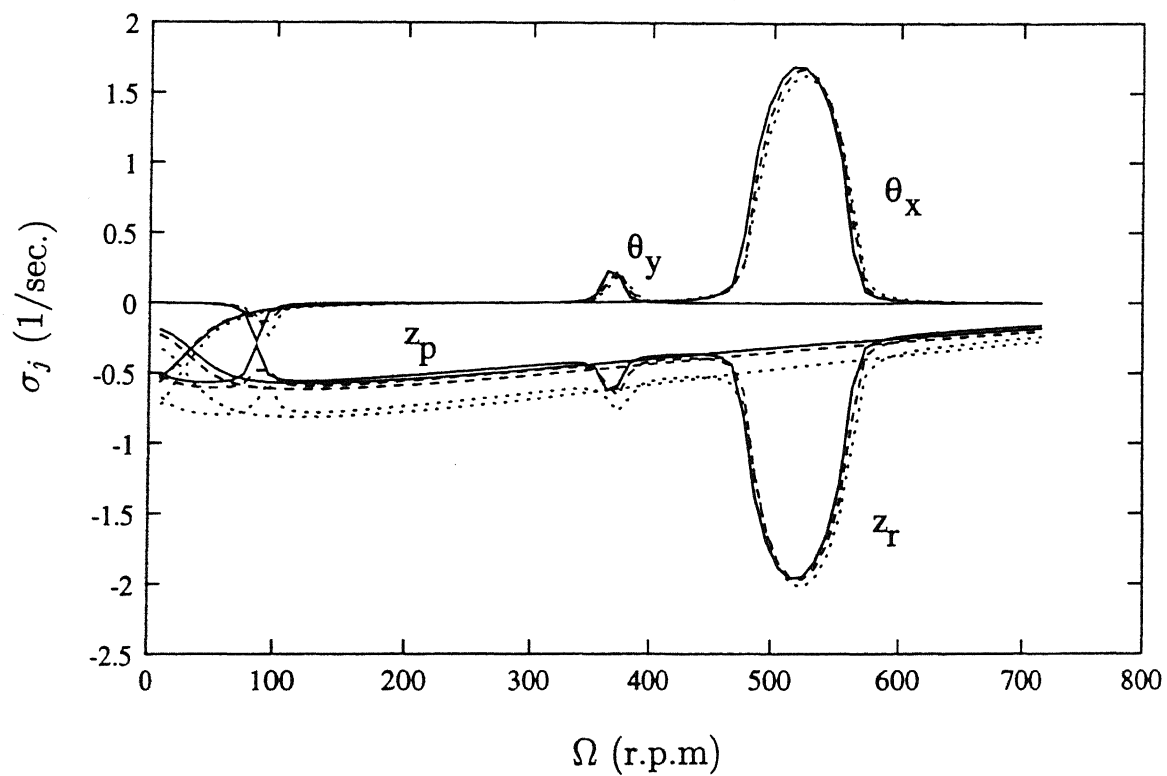


Fig. 4.4 Effect of amplitude of motion of the elastomer on modal damping.

..... Amp. = 0.0005m; - - - - Amp. = 0.001m; — Amp. = 0.002m.

$\xi_1 = 0.1$, $\xi_2 = 0.25$.

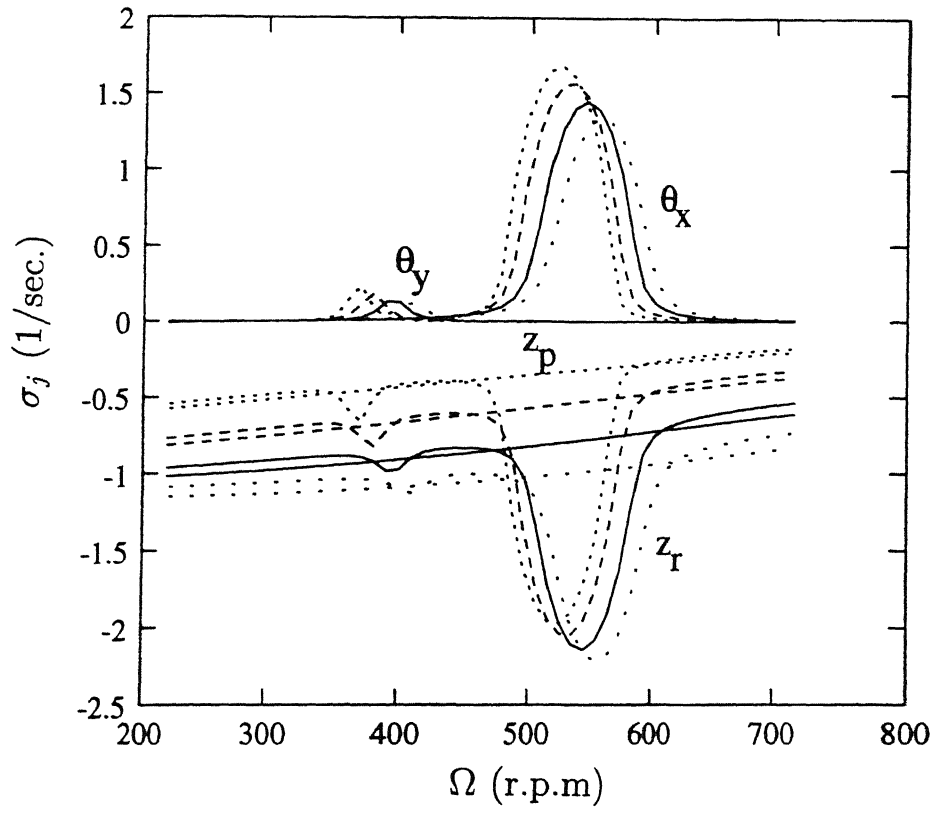


Fig. 4.5 Modal damping for different locations (ξ_1) of the elastomer (zero support damping).

- $\xi_1 = 0.1, \xi_2 = 0.25$;
- $\xi_1 = 0.07, \xi_2 = 0.25$;
- $\xi_1 = 0.04, \xi_2 = 0.25$;
- · · $\xi_1 = 0.02, \xi_2 = 0.25$.

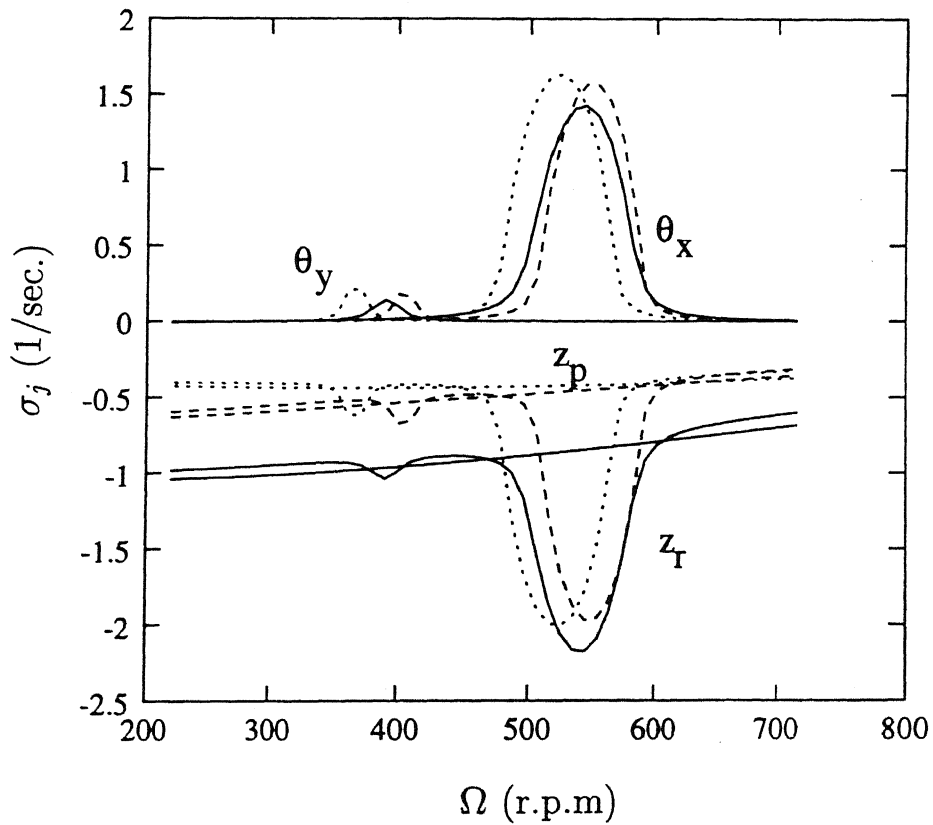


Fig. 4.6 Modal damping for different locations (ξ_2) of the torque tube attachment (zero support damping).

- $\xi_1 = 0.04, \xi_2 = 0.15$;
- $\xi_1 = 0.04, \xi_2 = 0.23$;
- - - $\xi_1 = 0.04, \xi_2 = 0.35$.

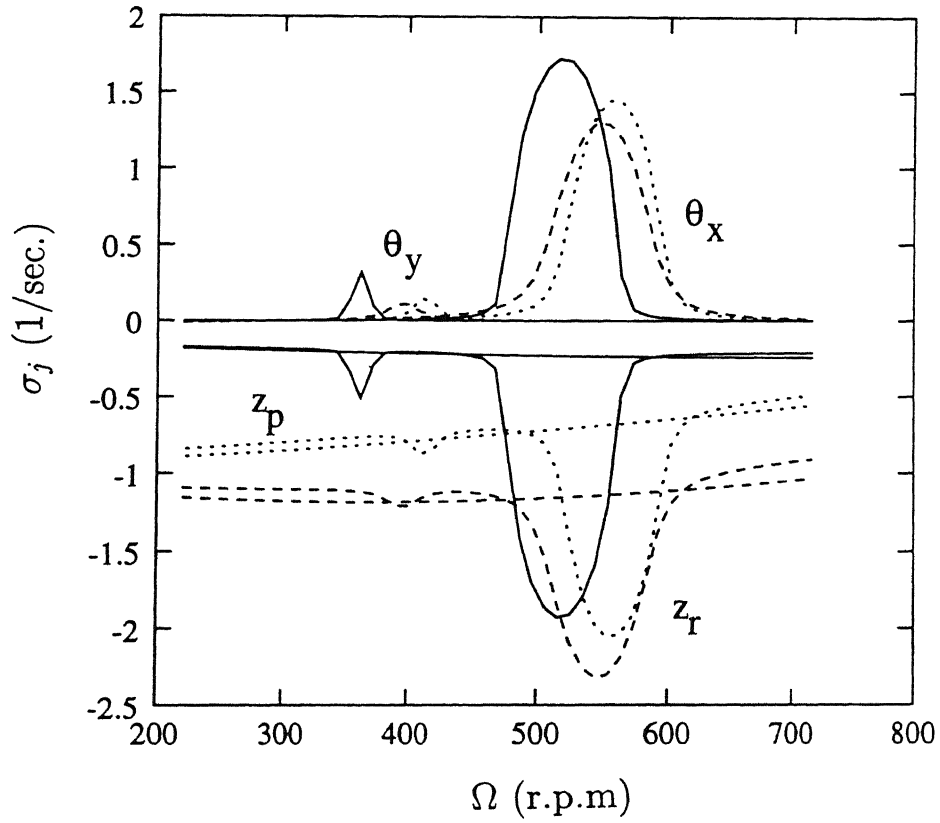


Fig. 4.7 Modal damping for different locations (ξ_2) of the torque tube attachment (zero support damping).

- $\xi_1 = 0.02, \xi_2 = 0.1;$
- - - $\xi_1 = 0.02, \xi_2 = 0.2;$
- $\xi_1 = 0.02, \xi_2 = 0.3.$

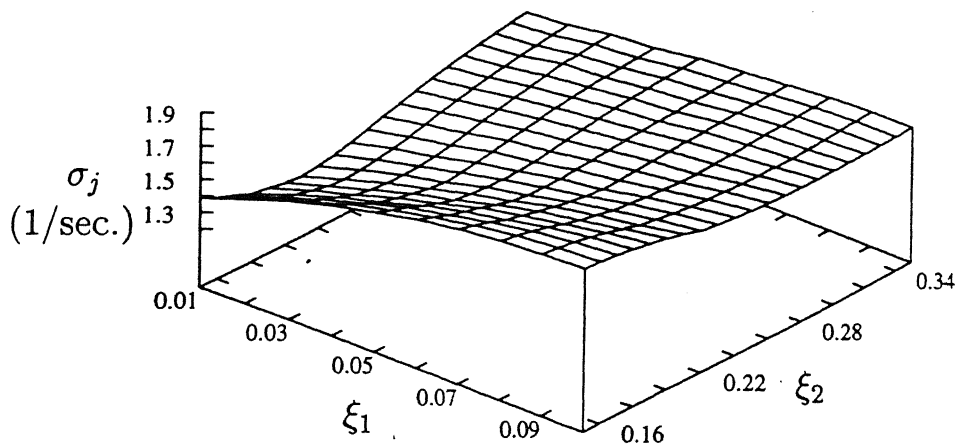


Fig. 4.8 Variation of maximum instability in roll mode for different combinations of ξ_1 and ξ_2 .

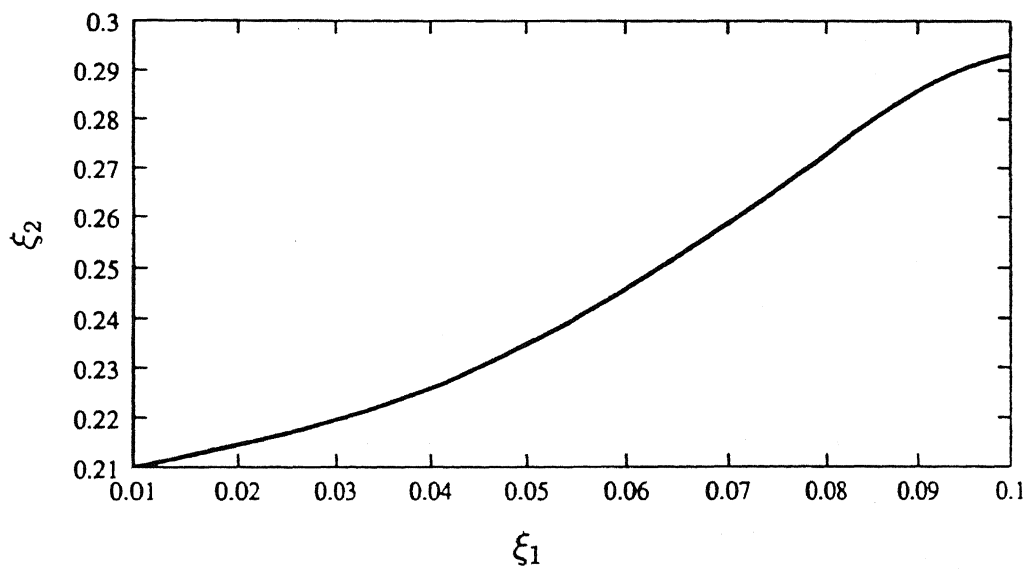


Fig. 4.9 Optimum combinations of ξ_1 and ξ_2 .

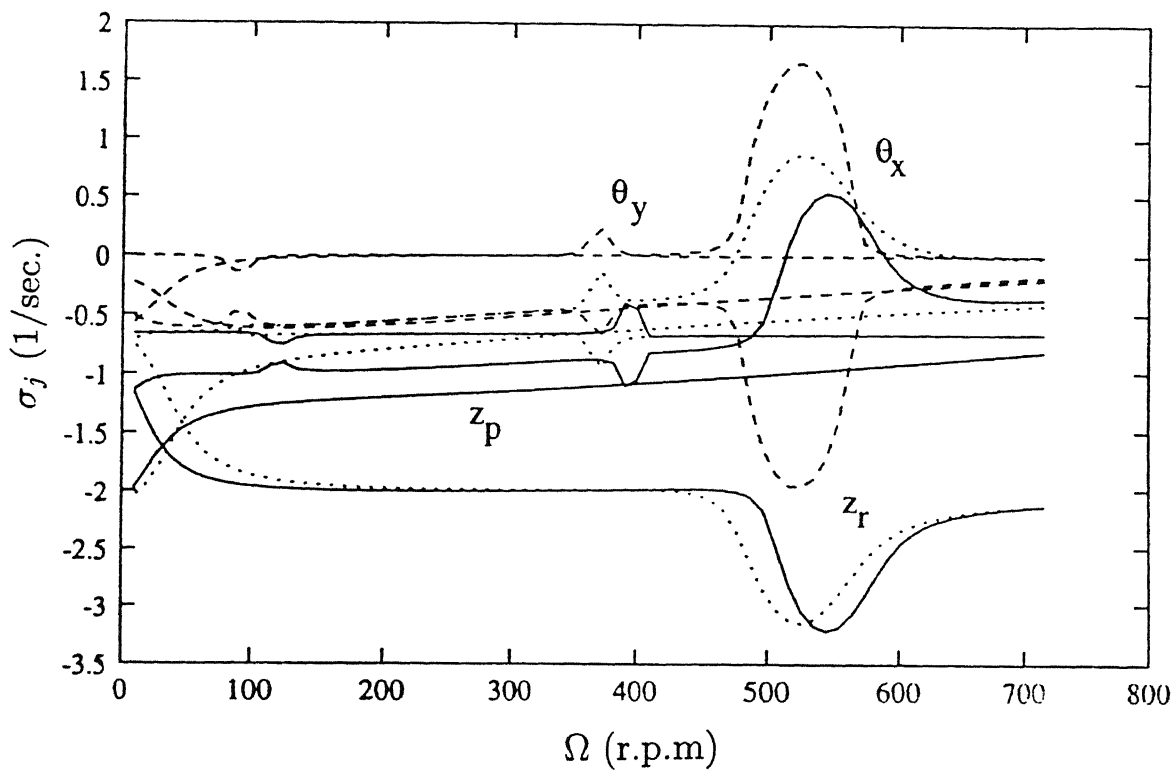


Fig. 4.10 Effect of support damping on stability ($\zeta_{\theta_x} = 0.082$, $\zeta_{\theta_y} = 0.0529$).

---- no support damping ($\xi_1 = 0.1$, $\xi_2 = 0.25$);

..... with support damping ($\xi_1 = 0.1$, $\xi_2 = 0.25$);

— with support damping ($\xi_1 = 0.04$, $\xi_2 = 0.25$).

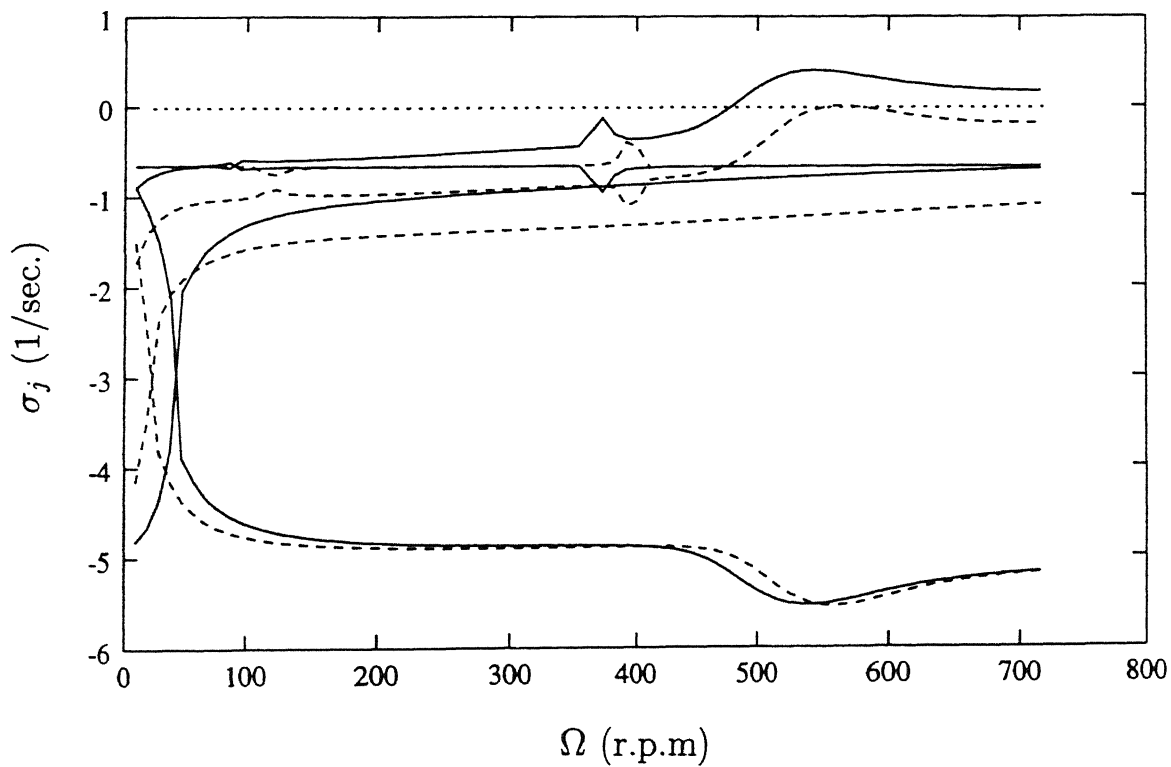


Fig. 4.11 Effect of support damping on stability ($\zeta_{\theta_x} = 0.020$, $\zeta_{\theta_y} = 0.0529$).

— $\xi_1 = 0.1$, $\xi_2 = 0.25$; - - - $\xi_1 = 0.04$, $\xi_2 = 0.25$.

Table 4.1 Input data for ground resonance analysis.

Parameters for non-dimensionalisation:

mass per unit length $m = 9.7 \text{ Kg/m}$

Length $L = 6.6 \text{ m}$

time $\Omega = 32.8 \text{ rad/s}$

Blade data:	
m	9.7 Kg/m
L	6.6 m
\bar{a}	0.0301
Ω	32.8 rad/s
Non-dimensional fuselage data:	
I_x	1.0511
I_y	3.1023
$\xi_h = \frac{\bar{h}}{L}$	0.2
$\omega_x = \left(\frac{K_x}{I_x}\right)^{1/2}$	$\frac{4}{\Omega}$
$\omega_y = \left(\frac{K_y}{I_y}\right)^{1/2}$	$\frac{2}{\Omega}$
ζ_{θ_x}	0.082, 0.20
ζ_{θ_y}	0.0529
$C_x = 2\zeta_{\theta_x}\omega_x, C_y = 2\zeta_{\theta_y}\omega_y$	

Chapter 5

TRANSIENT RESPONSE IN HOVER TO A STEP CONTROL PITCH INPUT

5.1 Introduction

Most of the aeroelastic response analyses of rotor blades address the problem of formulation and evaluation of the steady state response of the blade in forward flight for estimating the vibratory loads acting on the hub and the blade root. Very little information is available on the transient response characteristics of the rotor blades. In 1953, Carpenter and Fridovitch [106] performed a wind tunnel experiment to examine the transient response behaviour of a rotor blade, having only rigid flap motion. It was observed that for a step input in the pitch angle, the transient response of the blade in the flap mode exhibited dynamic overshoot leading to overstressing of the blade. In addition, the rotor thrust also showed a dynamic overshoot before reaching the steady state value. The dynamics of a bearingless rotor is much more complicated due to the

presence of non-linear elastomeric damper and multiple load path. The pitch input to a bearingless rotor blade, as opposed to that of a hingeless rotor blade, is provided by twisting the flexbeam through a vertical movement of the pitch control mechanism (Fig. 1.3a). Therefore, this configuration provides an additional kinematic constraint at the point P . It is expected that the non-linearity of the elastomer, multiple load path and kinematic constraint will have strong influence on the dynamic response characteristics of the blade. In addition, due to inherent differences in the construction of hingeless and bearingless rotors, there could be fundamental difference in their response characteristics.

The aim of this study is to examine the transient response to a step input of an isolated bearingless rotor blade in hovering condition simulating a wind tunnel test. An attempt is also made to quantify a measure of aeroelastic couplings (pitch-flap and pitch-lag couplings) from the steady state response and the dependence of these couplings on various geometric parameters of the bearingless rotor blade.

5.2 Formulation of Equation of Motion

The transient response analysis of a bearingless rotor blade requires the formulation of aeroelastic equations of motion representing coupled axial, flap, lag and torsional motions of the blade, including non-linear elastomer and kinematic constraint. The equations of motion are derived using Hamilton's principle. The important ingredients required for the formulation are:

- (i) the strain energy of the blade,
- (ii) the kinetic energy of the blade,
- (iii) the strain energy and dissipative energy associated with the elastomer,
- (iv) the work done due to aerodynamic loads

and

(v) a suitable model of the kinematic constraint.

5.2.1 Assumptions

Since the aim of the study is to understand the physics of the dynamical motion and aeroelastic couplings in a bearingless rotor due to multiple load paths, pitch link geometric constraint and non-linear elastomer, several assumptions have been made while formulating the equations of motion. These are:

- (i) the rotor blade is an Euler-Bernoulli beam made of homogeneous isotropic material, and undergoing coupled axial, flap, lag and torsional deformations.
- (ii) the torque tube and pitch link are rigid and massless elements (usually, the torque tube has a very high stiffness relative to that of the flexbeam or rotor blade section),
- (iii) the rotor blade has zero precone,
- (iv) the cross-section of the blade is symmetric,
- (v) the pitch control mechanism is infinitely stiff,
- (vi) the rotor is operating under hovering condition simulating a wind tunnel test, and (vii) the aerodynamic loads on the rotor blade are represented by a quasi-steady two dimensional aerodynamic model with a time varying inflow.

The mathematical procedure of formulating the equations of motion essentially follows the general steps adopted in Refs. [35, 46].

5.2.2 Ordering Scheme

In the formulation of equations of motion of a rotor blade, a large number of higher order terms are generated. In order to identify and eliminate the higher order terms in

a consistent manner, an ordering scheme is employed. This ordering scheme is based on the assumption that the slope of the deformed elastic blade is moderate, and of order ϵ ($0.10 \leq \epsilon \leq 0.20$). Orders of magnitude in terms of ϵ are then assigned to various non-dimensional parameters governing the rotor blade problem. In this formulation, terms of order ϵ^2 are neglected with respect to terms of order 1, *i.e.*,

$$O(1) + O(\epsilon^2) \approx O(1)$$

The order of magnitude of various non-dimensional parameters governing this problem are given below:

ORDER 1

$$\frac{x}{L}, L \frac{\partial}{\partial x}, \frac{\partial}{\partial \tau} = \frac{1}{\Omega} \frac{\partial}{\partial t}$$

ORDER $\epsilon^{1/2}$

$$\theta_{tw}, \theta_{in}$$

ORDER ϵ

$$\frac{\eta}{L}, \frac{\zeta}{L}, \frac{v}{L}, \frac{w}{L}, v_{,x}, w_{,x}, \phi, \theta_x, \theta_\eta, \theta_\zeta$$

ORDER ϵ^2

$$\frac{u}{L}, u_{,x}, \bar{\epsilon}_{xx}, \frac{m\Omega^2 L^2}{EA}$$

All symbols are explained in the nomenclature included at the beginning of the thesis.

5.2.3 Coordinate Systems

The description of complex deformation of a rotor blade requires several coordinate systems. Each coordinate system is represented by a triad of orthogonal unit vectors. Coordinate systems used in deriving the equations of motion are described below:

5.2.3.1 Hub Fixed Rotating Coordinate System

The $(\hat{e}_x, \hat{e}_y, \hat{e}_z)$ system shown in Fig. 5.1 rotates about Z -axis with constant angular speed Ω of the rotor. Its origin is fixed at the hub centre O and the direction of \hat{e}_x is along the elastic axis of the blade.

5.2.3.2 Undeformed Cross-section Fixed Rotating Coordinate System

The $(\hat{e}_{x1}, \hat{e}_{y1}, \hat{e}_{z1})$ system is parallel to the hub fixed rotating coordinate system. But its origin is located at O' at a distance x from the hub centre O as shown in Fig. 5.2.

5.2.3.3 Undeformed Curvilinear Cross-sectional Coordinate System

The curvilinear $(\hat{e}_x, \hat{e}_\eta, \hat{e}_\zeta)$ system has unit vectors \hat{e}_η and \hat{e}_ζ along the principle axes of the blade cross-section. The orientation of $(\hat{e}_\eta, \hat{e}_\zeta)$ with respect to $(\hat{e}_{y1}, \hat{e}_{z1})$ or (\hat{e}_y, \hat{e}_z) is represented by an angle θ (Fig. 5.3), where θ is the sum of pretwist θ_{tw} and pitch input θ_{in} .

5.2.3.4 Deformed Cross-sectional Coordinate System

The $(\hat{e}_{x'}, \hat{e}_{y'}, \hat{e}_{z'})$ system represents the deformed cross-sectional coordinate system. It is obtained after performing a rigid body translation and rotation of $(\hat{e}_{x1}, \hat{e}_{y1}, \hat{e}_{z1})$, corresponding to the local axial, flap and lag deformations at the elastic axis. The direction of $\hat{e}_{x'}$ is along the tangent to the deformed elastic axis. This system is used to define the directions of flow velocities for aerodynamic load calculations (Fig. 5.4).

5.2.3.5 Deformed Curvilinear Cross-sectional Coordinate System

The $(\hat{e}_{x'}, \hat{e}_{\eta'}, \hat{e}_{\zeta'})$ system represents the orientation of cross-sectional principal coordinates after axial, flap, lag and torsional deformations. The angle between the coordi-

nate systems $(\hat{e}_{x'}, \hat{e}_{y'}, \hat{e}_{z'})$ and $(\hat{e}_{x'}, \hat{e}_{\eta'}, \hat{e}_{\zeta'})$ represents the sum of pretwist (θ_{tw}) , pitch input (θ_{in}) and elastic twist of the blade (ϕ) , as shown in Fig. 5.5.

5.2.3.6 Local cartesian Coordinate System

The system (y_1, y_2, y_3) represents a local cartesian coordinate system with its unit vectors $(\hat{e}_1, \hat{e}_2, \hat{e}_3)$ parallel to the orthogonal triad $(\hat{e}_x, \hat{e}_\eta, \hat{e}_\zeta)$ of the cross-section. The Green strain measures are obtained in the undeformed curvilinear coordinate system $(\hat{e}_x, \hat{e}_\eta, \hat{e}_\zeta)$. These have to be transformed to the local cartesian system because the constitutive relation of the material is defined in the local cartesian system. The essential difference between $(\hat{e}_x, \hat{e}_\eta, \hat{e}_\zeta)$ and $(\hat{e}_1, \hat{e}_2, \hat{e}_3)$ is that the derivatives of $\hat{e}_\eta, \hat{e}_\zeta$ with respect to x represents the twist rate of the blade in the undeformed state, whereas, the derivatives of \hat{e}_2, \hat{e}_3 with respect to x are both zero.

5.2.4 Blade Model

The strain energy and the kinetic energy expressions of the blade are detailed in the following sections.

5.2.4.1 Strain Energy of the Blade

Details of the derivation of strain components are described in Appendix A. Consistent with the assumption of Euler-Bernoulli beam, the non-zero strain components at any arbitrary point (η, ζ) on the cross-section of the blade can be written in terms of u, v, w and ϕ as

$$\begin{aligned}\epsilon_{xx} &= u_{,x} + \frac{v_{,x}^2}{2} + \frac{w_{,x}^2}{2} - \Psi\phi_{,xx} + \frac{1}{2}(\eta^2 + \zeta^2)\phi_{,x}^2 \\ &- v_{,xx}[\eta \cos(\theta_{tw} + \theta_{in} + \phi) - \zeta \sin(\theta_{tw} + \theta_{in} + \phi)] \\ &- w_{,xx}[\eta \sin(\theta_{tw} + \theta_{in} + \phi) + \zeta \cos(\theta_{tw} + \theta_{in} + \phi)]\end{aligned}\quad (5.1)$$

$$\gamma_{x\eta} = -(\zeta + \Psi_\eta) \phi_{,x} \quad (5.2)$$

$$\gamma_{x\zeta} = (\eta - \Psi_\zeta) \phi_{,x} \quad (5.3)$$

where u , v and w are the elastic displacements of any arbitrary point on the elastic axis in the \hat{e}_x , \hat{e}_y and \hat{e}_z directions, respectively. The elastic twist is ϕ and Ψ is the warping function for the cross-section due to torsion.

The strain enegy of the blade is given as

$$\mathcal{U} = \frac{1}{2} \int_0^L \int \int_A (\sigma_{xx} \epsilon_{xx} + \sigma_{x\eta} \gamma_{x\eta} + \sigma_{x\zeta} \gamma_{x\zeta}) dVOL \quad (5.4)$$

where

$$dVOL = \sqrt{g} d\eta d\zeta dx$$

$$\sigma_{xx} = E \epsilon_{xx}$$

$$\sigma_{x\eta} = G \gamma_{x\eta}$$

$$\sigma_{x\zeta} = G \gamma_{x\zeta}$$

and g is the determinant (equal to 1) of the metric tensor defined in Eq. A.28 in Appendix A.

The variation of the strain energy is given by

$$\delta \mathcal{U} = \int_0^L \int \int_A (\sigma_{xx} \delta \epsilon_{xx} + \sigma_{x\eta} \delta \gamma_{x\eta} + \sigma_{x\zeta} \delta \gamma_{x\zeta}) d\eta d\zeta dx \quad (5.5)$$

where

$$\begin{aligned} \delta \epsilon_{xx} &= \delta u_{,x} + v_{,x} \delta v_{,x} + w_{,x} \delta w_{,x} + (\eta^2 + \zeta^2) (\theta_{tw} + \theta_{in} + \phi)_{,x} \delta \phi_{,x} - \Psi \delta \phi_{,xx} \\ &- [\eta \cos(\theta_{tw} + \theta_{in} + \phi) - \zeta \sin(\theta_{tw} + \theta_{in} + \phi)] (\delta v_{,xx} + w_{,xx} \delta \phi) \\ &- [\eta \cos(\theta_{tw} + \theta_{in} + \phi) + \zeta \sin(\theta_{tw} + \theta_{in} + \phi)] (\delta w_{,xx} - v_{,xx} \delta \phi) \\ \delta \gamma_{x\eta} &= -\hat{\zeta} \delta \phi_{,x} \end{aligned}$$

$$\delta\gamma_{x\zeta} = \hat{\eta} \delta\phi_{,x}$$

$$\hat{\eta} = \eta - \Psi_\zeta$$

$$\hat{\zeta} = \zeta + \Psi_\eta$$

and the subscript , denotes a partial derivative with respect to the subsequent subscript(s).

Performing cross-sectional integration and applying the ordering scheme, the variation of strain energy expression can be written as

$$\begin{aligned} \delta U &= \int_0^L \{ V_{x'} (\delta u_{,x} + v_{,x} \delta u_{,x} + w_{,x} \delta w_{,x}) + (S_{x'} + T_{x'}) \delta \phi_{,x} + P_{x'} \delta \phi_{,xx} \\ &+ [M_{z'} \cos(\theta_{tw} + \theta_{in} + \phi) + M_{y'} \sin(\theta_{tw} + \theta_{in} + \phi)] (\delta v_{,xx} + w_{,xx} \delta \phi) \\ &+ [M_{z'} \sin(\theta_{tw} + \theta_{in} + \phi) - M_{y'} \cos(\theta_{tw} + \theta_{in} + \phi)] (\delta w_{,xx} - v_{,xx} \delta \phi) \} dx \end{aligned} \quad (5.6)$$

where

$$\begin{aligned} V_{x'} &= EA \left(u_{,x} + \frac{v_{,x}^2}{2} + \frac{w_{,x}^2}{2} \right) + (\theta_{tw} + \theta_{in})_{,x} \phi_{,x} \\ &- EA\eta_a [v_{,xx} \cos(\theta_{tw} + \theta_{in} + \phi) + w_{,xx} \sin(\theta_{tw} + \theta_{in} + \phi)] \\ S_{x'} &= GJ \phi_{,x} \\ T_{x'} &= EAC_o \phi_{,x} \left(u_{,x} + \frac{v_{,x}^2}{2} + \frac{w_{,x}^2}{2} \right) \\ P_{x'} &= EAD_3 \phi_{,xx} + EAD_2 [w_{,xx} \cos(\theta_{tw} + \theta_{in}) - v_{,xx} \sin(\theta_{tw} + \theta_{in})] \\ M_{y'} &= EI_{\eta\eta} [v_{,xx} \sin(\theta_{tw} + \theta_{in} + \phi) - w_{,xx} \cos(\theta_{tw} + \theta_{in} + \phi)] - EAD_2 \phi_{,xx} \\ \text{and } M_{z'} &= EI_{\zeta\zeta} [v_{,xx} \cos(\theta_{tw} + \theta_{in} + \phi) + w_{,xx} \sin(\theta_{tw} + \theta_{in} + \phi)] \\ &- EA\eta_a \left(u_{,x} + \frac{v_{,x}^2}{2} + \frac{w_{,x}^2}{2} \right) - EAC_1 (\theta_{tw} + \theta_{in})_{,x} \phi_{,x} \end{aligned} \quad (5.7)$$

The sectional integrals in Eqs.(5.7) are defined as follows:

$$\begin{aligned} EA &= \int \int E d\eta d\zeta \\ EA\eta_a &= \int \int [E\eta] d\eta d\zeta \end{aligned}$$

$$\begin{aligned}
EI_{\eta\eta} &= \int \int [E\zeta^2] d\eta d\zeta \\
EI_{\zeta\zeta} &= \int \int [E\eta^2] d\eta d\zeta \\
EAC_o &= \int \int [E(\eta^2 + \zeta^2)] d\eta d\zeta \\
GJ &= \int \int [G(\hat{\eta}^2 + \hat{\zeta}^2)] d\eta d\zeta \\
EAC_3 &= \int \int [E(\eta^2 + \zeta^2)^2] d\eta d\zeta \\
EAC_1 &= \int \int [E\eta(\eta^2 + \zeta^2)] d\eta d\zeta \\
EAD_3 &= \int \int [E\Psi^2] d\eta d\zeta \\
\text{and } EAD_2 &= \int \int [E\zeta\Psi] d\eta d\zeta
\end{aligned}$$

Because of the antisymmetric character of Ψ and the assumed symmetry of the cross-section about η -axis

$$\begin{aligned}
\int \int [E\Psi] d\eta d\zeta &= 0 \\
\int \int [E\zeta] d\eta d\zeta &= 0 \\
\int \int [E\zeta(\eta^2 + \zeta^2)] d\eta d\zeta &= 0 \\
\int \int [E\Psi(\eta^2 + \zeta^2)] d\eta d\zeta &= 0 \\
\int \int [E\eta\zeta] d\eta d\zeta &= 0 \\
\text{and } \int \int [E\eta\Psi] d\eta d\zeta &= 0
\end{aligned}$$

5.2.4.2 Kinetic Energy of the Blade

Combining Eqs. A.17, A.14 and A.16 in Appendix A, the position vector of any point P on the deformed beam is given by

$$\begin{aligned}
\mathbf{R} &= (x + u)\hat{e}_x + v\hat{e}_y + w\hat{e}_z + \eta\hat{e}_{\eta'} + \zeta\hat{e}_{\zeta'} + \alpha\Psi\hat{e}_{x'} \\
&= x_1\hat{e}_x + y_1\hat{e}_y + z_1\hat{e}_z
\end{aligned} \tag{5.8}$$

where α is the warping amplitude. Noting that the warping amplitude α is taken as equal to elastic twist rate of the blade $-\dot{\phi}_{,x}$ (Eq. A.35) and using the transformation matrices, the expressions for x_1 , y_1 and z_1 can be written as

$$\begin{aligned}
 x_1 &= x + u - \Psi\dot{\phi}_{,x} - v_{,x} [\eta \cos(\theta_{tw} + \theta_{in} + \phi) - \zeta \sin(\theta_{tw} + \theta_{in} + \phi)] \\
 &\quad - w_{,x} [\eta \sin(\theta_{tw} + \theta_{in} + \phi) + \zeta \cos(\theta_{tw} + \theta_{in} + \phi)] \\
 y_1 &= v + \eta \cos(\theta_{tw} + \theta_{in} + \phi) - \zeta \sin(\theta_{tw} + \theta_{in} + \phi) \\
 \text{and } z_1 &= w + \eta \sin(\theta_{tw} + \theta_{in} + \phi) + \zeta \cos(\theta_{tw} + \theta_{in} + \phi)
 \end{aligned} \tag{5.9}$$

or,

$$\begin{aligned}
 x_1 &= x + u - \Psi\dot{\phi}_{,x} - v_{,x} (y_1 - v) - w_{,x} (z_1 - w) \\
 y_1 &= v + (y_1 - v) \\
 \text{and } z_1 &= w + (z_1 - w)
 \end{aligned} \tag{5.10}$$

where the terms $(y_1 - v)$ and $(z_1 - w)$ are introduced for convenience.

The velocity of the point P is given by

$$\begin{aligned}
 \mathbf{V} &= \frac{\partial \mathbf{R}}{\partial t} + \Omega \hat{e}_z \times \mathbf{R} \\
 &= (\dot{x}_1 - \Omega y_1) \hat{e}_x + (\dot{y}_1 + \Omega x_1) \hat{e}_y + \dot{z}_1 \hat{e}_z
 \end{aligned} \tag{5.11}$$

where

$$\begin{aligned}
 \dot{x}_1 &= \dot{u} - (\dot{v}_{,x} + \dot{\phi} w_{,x}) (y_1 - v) - (\dot{w}_{,x} - \dot{\phi} v_{,x}) (z_1 - w) - \Psi \dot{\phi}_{,x} \\
 \dot{y}_1 &= \dot{v} - \dot{\phi} (z_1 - w) \\
 \text{and } \dot{z}_1 &= \dot{w} + \dot{\phi} (y_1 - v)
 \end{aligned} \tag{5.12}$$

The kinetic energy of the beam is given by

$$T(t) = \frac{1}{2} \int_0^L \int \int_A \rho \mathbf{V} \cdot \mathbf{V} d\eta d\zeta dx \tag{5.13}$$

The variation of kinetic energy is

$$\delta T = \int_0^L \int \int_A \rho \mathbf{V} \cdot \delta \mathbf{V} d\eta d\zeta dx \quad (5.14)$$

Substituting for \mathbf{V} from Eq. 5.11 and integrating δT by parts with respect to time, one gets

$$\delta T = \int_0^L \int \int_A \rho [Z_u \delta u + Z_v \delta v + Z_w \delta w + Z_{v'} \delta v_{,x} + Z_{w'} \delta w_{,x} + Z_\phi \delta \phi] d\eta d\zeta dx \quad (5.15)$$

where the terms Z_u , Z_v , Z_w , $Z_{v'}$, $Z_{w'}$ and Z_ϕ are the coefficients of δu , δv , δw , $\delta v_{,x}$, $\delta w_{,x}$ and $\delta \phi$, respectively.

Integration of the expression over the cross-section yields

$$\delta T = \int_0^L [\bar{Z}_u \delta u + \bar{Z}_v \delta v + \bar{Z}_w \delta w + \bar{Z}_{v'} \delta v_{,x} + \bar{Z}_{w'} \delta w_{,x} + \bar{Z}_\phi \delta \phi] dx \quad (5.16)$$

After eliminating the higher order terms and assuming the cross-sectional symmetry about η -axis and an antisymmetric warping function Ψ , the expressions for \bar{Z}_u , \bar{Z}_v , \bar{Z}_w , $\bar{Z}_{v'}$, $\bar{Z}_{w'}$ and \bar{Z}_ϕ can be written as

$$\begin{aligned} \bar{Z}_u &= m (\Omega^2 x + 2\Omega \dot{v}) \\ \bar{Z}_v &= m\Omega^2 v + m\eta_m \cos(\theta_{tw} + \theta_{in} + \phi) - 2m\Omega \dot{u} \\ &\quad + 2m\eta_m \Omega [\dot{v}_{,x} \cos(\theta_{tw} + \theta_{in}) + \dot{w}_{,x} \sin(\theta_{tw} + \theta_{in})] - m\ddot{v} + m\eta_m \ddot{\phi} \sin(\theta_{tw} + \theta_{in}) \\ \bar{Z}_w &= -m\ddot{w} - m\eta_m \ddot{\phi} \cos(\theta_{tw} + \theta_{in}) \\ \bar{Z}_\phi &= -Im\ddot{\phi} - \Omega^2 (Im_{\zeta\zeta} - Im_{\eta\eta}) \cos(\theta_{tw} + \theta_{in} + \phi) \sin(\theta_{tw} + \theta_{in} + \phi) \\ &\quad - m\eta_m \Omega^2 x [w_{,x} \cos(\theta_{tw} + \theta_{in}) - v_{,x} \sin(\theta_{tw} + \theta_{in})] - m\eta_m \Omega^2 v \sin(\theta_{tw} + \theta_{in}) \\ &\quad - m\eta_m [\ddot{v} \sin(\theta_{tw} + \theta_{in}) - \ddot{w} \cos(\theta_{tw} + \theta_{in})] \\ \bar{Z}_{v'} &= -m\eta_m [\Omega^2 x \cos(\theta_{tw} + \theta_{in} + \phi) + 2\Omega \dot{v} \cos(\theta_{tw} + \theta_{in} + \phi)] \end{aligned} \quad (5.17)$$

$$\text{and } \bar{Z}_{w'} = -m\eta_m [\Omega^2 x \sin(\theta_{tw} + \theta_{in} + \phi) + 2\Omega \dot{v} \sin(\theta_{tw} + \theta_{in} + \phi)]$$

where sectional integrals are defined as

$$\begin{aligned}
m &= \int \int \rho d\eta d\zeta \\
m\eta_m &= \int \int \rho \eta d\eta d\zeta \\
Im_{\eta\eta} &= \int \int \rho \eta^2 d\eta d\zeta \\
Im_{\zeta\zeta} &= \int \int \rho \zeta^2 d\eta d\zeta \\
Im &= Im_{\eta\eta} + Im_{\zeta\zeta}
\end{aligned}$$

The integrals involving the terms $(y_1 - v)$ and $(z_1 - w)$, introduced for convenience in Eqs. 5.10, are given by

$$\begin{aligned}
\int \int \rho (y_1 - v) d\eta d\zeta &= m\eta_m \cos(\theta_{tw} + \theta_{in} + \phi) \\
\int \int \rho (z_1 - w) d\eta d\zeta &= m\eta_m \sin(\theta_{tw} + \theta_{in} + \phi) \\
\int \int \rho (y_1 - v)(z_1 - w) d\eta d\zeta &= Im_{\zeta\zeta} - Im_{\eta\eta} \cos(\theta_{tw} + \theta_{in} + \phi) \sin(\theta_{tw} + \theta_{in} + \phi)
\end{aligned}$$

and

$$\int \int \rho [(y_1 - v)^2 + (z_1 - w)^2] d\eta d\zeta = Im$$

5.2.5 Elastomeric Damper Model

An elastomer is placed between the torque tube and the flexbeam to provide adequate lag damping to the rotor blade. It also serves the purpose of a spacer between the torque tube and the flexbeam. During blade deformation, the elastomer provides constraints in flap, lag and torsional motions. The elastomer data are usually available [25, 26] for the lag mode only. Therefore, following the approach of Ormiston *et al.* [31], the elastomer is represented by a very stiff linear spring in the flap mode. In the lag mode, the elastomer is modelled as a parallel combination of a non-linear spring, a Coulomb damper and hysteretic damper (Fig. 2.6); and the effect of elastomer is not considered in the torsional mode.

5.2.5.1 Strain Energy of the Elastomer

Flap Mode:

The expression for the strain energy of the spring due to deformation Δ_f is

$$U_f = \frac{1}{2} K_1 \Delta_f^2 \quad (5.18)$$

$$\text{where } \Delta_f = \left[w(L_2, t) - (L_2 - L_1) \frac{\partial w(L_2, t)}{\partial x} - w(L_1, t) \right]$$

Variation in spring energy is given by

$$\delta U_f = K_1 \Delta_f \delta \Delta_f \quad (5.19)$$

Lag Mode:

The expression for the strain energy of the spring due to deformation Δ_l is

$$U_l = \frac{1}{2} K_1 \Delta_l^2 - \frac{1}{4} K_3 \Delta_l^4 + \frac{1}{6} K_5 \Delta_l^6 - \frac{1}{8} K_7 \Delta_l^8 \quad (5.20)$$

$$\text{where } \Delta_l = \left[v(L_2, t) - (L_2 - L_1) \frac{\partial v(L_2, t)}{\partial x} - v(L_1, t) \right]$$

Variation in spring energy is given by

$$\delta U_l = \left(K_1 \Delta_l - K_3 \Delta_l^3 + K_5 \Delta_l^5 - K_7 \Delta_l^7 \right) \delta \Delta_l \quad (5.21)$$

5.2.5.2 Work Done by the Dissipative Element

The expression for the virtual work done by the dissipative (Coulomb and hysteretic) elements of the elastomeric damper in the lag mode is given by

$$\delta W_d = F_d \delta \Delta_l \quad (5.22)$$

$$\text{where } F_d = \frac{h}{\omega} \dot{\Delta}_l + F_s \operatorname{sgn} | \dot{\Delta}_l |$$

5.2.6 Aerodynamic Model

The aerodynamic forces and moments are treated as external loads acting on the blade. The expressions for aerodynamic loads are not obtained explicitly, rather they are derived by an implicit formulation, following the procedure adopted in Ref. [52]. The aerodynamic loads are included separately in the computer programme. At each time step, these loads are evaluated knowing the response of the blade and other velocity parameters.

5.2.6.1 Aerodynamic Loads

The time varying aerodynamic lift and pitching moment acting on a typical cross-section of the blade are evaluated based on Greenberg's extension of Theodorsen's theory [112] developed for a two-dimensional airfoil undergoing harmonic motion in a pulsating incompressible flow. A quasi-steady approximation of the unsteady theory is used, by assuming the lift deficiency function $c(k) = 1$.

Based on the quasi-steady approximation [112], the expressions for aerodynamic lift L_A and pitching moment M_A per unit span are given by

$$L_A = \frac{1}{2}a_1\rho_A b_1^2 \left[\frac{d(\dot{h}_f + V_f\theta)}{dt} - \left(X_A - \frac{b_1}{2}\right) + \ddot{\theta} \right] + a_1\rho_A b_1 V_f [\dot{h}_f + V_f\theta + (b_1 - X_A)\dot{\theta}] \quad (5.23)$$

$$M_A = \frac{1}{2}a_1\rho_A b_1^2 \left\{ \left(X_A - \frac{b_1}{2}\right) \frac{d(\dot{h}_f + V_f\theta)}{dt} - \frac{1}{2}b_1 V_f \dot{\theta} - \left[\frac{b_1^2}{8} + \left(X_A - \frac{b_1}{2}\right)^2 \right] \ddot{\theta} \right\} + a_1\rho_A b_1 X_A V_f [\dot{h}_f + V_f\theta + (b_1 - X_A)\dot{\theta}] \quad (5.24)$$

where a_1 is the two dimensional airfoil lift curve slope; b_1 is the semi-chord ; ρ_A is the density of air; \dot{h}_f is the plunging velocity; V_f is the free-stream velocity; X_A is the blade offset of the aerodynamic centre from the elastic axis. The pitch angle θ with

respect to the free-stream is given by

$$\theta = \theta_{tw} + \theta_{in} + \phi$$

The resultant airfoil velocity relative to air (Fig. 5.4) is

$$U_R = \sqrt{V_f^2 + \dot{h}_f^2} \quad (5.25)$$

The components of U_R in the deformed coordinate system $(e_{x'}, e_{\eta'}, e_{\zeta'})$ are given by

$$U_{\eta'} = V_f \cos \theta - \dot{h}_f \sin \theta \quad (5.26)$$

$$U_{\zeta'} = -V_f \sin \theta - \dot{h}_f \cos \theta \quad (5.27)$$

For small values of θ , the velocity components can be approximated as

$$\dot{h}_f + V_f \theta = -U_{\zeta'} \quad (5.28)$$

$$V_f = U_{\eta'} - U_{\zeta'} \theta \quad (5.29)$$

Substituting Eqs. (5.28) and (5.29) into Eqs. (5.23) and (5.24), the expressions for aerodynamic lift and pitching moment per unit span are written as

$$\begin{aligned} L_A = & \frac{1}{2} a_1 \rho_A b_1^2 \left[-\dot{U}_{\zeta'} - \left(X_A - \frac{b_1}{2} \right) \ddot{\theta} \right] \\ & + a_1 \rho_A b_1 (U_{\eta'} - U_{\zeta'} \theta) [-U_{\zeta'} + (b_1 - X_A) \dot{\theta}] \end{aligned} \quad (5.30)$$

$$\begin{aligned} M_A = & \frac{1}{2} a_1 \rho_A b_1^2 \left\{ \left(X_A - \frac{b_1}{2} \right) \dot{U}_{\zeta'} + \frac{1}{2} b_1 (U_{\eta'} - U_{\zeta'} \theta) \dot{\theta} + \left[\frac{b_1^2}{8} + \left(X_A - \frac{b_1}{2} \right)^2 \right] \ddot{\theta} \right\} \\ & + a_1 \rho_A b_1 X_A (U_{\eta'} - U_{\zeta'} \theta) [-U_{\zeta'} + (b_1 - X_A) \dot{\theta}] \end{aligned} \quad (5.31)$$

The expression for the profile drag per unit span is given by

$$D = C_{dc} \rho_A b_1 U_R^2 = C_{dc} \rho_A b_1 (U_{\eta'}^2 + U_{\zeta'}^2) \quad (5.32)$$

Evaluation of the sectional lift and moment require $U_{\eta'}$, $U_{\zeta'}$, θ and $\ddot{\theta}$ which are obtained first as outlined below.

Blade Velocity Relative to Air

The velocity vector of a point on the elastic axis of the blade relative to air is given by

$$\begin{aligned} \mathbf{U} &= \mathbf{V}_o - \mathbf{V}_A \\ &= U_{x'}\hat{e}_{x'} + U_{\eta'}\hat{e}_{\eta'} + U_{\zeta'}\hat{e}_{\zeta'} \end{aligned} \quad (5.33)$$

where \mathbf{V}_o is the velocity vector of a point on the elastic axis of the blade and \mathbf{V}_A is the velocity vector of air due to inflow only, since the present analysis is performed for hover.

The velocity vector of a point on the elastic axis of the blade, \mathbf{V}_o , can be obtained from Eq. 5.11 as

$$\mathbf{V}_o = \mathbf{V}_{\eta=\zeta=0} = V_x^o\hat{e}_x + V_y^o\hat{e}_y + V_z^o\hat{e}_z \quad (5.34)$$

where

$$\begin{Bmatrix} V_x^o \\ V_y^o \\ V_z^o \end{Bmatrix} = \begin{Bmatrix} \dot{u} - \Omega v \\ \Omega x + \dot{v} + \Omega u \\ \dot{w} \end{Bmatrix} \quad (5.35)$$

The expression for \mathbf{V}_A can be given by

$$\mathbf{V}_A = V_x^A\hat{e}_x + V_y^A\hat{e}_y + V_z^A\hat{e}_z \quad (5.36)$$

where

$$\begin{Bmatrix} V_x^A \\ V_y^A \\ V_z^A \end{Bmatrix} = \begin{Bmatrix} 0 \\ 0 \\ -v \end{Bmatrix} \quad (5.37)$$

Where ν is the inflow velocity through the rotor disk. The velocity components $U_{\eta'}$ and $U_{\zeta'}$ are obtained by combining Eqs. (5.33), (5.34) and (5.36) as

$$\begin{Bmatrix} U_{x'} \\ U_{\eta'} \\ U_{\zeta'} \end{Bmatrix} = [\mathbf{T}] \begin{Bmatrix} V_x^o - V_x^A \\ V_y^o - V_y^A \\ V_z^o - V_z^A \end{Bmatrix} \quad (5.38)$$

where the transformation matrix, $[\mathbf{T}]$, between the deformed curvilinear co-ordinate system $(\hat{e}_{x'}, \hat{e}_{\eta'}, \hat{e}_{\zeta'})$ and the hub fixed rotating co-ordinate system $(\hat{e}_x, \hat{e}_y, \hat{e}_z)$ under small angle approximation, is given by Eq. A.12.

The components of the aerodynamic forces and moments per unit span in the deformed co-ordinate system $(\hat{e}_{x'}, \hat{e}_{\eta'}, \hat{e}_{\zeta'})$ are related to L and M (Fig. 5.5) by

$$p_{\eta'} = L \sin \alpha_A - D \cos \alpha_A \quad (5.39)$$

$$p_{\zeta'} = L \cos \alpha_A + D \sin \alpha_A \quad (5.40)$$

$$q_{x'} = M \quad (5.41)$$

where α_A is the local angle of attack of the blade and given by

$$\alpha_A = -\tan^{-1} \left(\frac{U_{\zeta'}}{U_{\eta'}} \right) \quad (5.42)$$

$$\sin \alpha_A = - \left(\frac{U_{\zeta'}}{U_R} \right) = - \frac{U_{\zeta'}}{\sqrt{U_{\eta'}^2 + U_{\zeta'}^2}} \quad (5.43)$$

$$\cos \alpha_A = \left(\frac{U_{\eta'}}{U_R} \right) = \frac{U_{\eta'}}{\sqrt{U_{\eta'}^2 + U_{\zeta'}^2}} \quad (5.44)$$

The aerodynamic forces and moments per unit span in the hub fixed rotating co-ordinate system $(\hat{e}_x, \hat{e}_y, \hat{e}_z)$ can be obtained as

$$\begin{Bmatrix} L_u \\ L_v \\ L_w \end{Bmatrix} = [\mathbf{T}]^T \begin{Bmatrix} 0 \\ p_{\eta'} \\ p_{\zeta'} \end{Bmatrix} \quad (5.45)$$

and

$$\begin{Bmatrix} q_x \\ q_y \\ q_z \end{Bmatrix} = [T]^T \begin{Bmatrix} q_{x'} \\ 0 \\ 0 \end{Bmatrix} \quad (5.46)$$

The effect of the non-conservative distributed forces and moments due to the aerodynamic loads are included by applying the principle of virtual work. In general, the components L_u , q_y and q_z are of much smaller order compared to L_v , L_w and q_x . Hence they are neglected in the formulation of virtual work.

The virtual work done by the distributed aerodynamic forces is given by

$$(\delta W_e)_f = \int_0^L (L_v \delta v + L_w \delta w) dx \quad (5.47)$$

Similarly, the virtual work done due to the distributed moment is given by

$$(\delta W_e)_m = \int_0^L q_x \delta \phi dx \quad (5.48)$$

Thus, the total virtual work (δW_e) due to aerodynamic forces and moments can be written as

$$\delta W_e = (\delta W_e)_f + (\delta W_e)_m \quad (5.49)$$

5.2.6.2 Inflow Model

Since the present study addresses the transient response of a rotor blade in hover, it is essential to model the time varying nature of inflow through rotor disk. In the quasi-steady aerodynamic model presented above, the rotor inflow (ν) is included as a parameter which has to be supplied at every instant during the transient analysis. It is known that the blade motion causes unsteady wake, which in turn affects the blade loading. The dynamic inflow model [113, 114] simulates the unsteady wake

effects in a simple form. In this model, the inflow variation in collective mode (all blades have identical response) is assumed to be uniform over the entire rotor disk. The dynamic inflow model has been successfully applied to several aeroelastic and aeromechanical stability problems [83, 85, 115]. An extension of the dynamic inflow model is the generalised wake model [116]. The generalised wake model takes into account the azimuthal and radial variations in the inflow velocities. Manjunath *et al.* [117, 118] applied the generalised wake model to analyse the flap-lag and flap-lag-torsional stability problems in hover and forward flight.

In the present study, a simple dynamic inflow model has been used to evaluate the inflow at every instant of time from the knowledge of the blade loading. In the present problem, a step input is given to an isolated blade in hover simulating a wind tunnel test, which essentially corresponds to the collective mode operation of the rotor. (It may be noted that in collective mode, all the blades in the rotor system execute identical motion). In the collective mode condition, the relation between the rotor thrust and inflow is given by [85, 113, 119]

$$\bar{T} = \bar{m}\dot{\nu} + 2\pi L^2 \rho_A \nu^2 \quad (5.50)$$

$$\text{where } \bar{m} = 0.637 \rho_A \frac{4}{3} \pi L^3 \text{ (apparent mass)}$$

$$\text{and } \nu = \text{induced inflow velocity uniform over the rotor disk.}$$

Assuming there are N blades in the rotor system, the expression for \bar{T} is also given by

$$\bar{T} = \int_0^L \sum_{i=1}^N (L_w)_i dx \quad (5.51)$$

where the subscript i represents the i th blade. Since in the collective mode in hover, all blades experience identical loading, one can write

$$\bar{T} = \int_0^L N L_w dx \quad (5.52)$$

where L_w is given by Eq. 5.45.

The non-dimensional thrust coefficient C_T is given by

$$C_T = \frac{\bar{T}}{\rho_A \pi L^2 (\Omega L)^2} \quad (5.53)$$

5.2.7 Kinematic Constraint due to Pitch Link Motion

Figure 5.6 shows a bearingless rotor blade with pitch link at the leading edge. For a step pitch control input, the point P on the pitch link is moved by the pilot in the vertical (\hat{e}_z) direction through a distance w_P^s and is held at that position. Since it is assumed that the pitch control system is rigid, the point P *cannot have any displacement in the vertical direction* (\hat{e}_z) during dynamical motion of the blade. It is to be noted that the point P is not constrained in other five degrees of freedom, namely displacements along \hat{e}_x , \hat{e}_y and rotations about \hat{e}_x , \hat{e}_y , \hat{e}_z . From kinematics, the vertical displacement at the point P due to the blade motion can be given by

$$w_P = w_C - w'_C b + \phi_C a \quad (5.54)$$

where w_P = vertical displacement of the pitch link,

w_C = flap bending deflection at the point C ,

w'_C = slope at the point C

and ϕ_C = torsional deflection at the point C .

The imposition of the kinematic constraint corresponds to satisfying the condition

$$w_P = w_P^s \quad (5.55)$$

at all instants of time.

Due to this kinematic constraint, a reaction force F_P in the vertical direction is developed at the point P . In the response analysis, this force is transferred to the

blade as an external loading at the point C . The external loads (bending moment M_b^C , a torsional moment M_t^C and a concentrated force F_P^C) are given by

$$F_P^C = F_P \hat{e}_z \quad (5.56)$$

$$M_b^C = -F_P b \hat{e}_y \quad (5.57)$$

$$M_t^C = F_P a \hat{e}_x \quad (5.58)$$

where ‘ a ’ is the pitch horn chordwise offset and ‘ b ’ is the distance of the pitch link from the section AA along the length of the blade (Fig. 5.6).

The values of F_P^C , M_b^C and M_t^C are changing continuously so as to maintain the constraint mentioned in Eq. 5.55. The virtual work (δW_{link}) by F_P^C , M_b^C and M_t^C are given as

$$\delta W_{link} = F_P^C \delta w_C + M_b^C \delta w_{C,x} + M_t^C \delta \phi_C \quad (5.59)$$

5.2.8 Treatment of the Axial Degree of Freedom

In solving aeroelastic stability and response problems of rotor blades, the treatment of axial degree of freedom of the blade is an important consideration in order to properly account for the centrifugal and coriolis effects associated with the axial mode. In the literature, there are three different approaches, namely, (i) elimination of the axial degree of freedom, (ii) substitution technique and (iii) use of axial inextensionality criterion. The details of these approaches are given in Refs. [58, 120].

In the present formulation, the axial inextensionality criterion is used to eliminate the axial degrees of freedom from the equations of motion. In this technique, the axial strain at the elastic axis is set equal to zero. This is based on the physical consideration that the blade is axially very stiff. Thus, the axial strain at the elastic axis (Eq. A.32)

$$\bar{\epsilon}_{xx} = u_{,x} + \frac{1}{2}v_{,x}^2 + \frac{1}{2}w_{,x}^2 = 0 \quad (5.60)$$

With this assumption, the axial displacement u at any distance x from the root of the blade, is expressed in terms of the bending displacements (v and w) as:

$$u = - \int_0^x \frac{1}{2} (v_{,x}^2 + w_{,x}^2) dx \quad (5.61)$$

The time derivative of u is expressed as

$$\dot{u} = - \int_0^x (v_{,x} \dot{v}_{,x} + w_{,x} \dot{w}_{,x}) dx \quad (5.62)$$

Using Eqs. 5.61 and 5.62, u and its time derivative are expressed in terms of the bending deformations in the energy expressions. By this process, the axial degree of freedom is completely eliminated from the equations of motion.

5.2.9 Equations of Motion

Using the variations of energy expressions given by Eqs. 5.6, 5.16, 5.19, 5.21, 5.22, 5.49 and 5.59, Hamilton's principle can be written as

$$\int_{t_1}^{t_2} (\delta T - \delta U - \delta U_l - \delta U_f + \delta W_d + \delta W_e + \delta W_{link}) dt = 0 \quad (5.63)$$

Following the assumed mode method, the flap, lag and torsional deformations of the blade are expressed in terms of the generalised coordinates (r_i , p_i , q_i) and shape functions ($\bar{\varphi}_i$, $\bar{\phi}_i$, $\bar{\gamma}_i$) as

$$\begin{aligned} w(\xi, \tau) &= \sum_{i=1}^{n1} \bar{\varphi}_i(\xi) r_i(\tau) \\ v(\xi, \tau) &= \sum_{i=1}^{n2} \bar{\phi}_i(\xi) q_i(\tau) \\ \phi(\xi, \tau) &= \sum_{i=1}^{n3} \bar{\gamma}_i(\xi) p_i(\tau) \end{aligned} \quad (5.64)$$

where $\tau = \Omega t$, $\xi = \frac{x}{L}$

The equations of motion are derived by substituting Eqs. 5.64 in the energy expression and taking variations of the generalised coordinates. These equations are non-linear, coupled ordinary differential equations which can be expressed in symbolic form as

$$[\mathbf{M}] \{\ddot{\mathbf{Y}}\} + [\mathbf{C}] \{\dot{\mathbf{Y}}\} + [\mathbf{K}] \{\mathbf{Y}\} + \{\mathbf{P}_{NL}(\mathbf{Y}, \dot{\mathbf{Y}})\} = \{\mathbf{Q}(\mathbf{Y}, \dot{\mathbf{Y}}, \ddot{\mathbf{Y}})\} \quad (5.65)$$

where \mathbf{M} , \mathbf{C} and \mathbf{K} are the mass, damping and stiffness matrices, respectively. All the non-linear terms are included in \mathbf{P}_{NL} , the vector \mathbf{Q} , represents the generalised force associated with the aerodynamic loading.

5.3 Solution Procedure

The transient response of an isolated bearingless rotor blade to a step control input in pitch angle is obtained by simultaneously solving the non-linear coupled equations (Eqs. 5.65) and the inflow equation (Eq. 5.50) by numerical integration satisfying the kinematic constraint given in Eq. 5.55 at every time step.

The step-by-step procedure of the numerical technique is given below:

- (i) At $t = 0$, the point P of the pitch link (Fig. 5.6) is given a vertical displacement w_P^s .
- (ii) An initial value of the pitch link load $F_P(t)$ is assumed. Knowing F_P , the external loads (F_P^C , M_b^C and M_t^C) acting at the junction of the flexbeam and blade are calculated using Eqs. 5.56, 5.57 and 5.58.
- (iii) At each time step, knowing the value of $F_P(t)$, blade response and inflow, the following sub-iteration is performed to estimate the correct value of $F_P(t+\Delta t)$ satisfying the kinematic constraint, at time step $t + \Delta t$.
 - (a) The inflow velocity and blade response are calculated at $t + \Delta t$.
 - (b) The elastic deformations at the point C (w_C , $w_{C,x}$ and ϕ_C) are evaluated and

using Eq. 5.54, the vertical displacement of the pitch link w_P^d (corresponding to F_P) is calculated.

(c) F_P is incremented by an amount ΔF_P . For this value of $F_P + \Delta F_P$ at time t , inflow velocity and blade response are obtained for time $t + \Delta t$.

(d) Knowing the blade response, the modified displacement, w_P^{d1} (for $F_P + \Delta F_P$), of the pitch link is evaluated.

(e) The proper value of $F_P(t + \Delta t)$ is estimated by linear interpolation of w_P^d (for F_P) and w_P^{d1} (for $F_P + \Delta F_P$) to match w_P^* .

(iv) With the new value of $F_P(t + \Delta t)$ and the response of the blade and inflow at $t + \Delta t$, step (iii) is repeated until a steady state is reached.

It may be noted that the response of the blade and inflow at $t + \Delta t$ correspond to the constraint load $F_P(t)$ at time t .

To initiate the response calculation starting from time $t = 0$, an initial estimate of $F_P(0)$ is required. This value of $F_P(0)$ is estimated from static analysis considering isolated flap bending and twisting of only the flexbeam portion of the blade. The out of plane deflection of the flexbeam at the point C due to a concentrated load F_P and bending moment M_b^C applied at C is taken to be that of a tip-loaded cantilever, given by

$$w_C = \frac{F_P L_2^3}{3EI} + \frac{M_b^C L_2^2}{2EI}$$

Substituting M_b^C from Eq. 5.57, one obtains

$$w_C = \frac{F_P L_2^3}{3EI} - \frac{F_P b L_2^2}{2EI} \quad (5.66)$$

where L_2 and EI are the length and flexural rigidity of the flexbeam.

The slope of the flexbeam at the point C due to a concentrated load F_P and bending moment M_b^C is given by

$$w_{C,x} = \frac{F_P L_2^2}{2EI} - \frac{F_P b L_2}{EI} \quad (5.67)$$

The elastic twist ϕ_C at the point C due to the twisting moment M_t^C is given by

$$\phi_C = \frac{M_t^C L_2}{GJ} = \frac{F_P a L_2}{GJ} \quad (5.68)$$

where GJ is the torsional rigidity of the flexbeam.

Combining Eqs. 5.66, 5.67 and 5.68, the following relation between w_P^s and F_P is obtained

$$w_P^s = \left(\frac{F_P L_2^3}{3EI} - \frac{F_P b L_2^2}{2EI} \right) - \left(\frac{F_P L_2^2}{2EI} - \frac{F_P b L_2}{EI} \right) + \frac{F_P a L_2}{GJ} \quad (5.69)$$

From Eq. 5.69, an initial estimate of F_P can be obtained for a given value of w_P^s .

5.4 Results and Discussion

The transient response analyses are carried out for two types of rotor blade configurations, namely, (i) hingeless blade and (ii) bearingless blade. In both cases, a step pitch input is applied to the blade operating in the hover condition simulating a wind tunnel test. The transient response analysis of a hingeless blade is carried out with the following objectives:

(i) to validate the equations of motion and the solution procedure

and

(ii) to compare qualitatively the dynamic response characteristics of hingeless and bearingless rotor blades. Such a comparison will provide a useful insight about the behaviour of these two different rotor configurations.

5.4.1 Hingeless Rotor Blade

For the hingeless blade configuration, the formulation of equations of motion essentially follows the same procedure outlined in Sec. 5.2. The terms involving the strain energy

of the elastomer (Eqs. 5.18 and 5.20) and the work done by the damping element of the elastomer (Eq. 5.22) are not included in the Hamilton's principle (Eq. 5.63). Since the pitching motion to the blade is given at the root (Fig. 1.2a), no kinematic constraint (Eq. 5.54) is imposed on the blade.

The assumed mode shapes (Eqs. 5.64) for bending and torsional deflections are the undamped and uncoupled free vibration modes of the rotating blade. In the response analysis, the six modes, namely, three modes in flap, two modes in lag and one mode in torsion are considered. The number of blades in the rotor system is taken as $N = 4$. The data used for numerical calculations are given in Table 5.1.

A step input of 0.1 rad ($\theta_{in} = 0.1$ rad) is provided at the blade root. The blade and inflow equations are solved simultaneously by a numerical integration routine (NAG) based on Runge-Kutta-Marson algorithm. To check the validity of the time step, time integration was carried out with three time steps viz., $\Delta t = 0.0015$ s, $\Delta t = 0.0035$ s and $\Delta t = 0.006$ s (in real time). In all the three cases, the results are found to converge to the same values. In all the subsequent computations, a time step of $\Delta t = 0.003$ s is used. The response calculations are continued till the steady state condition is reached. The results of the transient response are shown in Figs. 5.7a-c. In Fig. 5.7a, the non-dimensional flap response at the blade tip (w_{tip}) is plotted against non-dimensional time (τ). An overshoot in the flap response is observed the initial phase of the response. Subsequently, the flap response reaches the steady state value 0.019. The maximum value of overshoot is found to be (0.055), which is approximately 2.3 times the steady state value. This kind of overshoot in the transient response in the flap mode of a rotor blade was also observed in the experimental results reported in Ref. [106].

The variation of the lag tip response (v_{tip}) with τ is shown in Fig. 5.7b. Since aerodynamic damping in the lag mode is small, the response exhibits a large amplitude

of oscillation with a very low decay rate. Figure 5.7c shows the variation of torsional response (ϕ_{tip}) at the blade tip. The steady state value of the elastic twist is found to be -0.005 rad. with a very small overshoot during the initial phase. The variation of inflow velocity shown in Fig. 5.8 indicates that it starts from zero and reaches a steady state value 0.048 with a little overshoot. The thrust generated by the rotor, shown in Fig. 5.9, behaves like the flap response. The maximum value of thrust coefficient is 0.0057 which is 2.28 times the steady state value.

The variation in the maximum thrust overshoot with respect to the rate of pitch input has also been studied. The transient response calculations are performed with four different rates of blade pitch input. The initial rate of pitch inputs are 20 deg/s, 48 deg/s, 120 deg/s and 200 deg/s; after reaching a value of 0.1 rad. the pitch input is held constant. In each case, the ratio of the maximum ($C_{T_{max}}$) to the steady state values of rotor thrust (C_{T_s}) is obtained. Figure 5.10 shows the variation of $C_{T_{max}}/C_{T_s}$ Vs. rate of pitch input. It is seen that initially the ratio ($C_{T_{max}}/C_{T_s}$) increases with the blade pitch rate and reaches a steady state value 2.37 at high pitch rates.

Carpenter and Fridovich [106] carried out experiments on the transient response of a rigid rotor blade with varying pitch rate inputs. The blade is allowed to undergo only flap motion. They correlated their analytical results to the experimental results. (It may be noted that in Ref. [106], Carpenter *et al.* have not provided any blade data). Their experimental results are shown in Fig. 5.11 where thrust overshoot for a blade pitch rate of 200 deg/s is about 2 times the steady state value. In the present analysis, for the same blade pitch rate (200 deg/s), the overshoot is found to be about 2.37 times the steady state value. This difference in magnitude may be attributed to the differences in the blade model. The qualitative nature of the present results conforms with the experimental observation, thereby validating the blade equations, inflow model and the solution procedure.

5.4.2 Bearingless Rotor Blade

A thorough investigation is carried out to study the influence of the non-linear elastomer and kinematic constraint on the transient response characteristics of an isolated bearingless rotor blade to a step input in hover condition simulating a wind tunnel test. The parameters of the elastomer are given in Table 2.1. Since the transient response of the bearingless rotor blade is compared with that of the hingeless blade, the same blade data is used. It is important to point out that in a practical bearingless rotor blade configuration, the flexbeam and blade properties will be different. In this thesis, it is assumed that the blade and the flexbeam have same uniform properties. The reasons for this assumption are two fold; (i) practical blade data is not available, (ii) by considering uniform and same properties for both the hingeless and bearingless rotor blades, one can obtain a good physical insight on the effects of non-linear elastomer and kinematic constraint on the aeroelastic behaviour of the rotor blade.

Even though uniform properties have been assumed for the flexbeam and blade, the natural frequencies of the rotating blade in flap, lag and torsional modes are representative of a realistic rotor blade configuration. Therefore, it is expected that this study will provide useful and meaningful conclusions.

The uncoupled rotating mode shapes in flap, lag and torsion are used as the assumed modes. In determining the uncoupled rotating mode shapes, the effect of the elastomer is included as a linear spring element between the blade and torque tube; and the kinematic constraint introducing pitch-flap coupling is neglected. In the transient response analysis, six modes have been considered which correspond to three modes in flap, two modes in lag and one mode in torsion. Following the solution procedure outlined in Sec. 5.3, the transient response of a soft-in-plane rotor blade is obtained numerically incorporating a time-step of 0.003 s. These numerical results are presented

below in three sections.

- (i) In the first section, the blade response and the root loads are discussed for a particular configuration treated as the baseline configuration of the rotor blade.
- (ii) The second section focusses on the influence of the locations of the elastomer and torque tube on the transient response characteristics of the blade.
- (iii) The third section is devoted to the effect of the location of pitch link point P (defined by parameters a and b) on the transient response of the blade. When the parameter a is positive, the pitch link is in the leading edge side of the blade and when a is negative, it is in the trailing edge side of the blade. The parameter b represents the distance of the pitch link from the junction of blade-flexbeam-torque tube as shown in Fig. 5.6.

Since the blade pitch is provided by moving the pitch control point P up or down, the control input chosen for the transient response is the step displacement w_P^s at the point P in the \hat{e}_z direction.

5.4.2.1 Baseline Configuration

For the baseline configuration, the location of the elastomer and torque tube are set at $\xi_1 = 0.10$ and $\xi_2 = 0.25$ where ξ_1 and ξ_2 are shown in Fig. 5.6. The pitch link is considered to be located at the leading edge side of the blade. The location of the pitch control point P , defined by the parameters a and b are set equal to $a = 0.05$ and $b = 0.15$. The pitch link is given a step displacement $w_P^s = 0.00624$ in \hat{e}_z direction. In Figs. 5.12a-c, the tip responses of the blades in flap (w_{tip}), lag (v_{tip}) and torsional (ϕ_{tip}) modes, respectively, are plotted as functions of the non-dimensional time τ . The flap response of the baseline rotor blade reaches a steady state value 0.025 as shown in Fig. 5.12a. It is interesting to note that unlike the flap response of a hingeless blade (Fig. 5.7a), the flap response of a bearingless blade does not exhibit any dynamic over-

shoot even though there exists initial oscillatory behaviour. The qualitative difference between the flap response of these two types of blade configurations may be attributed to the presence of multiple load path and kinematic constraint in the bearingless blade.

As indicated in Fig. 5.12b, the tip response in the lag mode (v_{tip}) shows an oscillatory behaviour with a mean value of $(v_{tip})_{mean} = -0.007$. The amplitude of oscillation in the lag mode is small in comparison to that of a hingeless blade (Fig. 5.7b). The reduction in the response amplitude can be attributed to the presence of the elastomer damping in addition to the aerodynamic damping.

The torsional response deformation of the bearingless rotor blade at any cross-section is defined by the total pitch angle which is the sum of the elastic twist of the blade and the elastic twist at the end of the flexbeam produced by the control input w_p^* . Figure 5.12c shows the variation of the tip response (ϕ_{tip}) in the torsional mode as a function of τ . It is observed that the torsional response reaches a steady value 0.13 beyond time $\tau = 25$. The presence of higher frequencies is observed in the torsional response. The variation of the inflow velocity (λ) with τ is shown in Fig. 5.13. The inflow velocity for bearingless blade configuration, as compared to that of the hingeless blade configuration (Fig. 5.8), takes longer time to reach the steady state value and no overshoot is observed.

The variation of the constraint force F_P (acting at the point P of the pitch link) as a function of τ is shown in Fig. 5.14. The force F_P attains the steady state value of 0.037 without any overshoot. The qualitative nature of the curve is same as that of the torsional response, shown in Fig. 5.12c.

The loads at the flexbeam root are obtained by integrating the distributed forces and moments over the span of the blade. The variation of different root loads are shown in Figs. 5.15-5.19. It is seen from Fig. 5.15, that the out of plane root shear force exhibits an overshoot of 1.3 times the steady state value 0.0087. In addition,

it undergoes oscillation of moderate magnitude before reaching the steady state. The same figure also represents the response of rotor thrust coefficient (C_T) in a different scale. It is interesting to observe that unlike hingeless rotor, in this case, even though the flap response does not show any overshoot, rotor thrust exhibits overshoot (Fig. 5.15). Figure 5.16 shows the out of plane bending moment (flap bending) of the blade. No appreciable overshoot is observed in this case. For the sake of completeness, the variation of other root loads are shown in Figs. 5.17-5.19. The in-plane root shear and root moment exhibit high frequency content in their response, as shown in Figs. 5.17 and 5.18, respectively. The torsional moment shows a very mild oscillatory behaviour as shown in Fig. 5.19.

5.4.2.2 Influence of Varying Control Input w_p^s

The transient response of the blade for the baseline configuration is obtained with different values for the step control inputs. These values are $w_p^s = 0.00624$, 0.00936 (1.5×0.00624) and 0.01248 (2.0×0.00624). The tip responses of the blade in flap, lag and torsion, corresponding to these inputs are shown in Figs. 5.20a-c. It is evident from the figures that irrespective of the magnitude of the input, the qualitative nature of the response remains same for all the modes. The steady state responses in the flap mode for the three input values are 0.027, 0.042 and 0.058, respectively (Fig. 5.20a). It is evident from the values that the steady state response in the flap exhibits a mild non-linear characteristics with respect to change in input values. Similar mild non-linear behaviour of the steady state responses in lag and torsional modes with respect to control pitch input w_p^s are observed in Figs. 5.20b and 5.20c.

5.4.2.3 Influence of Elastomer Location (ξ_1, ξ_2)

In this section, the influence of the elastomer and torque tube locations (ξ_1 and ξ_2) on the transient response characteristics of the rotor blade is examined. The location of the control point P of the pitch link is set at $a = 0.05$ and $b = 0.15$. Three different torque tube locations ($\xi_2 = 0.20, 0.25$ and 0.30) are considered. For each value of ξ_2 , three different elastomer locations ($0.02, 0.04$ and 0.10) are considered. The control step input $w_P^* = 0.00624$ is same for all the cases.

In Fig. 5.21, the transient responses in flap, lag and torsional modes are shown for $\xi_2 = 0.20$ with different locations of the elastomer ($\xi_1 = 0.02, 0.04$ and 0.10). The qualitative nature of the response in each case is found to be the same. Out of three configurations considered, the steady state flap and torsional responses are maximum for $\xi_1 = 0.10$. The amplitude of oscillation in the lag mode is also maximum for $\xi_1 = 0.10$. Since the distance between the elastomer and torque tube locations is least for this configuration, the elastomer undergoes least deformation thus providing least damping and stiffness to the system. Therefore, the responses exhibit higher values.

Figures 5.22 and 5.23 present the response results corresponding to torque tube locations $\xi_2 = 0.25$ and $\xi_2 = 0.30$, respectively. No appreciable change is observed in the qualitative nature of the blade responses for these configurations; but the magnitude of the response is reduced with the increase in ξ_2 as can be seen by comparing the steady state values in Figs. 5.21-5.23. Comparing the lag responses for the blades with three different torque tube locations $\xi_2 = 0.20, 0.25$ and 0.30 (Figs. 5.21b, 5.22b and 5.23b), it is observed that the amplitude of oscillation is less for the combinations $\xi_1 = 0.04, \xi_2 = 0.25$, and $\xi_1 = 0.10, \xi_2 = 0.25$ as compared to those for other configurations. Based on the numerical values of these results, it can be stated that the influence of the elastomer and torque tube locations on the transient response in the lag mode of

the blade is more significant compared to flap and torsional response..

5.4.2.4 Influence of pitch link location (a , b)

A parametric study is conducted to examine the effect of geometric parameters a and b on the transient response characteristics of the blade under different pitch control inputs w_p^s . Towards this end, four different values of the parameter a are chosen. These are: $a = -0.02, 0.02, 0.03$ and 0.05 . The parameter b is also varied with $b = 0.10, 0.15$ and 0.23 . The elastomer and torque tube locations are set at $\xi_1 = 0.10$ and $\xi_2 = 0.25$.

The transient response characteristics for the configuration $a = 0.03$ and $b = 0.25$ are shown in Figs. 5.24a-c for three different values of control input $w_p^s = 0.00507, 0.0076$ and 0.01014 . Comparing these results with those shown in Figs. 5.20a-c, it is observed that the transient response characteristic of the blade in all the three modes is similar to that for the baseline configuration ($a = 0.05, b = 0.15$). The results obtained for other combinations of a and b (not presented for conciseness) reveal that the qualitative nature of the blade response remains the same so long as the pitch link is located at the leading edge side.

A comparison of the transient response characteristics with the pitch link at the leading ($a = 0.02$) and the trailing ($a = -0.02$) edge sides is shown in Figs. 5.25-5.27. The parameter b is set equal to 0.15 . The magnitude of the control input w_p^s is identical for the two cases. For the leading edge configuration, the control input is a positive step displacement $w_p^s = 0.00383$ (\hat{e}_x direction) and for the trailing edge side the control input is set $w_p^s = -0.00383$ ($-\hat{e}_x$ direction), resulting in a positive pitch input for the blade in both cases.

The transient responses in the flap (w_{tip}) and lag (v_{tip}) modes are shown in Figs. 5.25 and 5.26, respectively. From Fig. 5.25, it is interesting to note that the nature

of the flap response changes drastically depending on the sign of the value of a . The flap response of the blade with the trailing edge configuration exhibits an overshoot with a value of $(w_{tip})_{max} = 0.045$ which is about three times the steady state value of $(w_{tip})_s = 0.016$. In contrast, no overshoot is observed for the leading edge configuration. But the steady state values in both cases are about the same (around 0.017).

The lag response (Fig. 5.26) at the tip, for the trailing edge configuration shows a large variation with a mean value $(v_{tip})_{mean} = -0.007$. The variation for the leading edge configuration is considerably less with a mean value $(v_{tip})_{mean} = -0.0035$.

The torsional response of the blade is represented by the response at the blade section at a distance $0.75L$ from the root. This particular blade section is usually chosen as the typical section for aerodynamic loads. It can be seen from Fig. 5.27 that the torsional response $(\phi_{0.75})$ for the trailing edge configuration exhibits an overshoot of about one and half times the steady state value 0.10. The torsional response for the leading edge configuration reaches a steady state value 0.075 with no overshoot. It is important to note, that for the same control input, the blade experiences a larger pitch deformation $(\phi_{0.75})$ for the trailing edge than that for the leading edge configuration.

Figure 5.28 shows a substantial difference in the variation in inflow for these two configurations. For the trailing edge configuration, the inflow reaches a steady state value $\lambda = 0.05$ which is higher than that of the leading edge configuration which is $\lambda = 0.038$.

The magnitudes of the pitch link load ($|F_P|$) are plotted as a function of time (τ) for both the configurations in Fig. 5.29. The response for the trailing edge case exhibits a rapid rise before reaching a steady state value $(F_P)_s = 0.078$. On the other hand, the pitch link load for the leading edge configuration gradually attains the steady state value $(F_P)_s = 0.06$. It may be noted that the sign of the pitch link load is negative in case of trailing edge pitch link configuration of the blade.

In order to highlight the difference between the two configurations, the root loads have also been evaluated. These are shown in Figs. 5.30-5.34. The variation of the out of plane root shear as a function of time is shown in Fig. 5.30. Both the blade configurations exhibit overshoot. But for the trailing edge configuration, the overshoot is very large, *i.e.*, about five times the steady state value 0.006. For the leading edge configuration, the overshoot is about one and half times the steady state value 0.004. This steady state value of the out of plane root shear for the trailing edge configuration is 1.5 times that for the leading edge configuration. This increase is due to the effect of increased torsional response and inflow velocity as shown in Figs. 5.27 and 5.28, respectively. The out of plane root moment shown in Fig. 5.31, indicates that the overshoot for the trailing edge configuration is about four times the steady state value, while the overshoot for the leading edge is very small (about 1.1 times).

The variation of the in-plane root shear and moment are shown in Figs. 5.32 and 5.33, respectively. For the trailing edge configuration, the response seems to contain high frequency components. The amplitudes of the loads is much larger for the trailing edge configuration as compared to that for the leading edge configuration.

The torsional root moments for both configurations are shown in Fig. 5.34. There is a rapid rise in the torsional moment for the trailing edge at the initial stage whereas the rise is gradual for the leading edge configuration. The nature of the response is very similar to the torsional response of the blade as shown in Fig. 5.27. Based on these results it can be stated that there is a qualitative change in the nature of the response depending on whether the pitch link is at the leading or trailing edge.

It had been observed that for certain trailing edge configurations, the blade response did not converge. To highlight this behaviour, the blade response for the two cases corresponding to (i) leading edge configuration with $a = 0.03$ and $b = 0.23$, and (ii) trailing edge configuration with $a = -0.03$ and $b = 0.23$, have been evaluated. Control

input $w_p^s = 0.00525$ and $w_p^s = -0.00525$ are applied for the leading and trailing edge configurations, respectively. The transient response in the flap, lag and torsional modes are shown in Fig. 5.35 for both these configurations. The blade response reaches a steady state value for the leading edge pitch link configuration, but the response diverges for the trailing edge configuration indicating instability.

5.4.2.5 Aeroelastic Coupling

Aeroelastic couplings have a strong influence on the response and stability characteristics of a rotor blade. In the case of kinematic pitch-flap and pitch-lag couplings, quantitative measure of the couplings are defined based on the orientation of the lag or flap hinges [113]. In hingeless and bearingless rotors, due to the absence of hinges. It is difficult to quantify how much of blade torsional motion is due to elastic twist and how much is due to aeroelastic pitch-flap and pitch-lag couplings. Therefore the quantitative measure of the couplings have to be defined based on the blade response. Since the response depends on the blade loading, the couplings will also be dependent on the blade loading. In this section, using the steady state tip response of the blade, an attempt is made to identify a measure of the aeroelastic coupling present in the bearingless rotor blade system.

In Ref. [48] Hodges and Ormiston proposed a mathematical expression to measure the equivalent kinematic pitch-flap and pitch-lag couplings generated in elastic blades. Following this idea, the pitch-flap (k_β) and pitch-lag coupling (k_ζ) are defined as

$$k_\beta = \left(\frac{\phi_{0.75}}{w_{tp}} \right)_s \quad (5.70)$$

$$\text{and } k_\zeta = \left(\frac{\phi_{0.75}}{v_{tp}} \right)_s \quad (5.71)$$

where subscript s denotes the steady state response and

$\phi_{0.75}$ = the steady state value of the torsional response at $0.75L$ of the blade.

w_{tip} = the steady state tip response in the flap mode,

and v_{tip} = the steady state response in the lag mode.

Since the convergence in lag mode is very slow, the steady state value $(v_{tip})_s$ is taken as the mean value of the oscillatory lag response. This mean value is computed from the oscillatory lag response of the blade. The influence of the geometric parameters a , b and the magnitude of the control input on the aeroelastic coupling measures, defined by Eqs. 5.70 and 5.71, are evaluated. The step input of the control link displacement w_p^s is varied within a range of $w_p^s = -0.00255$ to 0.01248 . The elastomer location is set at $\xi_1 = 0.10$ and $\xi_2 = 0.25$. The values of the parameter a are chosen as $a = -0.02, 0.02, 0.03$ and 0.05 . In addition, three different values of the parameter b are also considered: $b = 0.10, 0.15$ and 0.23 .

The steady state response of the blade are obtained for several combinations of the parameters. In each case, the aeroelastic couplings are calculated using the steady state response of the blade. The numerical values of the couplings as a function of control input and parameter b are presented in Tables 5.2 and 5.3. Table 5.2 presents the results corresponding to the case $a = 0.03$ and Table 5.3 provides the results for the case $a = 0.05$. It is seen from Table 5.2 that with increase in the control input w_p^s , the magnitudes of the pitch-flap (k_β) and pitch-lag (k_ζ) couplings decrease. The reduction in the magnitude is more prominent in the case of pitch-lag coupling than for pitch-flap coupling. A similar behaviour is also observed for the case $a = 0.05$ as shown in Table 5.3. A pictorial representation of the variation of the aeroelastic couplings are also presented in 3-D plots. (Figures 5.36 and 5.37 correspond to the case $a = 0.3$ and Figs. 5.38 and 5.39 pertaining to the case $a = 0.05$.)

A comparison of the aeroelastic coupling measures between the leading and the trailing edge configurations is presented in Table 5.4. The two configurations are (i)

$a = -0.02$, $b = 0.15$, and (ii) $a = +0.02$, $b = 0.15$. The aeroelastic couplings are evaluated for three values of the control inputs w_P^* . It is observed from Table 5.4 that for both configurations the magnitudes of pitch-flap and pitch-lag couplings decrease with increasing control input. For both configurations, the reduction in pitch-flap coupling is found to be more pronounced than the pitch-lag coupling. In addition, the reduction in coupling values seems to be more for the trailing edge configuration than the leading edge configuration. While the pitch-flap coupling for trailing edge configuration is higher than the leading edge configuration, the magnitude of the pitch-lag coupling is lower for trailing edge configuration than the leading edge configuration. The reason for the difference in aeroelastic couplings for these two configurations may be attributed to the change in the direction of the constraint force and moments with a change in the sign of parameter a given in Eq. 5.54 and 5.58.

The dependence of pitch-flap and pitch-lag coupling with control input can be attributed to the non-linear elastomer and other non-linear effects in the blade dynamics. The results clearly indicate that the aeroelastic coupling in bearingless main rotor is dependent on the operating condition of the blade and also on the other geometric configuration.

5.5 Summary

A suitable numerical technique has been formulated to study the transient response of an isolated bearingless rotor blade to a step control pitch input. The blade is assumed to undergo coupled flap-lag-torsional deformation in hovering condition. A time varying inflow model (based on the dynamic inflow model) has been used for the analysis. The expressions for aerodynamic loads are not obtained explicitly, rather they are derived in an implicit formulation. The study is carried out for different locations of the

elastomer and pitch link. The transient response results of the bearingless rotor blade are compared with those of the hingeless blade. The comparison is made to highlight the difference in their response behaviour. It is noticed that the transient response characteristics of a bearingless blade depends on the pitch link locations. In particular, it is observed that the blade response with trailing edge pitch link configuration is significantly different from that of a leading edge configuration. For certain trailing edge configurations, the blade exhibits a divergence transient response indicating instability. A quantitative measure of the aeroelastic couplings (pitch-flap, pitch-lag), based on the steady state response has been evaluated and their dependence on the geometric configurations and control pitch input has been identified.

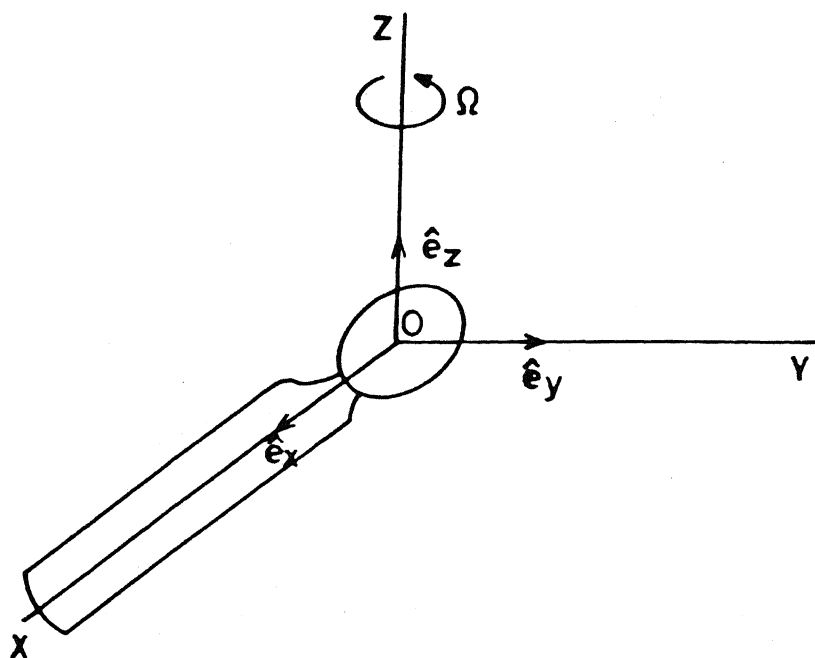


Fig. 5.1 Hub fixed rotating coordinate system.

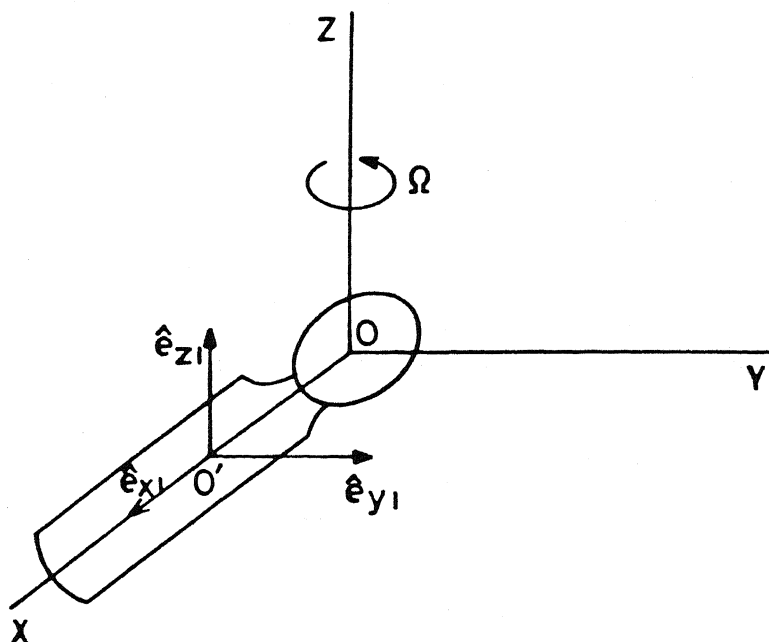


Fig. 5.2 Undeformed cross-section fixed rotating coordinate system.

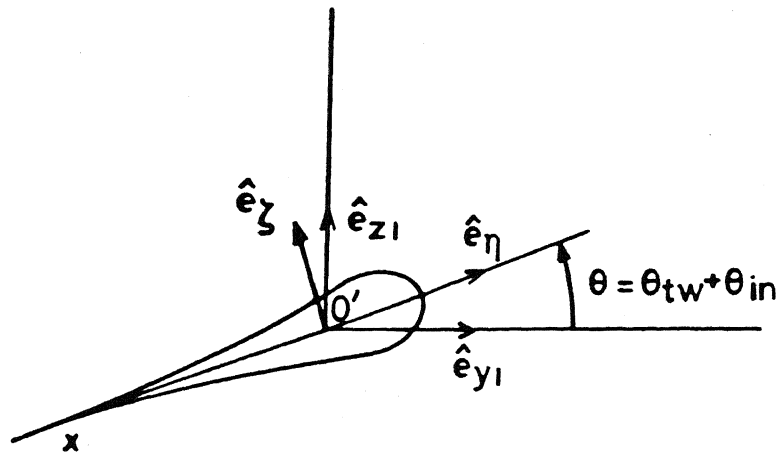


Fig. 5.3 Undeformed curvilinear cross-sectional coordinate system.

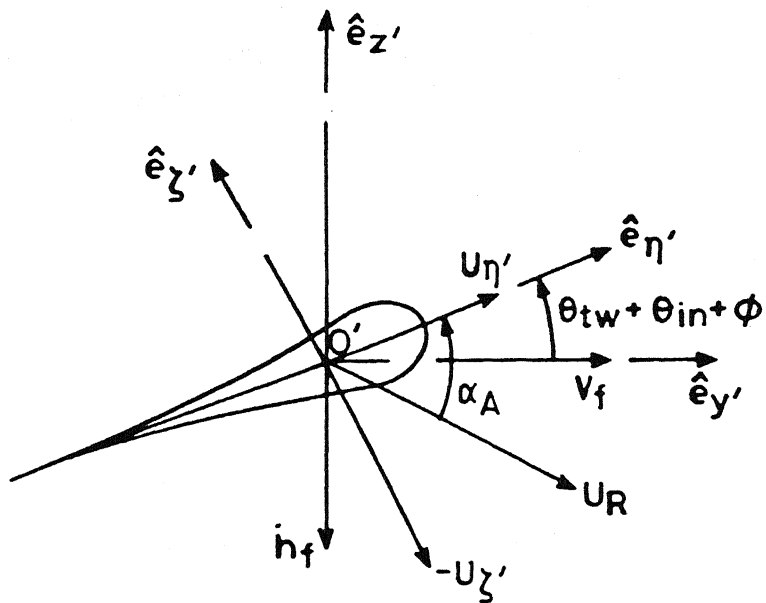


Fig. 5.4 Deformed cross-sectional coordinate system and components of blade velocity.

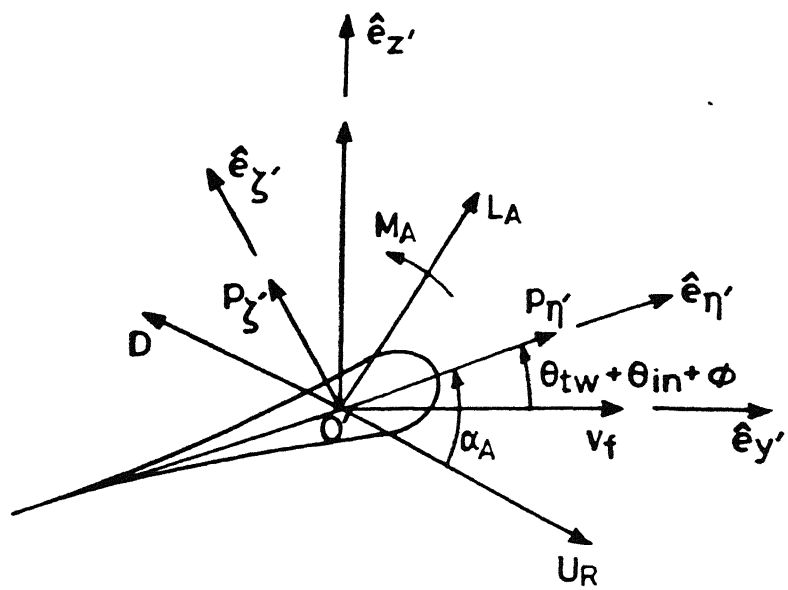


Fig. 5.5 Components of sectional aerodynamic forces.

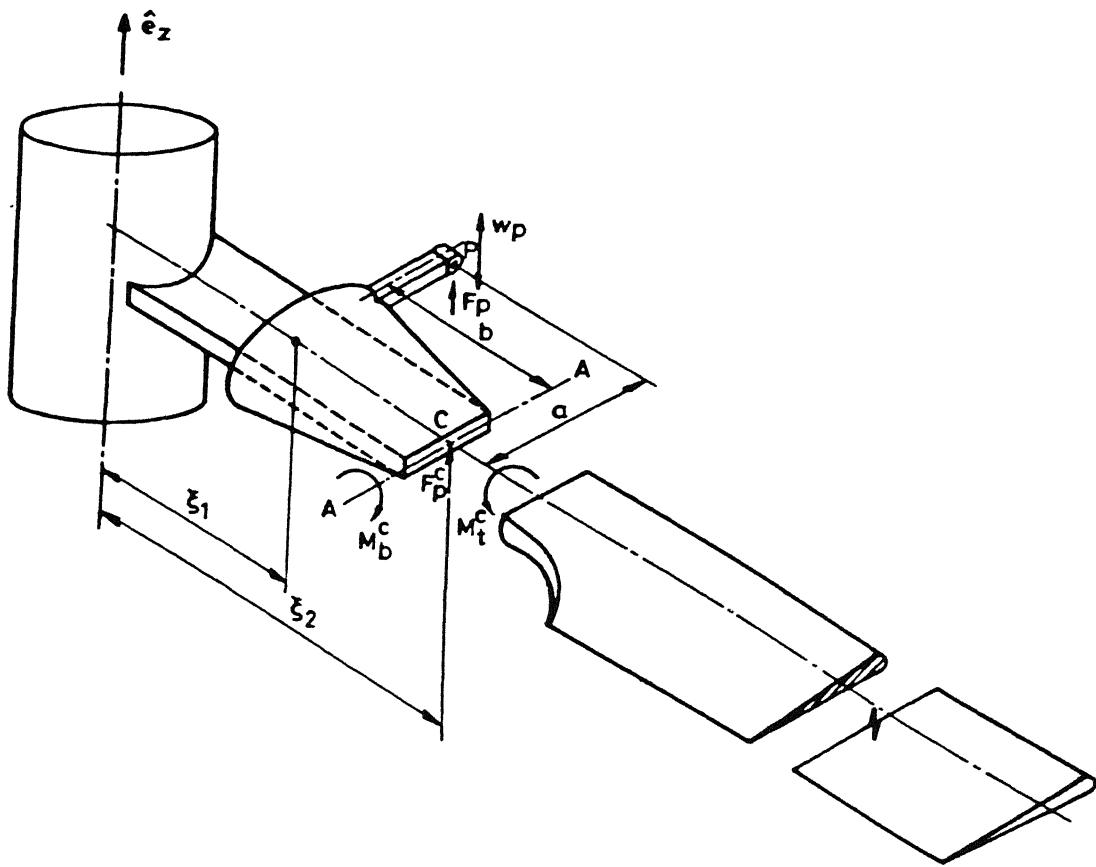


Fig. 5.6 Bearingless rotor blade with pitch link at the leading edge side.

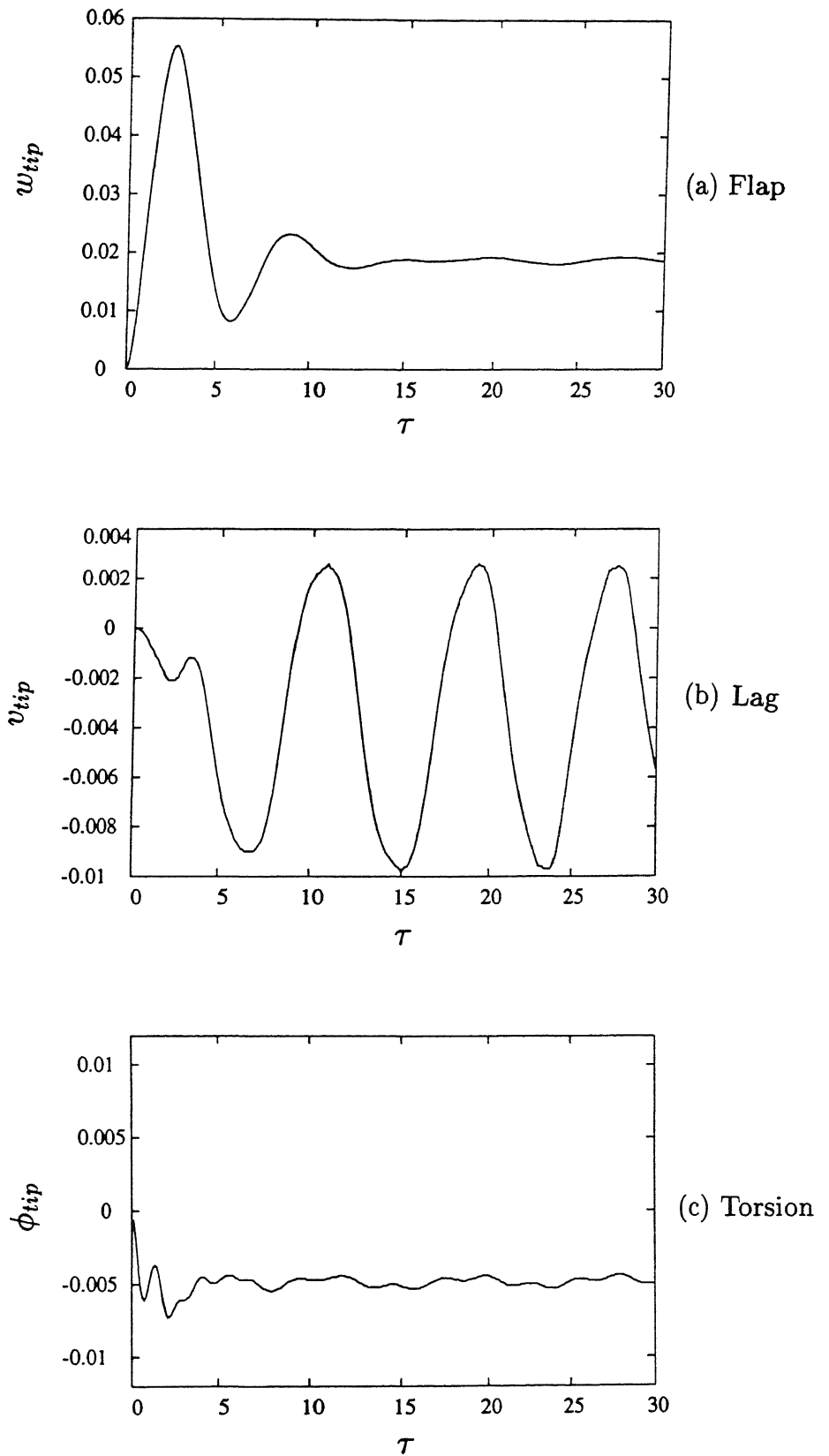


Fig. 5.7 Hingeless blade response to a step pitch input ($\theta_{in} = 0.1\text{rad}$).

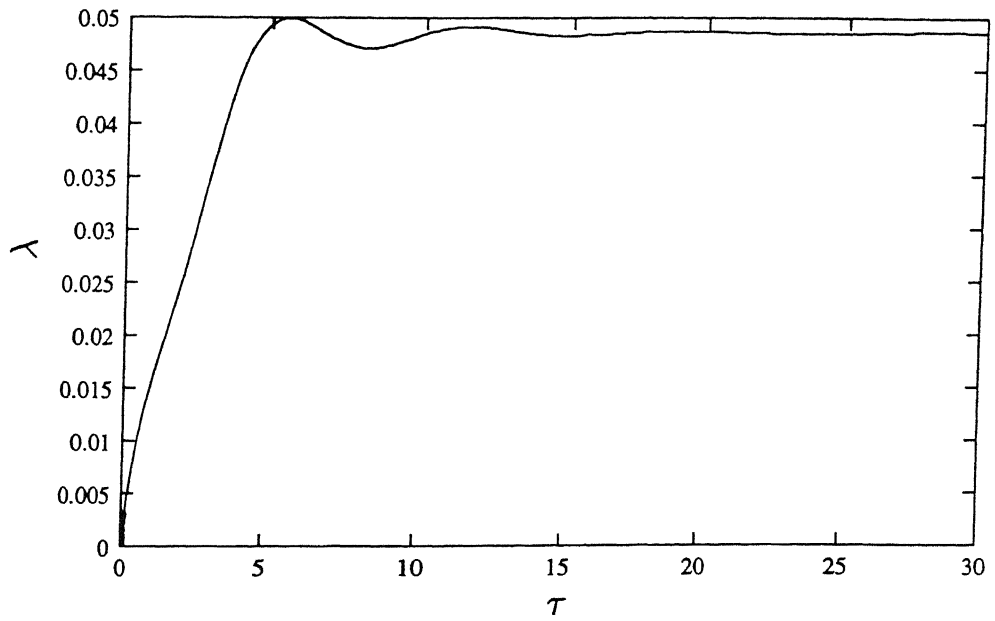


Fig. 5.8 Variation of inflow for hingeless blade to a step pitch input ($\theta_{in} = 0.1\text{rad}$).

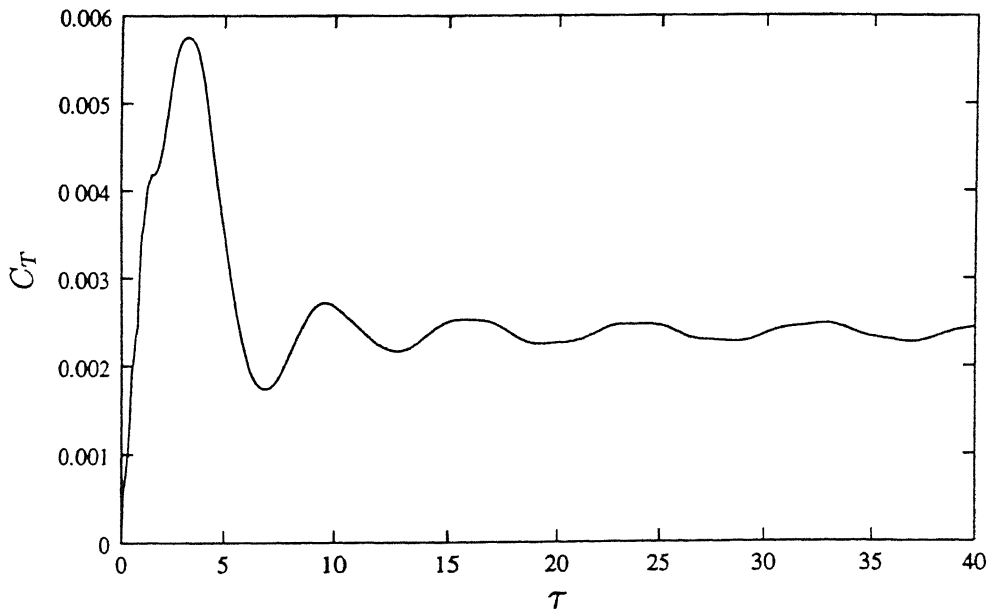


Fig. 5.9 Variation of thrust coefficient for hingeless blade to a step pitch input ($\theta_{in} = 0.1\text{rad}$).

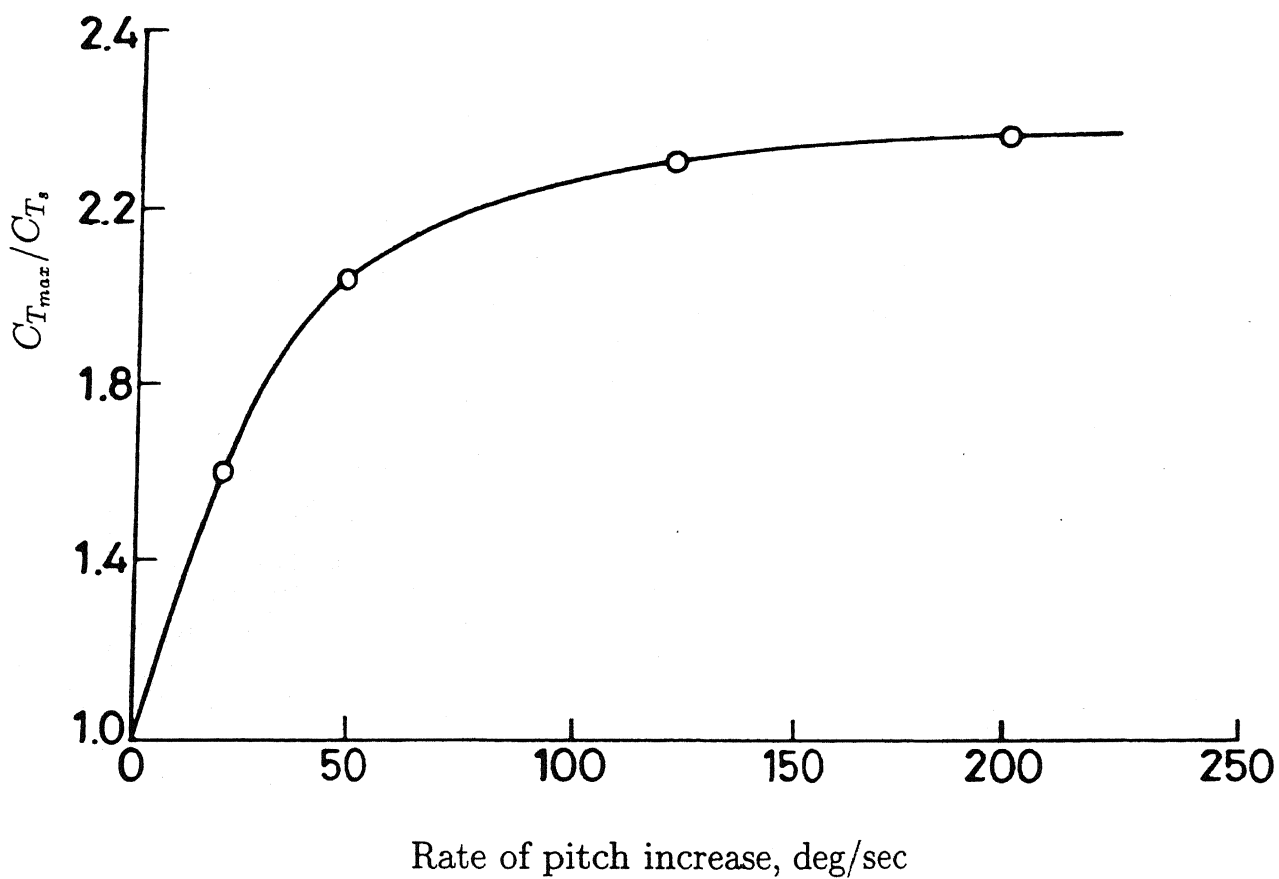


Fig. 5.10 Variation of $C_{T_{max}}/C_{T_s}$ for hingeless blade for various rates of pitch input.

○ different pitch rates.

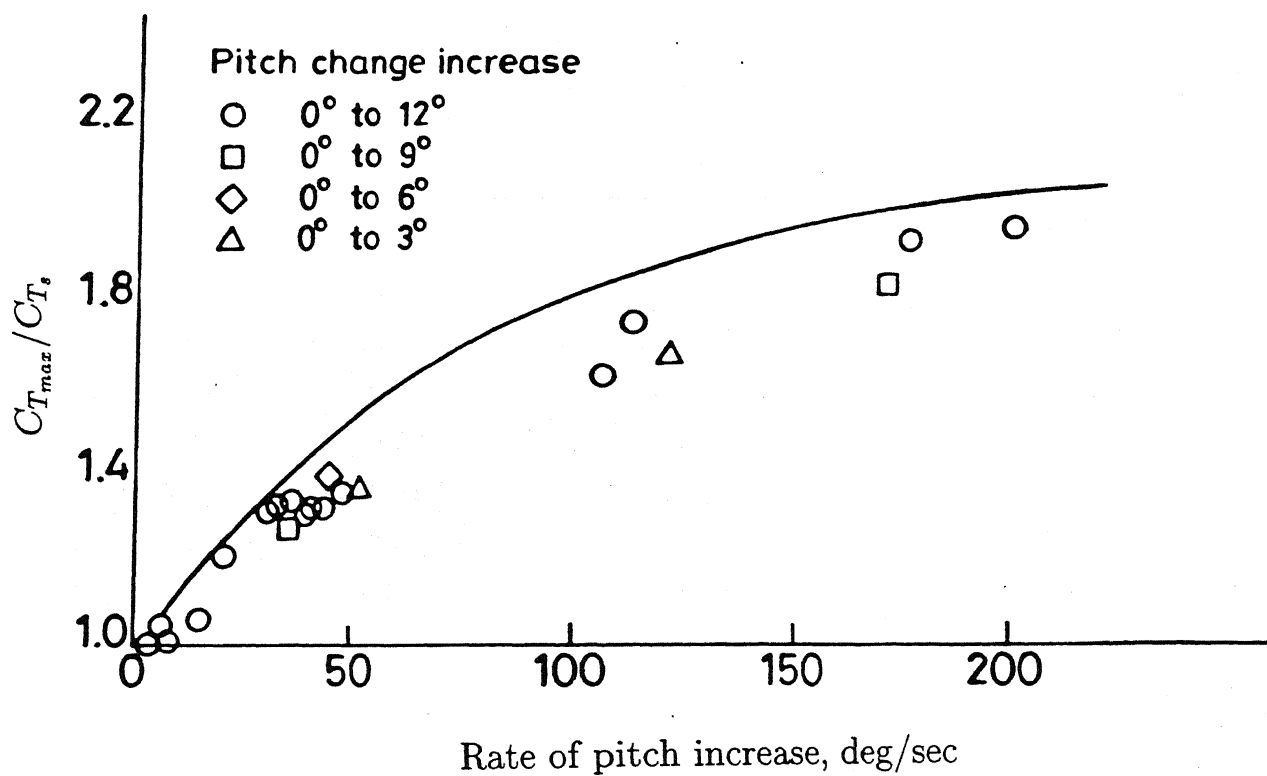


Fig. 5.11 Comparison of experimental and calculated ratios of $C_{T_{max}}/C_{T_s}$ for hingeless blade for various rates of pitch input.

— calculated curve; □, ○ △, Experimental data. (Taken from Ref. [106]).

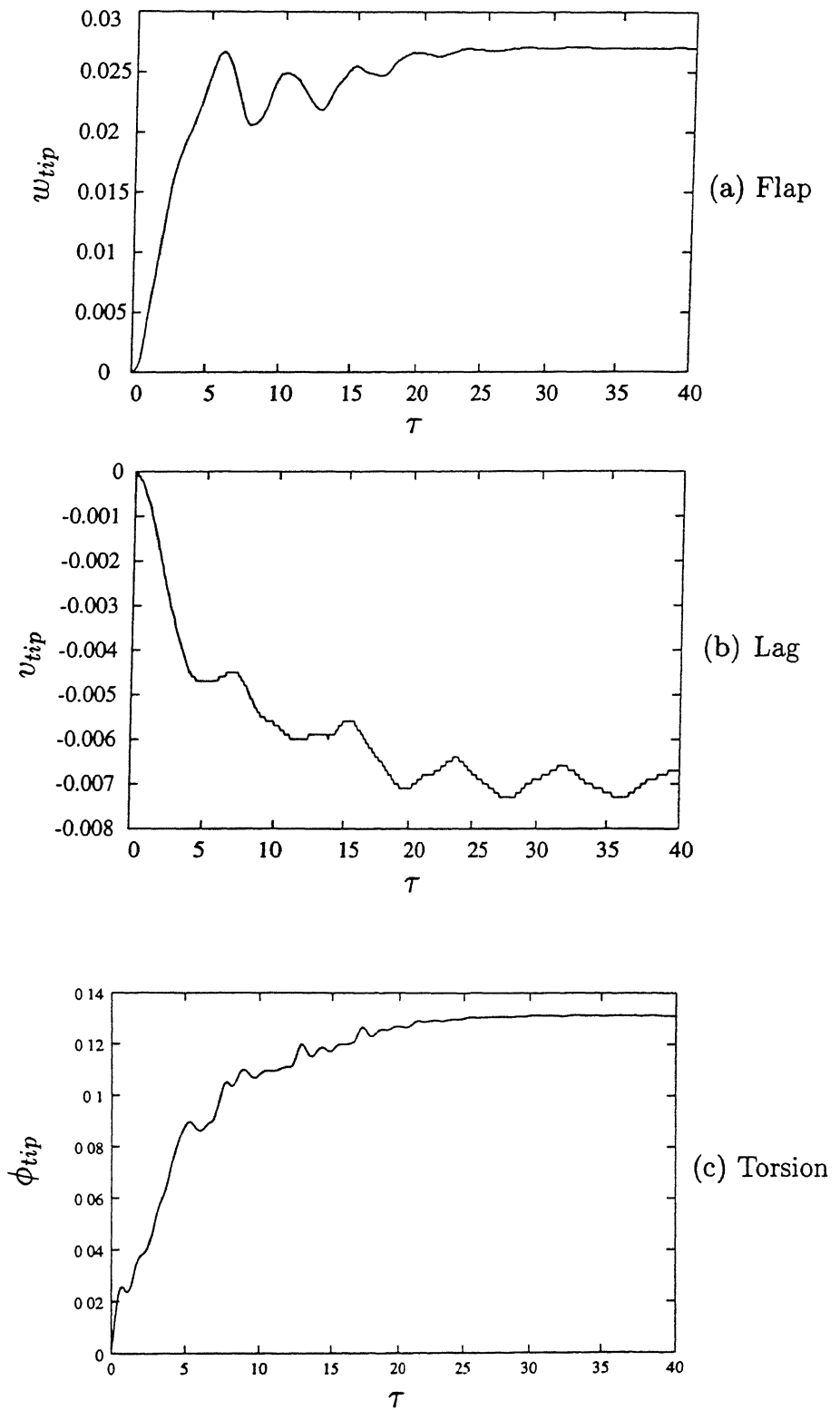


Fig. 5.12 Bearingless blade response to a step control pitch input ($w_P^s = 0.00624$).

Configuration: $\xi_1 = 0.10$, $\xi_2 = 0.25$ and $a = 0.05$, $b = 0.15$.

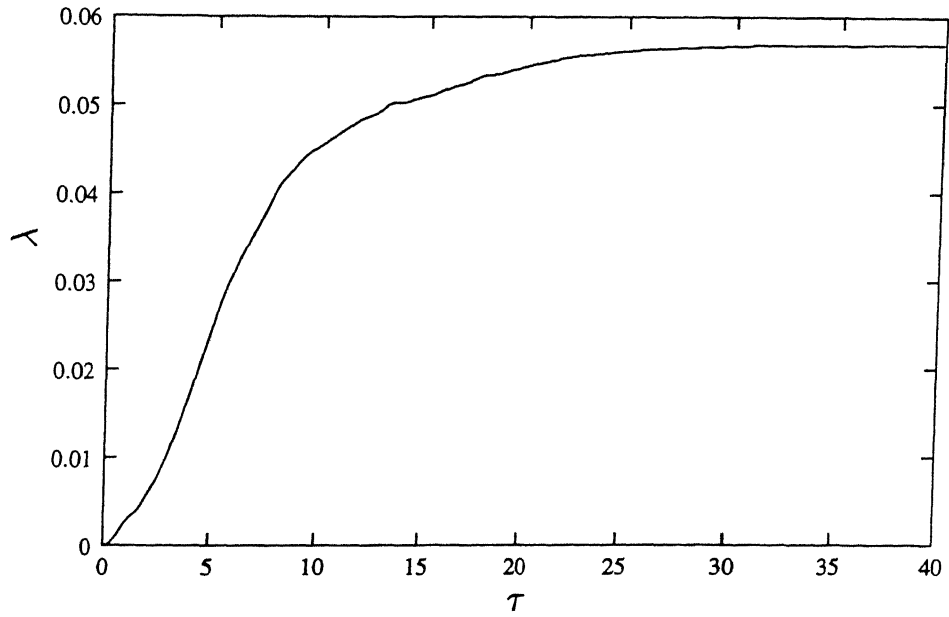


Fig. 5.13 Variation of inflow for bearingless blade to a step control pitch input ($w_p^s = 0.00624$).

Configuration: $\xi_1 = 0.10$, $\xi_2 = 0.25$ and $a = 0.05$, $b = 0.15$.

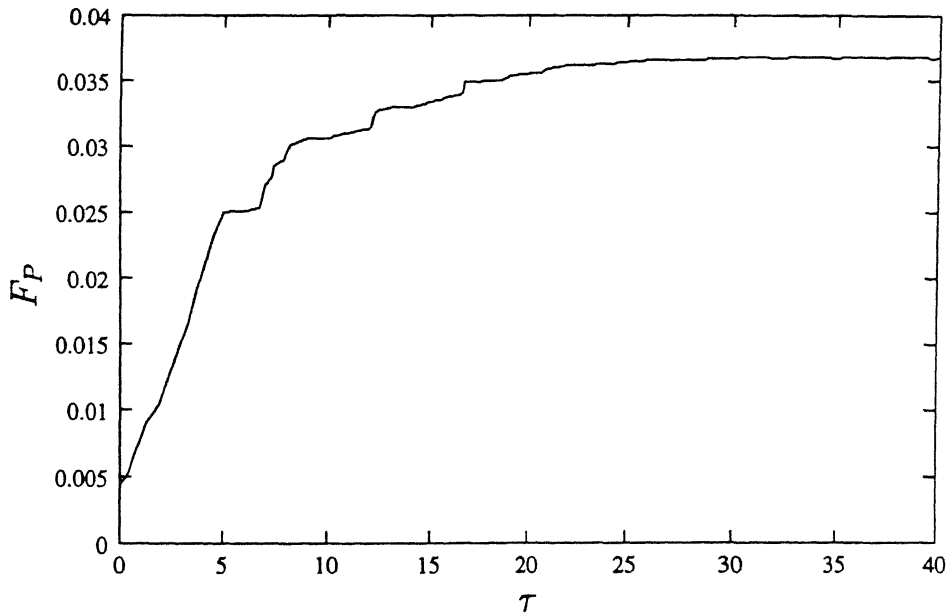


Fig. 5.14 Variation of constraint force F_P for bearingless blade to a step control pitch input ($w_p^s = 0.00624$).

Configuration: $\xi_1 = 0.10$, $\xi_2 = 0.25$ and $a = 0.05$, $b = 0.15$.

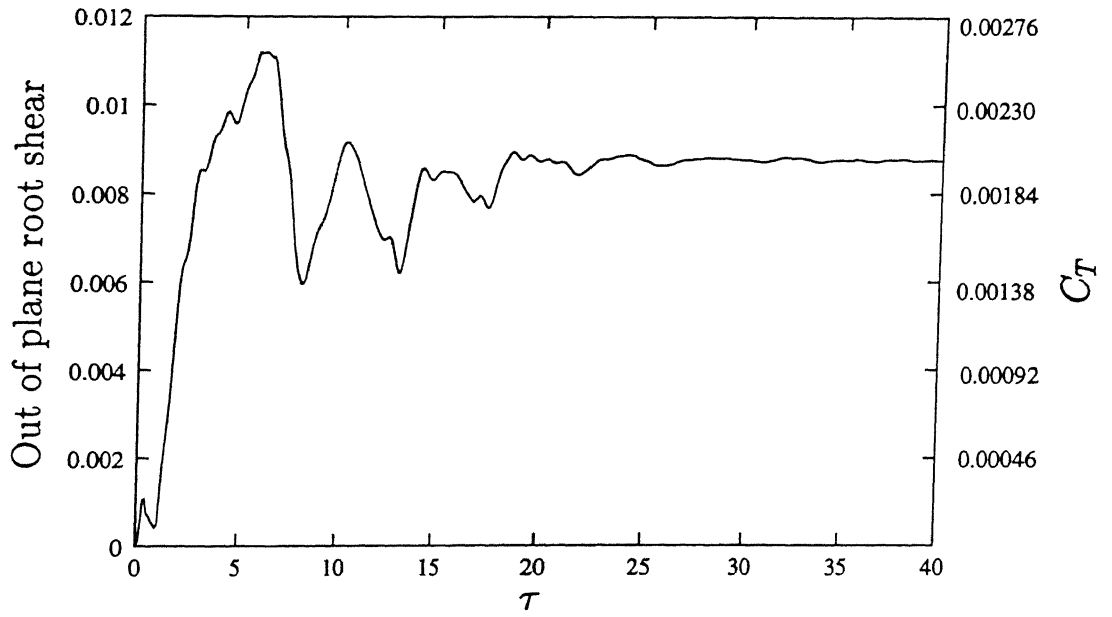


Fig. 5.15 Variation of out of plane root shear and thrust for bearingless blade to a step control pitch input ($w_p^s = 0.00624$).

Configuration: $\xi_1 = 0.10$, $\xi_2 = 0.25$ and $a = 0.05$, $b = 0.15$.

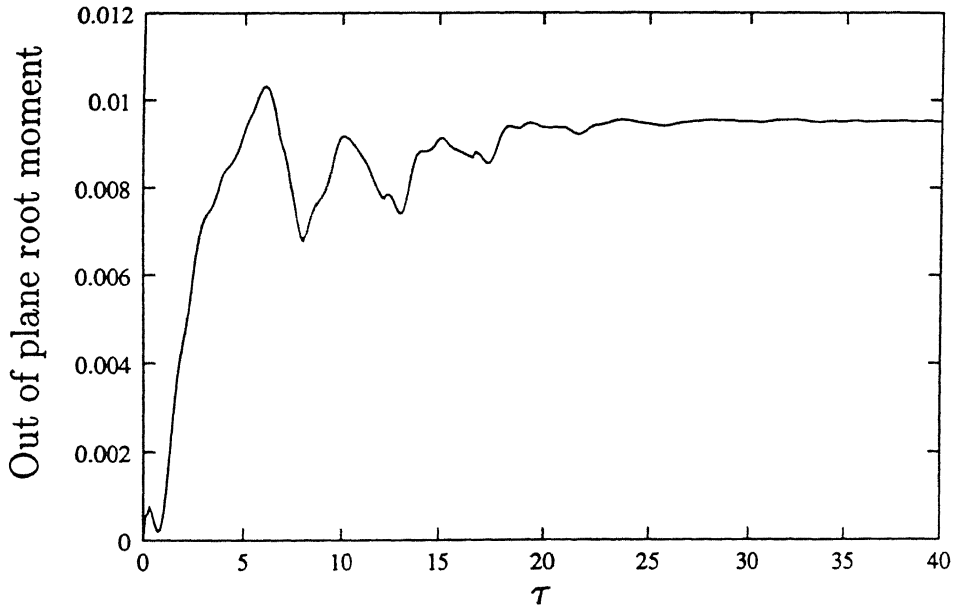


Fig. 5.16 Variation of out of plane root moment for bearingless blade to a step control pitch input ($w_p^s = 0.00624$).

Configuration: $\xi_1 = 0.10$, $\xi_2 = 0.25$ and $a = 0.05$, $b = 0.15$.

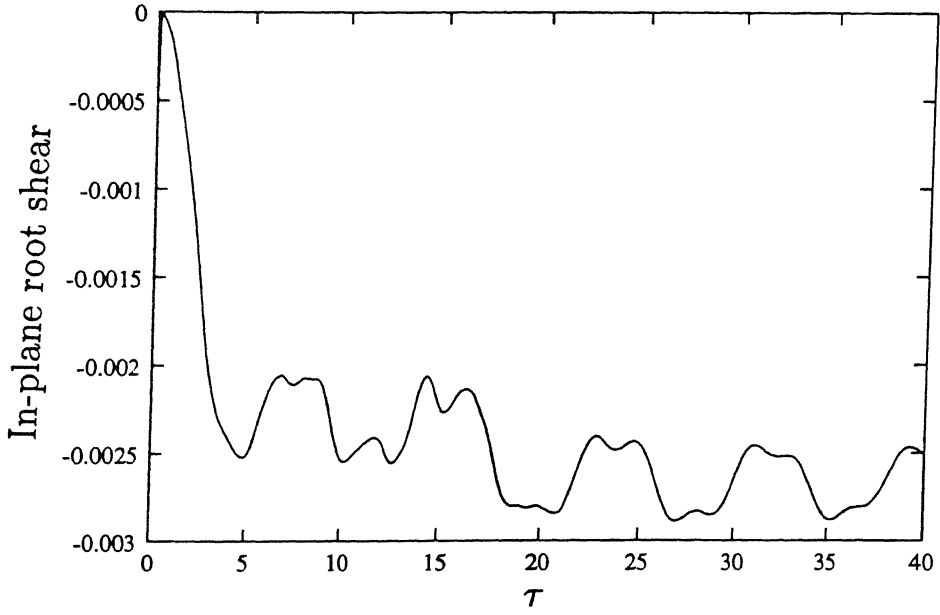


Fig. 5.17 Variation of in-plane root shear for bearingless blade to a step control pitch input ($w_p^s = 0.00624$).

Configuration: $\xi_1 = 0.10$, $\xi_2 = 0.25$ and $a = 0.05$, $b = 0.15$.

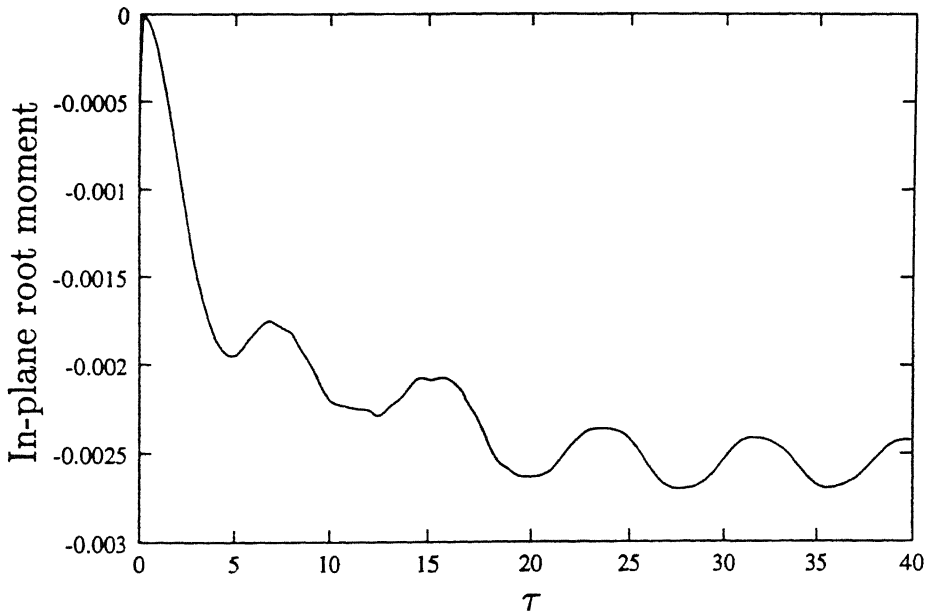


Fig. 5.18 Variation of in-plane root moment for bearingless blade to a step control pitch input ($w_p^s = 0.00624$).

Configuration: $\xi_1 = 0.10$, $\xi_2 = 0.25$ and $a = 0.05$, $b = 0.15$.

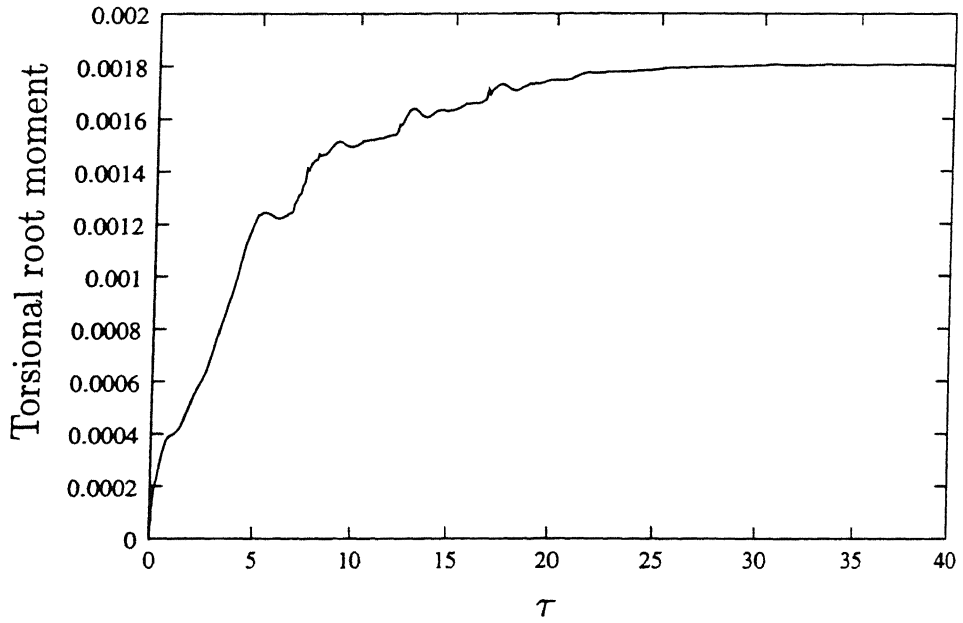


Fig. 5.19 Variation of torsional root moment for bearingless blade to a step control pitch input ($w_p^s = 0.00624$).

Configuration: $\xi_1 = 0.10$, $\xi_2 = 0.25$ and $a = 0.05$, $b = 0.15$.

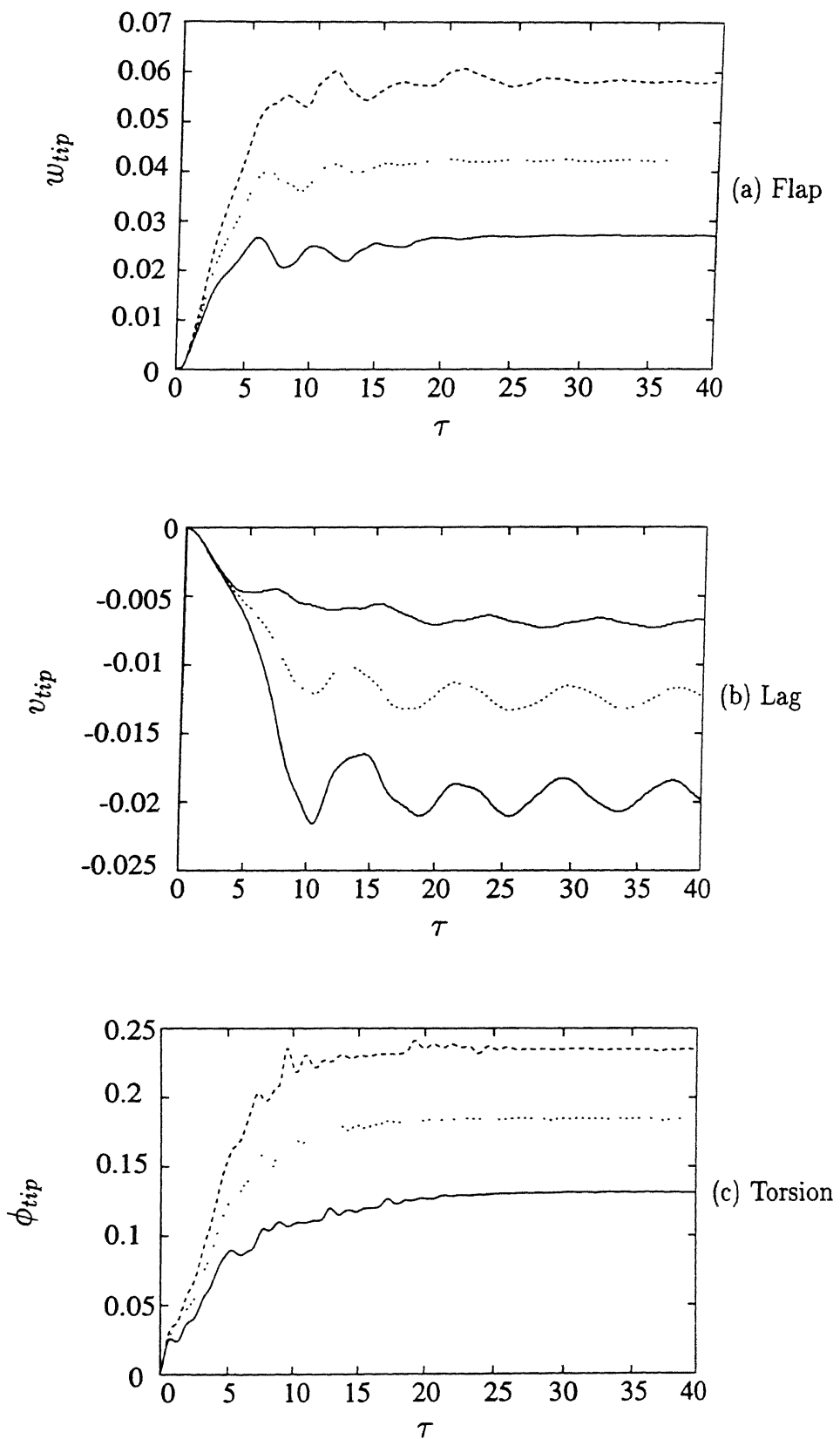


Fig. 5.20 Bearingless blade response with different values for step control pitch inputs. — $w_P^s = 0.00624$; $w_P^s = 0.00936$; - - - $w_P^s = 0.01248$.

Configuration: $\xi_1 = 0.10$, $\xi_2 = 0.25$ and $a = 0.05$, $b = 0.15$.

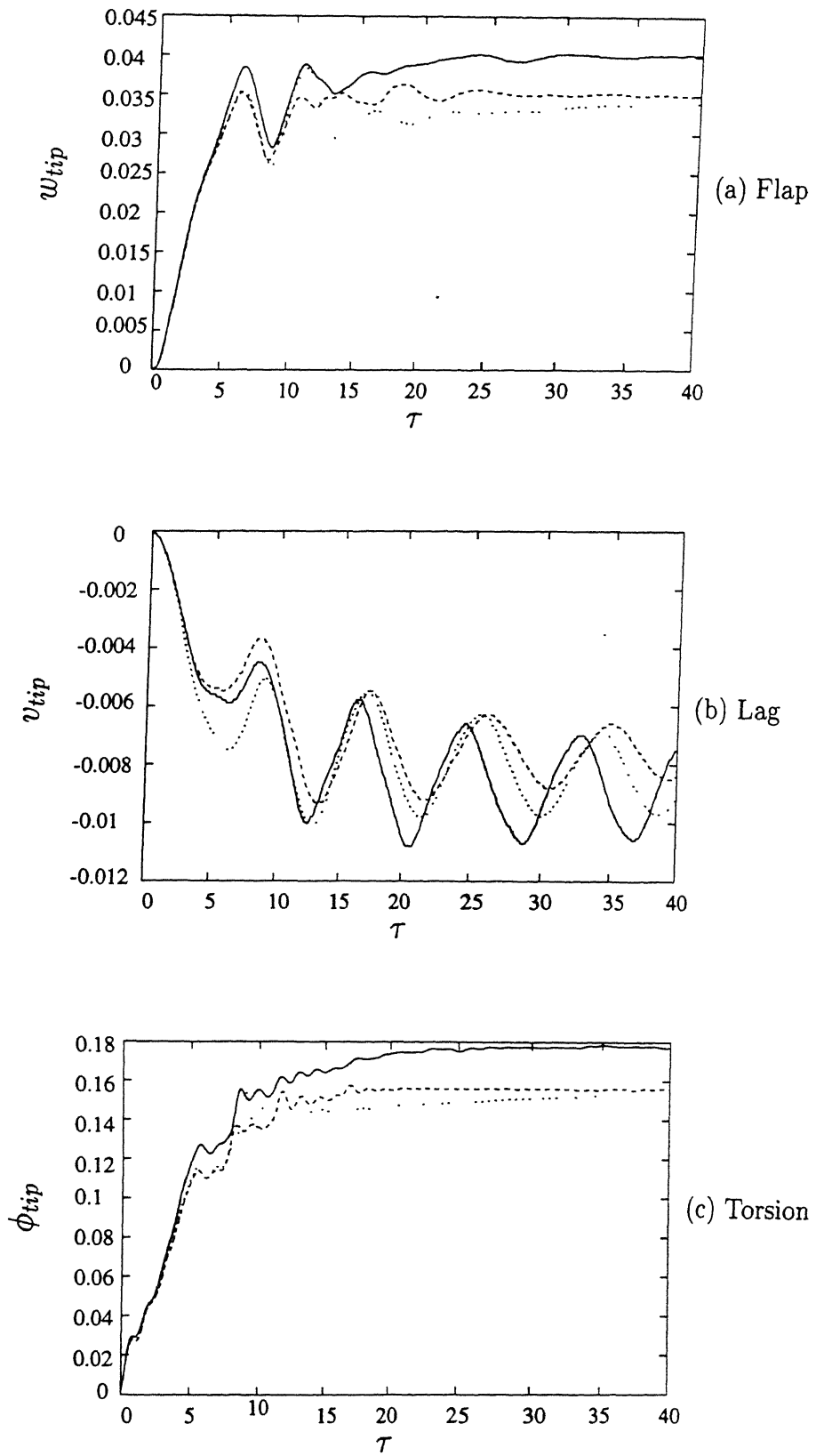


Fig. 5.21 Bearingless blade response with different locations of the elastomer (ξ_1).

..... $\xi_1 = 0.04$; ---- $\xi_1 = 0.02$; — $\xi_1 = 0.1$.

Configuration: $\xi_2 = 0.2$, Input: $w_p^s = 0.00624$; $a = 0.05$, $b = 0.15$.

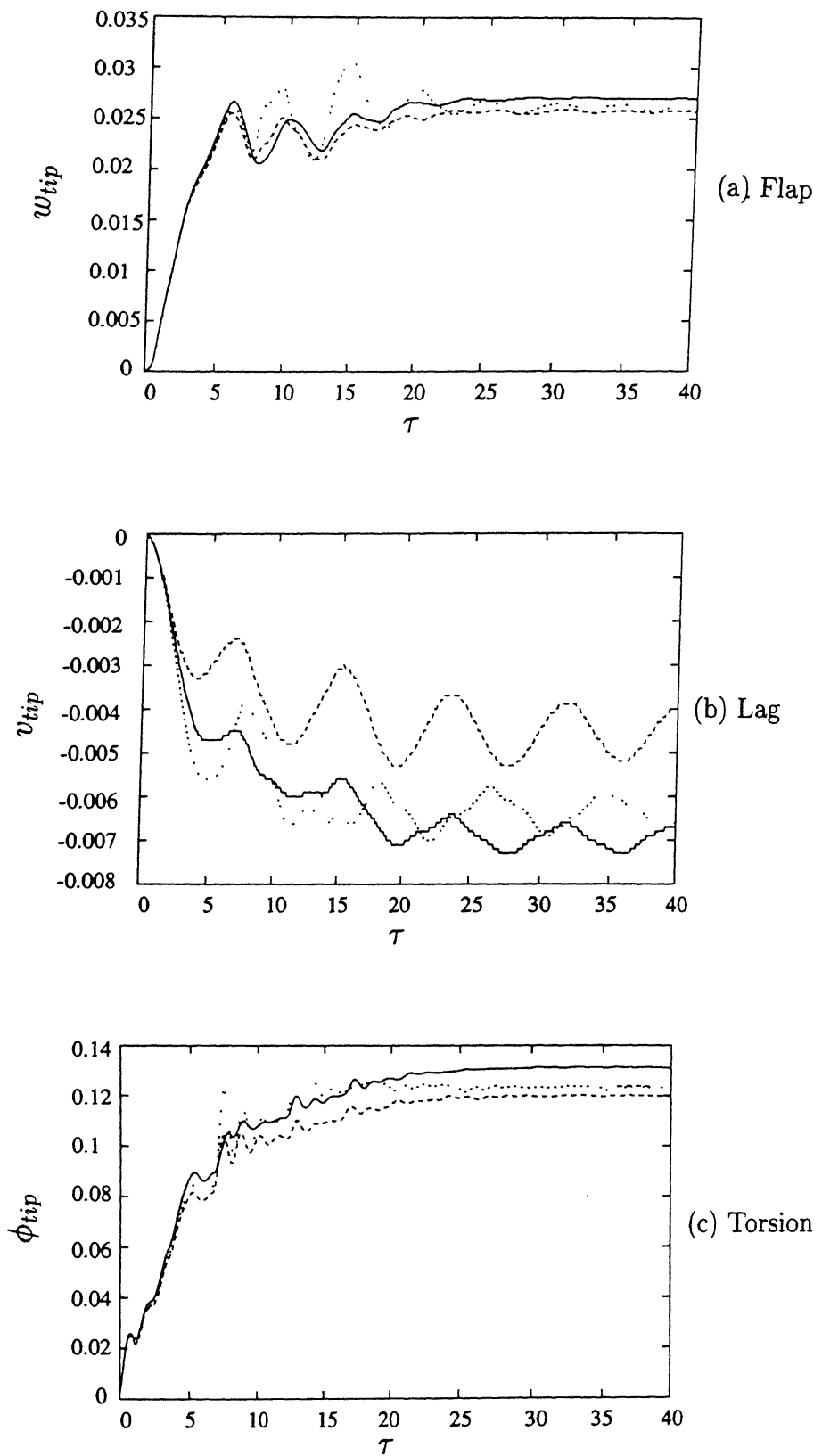


Fig. 5.22 Bearingless blade response with different locations of the elastomer (ξ_1).

..... $\xi_1 = 0.04$; - - - $\xi_1 = 0.02$; — $\xi_1 = 0.1$.

Configuration: $\xi_2 = 0.25$, Input: $w_p^* = 0.00624$; $a = 0.05$, $b = 0.15$.

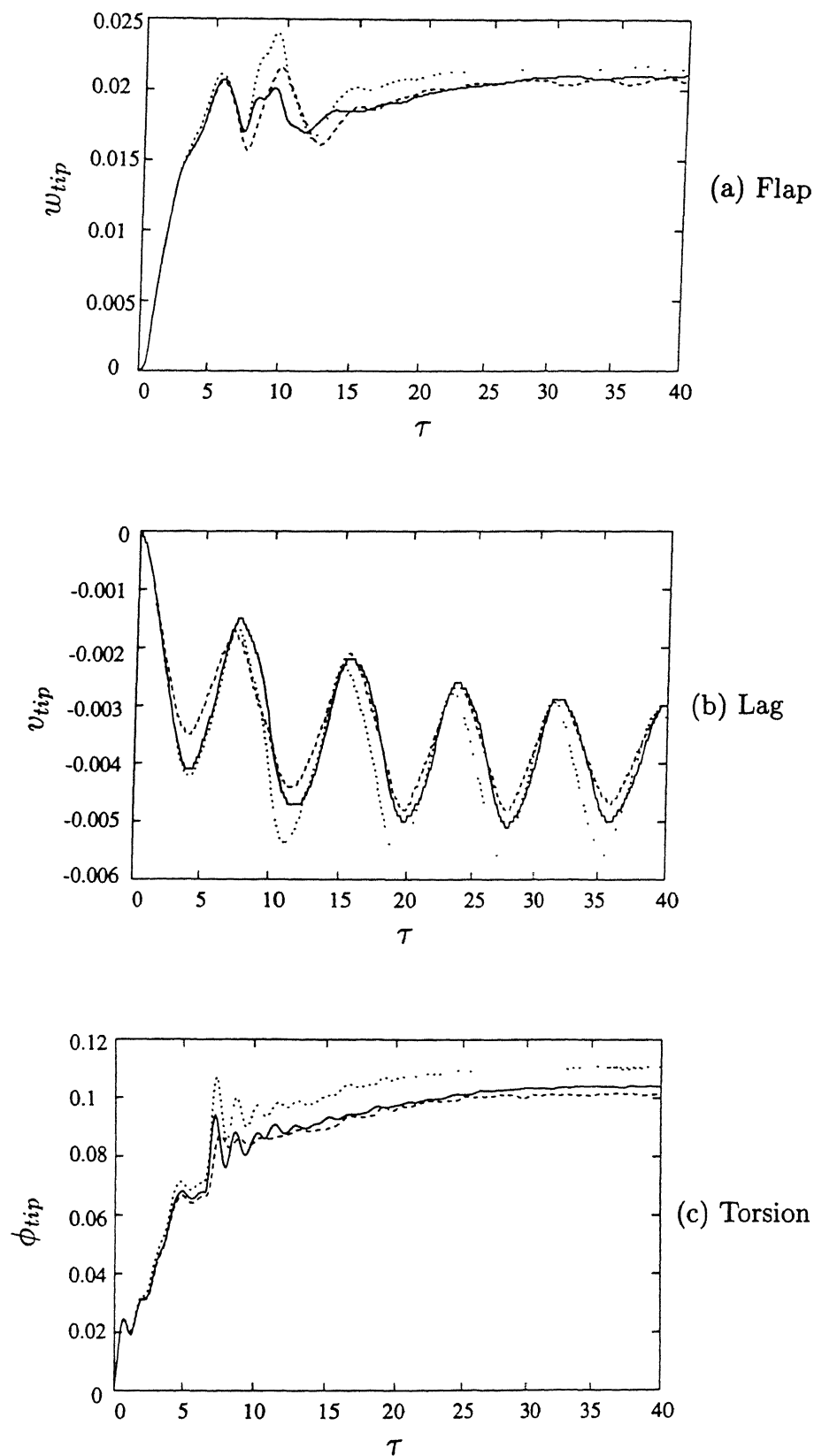


Fig. 5.23 Bearingless blade response with different locations of the elastomer (ξ_1).

..... $\xi_1 = 0.1$; ---- $\xi_1 = 0.02$; — $\xi_1 = 0.4$.

Configuration: $\xi_2 = 0.3$, Input: $w_p^s = 0.00624$; $a = 0.05$, $b = 0.15$.

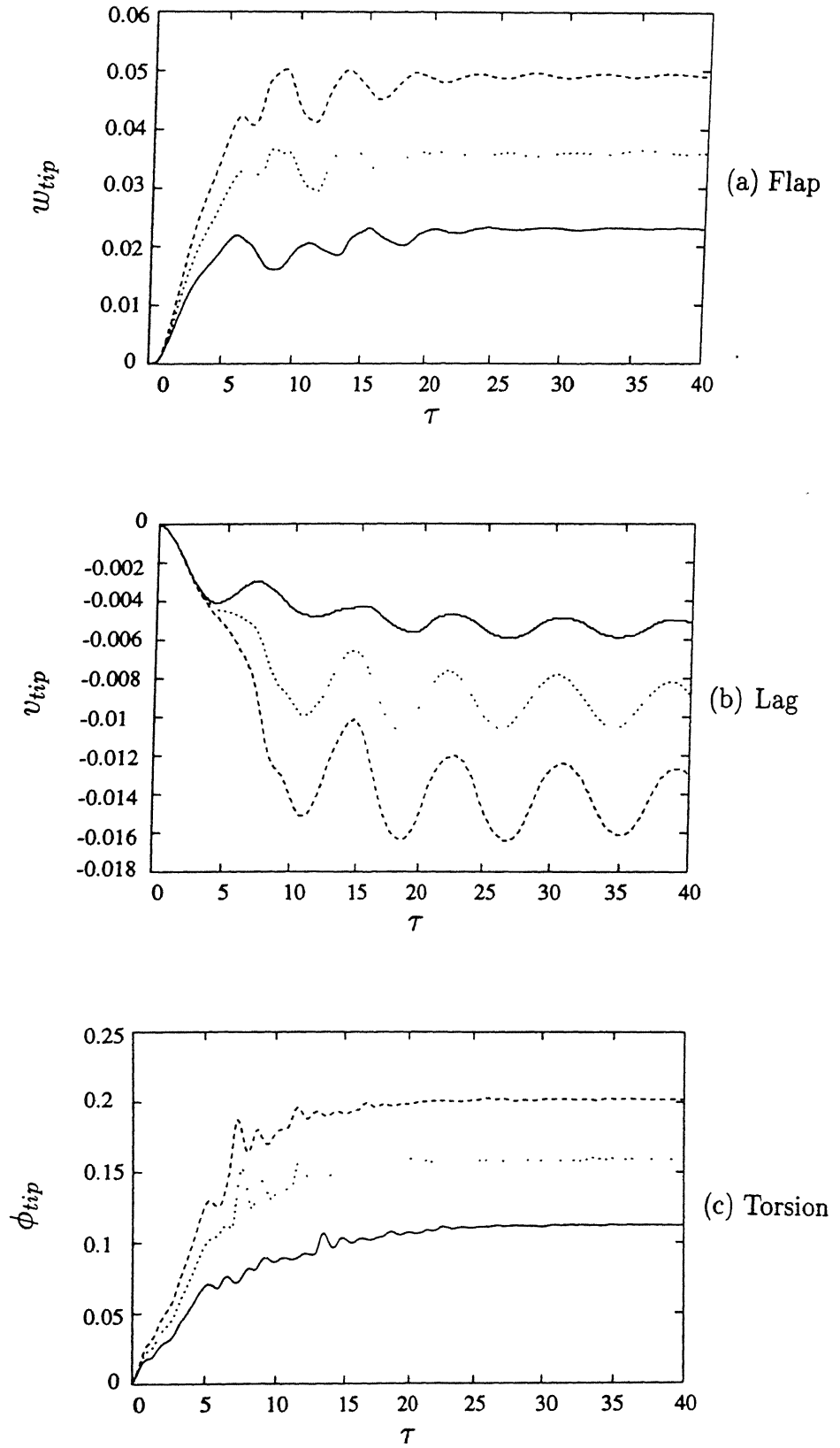


Fig. 5.24 Bearingless blade response with different values for step control pitch inputs. — $w_p^s = 0.00507$; $w_p^s = 0.00761$; - - - $w_p^s = 0.01014$.

Configuration: $\xi_1 = 0.10$, $\xi_2 = 0.25$ and $a = 0.03$, $b = 0.15$.

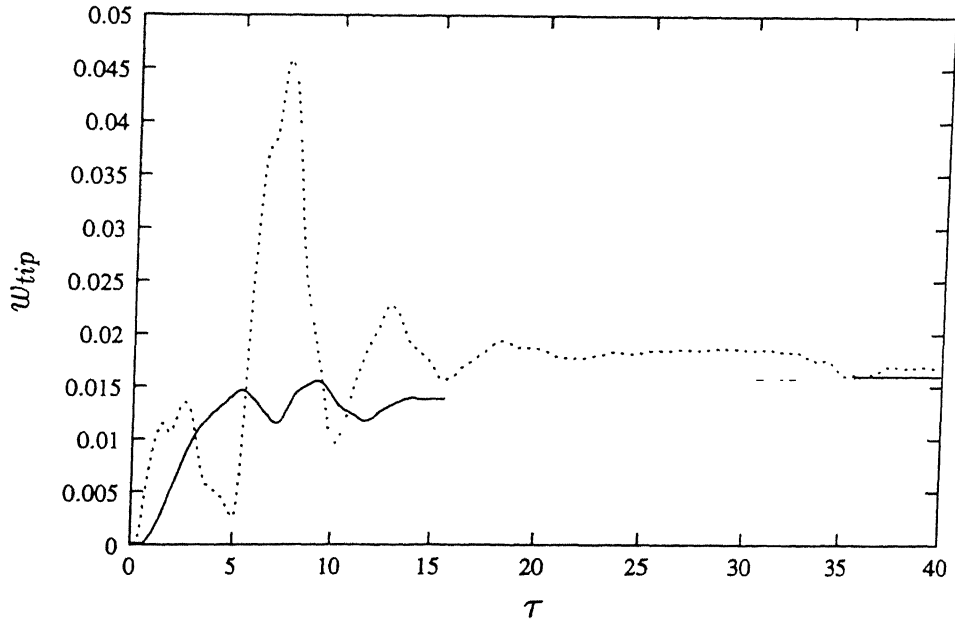


Fig. 5.25 Bearingless blade response in flap mode with different pitch link locations.

..... $a = -0.02$ and $w_p^s = -0.00383$; — $a = 0.02$ and $w_p^s = 0.00383$.

Configuration: $\xi_1 = 0.10$, $\xi_2 = 0.25$ and $b = 0.15$.

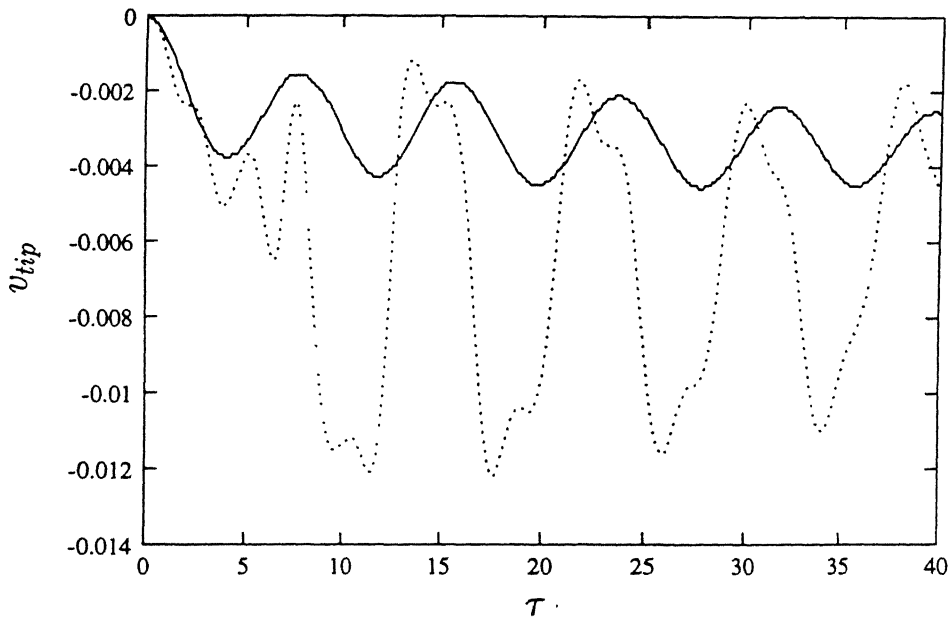


Fig. 5.26 Bearingless blade response in lag mode with different pitch link locations.

..... $a = -0.02$ and $w_p^s = -0.00383$; — $a = 0.02$ and $w_p^s = 0.00383$.

Configuration: $\xi_1 = 0.10$, $\xi_2 = 0.25$ and $b = 0.15$.

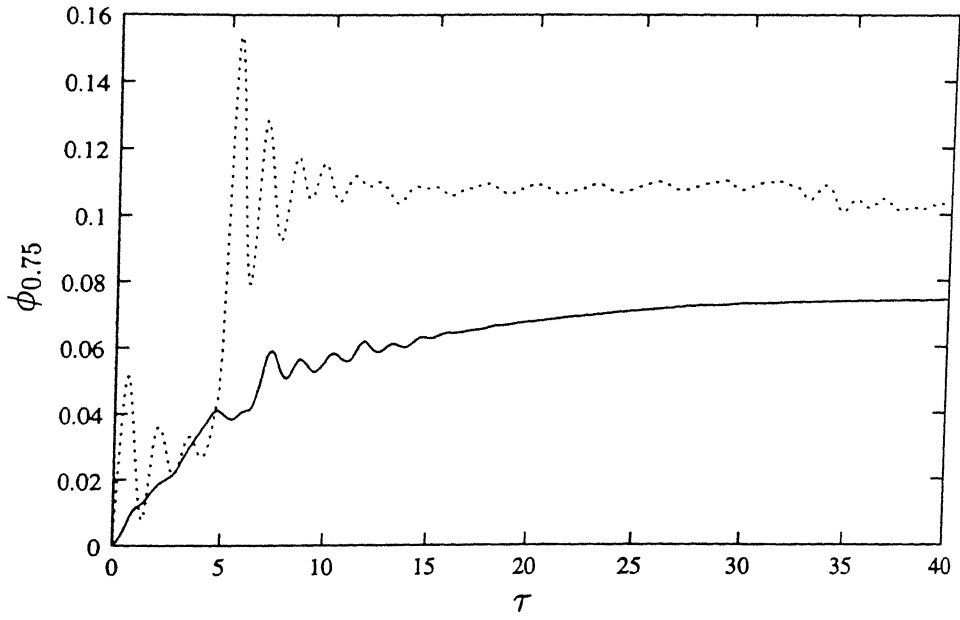


Fig. 5.27 Bearingless blade response in torsional mode with different pitch link locations. ····· $a = -0.02$ and $w_p^s = -0.00383$; — $a = 0.02$ and $w_p^s = 0.00383$. Configuration: $\xi_1 = 0.10$, $\xi_2 = 0.25$ and $b = 0.15$.

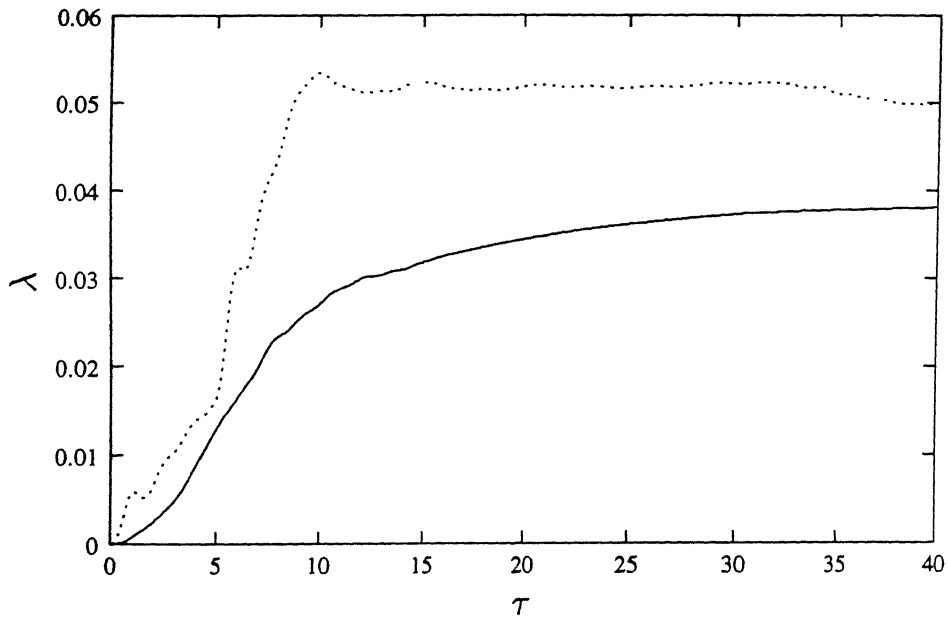


Fig. 5.28 Variation of inflow for bearingless blade with different pitch link locations. ····· $a = -0.02$ and $w_p^s = -0.00383$; — $a = 0.02$ and $w_p^s = 0.00383$. Configuration: $\xi_1 = 0.10$, $\xi_2 = 0.25$ and $b = 0.15$.

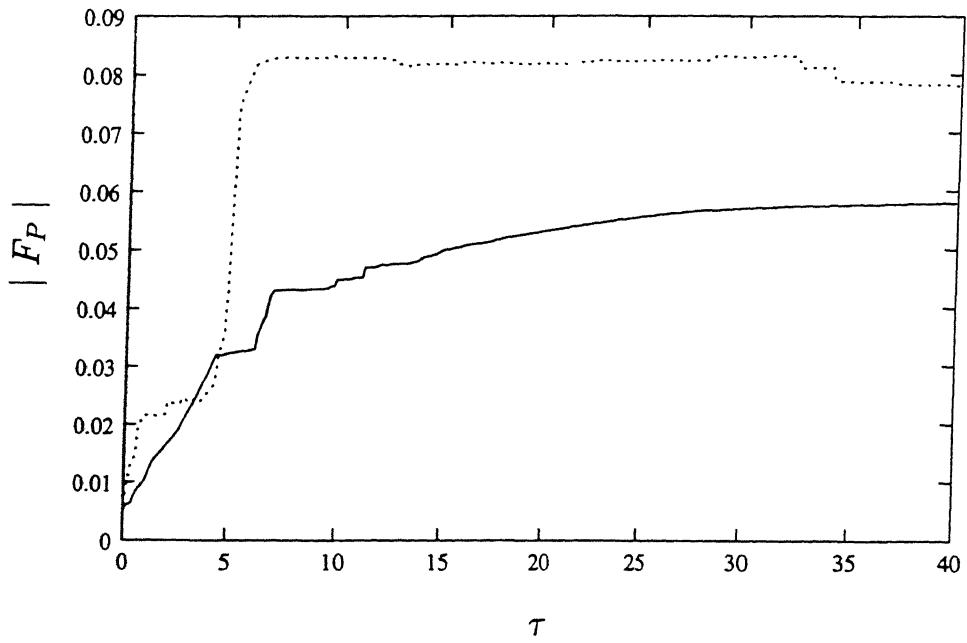


Fig. 5.29 Variation of constraint force F_P for bearingless blade with different pitch link locations.

..... $a = -0.02$ and $w_P^s = -0.00383$; — $a = 0.02$ and $w_P^s = 0.00383$.

Configuration: $\xi_1 = 0.10$, $\xi_2 = 0.25$ and $b = 0.15$.

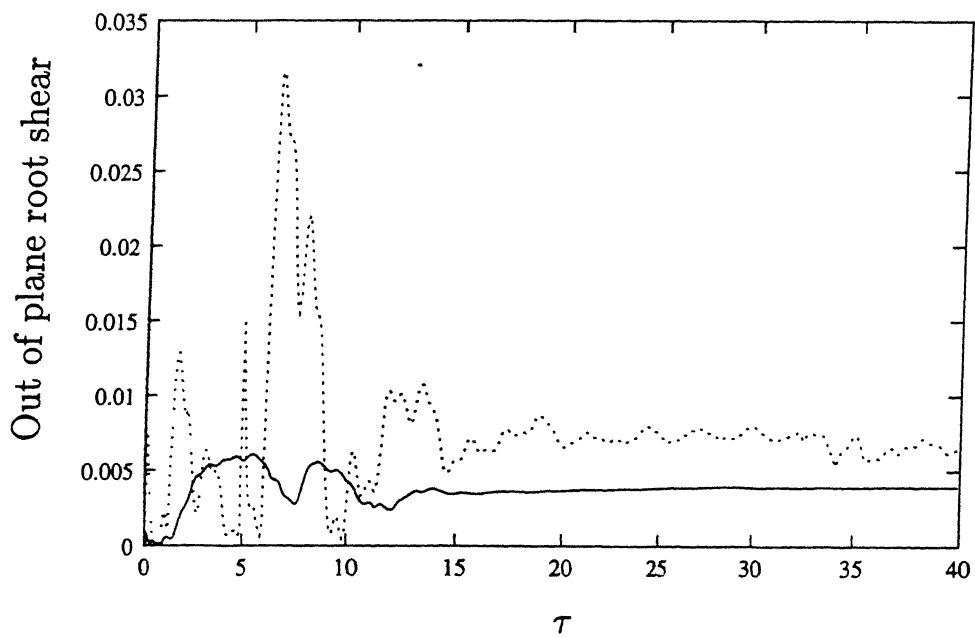


Fig. 5.30 Variation of out of plane root shear for bearingless blade with different pitch link locations.

..... $a = -0.02$ and $w_p^s = -0.00383$; — $a = 0.02$ and $w_p^s = 0.00383$.

Configuration: $\xi_1 = 0.10$, $\xi_2 = 0.25$ and $b = 0.15$.

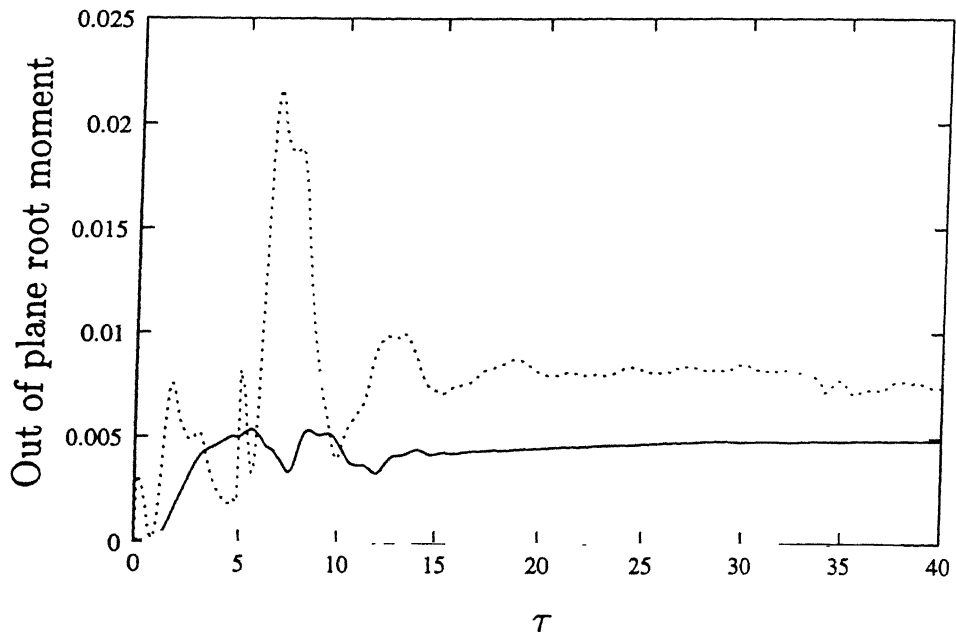


Fig. 5.31 Variation of out of plane root moment for bearingless blade with different pitch link locations.

..... $a = -0.02$ and $w_p^s = -0.00383$; — $a = 0.02$ and $w_p^s = 0.00383$.

Configuration: $\xi_1 = 0.10$, $\xi_2 = 0.25$ and $b = 0.15$.

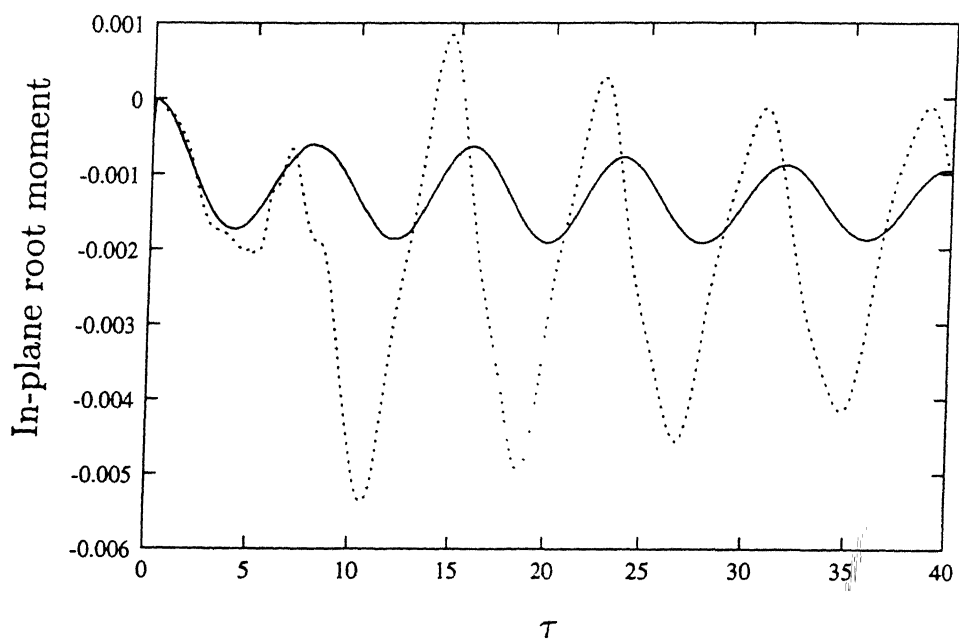


Fig. 5.33 Variation of in-plane root moment for bearingless blade with different pitch link locations.

..... $a = -0.02$ and $w_p^s = -0.00383$; — $a = 0.02$ and $w_p^s = 0.00383$.

Configuration: $\xi_1 = 0.10$, $\xi_2 = 0.25$ and $b = 0.15$.

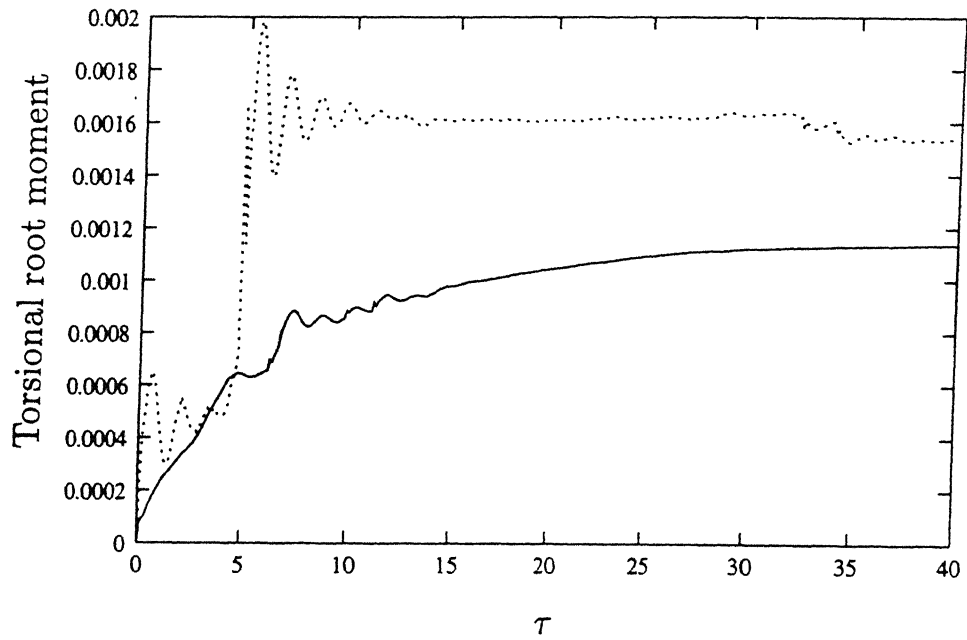


Fig. 5.34 Variation of torsional root moment for bearingless blade with different pitch link locations.

..... $a = -0.02$ and $w_p^s = -0.00383$; — $a = 0.02$ and $w_p^s = 0.00383$.

Configuration: $\xi_1 = 0.10$, $\xi_2 = 0.25$ and $b = 0.15$.

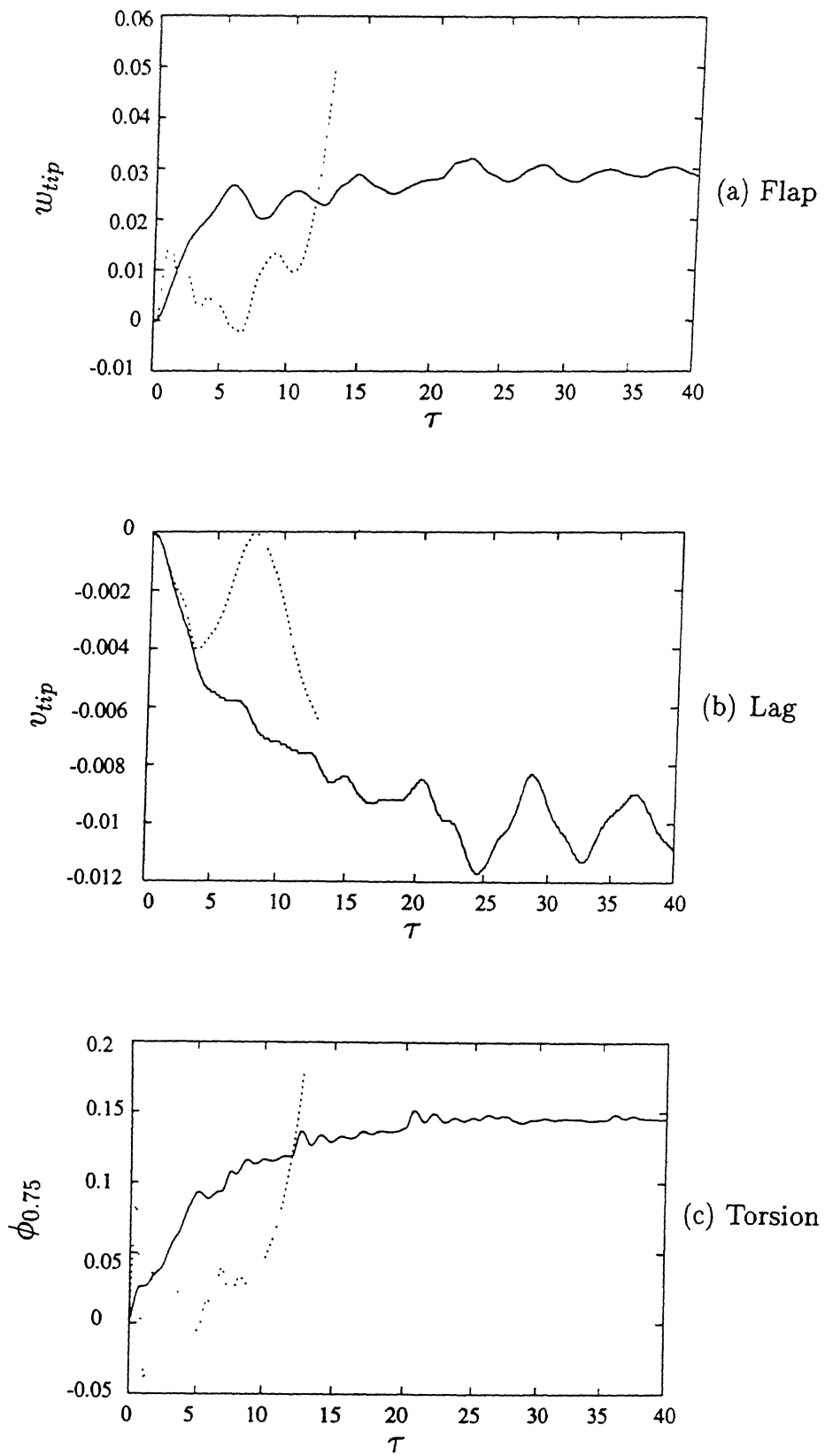


Fig. 5.35 Bearingless blade response for different pitch link locations.

..... $a = -0.03$ and $w_p^s = -0.00525$; — $a = 0.03$ and $w_p^s = 0.00525$.

Configuration: $\xi_1 = 0.10$, $\xi_2 = 0.25$ and $b = 0.23$.

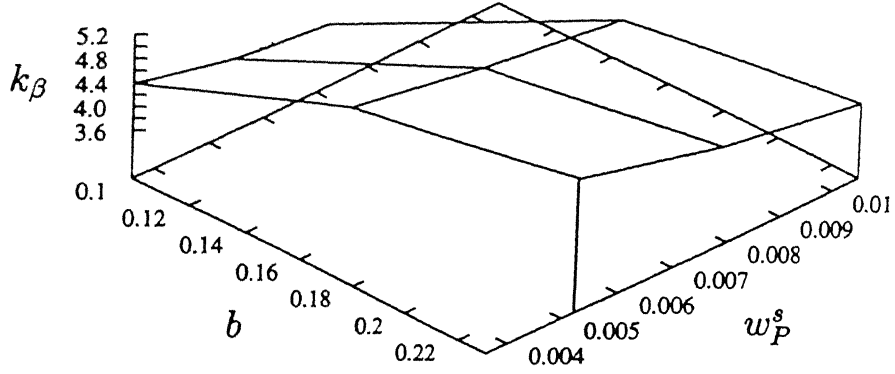


Fig. 5.36 Influence of pitch link location (b) and step control pitch input (w_P^s) on pitch-flap coupling of a bearingless blade.

Configuration: $\xi_1 = 0.10$, $\xi_2 = 0.25$ and $a = 0.03$.

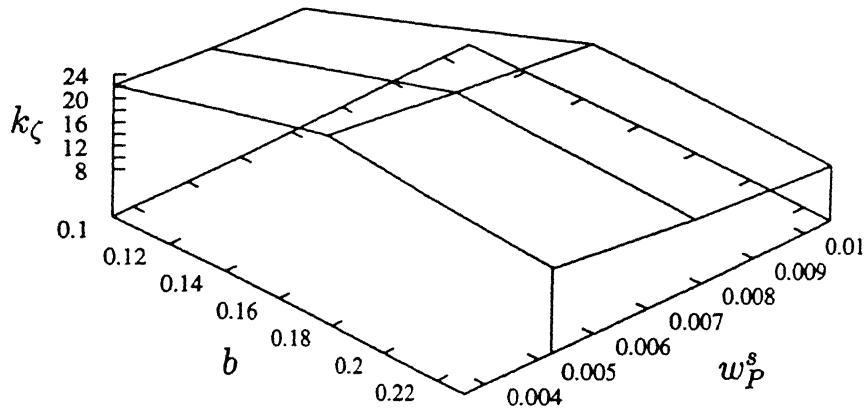


Fig. 5.37 Influence of pitch link location (b) and step control pitch input (w_P^s) on pitch-lag coupling of a bearingless blade.

Configuration: $\xi_1 = 0.10$, $\xi_2 = 0.25$ and $a = 0.03$.

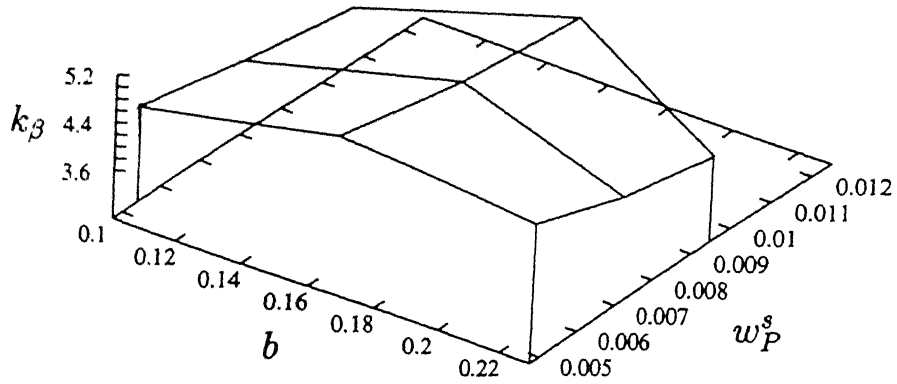


Fig. 5.38 Influence of pitch link location (b) and step control pitch input (w_P^s) on pitch-flap coupling of a bearingless blade.

Configuration: $\xi_1 = 0.10$, $\xi_2 = 0.25$ and $a = 0.05$.

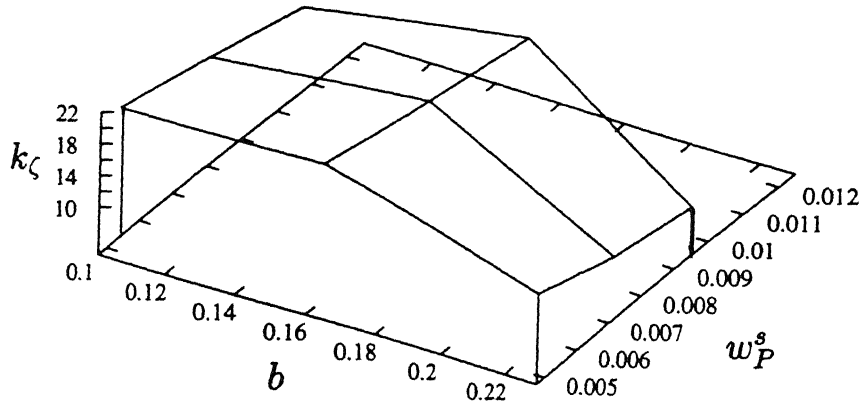


Fig. 5.39 Influence of pitch link location (b) and step control pitch input (w_P^s) on pitch-lag coupling of a bearingless blade.

Configuration: $\xi_1 = 0.10$, $\xi_2 = 0.25$ and $a = 0.05$.

Table 5.1 Input data for transient response analysis.

γ	5
$\frac{b_1}{L}$	$\frac{\pi}{20}$
a_1	2π
C_{do}	0.01
N	4
$\frac{GJ}{m\Omega^2 L^4}$	0.001473
$\frac{EI_{\zeta\zeta}}{m\Omega^2 L^4}$	0.0301
$\frac{EI_{\eta\eta}}{m\Omega^2 L^4}$	0.0106
$\frac{Im_{\eta\eta}}{mL^2}$	0.0004
$\frac{Im_{\zeta\zeta}}{mL^2}$	0.0
θ_{tw}	0.0
$(\frac{k_A}{k_m})^2$	1.5
$k_A^2 = \frac{EI_{\eta\eta} + EI_{\zeta\zeta}}{EA}, k_m^2 = \frac{Im_{\eta\eta} + Im_{\zeta\zeta}}{mL^2}$	

Offsets of mass centre, tension centre and aerodynamic centre from the elastic axis are zero.

Table 5.2 Variation of aeroelastic coupling with b and step control pitch input w_P^s .
 $\xi_1 = 0.1$, $\xi_2 = 0.25$ and $a = 0.03$.

b	w_P^s	k_β	k_ζ
0.10	0.00361	4.39	22.17
0.10	0.00542	4.02	20.67
0.10	0.00722	3.84	19.86
0.15	0.00507	4.50	18.98
0.15	0.00761	4.08	15.59
0.15	0.01014	3.80	13.03
0.23	0.00525	5.04	14.24
0.23	0.00787	4.45	11.31
0.23	0.01050	4.05	9.28

Table 5.3 Variation of aeroelastic coupling with b and step control pitch input w_P^s .
 $\xi_1 = 0.1$, $\xi_2 = 0.25$ and $a = 0.05$.

b	w_P^s	k_β	k_ζ
0.10	0.00537	4.40	20.41
0.10	0.00805	4.01	17.53
0.10	0.01070	3.74	14.71
0.15	0.00624	4.48	16.58
0.15	0.00936	4.03	13.73
0.15	0.01248	3.74	11.01
0.23	0.00475	5.15	15.40
0.23	0.00712	4.57	11.88
0.23	0.00950	4.22	10.04

Table 5.4 Variation of aeroelastic coupling with a and step control pitch input w_P^s .

$\xi_1 = 0.1$, $\xi_2 = 0.25$ and $b = 0.15$.

a	w_P^s	k_β	k_ζ
-0.02	-0.00255	7.79	-16.59
-0.02	-0.00383	6.12	-15.98
-0.02	-0.00511	5.88	-15.07
0.02	0.00255	5.01	-20.28
0.02	0.00383	4.63	-20.21
0.02	0.00511	4.35	-20.01

Chapter 6

ELASTOMERIC DAMPER MODEL AND LIMIT CYCLE OSCILLATION

6.1 Introduction

The review of the literature given in Sec. 1.2 indicates that some of the recent studies have focussed on the phenomenon of limit cycle behaviour of the rotor blades due to the elastomer nonlinearity. Ormiston *et al.* [31] considered an elastomer model in which the damping force was assumed to be proportional to a linear combination of different powers of velocity (powers of $1/2$, 1, 2 and 3). Using this non-linear elastomer model, they showed the presence of limit cycle oscillation for both hingeless and bearingless rotor blade configurations. It was also pointed out that there was no limit cycle when the elastomer damping is taken as linear.

The hover air-resonance test conducted by Panda *et al.* [4] also indicated that non-linearities in stiffness and damping characteristics of the elastomer seem to have

significant influence on the limit cycle oscillations. When they used a fluidlastic damper having linear characteristics, no limit cycle oscillation was observed. In Ref. [30], Gandhi and Chopra proposed a non-linear visco-elastic model for the elastomer in which the damping element is linear. The model shows a rapid decrease in the damping coefficient at very low amplitudes of oscillation; but its value is always positive. With this elastomeric damper, they showed a limit cycle oscillation for an *autonomous system* representing the isolated lag dynamics of a blade.

The theorem on the existence of a limit cycle [121] says that for the equation

$$\ddot{x} + f(x)\dot{x} + g(x) = 0 \quad (6.1)$$

to exhibit a limit cycle, $f(x)$ must be positive when $|x|$ is large, and negative when $|x|$ is small, and where g is such that, in the absence of the damping term $f(x)\dot{x}$, a periodic solution is expected for small x . In Van der Pol's equation

$$\ddot{x} + e(x^2 - 1)\dot{x} + x = 0, \quad e > 0 \quad (6.2)$$

i.e., the damping coefficient becomes negative in the strip $|x| < 1$ and positive for $|x| > 1$. Hence the system can show a stable limit cycle for any given initial disturbance. Therefore, it is difficult to physically understand as to why a damper whose coefficient is always positive would lead to a limit cycle oscillation under free vibration conditions as reported in Ref. [30]. For such a strictly dissipative system, the energy source for sustained oscillation is absent. To explore the phenomenon of limit cycle, in this chapter a study is carried out on the response of an isolated bearingless rotor blade using different elastomer models.

6.2 Formulation of Elastomer Model

Since experimental data are used in developing the analytical spring-damper model for the elastomer, there is a scope for formulating many different types of models. In Chapter 2, the elastomer is modelled (herein denoted as Model 1) as a parallel combination of a non-linear spring, a Coulomb damper and a hysteretic damping. A modified model (denoted as Model 2) consisting of a non-linear spring, a Coulomb damping element and a Rayleigh type hysteretic damping element can also be considered (Fig. 6.1). The constitutive differential equation of the elastomer model under harmonic loading for Model 1 and Model 2 can then be written, respectively, as

$$K_1x - K_3x^3 + K_5x^5 - K_7x^7 + F\text{sgn} |\dot{x}| + \frac{h_1}{\omega}\dot{x} = D_o \sin \omega t \quad \text{Model 1} \quad (6.3)$$

$$K_1x - K_3x^3 + K_5x^5 - K_7x^7 + F\text{sgn} |\dot{x}| + \frac{h_3}{\omega^3}\dot{x}^3 - \frac{h_1}{\omega}\dot{x} = D_o \sin \omega t \quad \text{Model 2} \quad (6.4)$$

Assuming a harmonic motion and following the procedure mentioned in Sec. 2.2, the in-phase stiffness (G') and the quadrature stiffness (G'') for Model 2 can be obtained as

$$G' = K_1 - \frac{3}{4}K_3X^2 + \frac{5}{8}K_5X^4 - \frac{1}{2}K_7X^6 \quad (6.5)$$

$$\text{and } G'' = \frac{4F}{\pi X} + \frac{3}{4}h_3X^2 - h_1. \quad (6.6)$$

6.3 Results and Discussion

Solving the minimisation problem described in Chapter 2, the parameters for the elastomer Model 2 are obtained. These are given in Table 6.1 along with the parameters of Model 1. Comparison of the experimental data with Model 1 and Model 2 is shown in Fig. 6.2. It can be seen that both the models fit the experimental values fairly well in the available range of data.

Using the Model 1 and Model 2, the transient response characteristics of the rotor blade (coupled flap, lag and torsion) are obtained following the solution procedure outlined in Sec. 5.3. The blade data is given in Table 5.1. The elastomer and torque tube locations are set at $\xi_1 = 0.10$ and $\xi_2 = 0.25$. The pitch link is located at the leading edge side of the blade with $a = 0.03$ and $b = 0.10$. A step control input of $w_p^s = 0.00361$ is applied. Figures 6.3 and 6.4 show the transient response in lag mode for the two cases. In the case of Model 2 (Fig. 6.3), it is observed that within a short time, the lag response settles down to a stable limit cycle oscillation with a constant amplitude of 0.0145. In the case of Model 1 (Fig. 6.4), the transient response in lag mode settles to steady state value of -0.0027 . The blade response shown in Figs. 6.3 and 6.4 are obtained with the inclusion of aerodynamic loading.

In order to ensure that the cause of limit cycle is due to the elastomer model and not due to aerodynamic loading, the transient analysis is also carried out by excluding the aerodynamic effects. For the same set of blade parameters and input, the response of the blade is computed. Figures 6.5 and 6.6 show the responses in the lag mode of the blade with elastomer Model 2 and Model 1, respectively. While the response of Model 2 exhibits a limit cycle oscillation (Fig. 6.5), no such oscillation is observed for Model 1 (Fig. 6.6).

6.4 Summary

Even though both elastomer models fit the experimental data fairly well, they give rise to totally different response characteristics. These results clearly indicate that the phenomenon of limit cycle oscillation is highly dependent on the elastomer model. Hence, care must be exercised in modelling the elastomer.

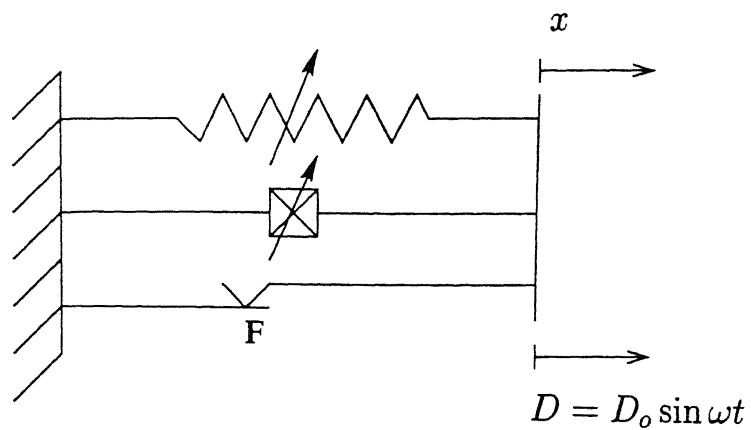


Fig. 6.1 Elastomer Model 2 with Rayleigh type damping.

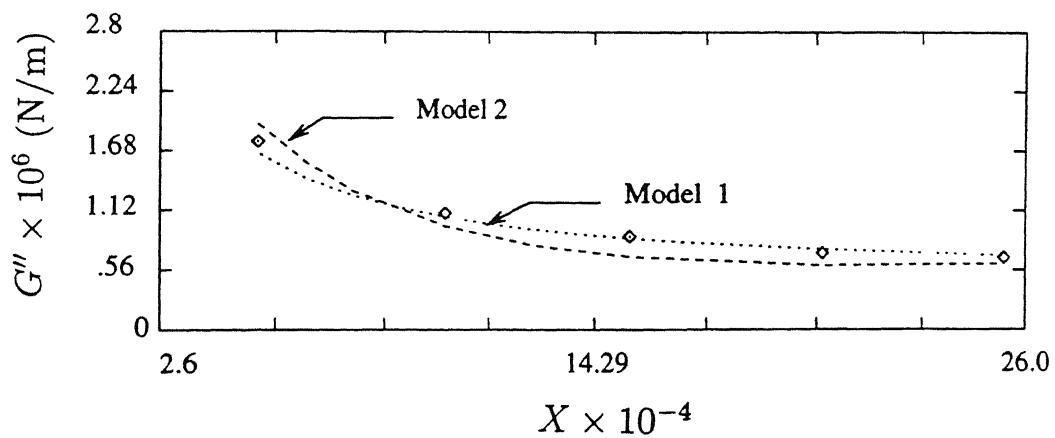


Fig. 6.2 Comparison of the experimental data with Model 1 and Model 2.

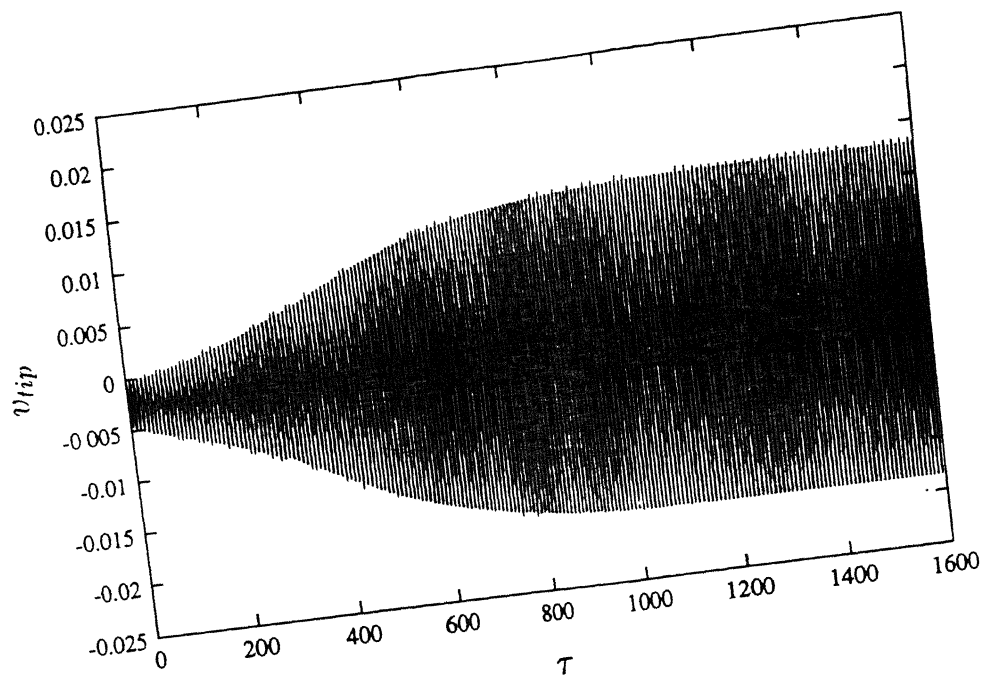


Fig. 6.3 Transient response in lag mode with Model 2 (with aerodynamic loading).

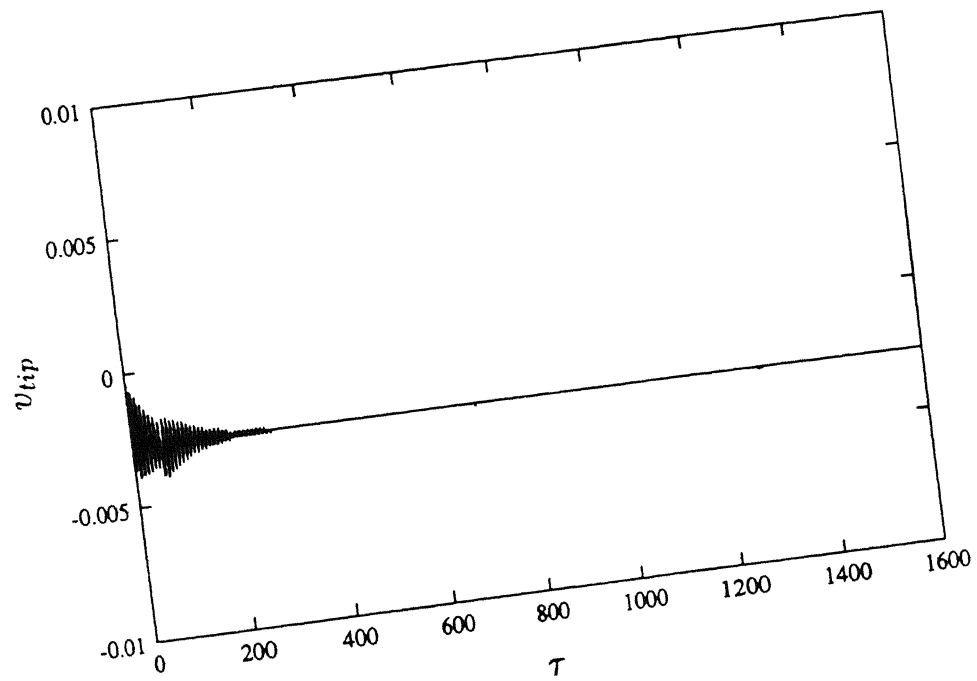


Fig. 6.4 Transient response in lag mode with Model 1 (with aerodynamic loading).

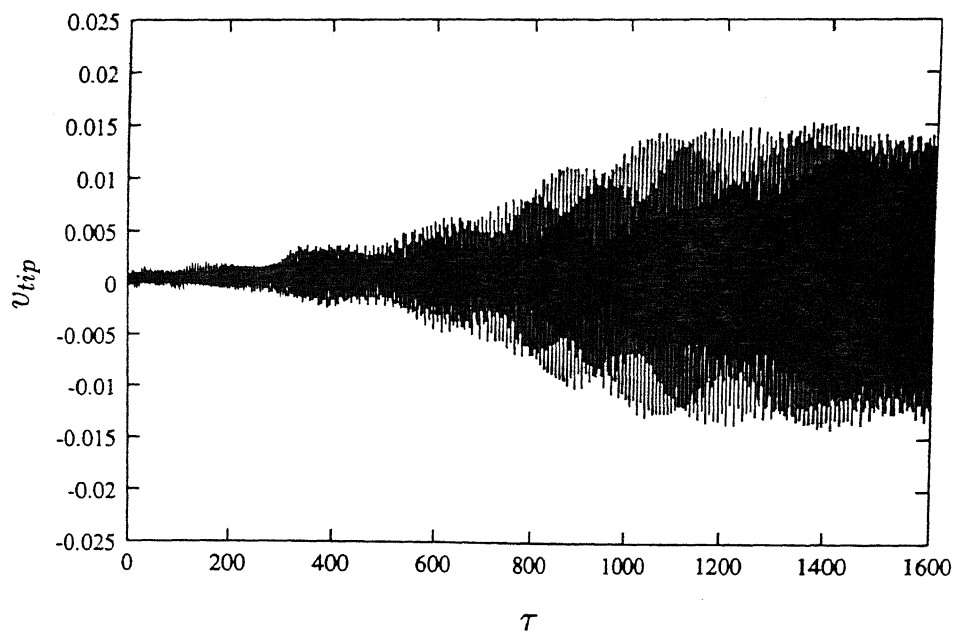


Fig. 6.5 Transient response in lag mode with Model 2 (without aerodynamic loading).

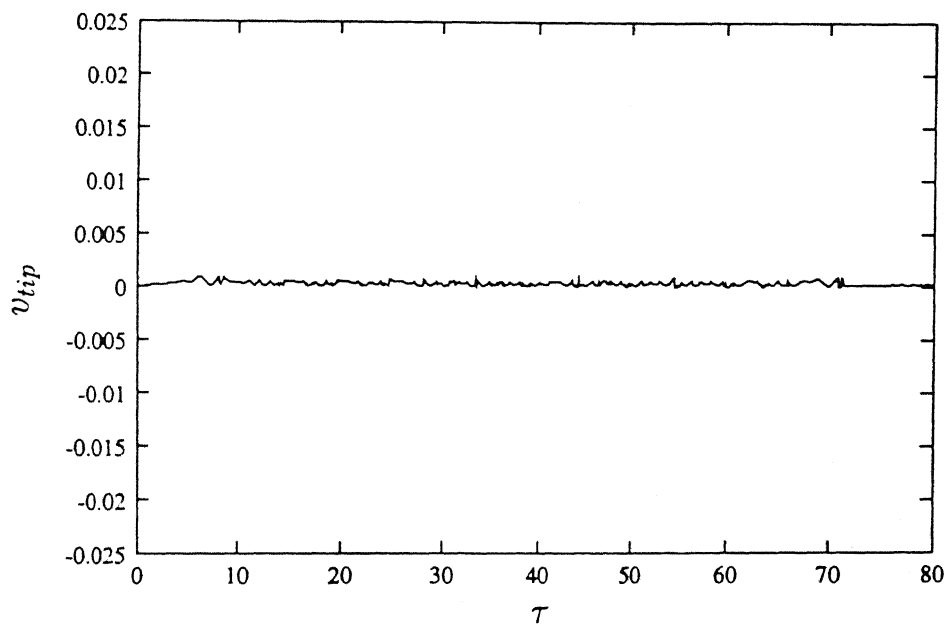


Fig. 6.6 Transient response in lag mode with Model 1 (without aerodynamic loading).

Table 6.1 System parameters of the elastomeric damper Model 1 and Model 2.

System Parameter	Model 1	Model 2
K_1 (N/m)	2.673989×10^6	2.673989×10^6
K_3 (N/m ³)	1.315287×10^{12}	1.315287×10^{12}
K_5 (N/m ⁵)	3.519586×10^{17}	3.519586×10^{17}
K_7 (N/m ⁷)	3.176266×10^{22}	3.176266×10^{22}
F (N)	4.797347×10^2	8.45909×10^2
h (N/m)	4.569120×10^5	—
h_1 (N/m)	—	1.44619×10^5
h_3 (N/m ³)	—	7.06419×10^{10}

Chapter 7

CONCLUSIONS

The effect of nonlinearity of the elastomer on the dynamics of an idealised bearingless rotor blade has been studied. Attempts have been made to analyse problems of increasing complexities with an aim to gain a fundamental understanding of the blade dynamics and aeroelastic transient response. In the absence practical blade data, uniform properties reported in research publications are used for the blade. The properties of the elastomer are taken from the experimental results published in the open literature. Even though the blade is assumed to be uniform, the natural frequencies of the blade in flap, lag and torsional modes are representative of an actual blade configuration. The major conclusions of the present study are summarised below. The results are valid within the framework of the assumptions on which the study is carried out.

1. The experimental data indicate that the stiffness and damping properties of the elastomer exhibit very weak dependence on frequency in the range of interest for rotor blade analysis. In view of this observation, a simple model for the non-linear elastomer has been developed which can be easily integrated with the blade model. The highly non-linear characteristic of the elastomer is modelled by a parallel combination of spring and damper elements.

2. Using an idealised model for a bearingless rotor, both linear and non-linear free vibration analyses of the rotating blade under uncoupled flap and lag bending have been studied. For the linear problem, two different solution techniques, one based on power series expansion and the other based on the Rayleigh-Ritz method are used. The natural frequencies obtained from these two methods are found to be in excellent agreement. For the flap motion, it is observed that the effect of the elastomer spring has a relatively high influence on the third mode; a moderate influence on the first mode; and less influence on the second mode. In case of lag motion, the effect of the spring is more pronounced on the first mode.

3. In the non-linear analysis, a numerical-perturbation technique based on multiple-time-scale is formulated to determine a closed form frequency-amplitude relationship for uncoupled flap and lag motions of the rotating blade. It is concluded that upto a fairly high value of amplitude, not normally to be exceeded in practice, a seventh order expansion of the non-linear spring force is sufficient to correctly predict the frequency-amplitude relationship. If the amplitude level is lower, one can use an expansion upto fifth order and still get accurate results while saving on the computational effort. The alternating signs in the polynomial, expressing the restoring force prevents the non-linear characteristic to be monotonically softening or hardening.

4. An amplitude dependent stability analysis has been performed for a coupled rotor/fuselage system under ground resonance condition. It is observed that the elastomer amplitude does not significantly alter the stability of the system at the region of maximum instability. But the damping in the progressive lag mode decreases appreciably with the increase in amplitude.

5. The locations of the elastomer and torque tube seem to have significant influence on the stability of the system. The results indicate that for a given location of the elastomer, there is an optimum location for the attachment of the torque tube providing

least instability in the system. The physical reason for this observation is that for a particular combination of elastomer and torque tube locations, the deformation of the elastomer is maximum, resulting in a maximum value of damping. Therefore, a judicious selection of the locations of the elastomer and torque tube is very important for enhancing the stability of the system under ground resonance condition.

6. A suitable numerical technique has been formulated to study the transient response, to a step input, of an isolated bearingless rotor blade undergoing coupled flap-lag-torsional deformation in hovering condition. A similar analysis is also performed for a hingeless blade to validate the equations of motion and solution technique. It is interesting to note that there is a qualitative difference in the nature of the blade response and rotor thrust for these two types of blades. The reason for the difference may be attributed to the presence of multiple load path and kinematic constraint in the bearingless blade.

7. It is also observed that the transient response characteristics change drastically depending on whether the pitch link is located at the leading edge or the trailing edge side of the blade. The root loads for these configurations also exhibit similar differences. These differences may be attributed to the change in the directions of the constraint force and moments when the pitch link is shifted from leading to the trailing edge side.

8. An attempt is made to define a measure of the aeroelastic coupling present in the bearingless rotor blade system. The influence of the geometric parameters a , b and the magnitudes of the control input on the aeroelastic coupling measures are evaluated. The magnitude of the pitch-lag coupling is found to be higher for the leading edge configuration than that for the trailing edge configuration. The trend is found to be reversed for the pitch-flap coupling. The aeroelastic coupling measures are observed to be dependent on the magnitude of the control input, exhibiting a non-linear relationship.

9. A study is carried out on the response of an isolated bearingless rotor blade using two different elastomer models representing the same experimental data. The results indicate that the phenomenon of limit cycle oscillation is highly dependent on the elastomer model. Hence, sufficient care must be exercised in modelling the elastomer.

Appendix A

Derivation of Strain Expressions

The procedure for deriving the strain expressions mentioned in Sec. 5.2.4.1 follows the method outlined in Ref. [46].

A.1 Coordinate Transformation

For the derivation of strain expressions, it is essential to establish transformation relations between various coordinate systems used in this formulation.

The transformation relation between the undeformed curvilinear cross-sectional coordinate system $(\hat{e}_x, \hat{e}_\eta, \hat{e}_\zeta)$ and the cross-section fixed rotating coordinate system $(\hat{e}_{x1}, \hat{e}_{y1}, \hat{e}_{z1})$ can be defined as (Fig. 5.3)

$$\begin{Bmatrix} \hat{e}_x \\ \hat{e}_\eta \\ \hat{e}_\zeta \end{Bmatrix} = [T_1] \begin{Bmatrix} \hat{e}_{x1} \\ \hat{e}_{y1} \\ \hat{e}_{z1} \end{Bmatrix} \quad (\text{A.1})$$

where

$$T_1 = \begin{bmatrix} 1 & 0 & 0 \\ 0 & \cos \theta & \sin \theta \\ 0 & -\sin \theta & \cos \theta \end{bmatrix} \quad (A.2)$$

Since the system $(\hat{e}_{x1}, \hat{e}_{y1}, \hat{e}_{z1})$ is parallel to $(\hat{e}_x, \hat{e}_y, \hat{e}_z)$ system, the transformation given by Eq. A.2 is also applicable between $(\hat{e}_x, \hat{e}_\eta, \hat{e}_\zeta)$ and $(\hat{e}_x, \hat{e}_y, \hat{e}_z)$

Differentiation of Eq. A.1 with respect to x yields

$$\begin{aligned} \begin{Bmatrix} \hat{e}_{x,x} \\ \hat{e}_{\eta,x} \\ \hat{e}_{\zeta,x} \end{Bmatrix} &= \begin{Bmatrix} 0 \\ \tau_0 \hat{e}_\zeta \\ -\tau_0 \hat{e}_\eta \end{Bmatrix} \\ &= \begin{bmatrix} 0 & 0 & 0 \\ 0 & 0 & \tau_0 \\ 0 & -\tau_0 & 0 \end{bmatrix} \begin{Bmatrix} \hat{e}_x \\ \hat{e}_\eta \\ \hat{e}_\zeta \end{Bmatrix} \end{aligned} \quad (A.3)$$

$$\text{where } \tau_0 = \theta_{,x} \quad (A.4)$$

represents the initial twist of the blade.

The transformation between the deformed curvilinear coordinate system and the undeformed curvilinear coordinate system is due to rigid body rotation. It can be defined as

$$\begin{Bmatrix} \hat{e}_{x'} \\ \hat{e}_{\eta'} \\ \hat{e}_{\zeta'} \end{Bmatrix} = [T_2] \begin{Bmatrix} \hat{e}_x \\ \hat{e}_\eta \\ \hat{e}_\zeta \end{Bmatrix} \quad (A.5)$$

where the transformation matrix $[T_2]$ is given by

$$[T_2] = \begin{bmatrix} 1 & 0 & 0 \\ 0 & \cos \theta_x & \sin \theta_x \\ 0 & -\sin \theta_x & \cos \theta_x \end{bmatrix} \begin{bmatrix} \cos \theta_\eta & 0 & \sin \theta_\eta \\ 0 & 1 & 0 \\ -\sin \theta_\eta & 0 & \cos \theta_\eta \end{bmatrix} \begin{bmatrix} \cos \theta_\zeta & \sin \theta_\eta & 0 \\ -\sin \theta_\eta & \cos \theta_\zeta & 0 \\ 0 & 0 & 1 \end{bmatrix} \quad (A.6)$$

The above transformation is obtained by following lag-flap-torsion sequence of motions. First the blade is rotated by θ_ζ about \hat{e}_ζ . Then it is rotated by θ_η about the rotated \hat{e}_η axis. Finally, it is rotated by θ_x about the rotated \hat{e}_x axis. The deformation sequence is shown in Fig. A.1.

Using Eqs. A.1 and A.6, the relation between the deformed curvilinear coordinate system and cross-sectional fixed rotating coordinate system can be written as

$$\begin{Bmatrix} \hat{e}_{x'} \\ \hat{e}_{\eta'} \\ \hat{e}_{\zeta'} \end{Bmatrix} = [\mathbf{T}] \begin{Bmatrix} \hat{e}_{x1} \\ \hat{e}_{y1} \\ \hat{e}_{z1} \end{Bmatrix} \quad (\text{A.7})$$

where

$$[\mathbf{T}] = [\mathbf{T}_1][\mathbf{T}_2] \quad (\text{A.8})$$

The relationships between the Euler angles $(\theta_\eta, \theta_\zeta, \phi)$ and the displacement variables (u, v, w) can be obtained from Fig. A.1 as

$$\begin{aligned} \theta_x &= \phi \\ \sin \theta_\eta &= \frac{v_{,x} \sin \theta - w_{,x} \cos \theta}{\sqrt{(1 + u_{,x})^2 + (v_{,x} \cos \theta + w_{,x} \sin \theta)^2 + (w_{,x} \cos \theta - v_{,x} \sin \theta)^2}} \\ \cos \theta_\eta &= \frac{\sqrt{(1 + u_{,x})^2 + (v_{,x} \cos \theta + w_{,x} \sin \theta)^2}}{\sqrt{(1 + u_{,x})^2 + (v_{,x} \cos \theta + w_{,x} \sin \theta)^2 + (w_{,x} \cos \theta - v_{,x} \sin \theta)^2}} \\ \sin \theta_\zeta &= \frac{(v_{,x} \cos \theta + w_{,x} \sin \theta)}{\sqrt{(1 + u_{,x})^2 + (v_{,x} \cos \theta + w_{,x} \sin \theta)^2}} \\ \cos \theta_\eta &= \frac{1 + u_{,x}}{\sqrt{(1 + u_{,x})^2 + (v_{,x} \cos \theta + w_{,x} \sin \theta)^2}} \end{aligned} \quad (\text{A.9})$$

Applying ordering scheme, the transformation relationship becomes

$$[\mathbf{T}] = \begin{bmatrix} 1 & v_{,x} & w_{,x} \\ -v_{,x} \cos(\theta + \phi) - w_{,x} \sin(\theta + \phi) & \cos(\theta + \phi) & \sin(\theta + \phi) \\ v_{,x} \sin(\theta + \phi) - w_{,x} \cos(\theta + \phi) & -\sin(\theta + \phi) + \tau'_c \cos \theta & \cos(\theta + \phi) + \tau'_c \sin \theta \end{bmatrix} \quad (\text{A.10})$$

where

$$\tau_c' = (v_{,x} \sin \theta - w_{,x} \cos \theta)(v_{,x} \cos \theta + w_{,x} \sin \theta) \quad (\text{A.11})$$

With the small angle approximation, Eq. A.10 reduces to

$$[T] = \begin{bmatrix} 1 & v_{,x} & w_{,x} \\ -v_{,x} - w_{,x}(\theta + \phi) & 1 & (\theta + \phi) \\ v_{,x}(\theta + \phi) - w_{,x} & -(\theta + \phi - v_{,x}w_{,x}) & 1 \end{bmatrix} \quad (\text{A.12})$$

The relationship between the undeformed curvilinear cross-sectional coordinate system and the hub fixed rotating coordinate system is also given by

$$\begin{Bmatrix} \hat{e}_{x'} \\ \hat{e}_{\eta'} \\ \hat{e}_{\zeta'} \end{Bmatrix} = [T] \begin{Bmatrix} \hat{e}_x \\ \hat{e}_y \\ \hat{e}_z \end{Bmatrix} \quad (\text{A.13})$$

A.2 Kinematics of Deformation

The position vector of a point P on the undeformed beam with respect to the hub centre is given by

$$\mathbf{r}(x, \eta, \zeta) = x\hat{e}_x + \eta\hat{e}_\eta + \zeta\hat{e}_\zeta \quad (\text{A.14})$$

The undeformed base vectors at P are

$$\begin{aligned} \mathbf{g}_x = \mathbf{r}_{,x} &= \hat{e}_x - \zeta\tau_0\hat{e}_\eta + \eta\tau_0\hat{e}_\zeta \\ \mathbf{g}_\eta &= \mathbf{r}_{,\eta} = \hat{e}_\eta \\ \mathbf{g}_\zeta &= \mathbf{r}_{,\zeta} = \hat{e}_\zeta \end{aligned} \quad (\text{A.15})$$

$$\text{where } \tau_0 = \theta_{,x}$$

The position vector of the point P in the deformed configuration can be written as

$$\mathbf{R}(x, \eta, \zeta) = \mathbf{R}_o(x) + \eta \mathbf{E}_\eta + \zeta \mathbf{E}_\zeta + \alpha \Psi(\eta, \zeta) \hat{e}_{x'} \quad (\text{A.16})$$

$$\begin{aligned} \text{where } \mathbf{R}_o(x) &= \mathbf{R}(x, 0, 0) \\ &= (x + u) \hat{e}_x + v \hat{e}_y + w \hat{e}_z \end{aligned} \quad (\text{A.17})$$

The first three terms of the right hand side of Eq. A.16 represent translations and rotations of cross-section. The last term is the out of plane warping of the cross-section where α is the amplitude of warping. Since the coordinate system $(\hat{e}_{x'}, \hat{e}_{\eta'}, \hat{e}_{\zeta'})$ is obtained by translation and rotation of the coordinate system $(\hat{e}_x, \hat{e}_y, \hat{e}_z)$, the unit vector $\hat{e}_{x'}$ can be assumed to be in the direction of \mathbf{E}_x *i.e.*, along the tangent to the deformed elastic axis of the beam, while the orientations of $\hat{e}_{\eta'}$ and $\hat{e}_{\zeta'}$ are approximately equal to \mathbf{E}_η and \mathbf{E}_ζ , respectively [122]. Following the definition given in Ref. [122], the deformed base vectors at a point on the elastic axis can be expressed as

$$\begin{aligned} \mathbf{E}_x &= (1 + \bar{\epsilon}_{xx}) \hat{e}_{x'} \\ \mathbf{E}_\eta &= 2\bar{\epsilon}_{x\eta} \hat{e}_{x'} + (1 + \bar{\epsilon}_{\eta\eta}) \hat{e}_{\eta'} + 2\bar{\epsilon}_{\eta\zeta} \hat{e}_{\zeta'} \\ \mathbf{E}_\zeta &= 2\bar{\epsilon}_{x\zeta} \hat{e}_{x'} + 2\bar{\epsilon}_{\eta\zeta} \hat{e}_{\eta'} + (1 + \bar{\epsilon}_{\zeta\zeta}) \hat{e}_{\zeta'} \end{aligned} \quad (\text{A.18})$$

The assumption of no shear deformation and no deformation of the cross-section leads to

$$\bar{\epsilon}_{\eta\eta} = \bar{\epsilon}_{\zeta\zeta} = \bar{\epsilon}_{\eta\zeta} = \bar{\epsilon}_{x\eta} = \bar{\epsilon}_{x\zeta} = 0$$

The deformed base vector at the elastic axis can be expressed as

$$\begin{aligned} \mathbf{E}_x &= (1 + \bar{\epsilon}_{xx}) \hat{e}_{x'} \\ \mathbf{E}_\eta &= \hat{e}_{\eta'} \\ \mathbf{E}_\zeta &= \hat{e}_{\zeta'} \end{aligned} \quad (\text{A.19})$$

The deformed base vectors at the point P are:

$$\begin{aligned}\mathbf{G}_x &= \mathbf{R}'_x = \mathbf{E}_x + \eta \hat{\mathbf{e}}_{\eta',x} + \zeta \hat{\mathbf{e}}_{\zeta',x} + \alpha_{,x} \Psi \hat{\mathbf{e}}_{x',x} \\ \mathbf{G}_\eta &= \mathbf{R}_{,\eta} = \hat{\mathbf{e}}_{\eta'} + \alpha \Psi_{,\eta} \hat{\mathbf{e}}_{x'} \\ \mathbf{G}_\zeta &= \mathbf{R}_{,\zeta} = \hat{\mathbf{e}}_{\zeta'} + \alpha \Psi_{,\zeta} \hat{\mathbf{e}}_{x'}\end{aligned}\tag{A.20}$$

The component of strain tensor can be defined in the curvilinear cross-sectional coordinate system as

$$f_{ij} = \frac{1}{2} \{ (\mathbf{G}_i \cdot \mathbf{G}_j) - (\mathbf{g}_i \cdot \mathbf{g}_j) \}, \quad i, j = x, \eta, \zeta \tag{A.21}$$

Combining Eqs. A.15, A.19 and A.20, the strain expressions can be rewritten as

$$\begin{aligned}f_{xx} &= \bar{\epsilon}_{xx} - \eta k_\eta - \zeta k_\zeta + \alpha_{,x} \Psi + \frac{1}{2} (\eta^2 + \zeta^2) (\tau^2 - \tau_o^2) \\ f_{x\eta} &= f_{\eta x} = \frac{1}{2} [\alpha \Psi_{,\eta} - \zeta (\tau - \tau_o)] \\ f_{x\zeta} &= f_{\zeta x} = \frac{1}{2} [\alpha \Psi_{,\zeta} + \eta (\tau - \tau_o)] \\ f_{\eta\eta} &\approx 0 \\ f_{\zeta\zeta} &\approx 0 \\ f_{\eta\zeta} &= f_{\zeta\eta} \approx 0\end{aligned}\tag{A.22}$$

where the derivatives of triad $(\hat{\mathbf{e}}_x, \hat{\mathbf{e}}_{\eta'}, \hat{\mathbf{e}}_{\zeta'})$ are related to the curvatures k_η, k_ζ and twist τ of the deformed elastic axis of the beam by [45]

$$\begin{Bmatrix} \hat{\mathbf{e}}_{x',x} \\ \hat{\mathbf{e}}_{\eta',x} \\ \hat{\mathbf{e}}_{\zeta',x} \end{Bmatrix} = \begin{bmatrix} 0 & k_\eta & k_\zeta \\ -k_\eta & 0 & \tau \\ -k_\zeta & -\tau & 0 \end{bmatrix} \begin{Bmatrix} \hat{\mathbf{e}}_{x'} \\ \hat{\mathbf{e}}_{\eta'} \\ \hat{\mathbf{e}}_{\zeta'} \end{Bmatrix} \tag{A.23}$$

Strain Component in Local Cartesian System

The stress-strain relation of a material is generally given in the local cartesian system (y_1, y_2, y_3) with unit vectors $\hat{\mathbf{e}}_j$ ($j = 1, 2, 3$). Therefore, it is essential to express

the strain components in the local coordinate system. The expression for the strain tensor ϵ_{ij} in the local cartesian coordinates can be written as [45, 46]

$$\epsilon_{ij} = \sum_{k=1}^3 \sum_{l=1}^3 \frac{\partial x_k}{\partial y_i} \frac{\partial x_l}{\partial y_j} f_{kl} \quad (\text{A.24})$$

where x_i ($i = 1, 2, 3$) refer to the curvilinear coordinates system. The transformation relation between curvilinear system (x_i) and local cartesian system (y_i) for a twisted straight blade is given by

$$\begin{aligned} \left[\frac{\partial x_i}{\partial y_j} \right] &= [\mathbf{g}_k \cdot \mathbf{g}_i]^{-1} [\mathbf{g}_k \cdot \hat{\mathbf{e}}_j] \\ &= \begin{bmatrix} 1 & 0 & 0 \\ \zeta \tau_o & 1 & 0 \\ -\eta \tau_o & 0 & 1 \end{bmatrix} \end{aligned} \quad (\text{A.25})$$

where

$$[\mathbf{g}_k \cdot \mathbf{g}_i] = \begin{bmatrix} 1 + (\eta^2 + \zeta^2) \tau_o^2 & -\zeta \tau_o & \eta \tau_o \\ -\zeta \tau_o & 1 & 0 \\ \eta \tau_o & 0 & 1 \end{bmatrix} \quad (\text{A.26})$$

and

$$[\mathbf{g}_k \cdot \hat{\mathbf{e}}_j] = \begin{bmatrix} 1 & -\zeta \tau_o & \eta \tau_o \\ 0 & 1 & 0 \\ 0 & 0 & 1 \end{bmatrix} \quad (\text{A.27})$$

\mathbf{g}_i 's are given in Eq. A.15. (It may be noted that $(\hat{\mathbf{e}}_1, \hat{\mathbf{e}}_2, \hat{\mathbf{e}}_3)$ are parallel to $(\hat{\mathbf{e}}_x, \hat{\mathbf{e}}_\eta, \hat{\mathbf{e}}_\zeta)$.)

The determinant of the matrix tensor $[\mathbf{g}_k \cdot \mathbf{g}_i]$ is represented by symbol g ,

$$g = \det [\mathbf{g}_k \cdot \mathbf{g}_i] \quad (\text{A.28})$$

Combining Eqs. A.22, A.25 and A.24, one obtains the strain components in the local cartesian coordinates as

$$\epsilon_{xx} = \bar{\epsilon}_{xx} - \eta k_\eta - \zeta k_\zeta + \alpha_{,x} \Psi + \frac{1}{2} (\eta^2 + \zeta^2) (\tau - \tau_o)^2$$

$$\begin{aligned}
\gamma_{x\eta} &= \alpha \Psi_{,\eta} - \zeta (\tau - \tau_o) \\
\gamma_{x\zeta} &= \alpha \Psi_{,\zeta} + \eta (\tau - \tau_o) \\
\epsilon_{\eta\eta} &= \epsilon_{\zeta\zeta} = \gamma_{\eta\zeta} = 0
\end{aligned} \tag{A.29}$$

where

$$\gamma_{x\eta} = 2\epsilon_{x\eta} \ , \ \gamma_{x\zeta} = 2\epsilon_{x\zeta} \ , \ \gamma_{\eta\zeta} = 2\epsilon_{\eta\zeta}$$

For the aeroelastic analysis, it is essential to express the above strain components in terms of the displacement components (u, v, w) of the elastic axis and the elastic twist angle (ϕ) . By differentiating Eq. A.17 with respect to x , the deformed base vector at the elastic axis is given by

$$\mathbf{E}_x = (1 + u_{,x}) \hat{e}_x + v_{,x} \hat{e}_y + w_{,x} \hat{e}_z \tag{A.30}$$

Combining Eqs. A.19 and A.30, the magnitude of E_x can be written as

$$|\mathbf{E}_x|^2 = (1 + u)^2 + v_{,x}^2 + w_{,x}^2 = (1 + \bar{\epsilon}_{xx})^2 \tag{A.31}$$

Neglecting the terms $\bar{\epsilon}_{xx}^2$ and $(u_{,x})^2$, the axial strain $\bar{\epsilon}_{xx}$ can be expressed in terms of the displacement components (u, v, w) as

$$\bar{\epsilon}_{xx} = u_{,x} + \frac{1}{2} v_{,x}^2 + \frac{1}{2} w_{,x}^2 \tag{A.32}$$

Combining Eqs. A.3, A.6, A.9 and A.23 and applying the consistent ordering scheme, expression for the deformed curvatures and twist can be given by

$$\begin{aligned}
k_\eta &= v_{,xx} \cos(\theta + \phi) + w_{,xx} \sin(\theta + \phi) \\
k_\zeta &= -v_{,xx} \sin(\theta + \phi) + w_{,xx} \cos(\theta + \phi) \\
\tau &= \tau_o + \phi_{,x} + \phi_o
\end{aligned} \tag{A.33}$$

where ϕ_o , the second order elastic twist effect of the beam can be given by

$$\phi_o = (-v_{,x} \sin \theta + w_{,x} \cos \theta) (v_{,xx} \cos \theta + w_{,xx} \sin \theta) \quad (\text{A.34})$$

Introducing Eqs. A.32 and A.33 into Eq. A.29 and assuming the warping amplitude to be equal to derivative of elastic twist

$$\alpha = -\phi_{,x} \quad (\text{A.35})$$

and neglecting the second order twist effect, the strain components can be expressed as

$$\begin{aligned} \epsilon_{xx} &= u_{,x} + \frac{1}{2}v_{,x}^2 + \frac{1}{2}w_{,x}^2 - v_{,xx}[\eta \cos(\theta + \phi) - \zeta \sin(\theta + \phi)] \\ &\quad - w_{,xx}[\eta \sin(\theta + \phi) + \zeta \cos(\theta + \phi)] + (\eta^2 + \zeta^2) \frac{\phi_{,x}^2}{2} \\ \gamma_{x\eta} &= \phi_{,x}\Psi_{,\eta} - \zeta\phi_{,x} \\ \gamma_{x\zeta} &= \phi_{,x}\Psi_{,\zeta} + \eta\phi_{,x} \end{aligned} \quad (\text{A.36})$$

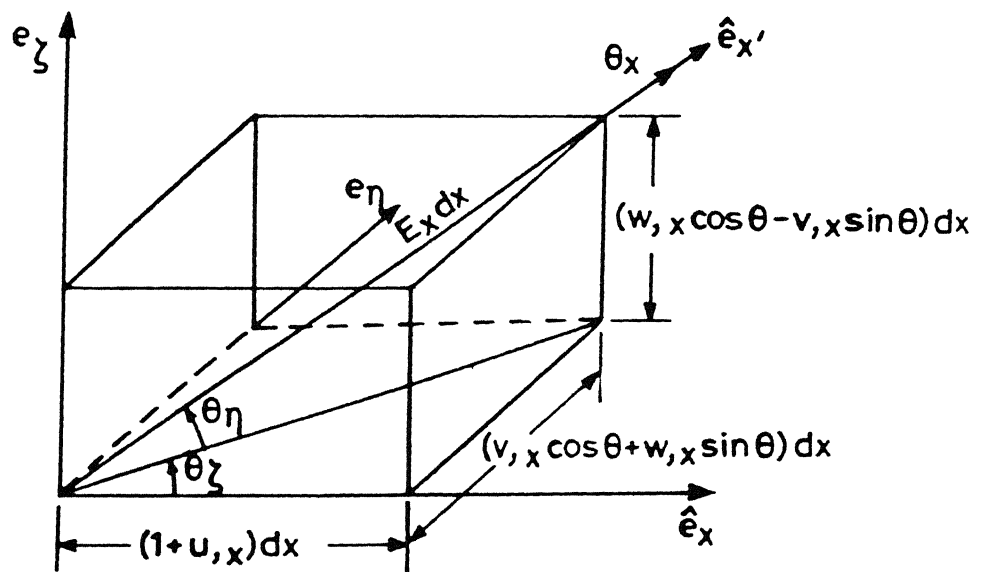


Fig. A.1 Deformation sequence and Euler angles.

REFERENCES

1. Schindler, R., and Pfisterer, E., "Impacts of Rotor Hub Design Criteria on the Operational Capabilities of Rotorcraft Systems," *AGARD CP-423, Rotorcraft Design for Operations*, Oct. 1986, pp. 15.1-15.23.
2. Bousman, W. G., Ormiston, R. A., and Mirick, P. H., "Design Considerations for Bearingless Rotor Hubs," *39th Annual Forum of the American Helicopter Society*, St. Louis, Missouri, May 1983, pp. 509-536.
3. Huber, H., "Will Rotor Hubs Lose Their Bearings? A Survey of Bearingless Main Rotor Development," *Eighteenth European Rotorcraft Forum*, Avignon, France, Sept, 1992, pp. 506.1-506.19.
4. Panda, B., and Mychalowycz, E., "Aeroelastic Stability Wind Tunnel Testing with Analytical Correlation of the Comanche Bearingless Main Rotor," *Journal of the American Helicopter Society*, Vol. 42, No. 3, 1997, pp. 207-217.
5. Weller, W. H., "Variation in Hover Aeromechanical Stability Trends with Bearingless Main Rotor Design," *Journal of the American Helicopter Society*, Vol. 39, No. 1, 1994, pp. 70-80.
6. Kampa, K., Enenkl, B., Polz, G., and Roth, G., "Aeromechanical Aspects in the Design of the EC135," *23rd European Rotorcraft Forum*, Dresden, Germany, Sept

1997, pp. 38.1-38.14.

7. Fung, Y. C., *Foundation of Solid Mechanics*, Prentice-Hall, Englewood Cliffs, NJ, 1965, pp. 412-420.
8. Lesieutre, G. A., and Mingori, D. L., "Finite Element Modeling of Frequency-Dependent Material Damping Using Augmenting Thermodynamic Fields," *Journal of Guidance, Control, and Dynamics*, Vol. 13, No. 6, 1990, pp. 1040-1050.
9. Lesieutre, G. A., and Bianchini, E., "Time-Domain Modeling of Linear Viscoelasticity Using Anelastic Displacement Fields," *Journal of Vibration and Acoustics*, Vol. 117, No. 4, 1995, pp. 424-430.
10. Golla, D. F., and Hughes, P. C., "Dynamics of Viscoelastic Structures—A Time-Domain Finite Element Formulation," *Journal of Applied Mechanics*, Vol. 52, No. 4, 1985, pp. 897-906.
11. Bagley, R. L., and Torvik, P. J., "A Generalized Derivative Model for an Elastomeric Damper," *Shock and Vibration Bulletin*, Vol. 49, No. 2, 1979, pp. 135-143.
12. Bagley, R. L., and Torvik, P. J., "Fractional Calculus—A Different Approach to the Analysis of Viscoelastically Damped Structures," *AIAA Journal*, Vol. 21, No. 5, 1983, pp. 741-748.
13. Bagley, R. L., and Calico, R. A., "Fractional Order State Equations for the Control of Viscoelastically Damped Structures," *Journal of Guidance, control, and Dynamics*, Vol. 14, No. 3, 1991, pp. 304-311.
14. Fenander, A., "Modal Synthesis with Modeling Damping by Use of Fractional Derivatives," *AIAA Journal*, Vol. 34, No. 5, 1996, pp. 1051-1058.

15. Bagley, R. L., and Torvik, P. J., "Fractional Calculus in the Transient Analysis of Viscoelastically Damped Structures," *AIAA Journal*, Vol. 23, No. 6, 1985, pp. 918-925.
16. Enelund, M., and Josefson, B. L., "Time-Domain Finite Element Analysis of Viscoelastic Structures with Fractional Derivatives Constitutive Relations," *AIAA Journal*, Vol. 35, No. 10, 1997, pp. 1630-1637.
17. Findley, W. N., and Lai, J. S. Y., "A Modified Superposition Principle Applied to Creep of Nonlinear Viscoelastic Material under Abrupt Changes in State of Combined Stress," *Transaction of the Society of Rheology*, Vol. 11, 1967, pp. 361-367.
18. Bernstein, B., Kearsley, E. A., and Zapas, L. J., "A Study of Stress Relaxation with Finite Strain," *Transaction of the Society of Rheology*, Vol. 7, 1964, pp. 391-410.
19. Schapery, R. A., "On the Characterization of Nonlinear Viscoelastic Materials," *Polymer Engineering and Science*, Vol. 9, No. 4, July. 1969, pp. 295-310.
20. Glockner, P. G., and Szyszkowski, W., "An Engineering Multiaxial Constitutive Model for Nonlinear Time-Dependent Materials," *Int. J. Solids Structures*, Vol. 26, No. 1, 1990, pp. 73-82.
21. Szyszkowski, W., and Glockner, P. G., "A Nonlinear Constitutive Model for Ice," *Int. J. Solids Structures*, Vol. 21, No. 3, 1985, pp. 307-321.
22. Potter, J. L., McGuire, D. P., and Brubaker, E. L., "Elastomers + Fluids + Electronics = Improved Comfort and Reliability for Aircraft," *Proceedings of the International Exhibition Cum Seminar on Helicopter Development and Utilisation*

- in South Asia-Pacific*, Bangalore, India, Oct. 1995, pp. 6.3.1-6.3.19.
23. McGuire, D. P., "The Application of Elastomeric Lead-lag Dampers to Helicopter Rotors," Lord Library No. LL2133.
24. Housmann, G., and Gergely, P., "Approximate Methods for Thermoviscoelastic Characterization and Analysis of Elastomeric Lead-Lag Damper," *Eighteenth European Rotorcraft Forum*, Avignon, France, Sept 1992, pp. 88.1-88.17.
25. Housmann, G., "Structural Analysis and Design Considerations of Elastomeric Dampers with Viscoelastic Material Behavior," *Twelfth European Rotorcraft Forum*, Garmisch-Partekirchen, Germany, Sept 1986, pp. 70.1-70.26.
26. Felker, F., Lau, B., McLaughlin, S., and Johnson, W., "Nonlinear Behavior of an Elastomeric Lag Damper undergoing Dual-frequency Motion and its Effect on Rotor Dynamics," *Journal of the American Helicopter Society*, Vol. 34, No. 4, 1987, pp. 45-53.
27. Smith, E. C., Beale, M. R., Govindswamy, K., Vascineci, M. J., and Lesieutre, G. A., "Formulation and Validation of a Finite Element Model for Elastomeric Lag Dampers," *51st Annual Forum of the American Helicopter Society*, Fort Worth, TX, May 1995, pp. 1101-1116.
28. Govindswamy, K. and Smith, E. C., "Aerothermoelastic Behavior of Helicopter with Elastomeric Lag Dampers," *American Helicopter Society Aeromechanics Specialists' Meeting*, Fairfield, CT, Oct 1995, pp. 8.52-8.70.
29. Gandhi, F., Chopra, I., and Lee, S. W., "A Nonlinear Viscoelastic Damper Model: Constitutive Equation and Solution Scheme," *(SPIE) North American Conference on Smart Structures and Materials*, Orlando, FL, Feb 1994.

30. Gandhi, F., and Chopra, I., "Analysis of Bearingless Main Rotor Dynamics with the Inclusion of an Improved Time Domain Nonlinear Elastomeric Damper Model," *Journal of the American Helicopter Society*, Vol. 41, No. 3, 1996, pp. 267-277.
31. Ormiston, R. A., Saberi, H., and Anastassiades, T., "Application of 2GCHAS to the Investigation of Aeromechanical Stability of Hingeless Rotor Helicopters," *51st Forum of the American Helicopter Society*, Fort Worth, TX, May 1995, pp. 1132-1155.
32. Kunz, D. L., "Influence of Elastomeric Damper Modeling on the Dynamic Response of Helicopter Rotors," *AIAA Journal*, Vol. 35, No. 2, 1997, pp. 349-354.
33. Houbolt, J. C., and Brooks, G. W., "Differential Equations of Motion for Combined Flapwise Bending, Chordwise Bending and Torsion of Twisted Nonuniform Rotor Blades," *NACA Report 1346*, 1958.
34. Friedmann, P. P., "Recent Developments in Rotary Wing Aeroelasticity," *Journal of Aircraft*, Vol. 14, No. 11, 1977, pp.1027-1041.
35. Hodges, D. H., and Dowell, E. H., "Nonlinear Equations of Motion for the Elastic Bending and Torsion of Twisted Non-uniform Rotor Blades," *NASA TN D-7818*, 1974.
36. Rosen, A., and Friedmann, P. P., "Nonlinear Equations of Equilibrium for Elastic Helicopter or Wind Turbine Blades Undergoing Moderate Deflection," *NASA CR-159478*, 1978.
37. Kaza, K. R., and Kvaternik, R. G., "Nonlinear Aeroelastic Equations for Combined Flapwise Bending, Chordwise Bending, Torsion and Extension of Twisted Nonuniform Rotor Blades in Forward Flight," *NASA TM-74059*, 1977.

38. Crespo, D. S., M. R. M., and Hodges, D. H., "Nonlinear Flexure and Torsion of Rotating Beams, with Application to Helicopter Blades-I. Formulation," *Vertica*, Vol. 10, 1986, pp. 151-169.
39. Crespo, D., M. R. M., and Hodges, D. H., "Nonlinear Flexure and Torsion of Rotating Beams, with Application to Helicopter Blades-II. Results for Hover," *Vertica*, Vol. 10, 1986, pp. 171-186.
40. Rosen, A., and Friedmann, P. P., "The Nonlinear Behavior of Elastic Slender Straight Beams Undergoing Small Strains and Moderate Rotations," *Journal of Applied Mechanics*, Vol. 46, 1979, pp. 161-168.
41. Bauchau, O. A., and Hong, C. H., "Large Displacement Analysis of Naturally Curved and Twisted Composite Beams," *AIAA Journal*, Vol. 25, No. 11, 1987, pp. 1449-1475.
42. Bauchau, O. A., and Hong, C. H., "Nonlinear Composite Beam Theory," *Journal of Applied Mechanics*, Vol. 55, No. 12, 1988, pp. 156-163.
43. Minguet, P., and Dugundji, J., "Experiments and Analysis for Composite Blades under Large Deflection: Part 1 - Static Behavior," *AIAA Journal*, Vol. 28, 1990, pp. 1580-1588.
44. Minguet, P., and Dugundji, J., "Experiments and Analysis for Composite Blades under Large Deflection: Part 2 - Dynamic Behavior," *AIAA Journal*, Vol. 28, 1990, pp. 1580-1588.
45. Washizu, K., "Considerations on a Naturally Curved and Twisted Slender Beam," *Journal of mathematics and Physics*, Vol. 43, No. 2, 1964, pp. 111-116.

46. Yuan, K. A., and Friedmann, P.P., "Aeroelasticity and Structural Optimization of Composite Helicopter Rotor Blades with Swept Tips, *NASA Report 4665*, May 1995.
47. Dowell, E. H., Traybar, J., and Hodges, D. H., "An Experimental Theoretical Correlation Study of Non-linear Bending and Torsion Deformations of a Cantilever Beam," *Journal of Sound and Vibrations*, Vol. 50, 1977, pp. 533-544.
48. Hodges, D. H., and Ormiston, R. A., "Stability of Elastic Bending and Torsion of Uniform Cantilever Rotor Blades in Hover with Variable Structural Coupling," NASA TN D-8192, 1976.
49. Shamie, J., and Friedmann, P. P., "Effect of Moderate Deflections on the Aeroelastic Stability of a Rotor Blade in Forward Flight," *Third European Rotorcraft and Powered Lift Aircraft Forum*, Aix-en-Provence, 1977, pp. 24.1-24.37.
50. Sivaneri, N. T., and Chopra, I., "Dynamic Stability of a Rotor Blade Using Finite Element Analysis," *AIAA Journal*, Vol. 20, No. 5, 1982, pp. 716-723.
51. Celi, R., and Friedmann, P. P., "Aeroelastic Modeling of Swept Tip Rotor Blade Using Finite Elements," *Journal of the American Helicopter Society*, Vol. 33, No. 2, 1988, pp. 43-52.
52. Celi, R., and Friedmann, P. P., "Rotor Blade Aeroelasticity in Forward Flight with an implicit Aerodynamic Formulation," *AIAA Journal*, Vol. 26, No. 2, 1988, pp. 1425-1433.
53. Bauchau, O. A., "A Beam Theory for Anisotropic Materials," *Journal of Applied Mechanics*, Vol. 52, 1985, pp. 416-422.

54. Bauchau, O. A., and Hong, C. H., "Finite Element Approach to Rotor Blade Modeling," *Journal of the American Helicopter Society*, Vol. 32, No. 1, 1987, pp. 60-67.
55. Bauchau, O. A., Coffenberry, B. S., and Rehfield, L. W., "Composite Box Beam Analysis: Theory and Experiments," *Journal of Reinforced Plastic and Composites*, Vol. 6, 1987, pp. 25-35.
56. Kosmatka, J. B., and Friedmann, P. P., "Vibration Analysis of Composite Turbopropellers Using a Nonlinear Beam-Type Finite Element Approach," *AIAA Journal*, Vol. 27, No. 11, 1989, pp. 1606-1614.
57. Yuan, K. A., Friedmann, P. P., and Venkatesan, C., "A New Aeroelastic Model for Composite Rotor Blades with Straight and Swept Tips," *AIAA Paper No. 92-2259*, 33rd AIAA/ASME/ASCE/AHS/ASC Structures, Structural Dynamics and Materials Conference, Dallas, TX, April 1992, pp. 1371-1390.
58. Yuan, K. A., Venkatesan, C., and Friedmann, P. P., "Structural Dynamic Model of Composite Rotor Blades Undergoing Moderate Deflections," Recent Advances in Structural Dynamic Modeling of Composite Rotor Blades and Thick Composites. *ASME AD-Vol.30*, ASME Winter Annual Meeting, Nov. 1992, pp. 127-155.
59. Smith, E. C., and Chopra, I., "Formulation and Evaluation of an Analytical Model for Composite Box Beams," *Journal of the American Helicopter Society*, Vol. 36, No. 3, 1991, pp. 23-35.
60. Friedmann, P. P., "Helicopter Rotor Dynamics and Aeroelasticity: Some Key Ideas and Insights," *Vertica*, Vol. 14, No. 1, 1990, pp. 101-121.

61. Hodges, D. H., "Review of Composite Rotor Blade Modeling," *AIAA Journal*, Vol. 28, No. 3, 1990, pp. 561-564.
62. Friedmann, P. P., and Hodges, D. H., "Rotary Wing Aeroelasticity with Application to VTOL Vehicle," edited by A.K. Noor and S.L. Venneri, Published by ASME, 1993, pp. 299-391.
63. Hong, C. H., and Chopra, I., "Aeroelastic Stability Analysis of Composite Rotor Blade," *Journal of the American Helicopter Society*, Vol. 30, No. 2, 1985, pp. 57-67.
64. Panda, B., and Chopra, I., "Dynamics of Composite Rotor Blades in Forward Flight," *Vertica*, Vol. 11, No. 1/2, 1987, pp. 187-209.
65. Tracy, A. L., and Chopra, I., "Aeroelastic Stability Investigation of a Composite Hingeless Rotor in Hover," *Journal of aircraft*, Vol. 35, No. 5, 1998, pp. 791-797.
66. Kim, K. C., and Chopra, I., "Aeroelastic Analysis of Swept, Anhedral, and Tapered Tip Rotor Blades," *Journal of the American Helicopter Society*, Vol. 37, No. 1, 1992, pp. 15-30.
67. Bir, G. S., and Chopra, I., "Aeromechanical Stability of Rotorcraft with Advanced Geometry Blades," *34th Proceeding of AIAA/ASME/ASCE/AHS/ASC Structures, Structural Dynamics and Materials Conference*, La Jolla, CA, April 1993, pp. 38-62.
68. Bielawa, R. L., "Aeroelastic Characteristics of Composite Rotor Blades," *Journal of the American Helicopter Society*, Vol. 2, No. 9, 1977, pp. 2-9.
69. Sivaneri, N. T., and Chopra, I., "Finite Element Analysis for Bearingless Rotor Blade Aeroelasticity," *Journal of the American Helicopter Society*, Vol. 29, No.

- 2, 1984, pp. 42-51.
70. Hong, C. H., and Chopra, I., "Aeroelastic Stability Analysis of a Composite Bearingless Rotor Blade," *Journal of the American Helicopter Society*, Vol. 31, No. 4, 1986, pp. 29-35.
71. Dull, A. L., and Chopra, I., "Aeroelastic Stability of Bearingless Rotors in Forward Flight," *Journal of the American Helicopter Society*, Vol. 33, No. 4, 1988, pp. 38-46.
72. Gandhi, F., and Chopra, I., "An Aeroelastic Analysis Methodology for Bearingless Main Rotor Helicopters," *Journal of the American Helicopter Society*, Vol. 43, No. 1, 1998, pp. 66-75.
73. Young, M. I., and Bailey, D. J., "Stability and Control of Hingeless Rotor Helicopter Ground Resonance," *Journal of aircraft*, Vol. 11, No. 6, 1974, pp. 333-339.
74. Straub, F. K., and Warmbrodt, W., "The Use of Active Controls to Augment Rotor/Fuselage Stability," *Journal of the American Helicopter Society*, Vol. 30, No. 3, 1985, pp. 13-22.
75. Straub, F. K., "Optimal Control of Helicopter Aeromechanical Stability," *Vertica*, Vol. 11, No. 3, 1987, pp. 425-435.
76. Weller, W. H., "Fuselage State Feedback for Aeromechanical Stability Augmentation of a Bearingless Main Rotor," *Journal of the American Helicopter Society*, Vol. 41, No. 2, 1996, pp. 85-93.
77. Tettenborn, G., Kessler, Ch., and Reichert, G., "Comparison of IBC with Active Controllers Using a Conventional Swashplate to Suppress Ground and Air res-

- onance," *23rd European Rotorcraft Forum*, Dresden, Germany, Sept 1997, pp. 13.1-13.9.
78. Ormiston, R. A., "Aeromechanical Stability of Soft-in-plane Hingeless Rotor Helicopter," *Third European Rotorcraft and Powered Lift Aircraft Forum, Aix-en-Provence*, France, Sept 1977, pp. 25.1-25.22.
79. Ormiston, R. A., "Rotor-fuselage Dynamics of Helicopter Air and Ground Resonance," *Journal of the American Helicopter Society*, Vol. 36, No. 2, 1991, pp. 3-20.
80. Bousman, W. G., "An Experimental Investigation of the Effects of Aeroelastic Coupling on Aeromechanical Stability of a Hingeless Rotor Helicopter," *Journal of the American Helicopter Society*, Vol. 26, No. 1, 1981, pp. 46-54.
81. Zotto, M. D., and Loewy, R. G., "Influence of Pitch-lag Coupling on Damping Requirements to Stabilize Ground/Air Resonance," *Journal of the American Helicopter Society*, Vol. 37, No. 4, 1992, pp. 68-71.
82. Nagabhushanam, J., and Gaonkar, G. H., "Rotorcraft Air Resonance in Forward Flight with Various Dynamic Inflow Models and Aeroelastic Couplings," *Vertica*, Vol. 8, No. 4, 1984, pp. 373-393.
83. Johnson, W., "Influence of Unsteady Aerodynamics of Hingeless Rotor in Ground Resonance," *Journal of Aircraft*, Vol. 19, No. 8, 1982, pp. 668-673.
84. Friedmann, P. P., and Venkatesan, C., "Coupled Helicopter Rotor/Body Aeromechanical Stability, Comparison of Experimental and Theoretical results," *Journal of Aircraft*, Vol. 22, No. 2, 1985, pp. 148-155.

85. Friedmann, P. P., and Venkatesan, C., "Influence of Unsteady Aerodynamic Models on Aeromechanical Stability in Ground Resonance," *Journal of the American Helicopter Society*, Vol. 31, No. 1, 1986, pp. 65-74.
86. Venkatesan, C., "Influence of Aeroelastic Coupling on Coupled Rotor/Body Dynamics," *6th International Workshop on Dynamics, Aeroelastic Stability Modelling of Rotorcraft*, University of California, Los Angeles, Nov. 8-10, 1995.
87. Gandhi, F., and Hathaway, E., "Optimized Aeroelastic Couplings for Alleviation of Helicopter Ground Resonance," *Journal of Aircraft*, Vol. 35, No. 4, 1998, pp. 582-590.
88. Gandhi, F., and Chopra, I., "An Analytical Model for a Nonlinear Elastomeric Lag Damper and its Effect on Aeromechanical Stability in Hover," *Journal of the American Helicopter Society*, Vol. 39, No. 4, 1994, pp. 59-69.
89. Hodges, D. H., "A Theoretical Technique for Analyzing Aeroelastic Stability of Bearingless Rotors," *AIAA Journal*, Vol. 17, No. 4, 1978, pp. 400-407.
90. Hodges, D. H., "An Aeromechanical Stability Analysis for Bearingless Rotor Helicopters," *Journal of the American Helicopter Society*, Vol. 24, No. 1, 1979, pp. 2-9.
91. Jang, J., and Chopra, I., "Ground and Air Resonance of an Advanced Bearingless Rotor in Hover," *Journal of the American Helicopter Society*, Vol. 33, No. 3, 1988, pp. 20-29.
92. Jang, J., and Chopra, I., "Air Resonance of an Advanced Bearingless Rotor in Forward Flight," *2nd International Conference on Rotorcraft Basic Research*, College Park, MD, Feb. 1988.

93. Tracy, A. L., and Chopra, I., "Aeroelastic Analysis of a Composite Bearingless Rotor in Forward Flight with Improved Warping Modeling," *American Helicopter Society Aeromechanics Specialists' Conference*, San Francisco, California, Jan. 19-24, 1994,
94. Nayfeh, A. H., Mook, D. T., and Lobitz, D. W., "Numerical-Perturbation Method for the Nonlinear Analysis of Structural Vibrations," *AIAA Journal*, Vol. 12, No. 9, 1974, pp. 1222-1228.
95. Lobitz, D. W., Nayfeh, A. H., and Mook, D. T., "Nonlinear Analysis of Vibrations of Irregular Plates," *Journal of Sound and Vibration*, Vol. 49, No. 4, 1977, pp. 203-217.
96. Anderson, G. L., "On the extensional and flexural vibrations of rotating bars," *International Journal for Non-linear Mechanics* Vol. 10, 1975, pp. 223-236.
97. Hodges, D. H., "On the Extensional Vibrations of Rotating Bars," *International Journal for Non-linear Mechanics* Vol. 12, 1977, pp. 293-296.
98. Venkatesan, C., and Nagaraj, V. T., "On the Axial Vibrations of Rotating Bars," *Journal of Sound and Vibration*, Vol. 74, 1981, pp. 143-147.
99. Venkatesan, C., and Nagaraj, V. T., "Non-Linear Flapping Vibrations of Rotating Blades," *Journal of Sound and Vibration*, Vol. 84, 1982, pp. 549-556.
100. Dowell, E. H., "Component Mode Analysis of Nonlinear and Nonconservative System," *Journal of Applied Mechanics*, Vol. 47, 1980, pp. 172-176.
101. Pakdemirli, M., and Nayfeh, A. H., "Nonlinear Vibration of a Beam-Spring-Mass System," *Journal of Vibration and Acoustics*, Vol. 116, 1994, pp. 433-439.

102. Birman, V., "On the Effect of Nonlinear Elastic Foundation on Free Vibration of Beams," *Journal of Applied Mechanics*, Vol. 53, 1986, pp. 471-473.
103. Szemplinska-Stupnicka, W., *The Behavior of Non-linear Vibrating System, Vol. II*, Kluwer Academic Publishers, 1990.
104. Nayfeh, A. H., and Nayfeh, S. A., "Nonlinear Normal Modes of a Continuous System with Quadratic Nonlinearities," *Journal of Vibration and Acoustics*, Vol. 117, 1994, pp. 199-205.
105. Nayfeh, A. H., Chin, C., and Nayfeh, S. A., "Nonlinear Normal Modes of a Cantilever Beam," *Journal of Vibration and Acoustics*, Vol. 117, 1995, pp. 477-481.
106. Carpenter, P. J., and Fridovich, B., "Effect of a Rapid Blade-Pitch Increase on the Thrust and Induced-Velocity Response of a Full-Scale Helicopter Rotor," *Technical Note 3044, National Advisory Committee for Aeronautics*, Nov. 1953.
107. Dowell, E. H., "The behaviour of a Linear, Damped System with a Non-linear Spring-Mass-Dryfriction Damper system Attached," *Journal of Sound and Vibration*, Vol. 89, No. 1, 1983, pp. 65-84.
108. Nayfeh, A. H., *Differential equation and chaos*, N.H.Ibragimov ed. New Age Internatioal(P)Ltd. Johannesburg, 1996.
109. Friedmann, P., Yuan, K., Millott, T., and Venkatesan, C., "Correlation studies for hingeless rotors in forward flight," *AIAA Dynamics Specialists Conference*, AIAA-94-1722, 1994.
110. Gupta, P. K., Venkatesan, C., and Singh, O., "Structural Dynamics of Rotor Blades with Precone-presweep-predroop-pretwist and Torque Offset including

- Hub Motion," *Proceedings of 48th Annual General Body Meeting, Aeronautical Society of India*, 1997, pp. 77-92.
111. Suresh, J. K., Venkatesan, C., and Ramamurti, V., "Structural Dynamic Analysis of Composite Beams," *Journal of Sound and Vibration*, Vol. 143, No. 3, 1990, pp. 503-519.
112. Greenberg, J. M., "Airfoil in Sinusoidal Motion in a Pulsating Stream," *NACA TN-1326*, 1947.
113. Johnson, W., *Helicopter theory*, Princeton University, 1980.
114. Pitt, D. M., and Peters, D. A., "Theoretical Prediction of Dynamic-Inflow Derivatives," *Vertica*, Vol. 5, No. 1, 1981, pp. 21-34.
115. Peters, D. A., and Gaonkar, G. H., "Theoretical Flap-Lag Damping with Various Dynamic Inflow Models," *Journal of the American Helicopter Society*, Vol. 25, No. 3, 1980, pp. 29-36.
116. Su, Ay., Yoo, K. M., and Peters, D. A., "Extension and Validation of an Unsteady Wake Model for Rotors," *Journal of Aircraft* Vol. 29, No. 3, 1992, pp. 374-383.
117. Manjunath, A. R., Nagabhushanam, J., Gaonkar, G. H., Peters, D., and Su, A., "Flap-Lag Damping in Hover and Forward Flight with a Three Dimensional Wake," *Journal of the American Helicopter Society*, Vol. 38, No. 3, 1993, pp. 37-49.
118. Manjunath, A. R., Chunduru, S. J., Nagabhushanam, J., and Gaonkar, G. H., "Flap-Lag-Torsional Stability in Hover and Forward Flight with Three Dimensional Wake," *AIAA Journal*, Vol. 34, No. 1, 1996, pp. 18-28.

119. Padfield, G. D., *Helicopter Flight Dynamics: The theory and Application of Flying Qualities and Simulation Modeling*, AIAA Education Series, 1996.
120. Venkatesan, C., "Treatment of Axial Mode in Structural Dynamic and Aeroelastic Analysis of Rotor-Blades— A Review," *Proceedings of the National Seminar on Aero Structures - 94*, Dec 1994, pp. 361-372.
121. Jordon, D. W., and Smith, P., *Nonlinear Ordinary Differential Equation*, Clarendon Press, Oxford, 1977.
122. Wempner, G., *Mechanics of Solids with Application to Thin Bodies*, Sijthoff and Noordhoff, 1981.

131087

131087

This book is to be returned on the
date last stamped.

[illegible]